The University of Hull

Ablation of ophthalmic tissues with fibre delivered UV and IR lasers.

Being a Thesis submitted for degree of Doctor of Philosophy

in the University of Hull

by

M.E. Khosroshahi

BSc (Appl. phys./Elect.) Lancaster University

MSc (Analytical Phys.) Swansea University

May 1993

Summary of the thesis

In this thesis investigations of short pulse XeCl, KrF and ArF excimer lasers and HF laser transmission in fused silica and fluoride glass fibres respectively are reported, together with studies of polymer and soft tissue ablation in air and saline. Etch rate and photoacoustic measurements have been used to study the ablation process for the tissue and polymer samples with excimer lasers.

The main emphasis is on the HF laser where a UV pre-ionized transverse discharge in SF_6 - C_3H_8 mixtures was used to generate ~400ns (FWHM) pulses of energy up to 380mJ. Transmission measurements made on a 500μm core diameter fluoride glass fibre gave a distributed loss coefficient of 1.5×10^{-3} cm^{-1}, and a maximum useful input fluence of ~15Jcm^{-2}, set by non-linear loss at the fibre input surface.

For bovine cornea in air the onset of ablation occured at a fluence of ~0.5Jcm^{-2}, removal rates increased slowly up to ~3Jcm^{-2} but above this increased sharply, reaching ~17μm per pulse at 8Jcm^{-2}.

In saline the interaction becomes considerably more complicated because strong heating of water at the fibre tip leads to the formation of a hot, high pressure vapour cavity (optical cavitation). Under these conditions the damage range may extend well beyond the beam penetration depth as a result of flow effects (eg. jetting) and intense acoustic emission associated with the 'bubble' growth and collapse. The dynamics of cavitation 'bubbles' have been investigated using pulsed dye laser shadowgraphy for various fibre-tissue geometries and results in free liquid modelled using the

Rayleigh-Plesset theory. Time resolved photoacoustic measurements have also been made and revealed that very large transient pressures are generated in tissue near the fibre tip when ablation occurs in liquid; for example, at $8Jcm^{-2}$, peak pressures reached about 1.5×10^{8} Pa. When the fibre-to-sample spacing was varied physical surface damage was evident out to distances of $\sim$250μm for cornea and $\sim$2mm for retina. As these are much greater than the characteristic beam absorption length in water ($\sim$1.6μm), the main damage mechanism is then not through photoablation but jetting or acoustic emission associated with optical cavitation.

Waste not your Hour, nor in the vain pursuit
Of this and that endeavour and dispute;
Better be merry with the fruitful Grape
Than sadden after none, or bitter, Fruit.

With them the seed of Wisdom did I sow,
And with my own hand labour'd it to grow:
And this was all the harvest that I reap'd -
"I came like water, and like wind I go".

OMAR KHAYAM (Ca. 1048-1122)
Persian mathematician,
philosopher and poet.

This thesis is dedicated to my parents and family who constantly provided me with every possible support through many years of difficulties, and to my wife for her understanding and patience.

Acknowledgements

I would like to acknowledge the Ministry of culture and Higher Education of Iran for research sponsorship support. Equally I like to take this opportunity to express my appreciation to Professor P.E. Dyer for his supervision, constant encouragement and contributive discussions. Gratitude is also due to B. Tait and P. Monk for their generous technical assistance during my research. I am most grateful to J. Halder and T. Sinclair for preparation of tissue samples and polymers for SEM evaluation.

Part I: General Background

Part II: Excimer laser experiments

Chapter 1

Introduction

Why are lasers used in surgery? To answer this question one ought to study the advantages and disadvantages of lasers in general. Modern sceptics point out the following disadvantages: They are costly, frequently bulky, relatively imobile, additional attachments are needed for cooling, personnel must be trained in setting up and handling the laser so that it may be used with safety. The last point is particularly important to notice since only recently a patient's neck and one shoulder was burned when accidently an unidentified member hit the foot pedal after the completion of operation (1). It is therefore appropriate to remember the words of Goldmann (2) who once remarked: "if you don't need a laser don't use it", and Schawlow who said how pleased he was that lasers could be used to weld the retina of the eye but he would probably not have requested funding to build a laser if he had wanted to cure eye disease (3).

In the mid 1960's there was a little hope that the laser would become an effective means against cancer, particularly in light of the papers published by Minton (4) and Ketcham (5). These authors had found viable cancer cells in the debries ejected explosively during the pulsed irradiation of tumours and they suggested that there was danger that such cells could be forced into surrounding normal tissue and into adjacent blood vessels. Despite their disadvantages lasers are being applied more frequently in surgery because there are many conditions in which current surgical techniques are

relatively ineffective due to inaccessibility of the problem site.

The subject of laser irradiation of biological systems is believed to have started soon after the invention of the ruby laser in 1960. Since that time laser technology has opened a new era in biology and promises to play an important role in medicine. It is generally being accepted as a tool for diagnosis and treatment. The early interest in medical applications of the lasers centered on the ability of focused laser beams to coagulate blood vessels in the retina and to cut tissue (6,7,8). Today a variety of laser wavelengths are available for ocular photocoagulation ranging from 488nm to 1.064μm (9-15). The aplication of lasers to different parts of the eye are also extensively studied namely: keratotomy (16-19), keratectomy (20,21), sclerotomy (22,23), posterior capsulatomy (24,25), trabecuplasty (26-29), and iridectomy (30-35).

In the clinical application of lasers one ideally wants to irradiate specific cells or tissues and cause a specific reaction in them without harming any other cells. If such an ideal laser wavelength is found it will likely have some problems; for example, it may not deliver enough power, it may not have the right pulse width or it may not be possible to deliver it through an optical fibre. Broadly medical lasers are classified in a number of ways including: type of laser, wavelength, power, tissue effects (eg. cutting, coagulation) and other relevant factors. Accordingly the applications are divided into three main groups:

(i) - endoscopic applications such as gyneocology where CO_2

lasers are mainly used due to their ability to work in a bloodless field, haemostatic properties and reduction of thermal damage to adjacent structures by the relatively superficial penetration of 10.6 μm light.

(ii) - open-beam applications such as dentistry where the Nd:YAG and recently excimer lasers are effective in removing the plagues in enamel.

(iii) - Microscopic delivery for use in areas such as ophthalmology which is an important as well as most used clinical case. Another example is in neurosurgery where likewise widespread use of the operating microscope to excise benign and malignant tissue is made.

The possibility of working without touching the target area is useful in many conditions - in working on vascular organs such as the spleen, physical touching frequently will stimulate more bleeding. The ability to transmit laser energy through air or fluid allows applications at a distance in hollow organs, like the bladder and the stomach where it is sometimes difficult to place the endoscope in a position where actual contact with the target area is not possible. Photodynamic therapy (PDT) is one useful method of treatment of cancer in inaccessible areas such as the brain, lung and stomach where a careless physical contact may cause paralysis, tumour development and bleeding. At the moment PDT is still an active area of research with efforts concerned with gaining a better understanding of the physics, chemistry and biology of the interaction of light with tissues and photosensitizers.

There are many lasers that are now used routinely in

surgical and therapeutic applications. Of these the CO_2 laser invented by Patel (36) operating at wavelengths between 9-11μm in the infrared has proved to be especially important because of two properties: Firstly it is an inherently powerful and efficient device capable of delivering high powers from a compact unit, (eg.>10W for medical applications). Secondly its infrared beam is highly absorbed by water allowing the depth of an incision in tissue to be precisely controlled. A major problem exists for this laser, however, in that there are no fibres that are well suited to its delivery in a medical environment.

Fibres available for transmission of 10.6 μm wavelength are KRS-5, alkali halides, silver halides, chalcogenide and fluoride glass. However, these fibres present problems; for example, KRS-5 is poisonous because it contains thalium; alkali halides are found to be very difficult to protect against the mechanical damage; silver halides are photosensitive, and cannot be exposed to UV light; chalcogenide and fluoride glass fibres are very brittle. To overcome such difficulties new hollow waveguides based on single crystal sapphire have been developed (37,38). The important feature of these fibres in contrast to other circular hollow waveguides is the lack of mode mixing which leads to excessive bending loss. The potential usefulness of silver halide fibres for CO_2 laser transmission has been widely reported (39,40) and 5 watts output power from 0.45mm core-clad fibre diameter for a few minutes and about 1 joule in 10 msec CO_2 laser pulses has been achieved. Also, a core-only fibre of 0.9mm diameter apparently transmits more than

30 watts CW radiation (40). The proponents of these fibres (39) suggest that the usefulness of hollow waveguides in medicine is limited by their bulkiness and the sharp decrease of transmission when they are bent.

Lasers based on the Neodymium (Nd) ion became available for medical use in the early 1970's in the form of for example, the CW Nd:YAG laser. The large penetration depth and scattering of Nd:YAG laser radiation (1.06μm) within biological tissue result in the heating of large volumes. Haemostasis or destruction of tumours by coagulation necrosis requires well controlled laser parameters to reach the desired thermal action in a predetermined volume of tissue. The technique of microdisruption by this laser has become widely accepted for treating several pathological conditions of the eye, both for the anterior and for the posterior capsules. Many other lasers which are used in different branches of medicine including angioplasty, ophthalmology, dermatology, dentistry and urology all require a precise and controllable ablation of tissue with minimum thermal and non-thermal damage to surrounding areas. These lasers are mainly excimer lasers (ArF,KrF,XeCl), tunable dye lasers, solid-state lasers (Alexandrite, Er:YAG, Ho:YAG, diode), chemical lasers (CO_2, HF) and free electron lasers (FEL). Since, the output wavelength of FEL is tunable and ranges between (0.7-3)μm, its 2.9μm wavelength can be used for tissue ablation. Some of the applications of these lasers are considered in the next chapter.

Generally, a doctor needs an instrument which operates reliably on the push of a button and at best it should be a

device that can be used for all medical treatments. But at the moment such a laser is not available and until then one must refer to a number of important points before any operation (i) - careful selection of laser and optimization of its parameters and accuracy for clinical use (ii) - easy delivery of the radiation to the location of the treatment. Once the radiation is transfered to the interaction area its ultimate result is the utmost importance. In most general terms the desired effect is selective absorption of radiation by cells and minimizing all other physical processes. Thus, the wave-length, energy level and pulse duration have to be chosen very carefully. In recent years the number of medical applications of lasers has been increasing rapidly with a great deal of emphasis on the physical mechanisms and the technology. One should therefore appreciate that in this particular field of activity neither the physicians nor the physicists can possibly alone gain a complete understanding of laser-tissue interaction. According to Spells (41) one of the difficulties about a purely physical approach is that the models selected by physicists usually ignore the structure of biological material often with disastrous results. It seems, likely however to expect that as the laser grows more reliable so will the models explaining their effects upon biological systems (42).

Several techniques have been used to alter the anterior curvature of the cornea to achieve a correction of its refractive power. Excimer lasers, particularly ArF at 193nm, have the potential for such clinical applications which makes them attractive as a non-contact corneal sculpting or non

destructive surgical correction of defective vision. Photo refractive keratectomy (PRK) is under investigation for vision correction and involves the use of the 193nm, ArF laser to remove (ablate) tissue from the corneal surface. This is exclusively applicable to cases of myopia (near sightness) where the laser ablates layers of cells near the apex of the cornea, flattening its curvature. Since PRK technique involves tissue ablation and reduces the cornea's curvature, it is limited to correcting myopia. Clinical research on PRK uses 193nm ArF lasers operating at a fluence level of 160-195 mJ/cm^2 and a pulse repetition rate of about 10Hz. Experiments (43-45) have shown that this wavelength produces the cleanest material removal for corneal tissue, with highly controllable cuts depths, at a rate of about 0.25-0.35μm/pulse. The interaction is thought to proceed via direct bond breaking in a mode known as ablative photo-decomposition. Another technical problem with the excimer laser and PRK procedure, apart from its limitation to myopia, is an effect called 'corneal remodelling'. Before collagen removal can effect re-shaping, the epithelium and Bowman's membrane must be removed. These layers regenerate after surgery, but often to an undesirable thickness. The post operative use of topical steroids has succeeded in correcting this problem. The procedure for treating hyperopia and higher degree of myopia is normally called radial thermal keratoplasty (RTK) which is based on the thermocoagulation of corneal collegen.

The greatest advantage of using mid IR laser light (Ho:YAG Er:YAG) is that corneal tissue can be removed from

within the cornea with only minimal damage to the epithelium. This method works by selectively vapourizing cells within the cornea. The tissue readily absorbs the vapour and collapses to fill the void, thus changing the shape of the cornea. One major problem of these systems is thermal damage to the collegen tissue. Endothelial damage is possible because of penetration of heat and thermal damage can cause an alteration of the helical structure of collegens. This would result in abnormal birefringence and irregular re-epithelialization. Plasma-mediated ablations were performed by Niemz etal (46) on human corneas with a short pulsed near IR Nd:YLF laser system at 1053 nm. The pulses were 60 psec in duration at a repetition rate of 1 KHz. Because of the short pulses of the Nd:YLF opthalmic laser and the ability to focus its TEM_{oo} beam to small spots it might also be useful for intrastromal refractive surgery (46).

There is currently much interest in the development of fibre delivery systems for tissue ablation using pulsed IR and UV lasers (47,48). Proposed ophthalmic applications include the formation of sclerostomies for management of glaucoma (49), lens ablation (50), and the cutting vascular membranes within the eye (51). Despite the usefulness of excimer lasers under correct conditions, there are however unresolved problems arising from the use of these lasers in a clinical environment. These include potential mutagenic and cataractogenic effects (52), the limited fibre lifetime at the shorter UV wavelength (53), and the undesirable toxicity of associated fill gases. An alternative approach has been to use mid-infrared laser wavelengths where tissue absorption is

strong and where there is a correspondingly limited zone of thermal injury, but where fibre delivery is efficient. Of particular interest for use in this regime are the Er:YAG, Ho:YAG and HF lasers which have been demonstrated in pulsed operation to produce well defined incisions with small zones of thermal injury (54-58).

Of these the HF laser has been recognised as valuable as its wavelengths corresponds to strong IR absorption peaks of water (59). However, whereas a considerable body of information on the fibre delivery of relatively long pulse (10-1000μs) mid-IR Er:YAG and Ho:YAG lasers has been reported (57,58,60,61) no information is available on the shorter pulse (<1μs) HF laser.

In this thesis the possibility of optical fibre delivery of UV and IR (HF) lasers under different conditions for ablation of biological materials is studied. Etch rate and photoacoustic measurements are used to study the parameters governing the etching process of tissue. The main emphasis of the thesis is on the application of HF laser for ablation of ophthalmic tissues in different conditions, though some work is also done with 193nm, 248nm and 308nm excimer lasers.

Chapter 2 outlines the basic photophysical mechanisms and principles involved in the laser-tissue interaction. This is important to any laser user for otherwise one would not be able to predict the outcome of the experiment. This is followed in Chapter 3 by experimental work concerning the coupling of UV light through different types of fused silica fibres and an investigation of their transmission properties for XeCl (308nm), KrF (248nm) and ArF (193nm) laser

radiation. Chapter 4 utilizes some of these fibre transmission results to study the ablation of organic polymers such as polyethylene terepathalate and polyimide and also lens tissue. The etch rate measurements and photoacoustic results are used to derive effective absorption coefficients and thresholds fluences for ablation with the fibre delivered UV lasers. Scanning electron microscopy (SEM) is also used to to evaluate the ablation sites produced with the UV lasers.

Since the mutegenity and carcinogenic effects of UV lasers are not completely resolved much attention has recently been given to development and application of pulsed mid-IR lasers as alternative sources for tissue ablation. Of particular interest is laser operation near 3um where water exhibits a strong absorption peak and the beam penetration depth is restricted to a similar range to that with excimer lasers. Under these conditions of strong absorption cleaner surgical incisions can be made with minimal thermal damage to adjacent sites. Although, lasers such as Er:YAG and Ho:YAG have already extensively been used for different clinical uses (57,58,60), these studies have been restricted to long pulse durations (250μs) which leads to a relatively large thermal damage zone. It was, therefore, of interest to study the effects of shorter pulse duration mid-IR lasers on tissues to see if similar quality of incisions to those with the excimer lasers are achieved.

To pursue this objective a short pulse (400ns, multi-line) HF laser was designed and constructed which is described in Chapter 5. In Chapter 6 studies of the delivery of pulsed HF laser radiation with output wavelengths ranging

between (2.6-3)μm through a fluoride glass fibre are reported. This is then followed in Chapter 7 by an investigation of the ablation of ophthalmic tissues under different conditions (air and saline) using the direct and fibre delivered HF laser. The etch rate measurements and photoacoustic studies were again used to provide information on the effective absorption coefficient, threshold fluence; SEM evaluation of the interaction zone was also carried out for specific tissue samples. For bovine cornea SEM evaluation of the irradiated site showed that the fibre-delivered HF laser produced sharply defined incisions. This is consistent with the high effective absorption coefficient in this spectral region and the short laser pulse duration which minimizes heat transfer to adjacent tissue.

In order to gain a better understanding of the laser tissue interaction and ablation in a liquid field with the optical fibre a number of experiments were carried out using nanosecond photography (shadowgraphy) to study vapour cavity growth (optical cavitation) at the fibre tip. These results together with photoacoustic and ablation rate measurements, in saline with the fibre delivered HF laser are described in Chapter 8. Similar types of experiments with longer mid-IR laser pulse durations such as 25μs Er:YAG (62), 250μs Ho:YSGG (63), and 500μs Ho:YSGG (64) have been carried out elsewhere. Of particular interest of this work was an assessment of relative contribution of the direct laser interaction, acoustic waves and bubble formation on tissue ablation and attendant damage range. The main conclusions and a discussion of this work is given in Chapter 9.

A few ground rules that seem logical in measuring the success of new procedures are as follows:

1. High technology simply for the sake of high technology is no improvement, and not a reason to supplant old procedures.
2. New procedures should show clinically significant advantages over our present practices before they are generally accepted as part of the norm.
3. Prospectively randomized clinical trials should be the standard for verifying results of new technology.
4. In determining when technology is acceptible, we must consider the financial cost and the expected benefit to society.

> "We all applaud the success of scientific advances, but are often careless in determining whether new technology is an improvement over the status quo or merely adding more excitement (and often more expense) to the nature of how something is done". (65).

1. Lasers and Optoronics
7:28:1988 (No.3).

2. Goldman L.
Lasers in medicine - Vol. 1:1971.

3. Private communication in:
Lasers focus world - April 1991.

4. Minton J.P., et al
An evaluation of physical response of malignant tumour implants to pulsed laser radiation.

5. Ketcham As., et al.
A surgeons appraisal of the laser, surg. clin. north. AM. 47:1249:1967.

6. Koester C., Snitzer E., et al.
Experimental laser retinal coagulator
J. Opt. Soc. Am., 52:607:1962.

7. Kapany N., Peppers N., et al.
Retinal photocoagulation by lasers
Nature, 189:146:1963.

8. Flocks M., Zweng H.
Laser coagulation of ocular tissues
Arch. Ophthalmol, 72:604:1964.

9. Peyman G.A., Voneya S.
Fundus photocoagulation with the argon and krypton lasers: a comparative sutdy.
Ophthalmic Surg., 12:481:1981.

10. Juarez C., Peyman G.A., Richard M.
Effects of argon and krypton laser on experimentally detached retinas.
Ophthalmic Surg., 13:928:1982.

11. Locas G., Saubrane G.
The effects of real krypton and green argon laser on the foveal region
Ophthalmol, 90:1013:1983.

12. Smiddy W., Fine S.L., et al.
Clinicopathologic correlation of krypton red, argon blue-green and argon green laser photocoagulation in the human funders.
Retinas, 4:15:1984.

13. L'Esparance F.A.
Clinical applications of the organic dye laser.
Ophthalmol, 92:1592:1985.

14. Vogel M., Shafer F.P., et al.
Animal experiments for the determination of an optimal wavelength for retinal coagulations.
Graefs Arch. Clin. Exp. Ophthalmol, 227:277:1989.

15. Romanelli J.F., Pulifato C.A.
Metabolic studies of eye laser retinal photocoagulation
Int. Oph. Clinics., 30:95:1990.

16. Trokel S., Srinivasan R., Braren B.
Am. J. Ophthalmol, 96:710:1983.

17. Marshall J., Trokel S.
Ophthalmol, 92:749:1985.

18. Pulifato C.A., Steinert F.R., Dartsch T., et al.
Ophthalmol, 92:741:1985.

19. Aron-rosa D., Carre F., et al.
J. Ophthalmol, 100:741:1985.

20. Hanna K.H., Chastang J.C., et al.
Excimer laser keratectomy for myopia with a rotating slit lamp delivery system.
Arch Ophthalmol, 106:745:1988.

21. Goodman G., Trokel S., et al.
Corneal healing following laser refractive keratectomy.
Arch. Ophthalmol, 107:1795:1989.

22. Jaffe G., Williams G., et al.
Ab interno sclerostomy with a high powered argon endolaser.
J. Am. Ophthalmol, 106:391:1988.

23. March W.F., Gherezghihev T., et al.
Safety of high energy Nd:YAG laser pulses in YAG sclerostomy.
Am. J. Ophthalmol. (abstract), 105:445:1988.

24. Pollock I., Brown R.H., et al.
Prevention of rise in intraocular pressure following Nd:YAG posterior capsulatomy using topical 1% Apradonidine.
Arch. Ophthalmol, 106:754:1988.

25. Ruiz R., Osman A., Saatcia A.
Extracapsular cataract extraction with intraocular lens implantation after scleral buckling surgery.
Am. J. Ophthalmol, 111:174:1991.

26. Sherwod M., Lattimer Z., et al.
Laser trabeculoplasty as supplementary treatment for primary open angle glaucoma.
Bri. J. Ophthalmol, 71:188:1987.

27. Rosenblatt M., Luntz M.
Interaocular pressure rise after argon laser trabeculoplasty.
Am. J. Ophthalmol, 106:682:1988.

28. Jorizzo P., Sampler J.
The effect of repeat argon laser trabeculoplasty.
Am. J. Ophthalmol, 106:682:1988.

29. Ticho U., Nesher R.
Laser trabeculoplasty in glaucoma.
Arch. Ophthalmol, 107:844:1989.

30. Copper R., Constable I.
Prevention of corneal burns during high-energy laser iridotomy.
Am. J. Ophthalmol, 91:534:1981.

31. Yassur Y., David P., et al.
Iridotomy with red krypton laser.
Bri. J. Ophthalmol, 70:295:1986.

32. Wise J., Munnerlyn C., et al.
A high-efficiency laser iridotomy sphincterotomy lens.
Am. J. Ophthalmol, 101:546:1986.

33. Karman G., Savir H.
Retinal damage after argon laser iridotomy.
Am. J. Ophthalmol, 101:554:1986.

34. Schwartz A., Martin N., et al.
Corneal decomposition after argon laser iridotomy.
Arch. Ophthalmol, 106:1572:1988.

35. De Guillbon H.J., Govignon J., et al.
Corneal decomposition after argon laser iridotomy.
Arch. Ophthalmol, 106:1572:1988.

36. Patel K.
CW high power N_2-CO_2 laser
Appl. Phys. Lett. 7:15:1965.

37. Harrington J.A., Gregory C.
Hollow sapphire fibres for the delivery of CO_2 laser energy.
Opt. Lett., 15:541:1990.

38. Harrington J.A., Gregory C.
Hollow curved Al_2O_3 waveguides for CO_2 laser surgery.
SPIE, 1420:169:1991.

39. Do V Gal, Katzier A.
Silver halide optical fibres for medical application.
IEEE J.QE. 23:1827:1987.

40. Pais s I., Moser F., Katzir A.
Core-clad silver halide fibres for CO_2 laser power transmission.
SPIE 1420:141:1991.

41. Spells K.E.
The production of radiation burns on the retina at the threshold level of damage: A literature survey and tentative mathematical theory. Flying personnal research committee R.A.F. institute of aviation medicine - 1964.

42. Wolbarsht M.L.
Lasers applications in medicine and biology.
Vol:1 1964.

43. Linsker R., Srinivasan R., et al.
Far UV laser ablation of atherosclerotic lesions.
Lasers Surg. Med., 4:201:1984.

44. Taylor R.S., Leopold K., et al.
XeCl Laser ablation of cardiovascular tissue: practical consideration.
Lasers in Life Sci., 2:227:1988.

45. Trokel, S.K., Srinivasan R., Branan B.
Excimer laser surgery of the cornea.
Am. J. Ophthalmol, 96:710:1983.

46. Niemz M., Klancnik E., Bille J.
Plasma-mediated ablation of corneal tissue at 1053 nm using Nd:YLF oscillator/regenerative amplifier laser.
Lasers Surg. Med., 11:426:1991.

47. Walsh, J.T., Flotte T.J., Deutsch T.
Er:YAG laser ablation of tissue:effect of pulse duration and tissue type on thermal damage.
Lasers Surg. Med. 9:314:1989.

48. Singleton D.L., Paraskevopouleus G., Taylor R.S.
Excimer laser angioplasty: Tissue ablation arterial response and fibre optic delivery.
IEEE. J.QE. 23:1772:1987.

49. Danbar Hoskins H., Iwach A.G., et al.
subconujunctival THC:YAG laser termal sclerostomy.
Ophthalmol, 98:1394:1991.

50. Naneviez T.M., Prince M.R., Gawande A.A., et al.
Excimer laser ablation of the lens.
Arch. Ophthalmol, 104:1825:1986.

51. Pellin M.J., Williams G.A., Green D.M., et al.
Endoexcimer laser intraocular ablative photodecomposition.
Am. J. Ophthalmol, 99:483:1985.

52. Kochevar E.
Cytotoxicity and mutagencity of excimer laser radiation.
Lasers Surg. Med., 9:440:1989.

53. Taylor, R.S., Leopold K.S., et al.
Dependence of the damage and transmission properties of fused silica fibres on the excimer laser wavelength.
Appl. Optics., 2:3124:1988.

54. Seiler T., Marchall J., et al.
The potential of an infrared HF (3um) laser for corneal surgery.
Lasers in Ophthalmol, 1:49:1986.

55. Leorstscher H., Mandelbaum S., et al.
Preliminary report on corneal incisions created by an HF laser.
Am. J. Ophthalmol, 102:217:1986.

56. Valderrama G.L., Menefee R.F., et al.
chemical laser interactions with human cardiovascular tissue.
SPIE-1202:149:1990.

57. Peyman G.A., Katoh N.
Effects of Er:YAG laser on ocular structures.
Int. Ophthalmol, 10:245:1987.

58. Kopchock G.E., White R.A., et al.
Ho:YAG laser ablation of vascular tissue.
Lasers Surg. Med., 10:405:1990.

59. Wolbarsht M.L.
Laser Surgery: CO_2 or HF.
IEEE J.QE, 20:1427:1984.

60. Bonner R.F., Smith P.D., et al.
Quantification of tissue effects due to a pulsed Er:YAG laser at 2.9um with beam delivery in a wet field via zirconium fluoride fibres.
SPIE 713:2:1986.

61. Whitehurst C., Dickinson M.R., et al.
Transmission of 2.94um laser radiation by zirconium fluoride optical fibres.
SPIE 1048:141:1989.

62. Lin C.P., Stern D., Puliafito C.A.
High-speed photography of Er:YAG laser ablation in fluid.
Invest. Ophthal./Vis. Sic., 31:2546:1990.

63. Domankevitz Y., Nishioka N.
Measurement of laser ablation threshold with a high-speed framing camera.
IEEE J.QE, 26:2276:1990.

64. Van Leeuwen T.G., Maurits J., et al.
Non contact tissue ablation by Ho:YSGG laser pulses in blood.
Lasers Surg. Med., 11:26:1991.

65. Olson R.J.
The alter of high technology and the excimer laser.
Arch. Ophthalmol., 109:489:1991.

Chapter 2

Review of some recent medical applications of lasers.

2.1 - Interaction processes:

A brief discussion is now given of the basic mechanisms involved in laser-tissue interactions, with examples of specific applications in each of the broad areas considered. Fig. (2.1) shows the possible effects in the laser-tissue interaction and in most general terms the wanted effect is a cell specific absorption in the irradiated cell material, minimizing all other physical processes. Hence, the wavelengths have to be selected carefully.

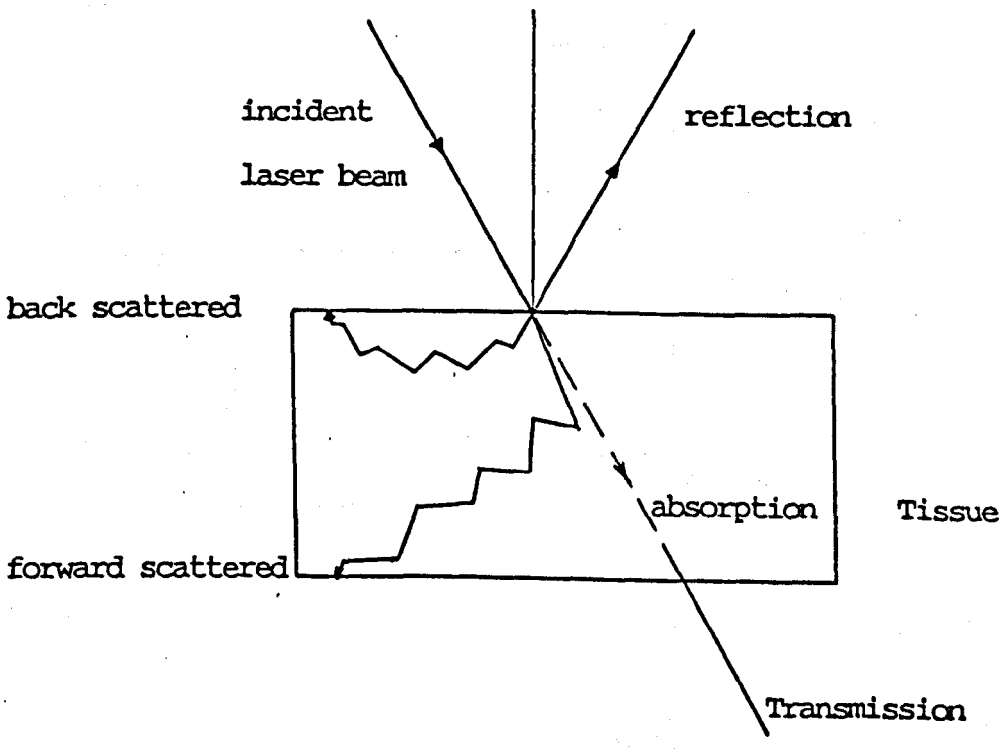

Fig. 2.1 - Effects in laser-tissue interaction.

The photophysical processes are conveniently grouped under the following headings:
(1) - photothermal, (2) - photochemical, (3) - photomechanical, and (4) - photoablative.

1 - Photothermal effect.

The thermal action of laser light on living tissue can be visualized by considering the simplified block diagram shown in Fig. (2.2). The actual processes involved may well be more complex.

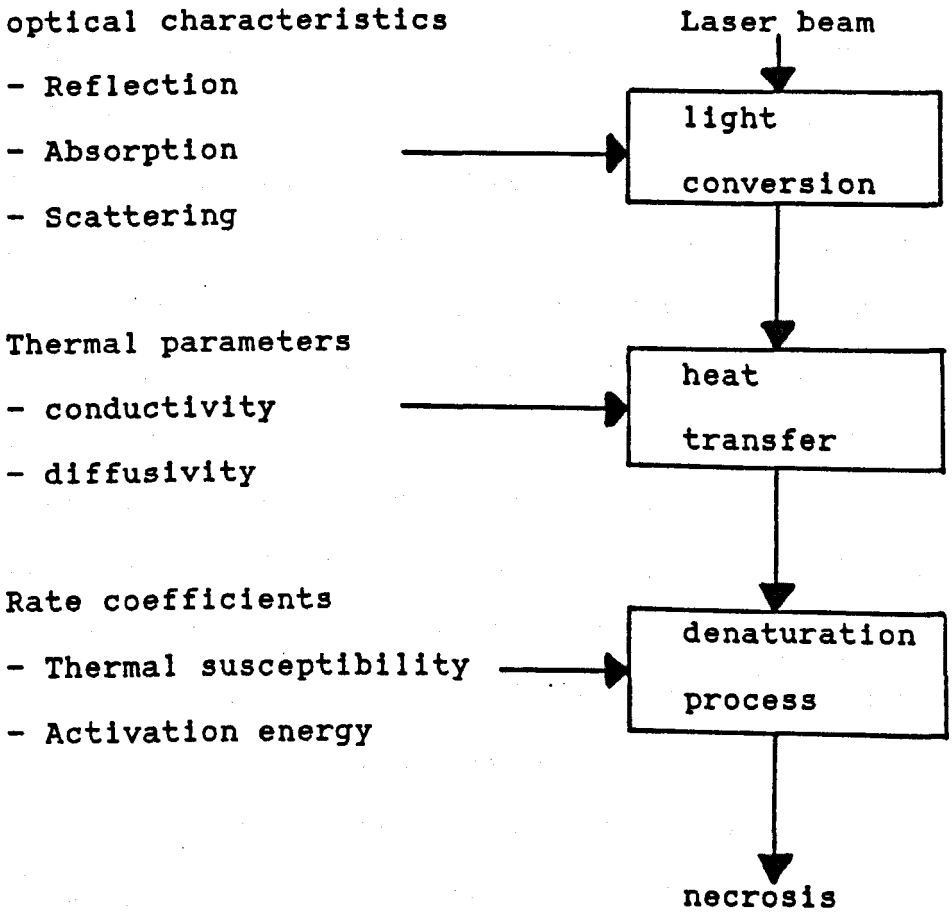

Fig. (2.2) - Model of laser thermal action in living tissue.

Light conversion

Thermal effects are induced by the conversion of laser light in to heat. The optical characteristics of the tissue determine the surface reflection and the distribution of the incident laser radiation in the tissue. The distribution of absorbed energy within the irradiated volume is governed both by the absorption and by the scattering properties of the tissue at the specific wavelength used. For example, at the Nd:YAG wavelength of 1.06um, Halldorsson (1) has used a value of 0.11 cm^{-1} for absorption coefficient which corresponds to an absorption depth of about 9cm. In tissue, however, the actual penetration is limited by scattering to a few mm. Solid-state Er:YAG lasers operating at 2.94μm and the chemical HF laser operating on a single line at 2.9μm have wavelengths that correspond to an absorption peak of water = ($\alpha \simeq 10^{4} cm^{-1}$) and the CO_2 laser operating at about 10um has an absorption depth of about 20μm ie, its absorption coefficient is about ten times smaller than those of Er:YAG and single line of HF lasers. Therefore every wavelength has a different penetration depth which is mainly limited by scattering and the absorption mechanism inside tissue.

On heating tissue its physiochemical structure changes along with its optical properties. Halldorsson [1] using an IR camera concluded that there exists a critical power density above which the rate of temperature rise was sufficiently rapid to modify the superficial tissue, and the thermal reaction of absorbed radiant energy in tissues during exposure is strongly dependent on the duration and area of the exposure. Thermal effects are produced by both pulsed

lasers and continuous wave lasers. In pulsed laser exposures it is important to notice that the temperature rise in tissues exposed to relatively moderate irradiant energy densities can reach a level (>100°C) at which vapourization can occur. The final temperature is very dependent on the laser parameters such as energy, beam divergence, pulse duration, and on the target characteristics eg. absorption and scattering coefficients, refractive index and reflection coefficient.

Heat transfer

The two important mechanisms of heat transfer in tissue are conduction and convection. The separation of cells by their membranes restricts heat convection to a microscopic scale (2). When a temperature gradient exists in a stationary medium, heat transfer will occur across the medium by conduction. The heat transfer is proportional to the temperature gradient (dT/dt) and to the thermal conductivity, K. Another important thermophysical property is the ratio of the thermal conductivity of the medium to the thermal capacitance. This ratio is called the thermal diffusivity, k. A large value of thermal diffusivity implies that a medium is more effective in transferring energy by conduction than it is in storing energy. Conduction during periods between pulses allows laser-generated heat to diffuse in to the tissue and prevents the surface temperature exceeding the vapourization point (3). The rise in temperature is almost instantaneous and measurement of such fast thermal effects presents some technical difficulties. A typical thermocouple is not suitable for measuring a temperature increase caused

by pulsed laser devices, since accurate measurements can be made only after thermal equilibrium between the probe and the material has been established. In order to prevent the thermal diffusion into adjacent areas, the pulse duration , should be much smaller than the relaxation time, t_r (or the characteristic cooling time of material) which is defined by Carslaw and Jaeger (4) as:

$$t_r = \frac{d^2}{4k} \qquad 2.1$$

where $d \doteq \frac{1}{\alpha}$ and $k = \frac{K}{\rho C}$ 2.2

d, α, k, K, ρ and C are the absorption depth, absorption coefficient (cm^{-1}), thermal diffusivity ($cm^2 s^{-1}$), thermal conductivity ($Wm^{-1}\ {}^{o}K^{-1}$), density ($kg\ m^{-3}$) and specific heat capacity ($J\ Kg^{-1}\ {}^{o}K^{-1}$).

For example, for tissue where it contains about 80% water, it can be assumed that at wavelength of 2.94μm, the absorption coefficient is 13000 cm^{-1} which gives an absorption depth of about 0.8μm. Also assuming k $\simeq$1.30 x 10^{-3} $cm^2\ s^{-1}$ (water), it can be deduced from the equation (2.1) that the thermal relaxation time t_r, is approximately 1.2μs.

i. Adiabatic case

For a pulsed laser of duration τ ,heat flow during pulse can be neglected if the absorption depth is much greater than the thermal diffusion depth;

ie, $$\frac{1}{\alpha} >> \sqrt{4k\tau}$$

ii. Diffusion case

For a pulsed laser of duration τ , heat will flow or diffuse to surrounding areas if absorption depth is much smaller than thermal diffusion depth.

ie, $$\frac{1}{\alpha} << \sqrt{4k\tau}$$

In our experiments which will be discussed in the following chapters, is about 400ns this gives a thermal diffusion depth of 0.45μm. Therefore, the case (i) is just satisfied. Conduction during the pulse becomes important only when exposures are relatively long, for example > 1ms. Therefore, highly localized region of thermally induced necrosis can be produced if the pulse duration and exposure time are not clearly defined. In an experiment Walsh et al (5) studied the effect of a pulsed CO_2 laser on tissue using different pulse durations. They found depths of damage of 50μm, 70μm, 170μm and 750 μm for pulse durations of 2μsec, 600 μsec, 2msec, and 50 msec, respectively. This clearly shows how a depth of damage can vary with the pulse duration of laser.

There are a number of reports on measurements of temperature during laser irradiation (6) and following a single pulse (7). It has been confirmed using gas

chromatographic analysis of the vapour-phase photoproducts liberated during continuous wave Argon laser irradiatiion that vapourization is caused by a thermal process (8). In contrast, the underlying mechanism of excimer laser photo-ablation has been the subject of some controversy. There is convincing evidence for both a non-thermal and thermal mechanism in the case of, for example, ArF irradiation. Srinivasan (9) has suggested that excimer laser photoablation proceeds on a non-thermal basis because of the high absorption coefficient of organic materials for UV light, together with the high peak powers attainable with these lasers. The influence of energy density and interaction time on specific interaction processes has been given by Muller et al (10), see fig (2.3). The term 'photoablative decom-position' was used to describe the process by which direct bond breaking resulted in the production of small volatile fragment molecules. According to Lune (11) three empirical observations favour a photochemical process as the mechanism responsible for excimer laser-tissue ablation:

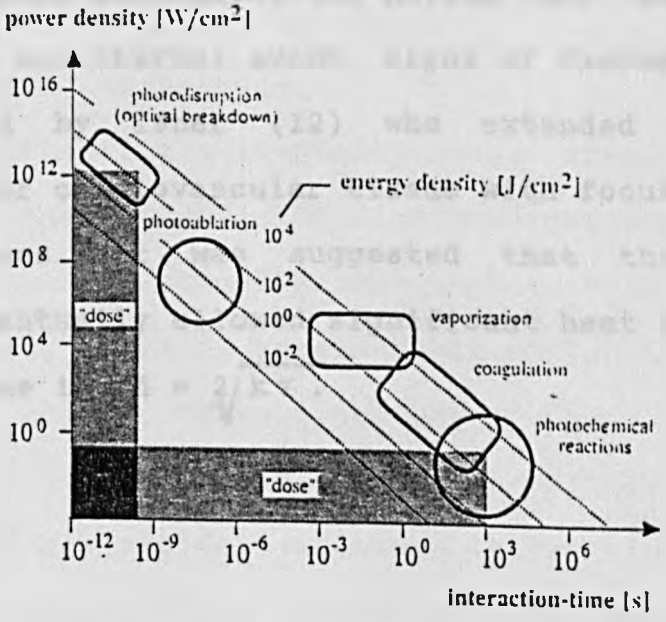

Fig. 2.3 - Energy density - interaction time diagram (10).

i - Histologically evident thermal injury is absent,

ii - The velocity of fragments directed away from the tissue surface exceeds that expected from thermally evaporated fragments.

iii- Temperature calculations based on measurements of the velocity spread of ablated particles and internal degrees of excitation yield a temperature below that corresponding to thermal evapouration.

On the other hand, the energy of a single IR photon (0.12ev for CO_2, 0.43 - 0.48 ev for HF lasers) is far less than that of most biomolecular bonds, and as a result direct photochemical bond disruption is unlikely to occur with infrared lasers. Consequently, the results obtained with such lasers suggest that the absence of thermal injury or its restriction to small zone is the result of a thermal process in which thermal diffusion has been minimized. Results observed with excimer laser (or high peak power CO_2 laser) irradiation also contradict the notion that excimer tissue ablation is a non-thermal event. Signs of thermal energy have been observed by Isner (12) who extended the time of irradiation of cardiovascular tissue with focused KrF laser beyond 200 secs. It was suggested that these prolonged exposures eventually allowed significant heat flow from the irradiated zone ie, $d = 2\sqrt{kT}$.

Hyperthermia

This is one of the thermal effects and manifests itself when there is a small increase of temperature above the physiological temperature to about 41-45°C. There is biological evidence that heat can destroy cells directly, can sensitise them to the effects of ionising radiation and can modify the cytotoxicity of some drugs. There are four different techniques in use and an important aim is a method of producing therapeutic temperatures throughout tumours deep in the body in a predictable way.

(i) - Electromagnetic technique

This involves the deposition of energy throughout a substantial volume of normal tissue as well as the tumour. Possible differences in blood perfusion within the tumour and normal tissues are then relied on to obtain differences in temperature. One method is to use a pair of disc electrodes operating at between 8 and 13 MHz. Another method is to surround the patient with a circumferential aperture radiating an E.M. field with a frequency about 70Hz.

(ii) - Ultrasound techniques

For ultrasound the frequency range extends from 300KHz to 3MHz. The most significant disadvantages are the significant differences in acoustic impedance between soft tissue and gas or bone, causing considerable reflection and little transmission across these interfaces; there is also high absorption for ultrasound in bone. The main advantage is the possibility of scanned focused beams in the range of 300-750 KHz to achieve selective heating of deep tumours by non-

invasive means.

(iii) - Interstitial techniques

The goal is to achieve more control over the temperature distribution since it is a function of blood flow, thermal properties and tissue geometry. The first method is to use RF power at a frequency between 500KHz and 10MHz for deep tumours and the second method involves implanting small coaxial microwave antennas typically (1-2)mm in diameter in to the superficial tumours. The frequencies are in the range range of 300-2450MHz. The third technique is to implant 'seeds' of ferromagnetic material into the tumour and subsequently heat them in an RF magnetic field. The ferromagnetic material is heated to a much greater extent than the surrounding tissues and a local region of therapeutic temperatures can be achieved due to heat transport from the seeds.

(iv) - Laser-induced technique

In surgical applications, lasers can provide an accurately controllable means of removing unwanted biological tissue by vapourizing it. Alternatively, a lower power can be used so that less severe thermal damage is caused which the body then heals with scar tissue or healthy regenerated tissue. The medical use of lasers can rely on either of these techniques but laser hyperthermia is based on the second method. A low power beam typically of 1-2 W can be directed down an optical fibre to the tumour to be treated. The optical energy in the laser beam is absorbed by the tissue and converted to heat. Although temperatures close to the

fibre tip are quite high, they fall away rapidly as distance from the tip increases as a consequence of thermal conduction and the cooling effect of perfusion. This technique requires a judgement about the optimum position for the fibre tip, length of exposure, power used, and choice of laser type. The scattering and absorption depends on the laser wavelength, and is chosen to be suitable for the intended application (13). It is also believed that a pulsing frequency slower than 40Hz would decrease the amount of hyperthermia. However, Matthewson (14), demonstrated that the consequences of exposing rat liver to Nd:YAG laser light at 1W for 400 s are no different, whether the laser energy is delivered in 100 μs pulses at 10Hz, in 100μs pulses at 40Hz, or in CW form. It is possible for theoretical analysis to provide an insight into the effects of treatments of this kind, thereby complementing the experimental work. The two approaches can illuminate each other and information gained from both can help the surgeon in the choice of treatment. Such mathematical analysis can be found in the references (15,16).

Photocoagulation

Coagulation is not an ordinary type of burn that we are familiar in our every day life, but manifests itself in a macroscopic change observable as a blanching of the irradiated surface. This whitening signifies increased reflection of all visible wavelengths and is caused by a fundamental change in the structure of the tissue which leads to increased scatter, multiple refraction and reflection of the illuminating light.

Coagulation corresponds to an irreversible necrosis of

tissue, and to shrinkage of collagen fibres that leads to vessel occlusion. This effect is required to stop haemorrhage and to destroy tumours. It is likely to occur above 50°C for heating durations of a few seconds. However, above about 80°C, collagen denaturation occurs. At temperature above 100°C vapourization of intracellular water occurs. At still higher temperatures there is further decomposition of the organic molecules, resulting in carbonization and burning of the tissue. It is important to notice that the shrinkage of collagen fibres leading to vessel occulsion is because of the cell membranes that are loosened and hence the cells become oedemized (or 'dropsy'). Protein fibrils migrate out of the cells and when the tissue cools down these will adhere to each other, thus fusing neighbouring cells. This effect can be utilized for tissue welding to prevent haemorrhage and also to destroy tumours. Mordon (17) conducted a series of *invivo* experiments on the livers of wistar rats which were selected as a suitable homogenous medium. Pulsed and CW Nd:YAG lasers were used, the former providing 500W peak power and pulse durations of (2-500)ms. The CW YAG laser had a maximum continuous power of 50W. The surface temperature of tissue during and after the irradiation was measured by using an IR thermographic video camera. Driver et al (18) found the power levels of coagulation and charring at the end of plane-cut fibres immersed in whole blood and red blood cells lower than those required to give a clinically useful dose in a reasonable time.

Vapourization

When tissue is heated above 100°C, the cell water boils and in the process of the conversion of water into steam the cell walls are ruptured explosively, allowing the steam to escape. Tissue 'ablated' in this way is commonly said to have been 'vapourized'. For water, the heat of vapourization is much higher (2200 Jg^{-1}) than for most other substances. This allows the steam to carry away most of the heat which went into its creation, thus preventing further heating of the adjacent tissue. The overall effect of the boiling transition is that the spread of heat and therefore damage to tissue is limited more or less to the site of absorption of the laser radiation. When the water has dried up continued irradiation rapidly increases the temperature of the residual material until a temperature of between (300-400)°C is reached. At this point the tissue blackens and becomes carbonized and begins to outgas and smoke. At over 500°C in the presence of atmospheric oxygen, tissue will burn and evaporate. To minimize thermal denaturation of tissue adjacent to the site of exposure, short-duration, high power lasers such as CO_2 or HF are required. As the amount of tissue removed at each pulse is very small many pulses will be needed to make incisions of any appreciable depth. The peak powers and repetition rates must be optimized in relation to the phase change of water from liquid to steam. One of the important applications of CO_2 lasers is the treatment of lesions in the uterine cervix. Rubinstein (19) has shown that CO_2 laser vapourization of cervical lesions gives excellent results.

2 - Photochemical effect

It can be seen in fig. (2.3) that at the very end of the exposure scale, for extremely long interation times (1000 s) and low power densities (below 1W cm^{-2}), lies the family of photo chemical transformations. Two therapeutic modalities based on photochemistry are used, termed phototherapy and photochemotherapy. In phototherapy, the effective light is absorbed by endogenous molecules in tissues. Photochemotherapy involves administrating an exogenous photosensitizing drug to the patient, then, after an appropriate length of time, the diseased area of the body is illuminated with light of wavelengths absorbed by the photosenitizer. A photosensitizer is defined as a chromophore compound capable of causing light-induced reactions in molecules that do not absorb light (20). The essence of photochemical interaction lies in the exogenous chromophore receptor which acts as a photocatalyst: It is first activated by resonant absorption, thereby storing energy in one of its excited states, only when it deactivates can a reaction take place, but with a reactant that is not the photosensitizer. It is the release of this highly reactive cytotoxic species which cause irreversible oxidation of some essential cellular component and destroy the affected host tissues (21).

Photodynamic therapy (PDT) as a particular case of photochemotherapy is mainly used for treatment of different types of cancers such as lung (22,24), brain (25,26) and bladder (27,28). In PDT the photosensitizing drug such as HPD (see Fig. 2.4) causes no chemical damage to the irradiated cells or tissues in the absence of oxygen. One mechanism in

which oxygen is involved is that it acts as an energy acceptor from the photo-excited sensitizer. In this process it is converted into a reactive highly toxic species, singlet oxygen ($^1O_2$). Since the absorption band of most photosensitizers lies above 600nm, they can be photoactivated by illuminatiion with light in the red spectral region such as He-Ne laser 632nm.

Generally, the physics involved in PDT includes light delivery, light detection, optical characteristics of tissue, the behaviour of light within tissue and methods of quantifying the photosensitizor in vivo. Many of these topic have already been reported in earlier publications. A good overview has been given by Wilson (29).

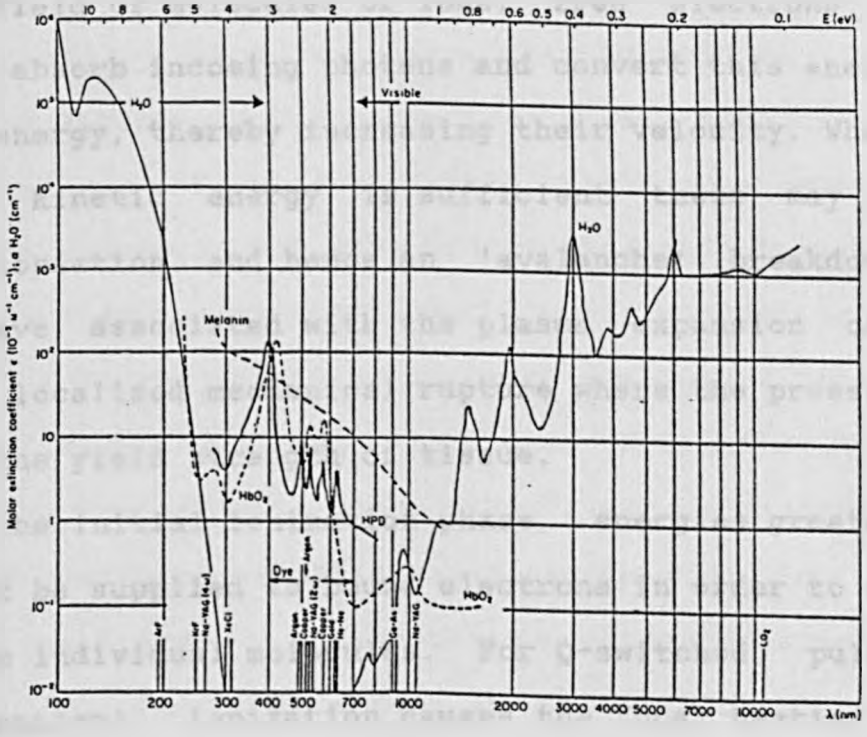

Fig. (2.4) - Absorption curves of various bilogical chromospheres (30).

3 - Photomechanical effect

The main physical element of the electro-mechanical mode of interaction is rooted in the photoproduction of extraneous free electrons by a process known as 'electron avalanche'. This can occur when powerful lasers are focused at a target, creating high irradiance levels eg. $\tilde{}$ 10^{10} W/cm^2 for ns and 10^{12} W/cm^2 for pS pulses. This locally generates a high electric field (10^6-10^7) V/cm which can become comparable to the average atomic or intermolecular Coulomb electric field. These large fields can induce dielectric breakdown of the target material resulting in the formation of a micro plasma ie, an ionized volume with a very large free electron density.

At this stage the avalanche process begins to grow when in the field of molecules or ions, free electrons already produced absorb incoming photons and convert this energy into kinetic energy, thereby increasing their velocity. When their relative kinetic energy is sufficient these may produce further ioniation and hence an 'avalanche' breakdown. The shock wave associated with the plasma expansion can then generate localized mechanical rupture where the pressure rise exceeds the yield strength of tissue.

In the initial ionization phase, energies greater than 10ev must be supplied to bound electrons in order to separate them from individual molecules. For Q-switched, pulses (3-10ns duration), ionization causes the focal heating of the target, where local temperatures exceed several tens of thousands of degrees are reached. For very short mode-locked pulse trains ($\tilde{}$20pS individual pulse) ionization can occur

through 'multiple photon absorption'. Due to the extremely high irradiance at the focal point, photons can add coherently and provide the ionization energy that produces free electrons. The threshold irradiance for optical breakdown is higher for picosecond mode-locked pulses than for nano-second Q-switched pulses. For example, in air, the threshold for a single 25 pS pulse is about 10^{14} W/cm^2 whereas it is only 10^{11} W/cm^2 for a 10ns pulse (31). For biological systems, the fluence for breakdown is similar for a mode-locked pulse train and a Q-switched pulse ($\tilde{}$10Jcm^{-2}), even though the peak power density is on average 100 times higher for pS pulses (32).

The presence of impurities in the target enhances thermionic emission but has little effect on multi-photon ionization. Plasma shielding can be useful and important in ophthalmology - once a plasma is formed it 'shields' underlying structures which are in the beam path by absorbing and scattering the incident light. Light absorption by the plasma is through the same process as in plasma growth, namely 'inverse - bremsstrahlung'. In the case of ns pulses, in addition to absorption, the plasma scatters light, through Brillouin scattering and stimulated Brillouin scattering (SBS). In the former case, the light is scattered by thermally excited acoustic waves and shifted in frequency equal to the frequency of the phonons characteristics of the material. In SBS which occurs at higher irradiances, the laser light itself creates the acoustic wave which scatters it. In an experiment Fleix et al (33) reported that shock waves begin as soon as the plasma formation occurs and expand

at a hypersonic velocity of 4km/s. The wavefront propagation falls to sonic velocity (1.5 km/s in water) within 200μm. The shock wave is followed by cavitation or bubble formation.

To prevent retinal injury during intra-ocular surgery using the Nd:YAG laser a strong focused optical system can be used so that the beam diverges rapidly beyond the focal point of the delivery system. The retinal effect of copper vapour laser has been studied (34) where each pulse had a duration of 15ns, maximum energy of 3mJ and a peak power of more than 100kW. The histological analysis of the lesion produced at pulse rates of 4kHz showed an undesired retinal effect, whereas the use of 18kHz showed a desired coagulation effect. Recently, Stern et al (35) used ns, pS and fS lasers at 532 and 625nm for corneal ablation. They concluded that excisions made with pS and fS lasers were ultrastructurally superior to those made with ns lasers. This is due to the fact that with ns lasers, the smallest plasma that can be created is much larger and more energetic, because the pulse energy required for optical breakdown is much higher than for pS lasers. Also, with pS lasers at pulse energies just above the ablation threshold, the shockwave and cavitation bubble should be much smaller and less damaging than with ns lasers, and the fluence at the retina should be much lower (35).

4 - Photoablation effect

In 1982, the term ablative photodecomposition was used by Srinivasan et al (36) when they reported that the ArF (193nm) excimer laser can be used for etching polymeric materials with little or no thermal damage. Since then the ablation of polymers and biological tissues has been studied

extensively by other investigators (37-41). This effect occurs when using high laser fluences and short pulse durations so that the effect is in the form of a small but fast and strong explosion. Under these conditions, the irradiated tissue volume is modified and then removed (42). In interactions when water is not the main absorber ie, with visible radiation, there is considerable damage such as dehydration or charring (43). However, at laser wavelengths which match the water absorption well, particularly in sub-microsecond region, damage to the adjacent material can be negligible. The rapid vapourization of the water alone can provide enough propulsive force to expel the adjacent tissue which is ablated (44). Infrared photons with energies of <1.5ev/photon give rise to vibrational and rotational excitation of the absorber. By absorption of many repeated photons, enough energy to overcome the activation barrier can be provided so that thermal decomposition of the material will result. Ultraviolet photons with energies >3.5ev give rise to electronic excitation which can lead to photochemical decomposition. In the U.V. range, the principal coupling of laser wavelenghth is to chromophores in the stuctural proteins. In the UV laser-tissue interaction rapid bond breaking is believed to be a photochemical process that occurs from a high-lying electronic state. This will in turn, cause a local increase in the pressure in the irradiated volume which will lead to ablation. Comparative studies of synthetic polymers (45) and bovine cornea 'in vitro' has shown remarkably similar UV photoreactions in both materials. This has been attributed to the similarity of their

respective polymeric structure. The photoablation effect does not exist for fluences below a certain threshold depending on material. Once this threshold is exceeded a single pulse can remove material. The thickness of the tissue layer removed with one pulse increases with the fluence. However, at high fluence the ablation rate tends to saturate due to plasma sheilding of the laser beam or by optical changes of the irradiated tissue.

Generally, the physics of the process involves: absorption of the photon, bond breaking, and ablation of the products. However, to understand the chemistry of the decomposition of organic matter by laser radiation, it is essential to have information about: the rate of material transformation, the time scale in which the reaction occurs, and the composition of the products (46). The main reasons for considering this process as 'non-thermal' are because the heat transfer to non-irradiated regions can be neglected and because of the short pulse duration, the ablated tissue material takes most of the absorbed laser energy away from the remaining tissue. Therefore, only a very thin layer of the order of the optical penetration depth is thermally damaged. Fig. (2.5) shows the physical principles in laser photoablation of tissue.

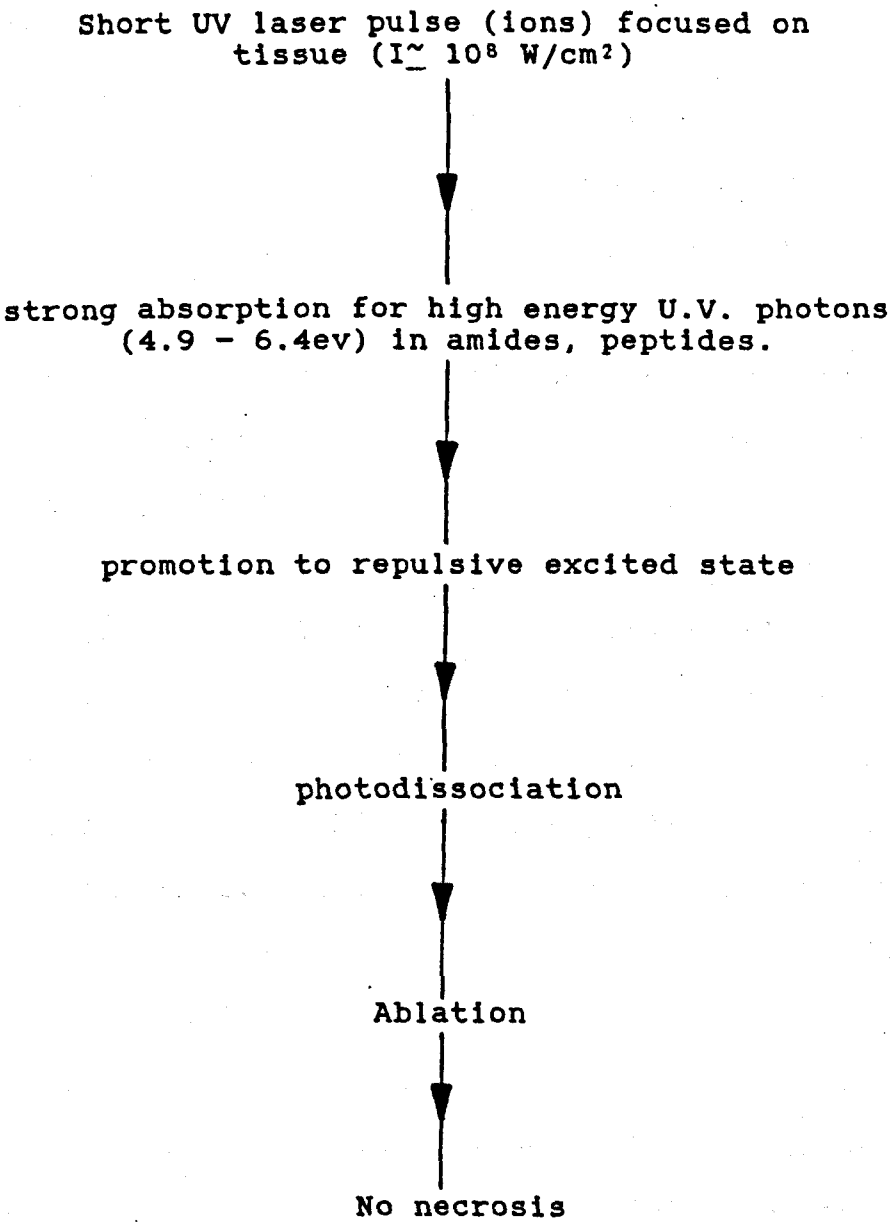

Fig. (2.5) - The physical principles of laser photoablation.

Time-dependent effects

In order to produce a physical effect, laser energy must be absorbed. This absorption is dependent on the optical properties of that tissue. In effect, certain anatomical structures will become generators of thermal, electrical, and acoustical energy that will ultimately produce the damage. According to Wolbarsht (47) the direct effects of the laser energy in any kind of application site often produce immediate damage over a large area. This process has been termed 'physical amplification'. There is also a delayed amplification of the size of the exposure site in a living system that requires seperate understanding. This delayed change has been termed 'biological amplification'. A combined example of these effects can be seen in for example CO_2 laser surgery where the main absorber is water and peak powers are low. The laser radiation and resulting heat give the physical amplification mostly by thermal denaturation and steam formation, while the biological amplification is achieved by some chemical transmitter such as histamine released by injured cells or haemorrhage and edema (47). Another example of physical amplification is the bubble formation resulting from the boiling of water during the thermal events of laser exposure in brain surgery. When water is vapourized within the cavity this leads to explosive displacement of the brain stem and hence instant death.

2.2 - Examples of clinical lasers

The effects created by surgical lasers - namely cutting, vapourizing, coagulation and haemostasis are all caused by heating of the tissue. The wavelength of the laser is perhaps the most important parameter in determing how efficiently this heat transfer occurs, and over what volume of tissue. In order for light to heat tissue it must be absorbed. If it is reflected from or transmitted through tissue no effect will occur, and if the light is scattered it will be absorbed over a larger volume so that its effects will be more diffuse. Cutting is simply vapourizing tissue along a line using very small spot sizes of (100-500)μm. Defocusing the beam slightly, using higher power to maintain power density and cutting with this would result in less precision but better haemostasis for vascular areas. Coagulation of tissue with a laser has a broader meaning than simply achieving haemostasis, ie the laser has the ability to destroy cells by denaturing the protein without necessarily vapourizing it. The cutting and other effects are mainly determined by the absorption characteristics of the laser beam in water which is the main component of soft tissue. Haemostasis is achieved by sealing the ends of the capillaries or vessels by laser heating. The greater the blood flow through a vessal, the more it acts as a heat sink and the greater the difficulty in achieving the end result.

The choice of wavelength can therefore change the depth of penetration of the light, and hence the region in which heat is deposited. Laser-induced heating may result in changes in the configuration of many types of macromolecules

within the tissue. This can, in turn, result in alteration of membranes, denaturation, dehydration or carbonization of molecules which leads to tissue modification. Thus, the tissue properties change during irradiation. Irridiation with short pulses may lead to very rapid temperature rises in the tissue and create pressure waves (ie acoustic transients) which can cause damage away from the irradiation site. Such damage may be actual tissue rupture, or changes in membrane function. For a complete assessment of laser-tissue interaction, both photophysical events and photobiological response are needed. It is the latter which makes laser interaction with living tissue more complicated than those of inert materials.

2.2.1 - Solid-state lasers

These lasers use small concentrations of impurity ions doped into an ionic crystal or glass host material. By far the most commonly used solid-state laser is Nd:YAG with the strongest wavelength lasing at 1.06um. Other lasers with Nd^{3+} ion impurities in different host materials are Nd:YLF (1.06μm), Nd:YAP (1.08μm), Nd:Si glass (1.062μm), and Nd:P glass (1.054μm). Nd lasers appears to be useful for liver, kidney and bladder tumour surgery because of their good transmission in fluid environment and haemostatic effect. Nd:YAG laser radiation, for example, scatters over a large blood volume of tissue causing coagulation as deep as (2-6)mm if desired. At high power densities it will vapourize but leaves an underlying deep layer of coagulated tissue beneath the base of the crater. The vapourization of tissue occurs when cellular fluid is heated to its boiling point. The rapid

rise in intracellular temperature and pressure causes an explosion of the cell, throwing out steam and cellular debris.

The Nd:YAG laser can be frequency doubled to produce output at a wavelength of 532nm. The 532nm output is mainly used for cutting, coagulation, vapourizing, and if a large 'bleeder' occurs or deep coagulation and ablation of large masses are required then the wavelength can be switched to 1.06um. Both wavelengths are easily delivered through optical fibres.

The second class of solid-state lasers emit in the mid-IR and are based on the use of high concentrations of Er^{3+} ions in various host materials eg. Ho:YLF (2.06μm), Ho:YAG (2.1μm), and Er:YAG (2.94μm). These lasers have opened up the possibility of new and improved surgical techniques because of their relatively strong absorption in biological tissue. This is illustrated in fig. 2.6 where the absorption depth varies as a function of wavelength for both water and haemoglobin.

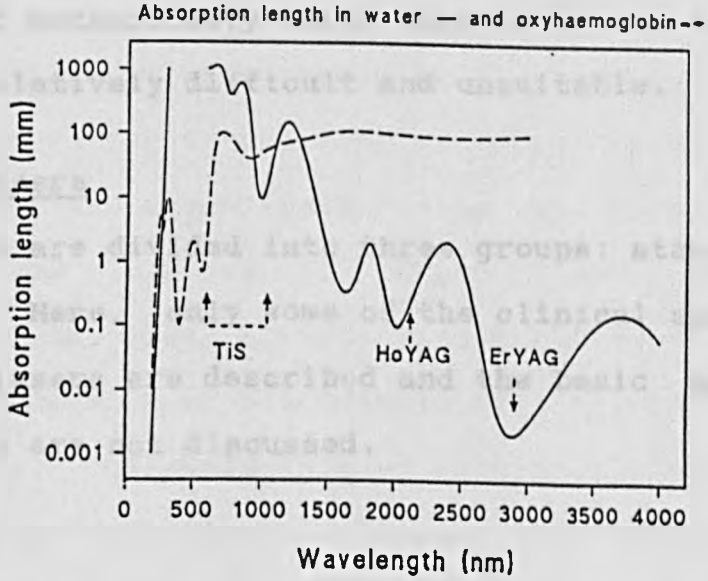

Fig. 2.6 - Absorption depth as a function of wavelength for water and haemoglobin.

The consequence of this strong absorption is rapid and efficient ablation of tissue leading to minimum heat loss by conduction and hence minimum thermal damage. Walsh et al (48) found that the normal spiking-mode pulses of Er:YAG laser typically leave 10-50μm of collagen damage, and at high fluences the damage produced in cornea and aorta was even higher. Q-switched pulses caused less thermal damage in all tissues. The depth of damaged tissue surrounding an Er:YAG laser incision has been measured by Charlton et al (49) to be of the order of 5μm. Ho:YAG operating at 2.1μm, however, is much less strongly absorbed by water and hence penetrates more than Er:YAG laser. The thermal damage for soft tissue varies between a few microns (50) and several hundred microns (51) depending on the fluence.

Fused silica is by far the most flexible optical fibre for transmission of Ho:YAG and other lasers. However, for the Er:YAG laser zirconium flouride or sapphire fibres are normally used. The zirconium flouride fibres are brittle and easily damaged mechanically which make their use in medical applications relatively difficult and unsuitable.

2.2.2. - Gas lasers

Gas lasers are divided into three groups: atomic, ionic, and molecular. Here, only some of the clinical applications of a few gas lasers are described and the basic physics of their operation are not discussed.

Argon laser

The first significant medical use of lasers was in the treatment of diabetic retinopathy in 1965 with the argon ion

laser (λ = 488nm). Since then, the extensive experience with argon lasers has resulted in its use as a photo-coagulator. Perhaps two of the most practical areas where argon laser are being used in ophthalmology are Argon Laser Iridotomy (ALI) and Laser Trabeculoplasty (LTP). In simple terms, ALI is an operation on the eye in which an incision is made in the iris. This perforation in the iris can then prevent it from inflammation due to interocular pressure or aqueous outflow pressure. This in turn can be used to treat glaucoma. Extensive clinical experiments have been conducted by different researchers (52-57) to study the use and potential retinal damage after ALI. LTP is used where a blue-green argon laser (488-514)nm used for removing small segments of tissue from part of the wall of the 'schlemm' canal. This area is called the trabecular meshwork. This is an effective technique for lowering intraocular pressure in occular hypertensive and in glaucoma. However, the complications are a transient increase in intraocular pressure that may need additional drugs, and visual field loss. It has been suggested (58) that patients should be followed up carefully after LTP for immediate intraocular pressure rises.

Major use of argon (488-514)nm is also made in dermatology. The visible blue-green light is easily transmitted through clear aqueous tissue but certain tissue pigment such as melanin or haemoglobin will absorb the light very effectively. This principle of selective absorption is used to photocoagulate pigmented lesions like portwine stains (59-61). This light passes through overlying skin without significant absorption and reaches the pigmented layer of

portwine stains or other coloured lesions to affect capillary dessication and protein coagulation. Gradual blanching will then take place and within 6 to 9 months the stain will fully fade away. This blanching or whitening effect indicates the reflection of visible light by a fundamental change in the structure of the tissue which results in increased scatter and multiple refraction and reflection of illuminating light. Fig. 2.7 shows an example of portwine stain before and after the argon laser operation. Recently, Van Germart et al (62) reported that the argon laser wavelengths of 488 and 514nm cannot deliver an output which would enable it to achieve the other ideal parameters of irradiation time, spot size and energy density.

(a)

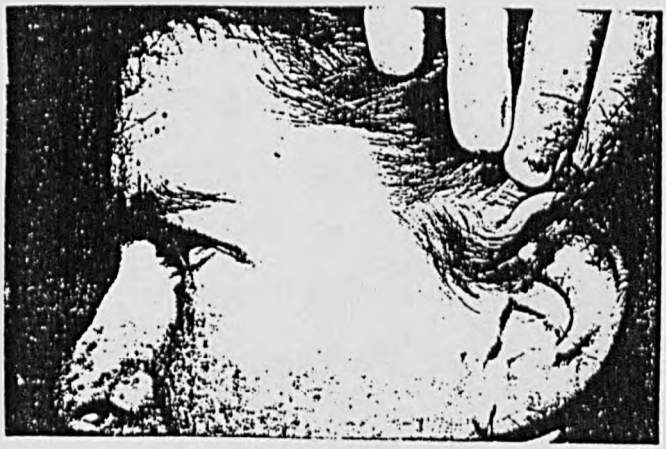

(b)

Fig. 2.7 Portwine stain before (a) and after (b) treatment by Argon laser.

With the argon laser many satisfactory results have been achieved, but in general the results have been unpredictable particularly in children. Of the lasers used to date for treatment of portwine stains only the pulsed Dye laser produces parameters which are almost ideal: (wavelenth 585nm, pulse duration of 0.45ms, spot size 5mm and energy densities up to 10 Jcm^{-2}). With this laser, excellent clinical results have been reported, especially in children (62).

Metal-vapour lasers

There are copper (578nm), gold (628nm), manganese (1289nm), lead (723nm), and barium (1500nm) lasers with typical pulse duration range between (10-60)ns. By far the most suitable lasers for medical applications are copper and gold. The high average power copper-vapour laser can produce blue-green and yellow lines, which means it can be used for the same applications as argon laser. Also, as the yellow light (578nm) matches with the absorption peak of haemoglobin, it can also be a very useful tool in dermatology

and ophthalmology particularly with respect to yellow macular pigment in the eye. The reason for the prefered use of the yellow emission from copper-vapour rather than blue-green (488-514)nm output of the argon laser is two fold: first, less light is absorbed by the melanin at 577-578nm than at 458-514nm and consequently there is less epidermal heating. Secondly more light is absorbed by haemoglobin at 577-578nm than at 514nm. This results in cataneous damage that is specific to the ectatic blood vessels, rather than wide spread damage throughout the epidermis and upper dermis (63). The copper-vapour laser can also be used for pumping dye lasers and have been used in angioplasty to vapourize atherosclerotic plaques (64). The output of these lasers is attractive for vascular use because it lies within the wave-band of preferential absorbance of atheroma (65). The importance of gold-vapour laser is that its wavelength (628nm) concides with absorption peak of haemotoporphyrin derivative (HPD). This is one of the drugs which is used in PDT for treating tumours. The main advantage of this laser is its convertability to copper-vapour in the event that more and new effective drugs with different absorption peak are found.

CO_2 and CO lasers

The CO_2 is an infrared laser operating on a molecular vibrational energy transition and lases at 10.6μm. The laser can be operated at high power levels on a CW or pulsed basis. It is known that a CO_2 laser is poorly absorbed by haemoglobin but it is strongly absorbed by water unlike the visible and near IR lasers. Since about 80% of the

composition of all cells in the body is water, the CO_2 laser produces local superficial heating and is very useful for vapourization and cutting tissue. The intense heat produced by the absorption of the CO_2 laser light by cellular water results in the generation of steam with subsequent rupture of cells. There is very little diffusion of heat to surrounding tissue with typical thermal injury limited to (50-200)μm, though this value varies with the pulse duration of laser. One reason for its limited thermal injury in tissue is due to its high absorption and negligible side scattering which means the tissue surrounding the ablated area is not affected by this side scattered radiation. When used for cutting, the beam is focused to a small spot, and the depth of cut is determined by irradiance and the speed of the incision. The slower the movement or higher the irradiance, the deeper will be the cut. Vapourization of tissue may be done with a focused or defocused beam. Although small areas can be vapourized with a small spot, larger areas are handled with a wider spot and a higher power applied to compensate for loss of irradiance. The CO_2 laser has found a wide acceptance for use in medical procedures but its utility is limited by the lack of suitable flexible, non-toxic fibre optic delivery. It is normally delivered by means an articulated arms or hollow waveguide tubes. Generally, the advantages of the CO_2 laser as confirmed by various experimental studies are: (a) minimal tissue damage, (b) haemostatic effect and (c) sterilizing effect.

Lasers based on vibrational transitions in CO radiating in the range (2.7-6)μm are also promising in surgery. These

lasers have high powers as well as high efficiency (20%), and can have safe, sealed, active elements with a small volume of the working mixture. Some early work by Aleinikow (66) showed that the coagulation properties of CO lasers may be better than those of CO_2 lasers because of considerably deeper penetration of the light into the tissue. This supposition is based on the comparison of the attenuation of the radiation for wavelength (5-6)μm and 10.6μm in water See Fig.(2.4). Recently in a comparison between CO and CO_2 lasers Clement (67) has shown the followings:

(i) - The interaction of CO lasers with human tissue is similar to that of CO_2 lasers.
(ii) - The thermal damage induced in tissue in the vicinity of laser exposure is less for CO than for a CO_2 laser of identical parameters.
(iii)- The CO laser can be transmitted through medically acceptable fibre.

HF Laser

The hydrogen flouride (HF) lasers which can operate as both multiline and single line (2.9μm) with sub-microseconds pulse durations are used for medical applications. Some of these applications (49, 50, 51) were described in chapter 1 and also discussed in the next section of this chapter.

Excimer Laser

The term excimer is derived from excited dimers of the inert gas. Excited dimers are two atoms of an inert gas bound in a highly excited state with atoms of halogen to form a temporary association as a diatomic rare gas halide. The

decay of these unstable molecules is accompanied by the emission of a highly energetic photon of ultraviolet light. There are two main properties: (i)- once the molecule decayed and reached the ground state, it immediately dissociates and (ii)- there are no well defined rotational vibrational transitions ie, the transition is broad-band. This allows the possibility of tunable laser radiation over this broad-band transition. Discharge excited rare gas halide excimer lasers provide pulses of (10-30)ns duration at several fixed wavelengths. For example, the emission for argon fluoride (ArF) occurs at 193nm, krypton fluoride (KrF) at 248nm, xenon cloride (XeCl) at 308nm, and xenon fluoride (XeF) at 351nm (See Fig. 2.8). Commercially available systems are capable of producing output ranging from a few mJ to 1J per pulse at repetition rates from 1-500Hz. ArF (193nm) is normally transmitted via an articulated arm similar to the CO_2 laser and although special types of fibres are under development these are not yet practical. More on this subject will be discussed in Chapter 4. The excimer lasers can produce a high degree of precision, creating incisions in tissue with no or very little thermal shrinkage, and hence achieving predictable depths per pulse in the micron range. The so-called ablative photodecomposition mechanism which is responsible for such precision was described in section 2.1.

The KrF laser produces light of 248nm and given the mutagenicity of this wavelength its medical use has been limited. The XeCl excimer laser, on the other hand can be easily transmitted through optical fibres and is mainly used in angioplasty and urology for ablation of atherosclerotic

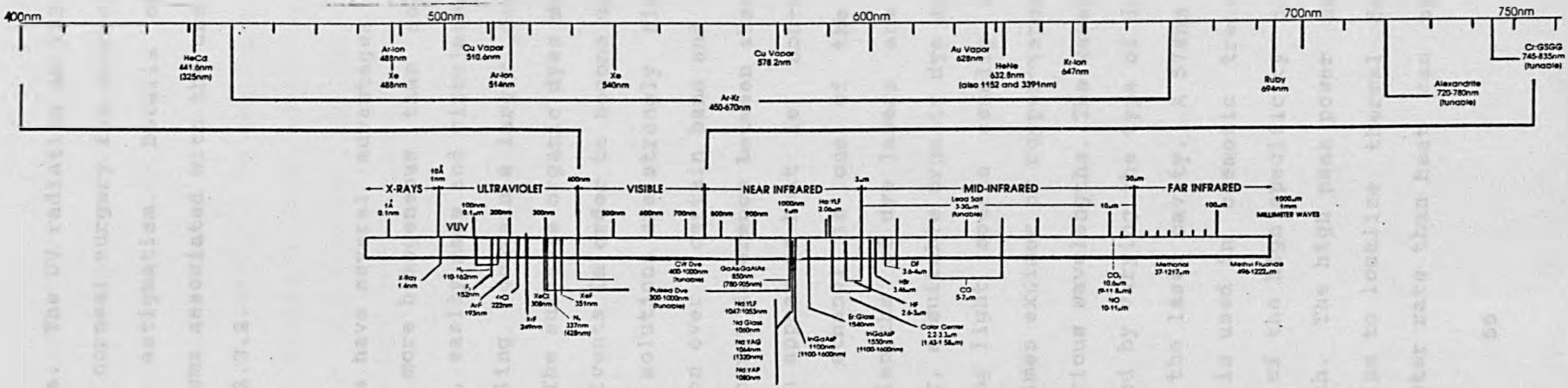

Fig. 2.8 - The electromagnetic spectrum with commercial laser lines.

plaque and urinary stones. The UV radiation at 193nm wavelength is mainly used in corneal surgery for correcting the myopia, hyperopia and astigmatism. Details of these proceedures and the problems associated with the use of 193nm are discussed in section 2.3.2.

2.2.3. - Liquid Laser

These type of lasers have several advantages compared with solids and gases: more homogeneous than solids but poorer quality than gases, easily made and circulated through the laser cavity for cooling, contain a larger density of active atoms than gases. The suitable organic dyes must first be dissolved in liquid solvents in order to become useful for practical purposes. The solutions are strongly fluorescent ie, they absorb radiation over a certain band and emit at longer wavelengths. The energy diference between absorbed and emitted photons will then appear as heat ie, non-radiative loss. Rhodamine 6G in ethanol is one of the typical solutions. Several wavelengths of dye lasers are now in medical use. In the laser, a suitable organic dye such as Rh 6G is pumped by a strong light source usually argon or nitrogen laser and sometimes excimer or copper-vapour laser to produce emission at various wavelengths. The wavelength of the laser can be controlled by varying the type of dye and by using tuning elements in the laser cavity. A 578nm (yellow light) pulsed dye laser is used in cosmetic treatment of vascular lesions because of the high specificity of haemoglobin to this wavelength. The high peak power and short pulse duration also helps to localize thermal damage by applying the beam at faster rate than heat can spread to

adjacent tissue. A 504nm pulsed dye laser is used to fragment kidney stones impacted in the ureter or otherwise inaccessible to shockwave lithotripsy. This laser sets up a number of shockwaves on the stone when the fibre is in direct contact with it. Other example is the use of a CW dye laser at 630nm (red light) in PDT where this wavelength corresponds to a particular absorption peak of a drug such as HPD, although recently new drugs such as DHE, TPP have been used.

2.3 - Ophthalmology

The main goal of this section is to provide an updated literature survey concerning the application of lasers in ophthalmology, in particular with regard to excimer and infrared lasers. However, it would be helpful first to have some basic ideas about the mechanism of the eye itself. For this reason the first part of this section (2.3.1) deals with the anatomy and physiology of the eye, where the main emphasis is placed upon the origin of transparency.

2.3.1. - Anatomy and physiology of the eye

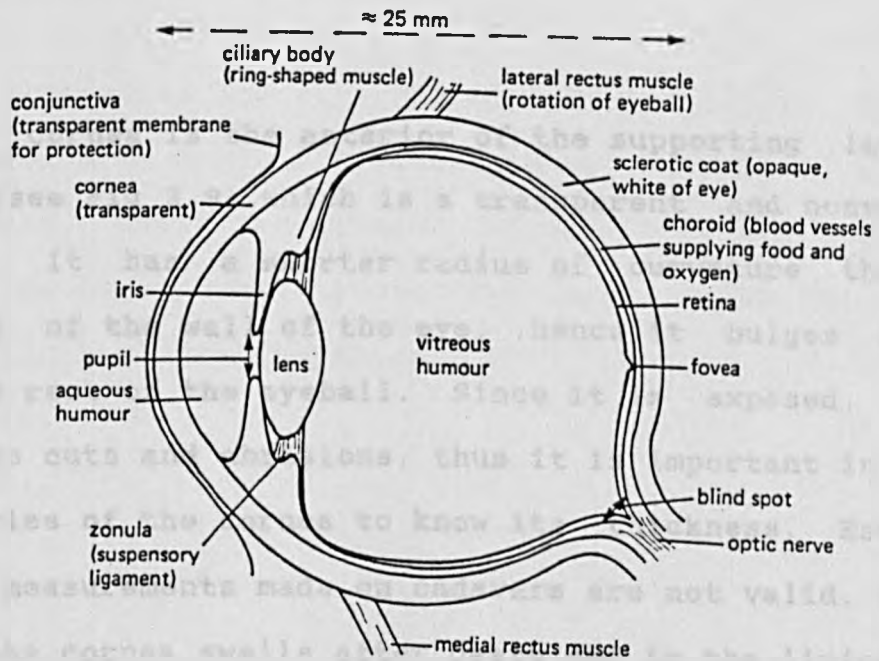

Fig. 2.9 - Diagram of horizontal section of the eye.

Broadly, the function of the eye is to receive light rays and transmit impulses to the brain where they are interpreted as 'seeing' ie, being aware of light intensity, shape, size, colour, position and movement. Light enters the

eye through the cornea, which refracts it through the aqueous humour onto the lens. By adjustment of the shape of the lens light is focused through the vitrous humour onto the retina. In the retina light-sensitive cells (rods and cones) send nerve impulses to the brain via the optic nerve. The arrangement of the two eyes at the front of the head provides binocular vision.

Since in this thesis, the experimental work was carried out on bovine cornea, lens and retina it is appropriate to describe some of their physiological aspects. This helps in understanding the possible reasons for chosing a specific laser wavelength for treatment.

Cornea:

The cornea is the anterior of the supporting layer of the eye (see Fig 2.9) which is a transparent and nonvascular membrane. It has a shorter radius of curvature than the remainder of the wall of the eye, hence it bulges forward from the rest of the eyeball. Since it is exposed, it is subject to cuts and abrasions, thus it is important in treating injuries of the cornea to know its thickness. Estimates based on measurements made on cadavars are not valid. This is because the cornea swells after death and in the living it is about 600μm. The periphery is slightly thicker than the central part. The photobiologic responses can only be studied in living tissue. However, to study the photophysical processes both the living and cadavar tissues can be used for analysing purpose. The epithelium covering the cornea is several layers in thickness and is replete with nerves that are chiefly of the pain type. Their stimulation results in

the blinking of the eye lids and in the flow of tears.

The cornea consists chiefly of dense connective tissue containing both cells and inter cellular substance called stroma (see Fig. 2.10). The corneal stroma consists of collagen fibres of uniform diameter gathered together in parallel inside lamellae. These lamellae are then placed at right angles to each other and each contains 75% of the water that it is capable of binding. The origin of water is due to 60% keratan sulphate and 40% chondroitin sulphate giving the total amount of glycosaminoglycans. These then act as anions and bind cations and water. If these glycosaminoglycans accumulate in the cornea it will result in its clouding and hence the loss of transparency. Because the central cornea is avascular it must derive oxygen from the atmosphere and metabolic materials by diffusion from the capillaries, tears and aqueous humour. Bowman's membrane is regarded as an important protective layer, being resistant to trauma and bacterial invasion, once destroyed it does not regenerate.

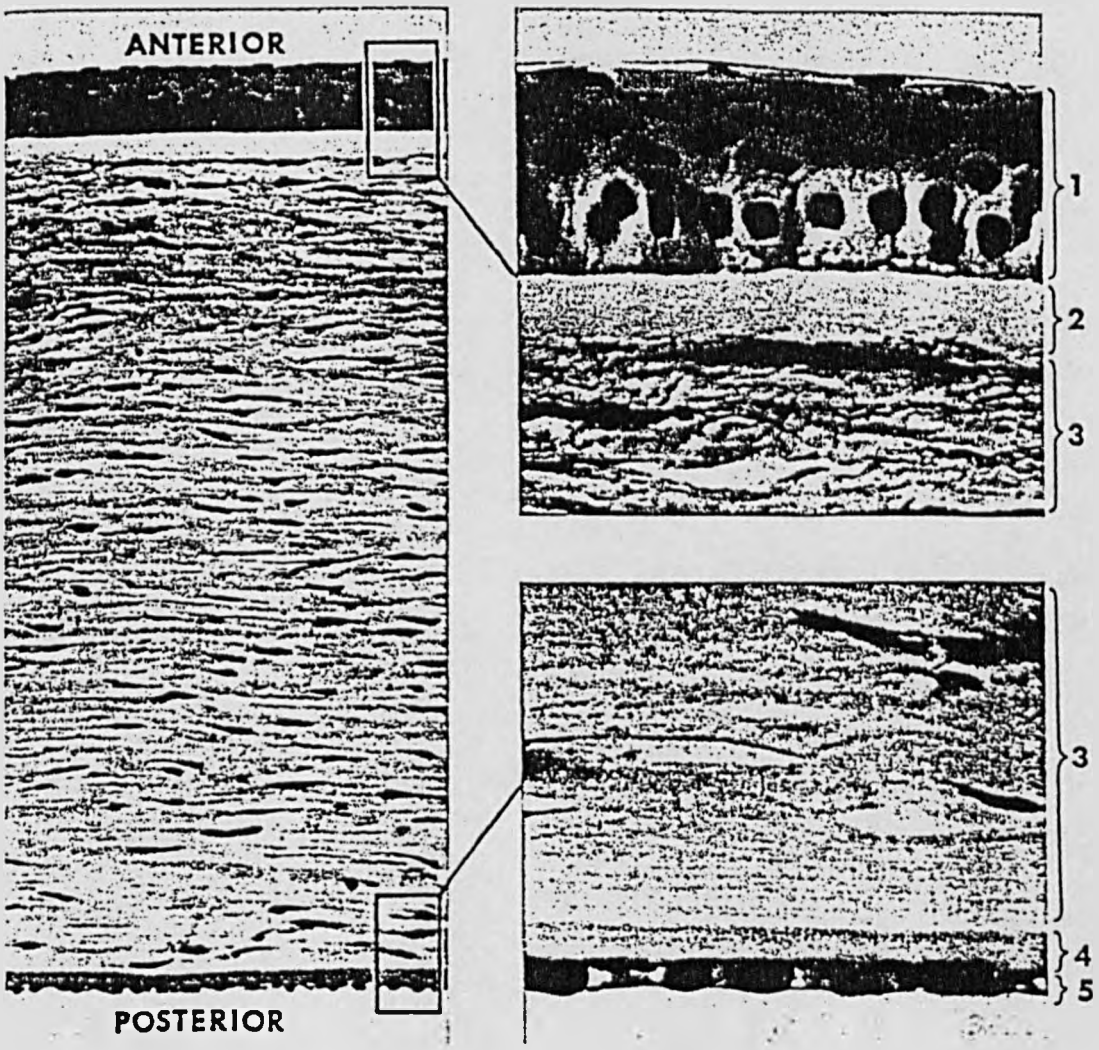

Fig 2.10 - Different sections of the cornea.

(1) epithelium, (2) Bowman's membrane

(3) stroma, (4) Descemet's membrane

(5) Descemet's endothelium.

Transparency:

The cornea transmits electromagnetic radiation having a wavelength of between 300nm in the U.V. and 2.5μm in the IR Transmission is about 80% at 400nm and 100% at 500 to 1200nm. The transparency of the cornea is a result of followings: (1) - the anatomic structure which include absence of blood vessels and pigment in the cornea. Also, the regular arrangement of the epitheliam and endothelial cells (2) - the tight junctions of the epithelial cells that are not permeable to aqueous solutions (3) - the dynamic balance between ions and water in the stroma that is maintained by an endothelial pump mechanism that controls corneal dehydration. The endothelium constantly pumps fluid from the cornea stroma to the aqueous humour. This process generates an electrical potential difference across the endothelium of about 1mv (aqueous negative). The negative charge of the aqueous is the opposite of that which would occur if there was an electrogenic transport of Na+. More information about the mechanism of corneal polarity can be obtained from Fischburg et al (68).

To understand the transparency it is necessary to consider the correlation in the phases of the waves scattered from each long collagen fibre in the ground substance. The collagen fibres in human stroma are spaced by distances small compared to the wavelength of light. As a result there is considerable correlation between the phases of light waves scattered by neighbouring fibres, and this will produce the required reduction in the scattered intensity. Large scattering and hence opacity results only if there are

substantial fluctuations in the index of refraction which take place over distances comparable to or larger than the wavelength of light (69). Opaque corneas in fact contain irregularities in the density of the collagen fibres and so-called 'lakes' where there are no collagen.

The corneal stroma consists of lamellae within which collagen fibres are laid down approximately parallel to each other in the ground substance. The arrangement of these collagen fibres in a lamella is shown in Fig. (2.11).

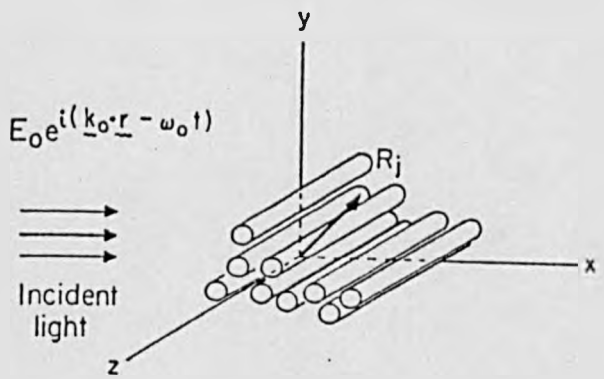

Fig. (2.11) - Schematic diagram of arrangement of collagen fibres in a lamella.

A thorough examination and mathematical treatment of the eye transparancy is given by Benedek (70).

Lens

The animal lens differs from the human lens in many respects. For example, the bovine, rabbit, and rat lenses grow fast initially but slow in maturity. Thus, there is little increase in weight in the second half of the life span. In contrast, the human lens grows slowly throughout life. The crystalline lens is mainly a transparent biconvex

structure located directly behind the iris, pupil and anterior chamber. The anterior surface has a radius of curvature of 10mm, and the posterior a curvature of 6mm. The equator is separated from edge of the processes of the ciliary body by a distance of 0.5mm. It is composed essentially of lens fibres that are held together to constitute a transparent medium. When the ciliary muscle is relaxed, the lens becomes spherical and hence causing the refractive power to increase. As the lens ages it loses water and becomes denser and less elastic, and its colour gradually becomes yellow; thus decreasing the amount of the blue and violet light that reaches the retina. The lens is composed of the following: (1) - lens capsule that covers the entire lens and is much thicker anterioraly than posteriorly and is thicker towards the periphery than it is over the centre of the lens, (2) - anterior lens epithelium located immediately beneath the anterior lens capsule, and (3) - lens substance consisting of cortex ie, newly formed soft lens fibres with nuclei, see Fig (2.12). These lens fibres continue to be formed through-out life, and as it ages, the old fibres are pushed towards the centre by new fibres so forming the nucleus. This explains the concentric and layered 'onion-like' appearance.

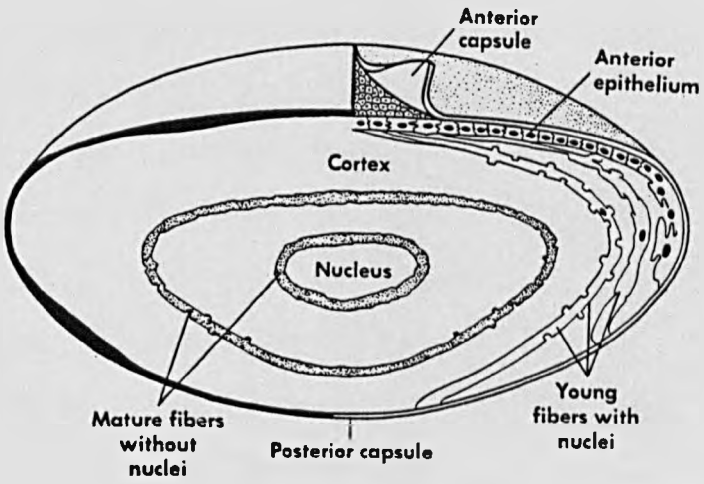

Fig. 2.12 - Schematic diagram of the lens cross section.

The main constitutents of the lens are water and proteins. The amount of water decreases as the lens ages and is greatest in the cortex where the younger fibres are found. The lens consists of about 60% proteins mainly water-soluble α, β, γ crystallins. Alpha (α) is the largest crystallin which first appears in the lens epithelium in embryonic life. The most abundant water-soluble protein is beta (β) crystallin mainly in the lens fibre. Gamma (γ) crystallin is the smallest and least abundant water-solluble protein with albumonoid being the water-insoluble protein material.

Other chemical constituents include the salt (NaCl) which increases with age along with the decrease in water content. Potassium, calcium and lipid are also present in the lens.

Transparency:

The lens transmits greater than 80% of electro-magnetic energy between (400-1400)nm. Despite the homogeneity of the lens it has a concentric structure of layers (nucleus) in

which the older central layers have a greater index of refraction than the surrounding younger layers (cortex).

In the normal lens, light is scattered by each of the proteins in the lens. However, it is important to notice that each protein does not scatter the light independently of its neighbours. The correlation in the position of pairs of proteins reduces the scattering in the lens just as the correlation between the positions of pairs of collagen fibres reduced the scattering in the cornea. In the normal lens, the fluctuation in the number of protein molecules over a dimension comparable to the light wavelength is small because the proteins are densely packed, and therefore transparency results. The presence of substantial numbers of large protein aggregates, for example, randomly distributed within the background of the α,β,γ protein constituents of the lens can affect the transparency. If the aggregated units have an index of refraction different from that of the average refractive index of the lens, and distributed randomly throughout the lens, they will scatter light proportionately to their number. In a cataractous eye, there is an aggregation of high molecular weight proteins into microsize particles causing the scattering of light and hence loss of transparency. In addition to aggregation it has been observed that the lens proteins undergo chemical and physical changes such as increasing fluorescence (71) and pigmentation (72).

Lens transparency depends on the spatial ordering of lens proteins in the fibre cells. Thus, any localized alteration in the density and structural integrity of this ordering due to aggregation, pigmentation, hydration etc. can

result in regional changes in refractive index, and lens transparency leading to development of opacities (cataracts). Conventional invivo techniques such as optical techniques and slit lamp for assessing lens changes have relied on the use of visual transparency as an index for normal lens function. They also, require making optical density measurements from photographic negatives which is time consuming, and above all the results do not provide information on the primary causes of cataractogensis namely, lens metabilism changes and lens protein conformational changes.

A different approach has recently been used by Ahmed et al (73) where they have shown that measurements of the temporal profile of the backscattered pulse has the potential to monitor the extent of cataract development in the eye. This monitoring is based on the use of an ultrafast short pulses of 100 fs at 82MHz. According to Nai-Tung Yu et al (74) the major disadvantage of light scattering method is its restriction to in vitro measurements from thin lens sections and as such is not readily applicable to in vivo clinical evaluations. Other techniques showing considerable promise for detection of pre cataractous changes in the lens are: Nuclear magnetic resonance (NMR) which provides information on lenticular pH, phosphur concentration (75); autofluorescence which determines the concentration of long wavelength absorbing chromophores resulting from abnormal lens metabolism (76); and Raman spectroscopy (77). Raman spectoscopy holds a number of advantages for the study of the lens proteins. These are: non destructive structural probe, the use of laser makes local analysis of an intact lens possible,

a variety of information about the lens proteins can be obtained simultaneously from a single Raman spectrum in the (4000-300)cm^{-1} region (78). The physical constants of some occular media are shown in Table 2.1.

Medium	Thermal conductivity K($Wm^{-1}{}^{o}K^{-1}$)	specific heat capacity C($Jkg^{-1}{}^{o}K^{-1}$)	density ρ(kgm^{-3})	refractive index n	Thickness t(mm)
Cornea	0.58	4178	1050	1.376	0.6
Aqueous humour	0.58	3997	1000	1.336	3
Lens	0.40	3000	1050	1.424	3.6
Vitreous humour	0.603	4178	1000	1.336	17

Table 2.1 - Physical constants of some of the ocular media.

2.3.2 - Background information on lasers in ophthalmology

Excimer lasers

Lasers currently available or under development can produce light energy across much of the visible and ultraviolet ranges into the x-ray regions, from microwatt to terawatt power levels, and with pulse durations of only a few femtoseconds to continuous irradiation. It has become apparent that the effects of laser energy on tissue differ widely according to lasing parameters and the specific characteristics of the tissue and surrounding medium. To evaluate adequately the potential uses of laser technology for treatment of ocular disease, systematic studies are needed to observe short and long-term tissue effects according to laser wavelength, energy level, and exposure time as well as monitoring the effects on adjacent medium. This section is intended to concentrate on some of the applications and comparison of excimer and infrared lasers in ophthalmology.

Ophthalmologists were among the first to use lasers in surgery, first experimentally (79) then in the human eye (80). One medical application - retinal photocoagulation - was rapidly pursued. Although the incandescent xenon source had been used successfully it gave way to the ruby laser and later to the argon and krypton lasers.

Interest in surgical application of excimer lasers were generated by reports that their intense ultraviolet radiation could be used to etch submicron patterns into the surfaces of plastics and polymers with a high degree of accuracy and with no degradation processes being conducted to

unirradiated areas (81-83). Two theories have been suggested to account the effects observed. The first theory which was first proposed by Srinivasan et al (84-86) asserts that the UV laser interaction with polymers and tissue is basically a non-thermal event known as photablative decomposition. This theory suggests that ultraviolet photons with energies greater than 3.5ev can be converted to electronic excitation leading to the breaking of molecular bonds without the energy degradating into heat. The long-chain polymers molecules break up into smaller volatile fragments which are rapidly expelled from the surface. The fragments carry away almost all the energy deposited in the surface by the laser beam. If the energy were not carried away, it would transform into heat diffusing into surrounding material and eventually produce thermal damage. The pulse duration must therefore be suitably short so that the entire process take place in less time than required for heat to diffuse into the surrounding material (ie, less than the thermal relaxation time). Similar results were obtained in biological tissues with 193nm (86-89), 248nm (89-91), and 308nm (92) radiation. Fig. (2.13) shows the different stages of photo-ablative decomposition process in materials.

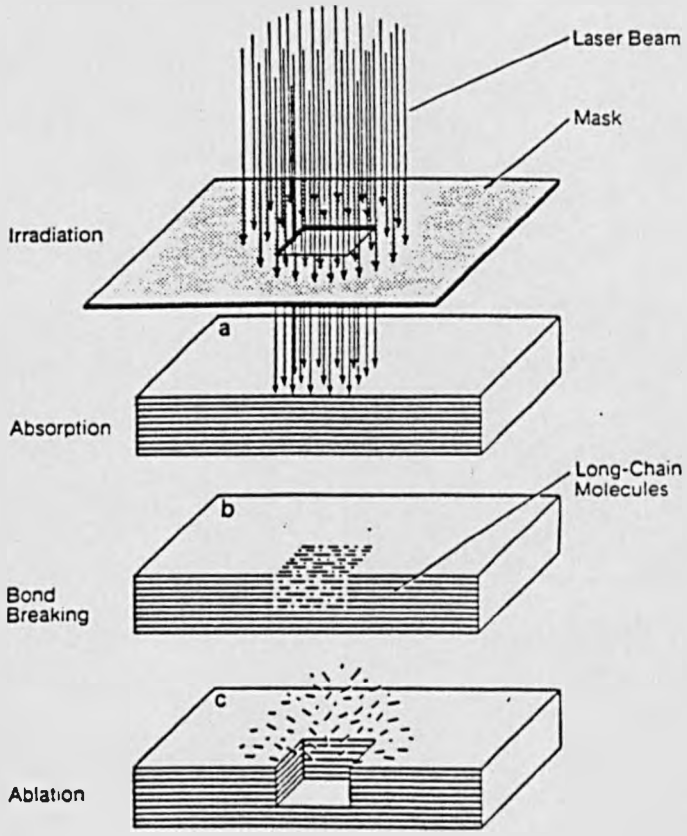

Fig. 2.13 - schematic diagram of photoablative decomposition process (93).

Srinivasans hypothesis that excimer lasers induce primarily photomolecular decomposition has received frequent support. Marshall et al (94) in a comparative study conclude that ablation induced by excimer laser results from highly localized photochemical reactions and that 193nm is the optimal wavelength and superior to 248nm radiation. They also support the idea that the ablation process requires a balance between the photon energy which determines the quantum yield for bond breaks, and the excess energy of the photon over the bond energy which is then available to expel the products at supersonic velocity. Thomson et al (95) used a 157nm excimer laser for corneal ablation and agree in support of Srinivasan

hypothesis.

An alternative theory put forward by Andrew et al (96) proposes that beam tissue interactions are predominately the result of fast thermal events, and that the induced change arises because of the very short penetration or absorption depth of ultraviolet radiation. This idea mainly applies to longer UV radiation wavelengths such as 308nm and 351nm rather than shorter wavelengths like 157nm and 193nm. The theory was later supported by Murphy et al (97) who suggested that the effect of excimer irradiation on vascular tissue is predominantly by a thermal process and similar to that of other wavelengths. It may be the manner in which laser energy is delivered and not the wavelength which allows precise ablation of tissue (97). In an experiment with post mortem human artery Singleton et al (98) concluded that the laser wavelength, pulse width and fluence have important effects on the cut quality and that in air with fluences near the ablation threshold for a 308nm laser, the irradiation results in ragged cuts with evidence of thermal damage which appeared as orange colour on the crater. With fluences slightly higher than threshold sharp tissue cuts were observed with little or no thermal or acoustic damage. However, as the fluence increased to much higher level than threshold it resulted in the disruption of the tissue as well as the production of acoustic damage.

Analysis of the mechanism of UV laser ablation of the cornea requires a knowledge of the products of the ablation process and the time frame in which ablation occurs. In a high-speed photography study Pulifito et al (99) demonstrated

that much of the ablation process occurs over a much longer time scale of nanoseconds and continue to be ejected from the cornea for 5 to 15 μs following the excimer laser pulse. Greater corneal endothelial injury was observed (100) for 248nm compared with 193nm ablation of the corneal stroma. Because the ablation process is an explosive one, the larger particles ejected at 248nm generate greater recoil forces, which are speculated to have capability of producing cell loss (100).

Having briefly outlined the possible mechanisms of UV excimer lasers ablation of material, some of the recent ophthalmological applications are now described. In 'Radial Keratotomy' where the incisions are made with the steel and diamond blades disruptions of corneal lamellae, mild stromal hypercellularity, collagen deposition, and epithelial ingrowth in the superficial portion of the wound are observed (94). Cuts that are too shallow result in undercorrection or no correction, and incisions that are too deep risk perforation, cataract or overcorrection. Interest has turned to lasers as the ultimate programmable mechanism for making the most precise corneal incisions possible. Keates et al (101) have experimented with corneal surgery performed with a CO_2 laser. The collagen-water content of the cornea makes it extremely susceptible to the heat generated by CO_2 laser wavelengths, resulting in distortion and vapourization of tissue. This leads to poor wound healing and unacceptable irregular cornea scars. In a photoacoustic study of bovine cornea with CO_2 laser Dyer et al (90) suggested that one possible reason for such an irregular incisions can be due to

energy absorption of laser by cornea content, mainly the stroma which contains about (75-80)% water, consequently leading to a high degree of super-heating. Thus, the combination of vapour bubbles due to superheating and extra laser energy which suports the vapour production at high pressure results in protein content of the tissue being mechanically ruptured and expelled instead of thermally decomposed.

On the other hand research has shown that the ArF (193nm) excimer laser is an excellent tool for polymer ablation and corneal surgery with minimum thermal damage to adjacent areas (82-93). These studies have resulted in some of the most interesting and important non destructive surgical techniques. Excimer lasers have been used to perform two types of operations:

(1) - Those systems which are used to create radial (or transverse) incisions for therapeutic reasons - called Radial Keratectomies (RK). It must be noted that when the surgical procedure of radial keratotomy was pioneered in Russia, a dimond knife was used to make the incisions. However, since a dimond or steel knife splits tissue without removing it, and excimer laser ablation by definition must remove some tissue, therefore it is appropriate to use radial keratectomy rather than radial keratotomy.

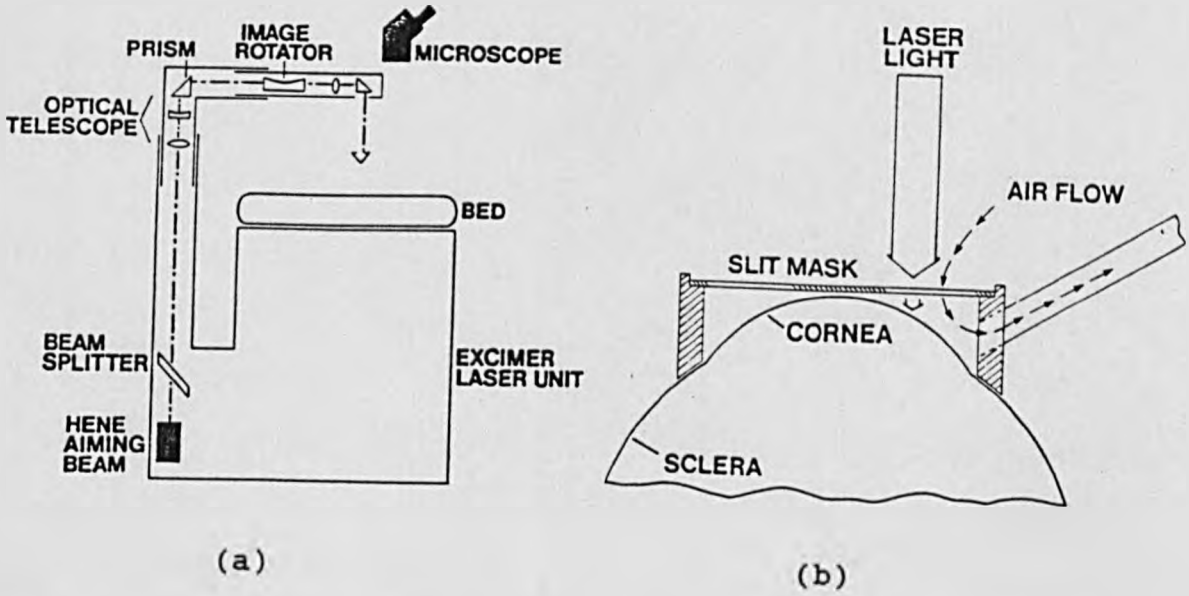

Fig. 2.14 - Schematic cross section of the Meditec excimer laser 50 (a) and Meditec slit mask (b).

Schroder et al (102) have described the special design feature of the first commercially available ophthalmic excimer laser (meditec excimer laser 50). The excimer laser is located beneath the bed, to save space. Beside the bed is the delivery system which brings the laser light into position above the patient's head and directs it onto the cornea. The beam from the laser source is directed upward by a beam splitter. An optical telescope changes the beam shape to create a higher energy density and a prism is controlled by a micromanipulator so that the laser light slit can be easily shifted across the eye and can also be rotated. The projected laser light slit serves as the illuminating system for a special mask that is positioned directly on the eye. The mask consists of a plastic ring that is positioned on the sclera

and carries a circular metal plate with fine radial slits. A pipe is connected to a pump that sucks air out of the cavity between the cornea and the mask. However, air enters continuously through the slits so that the mask is not vacuum tight. The air flow serves two important functions: first, it cools the mask which heats up during the laser exposure, secondly, it carries away the gaseous products created by the photoablation of the cornea.

Theoretical advantages of using an excimer laser for radial keratectomy are:

i. Two or more of the incisions could be made simultaneously with a high degree of spatial resolution, accuracy in localization and reproducibility.

ii. The absence of contact during the procedure, without deformation of the cornea as the cuts are made, might allow for real-time topographical analysis to monitor and control the surgical process.

iii. Since these full-depth incisions could be made in approximately (20-30) seconds, variations in corneal thickness due to dehydration would presumably be reduced.

(2) The lamellae keratoplasty is an eye operation which any superficial diseased part of the cornea is replaced by a donor tissue leaving the deeper layers in tact. If, however, all parts of the cornea is to be replaced, it is called penetrating keratoplasty. Those systems which are designed to ablate large area of tissue for lamellae or refractive surgery known as 'Large Area Ablation' (LAA). In 1983, Trokel et al (86) described the use of an ArF (193nm) laser to

ablate precise areas of the cornea and achieved a very clean cut.

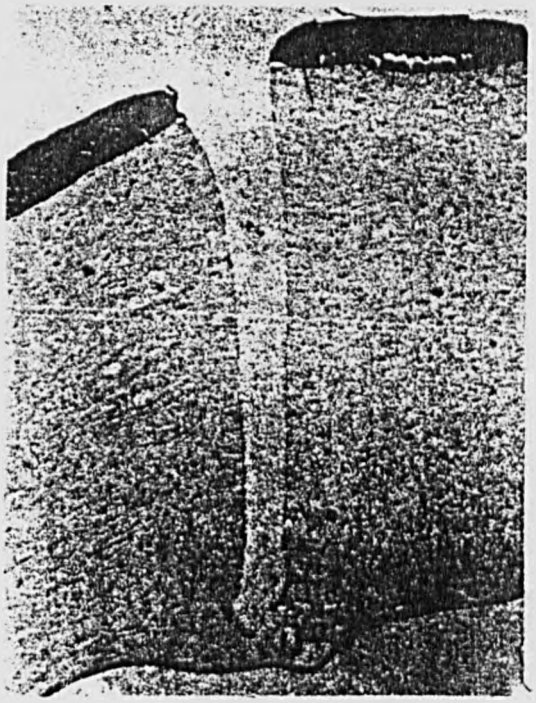

Fig. 2.15 - Histological section of cornea after 193nm laser exposure through a 100 μm hole (86).

Marshall et al (103) have termed such an operation of LAA 'photorefractive keratectomy' (PRK) which is mainly used to change the refractive power of the cornea. An example of such a clinical system is shown in Fig. 2.16. Before an operation takes place, a corneal surface scan (refractive data) is fed into a computer connected to the laser. The aligorithms programmed into the computer system determine how much corneal stromal tissue must be removed to produce the desired corrective effect.

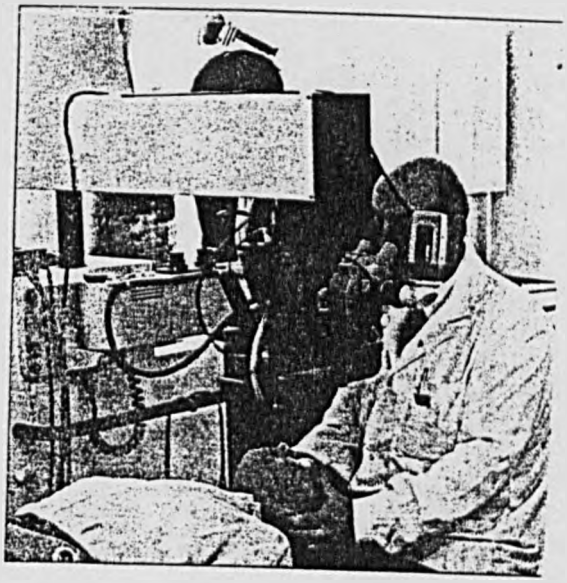

Fig. 2.16 - A clinical example of PRK.

In this approach, an optical zone is exposed to excimer laser radiation, the intensity and duration of which are varied to create the desired optical change. To correct myopia (short-sightedness), the central corneal power would be reduced by ablating a known amount of optical zone (apex) of cornea using a series of apertures with decreasing diameter, tapering off in depth towards the periphery of the determined optical zone. Fig. (2.17) shows an example of myopia correction where the cornea is contoured by successive ablation before regrowth of epithelium. After this regrowth, the edges of these step-wise discs will be joined together, hence leaving a relatively smooth surface with a smaller curvature compared with initial value.

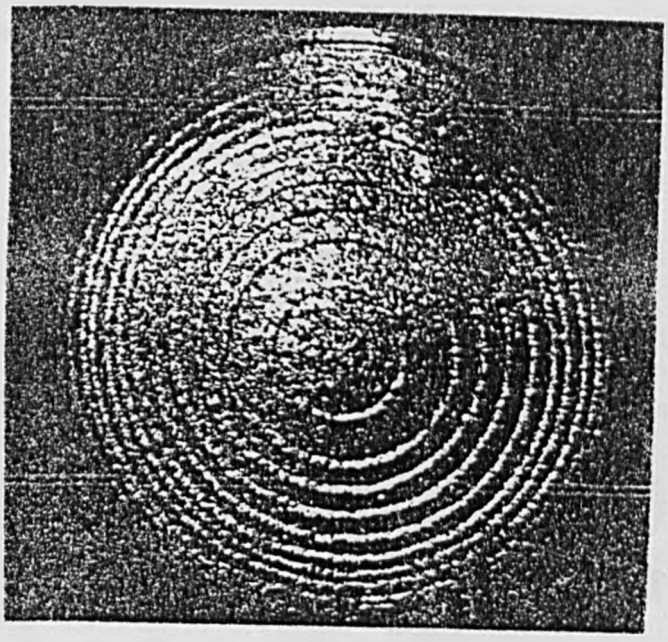

Fig. 2.17 - A contoured cornea by excimer laser for myopia correction.

Hyperopia (far-sightedness) can be corrected by the same laser provided the circular aperature is replaced by annular apertures with decreasing radial width. In this case, the ablation is deepest in the periphery and tapers to zero at the centre, hence increasing the curvature of cornea and reducing the hyperopic effect. Astigmatism is corrected in a similar way except that here a series of slit-shaped apertures of varying width is used. The depth of maximum central ablation necessary for a given optical change can be predicted by the following formula:

$$D_e = (D_o)^2 \times \frac{\Delta R}{3} \qquad 2.6$$

where D_e, D_o and ΔR are the total depth of ablation (μm), diameter of optical zone, and change in refraction (Diopters) respectively. Note that diopter (D) is measured in (m^{-1}) and is defined as reciprocal of effective focal length measured in meter. For example, if D_o= 6mm, then 4D of myopia is corrected with a 48μ m deep ablation. Marshall et al (103)

ablated discs in rabbit and monkey corneas. Dosage parameters were 50 to 600 pulses, 10Hz and 140 to 310 $mJcm^{-2}$ per pulse. Ablation at 193nm produced smooth borders and surfaces, whereas at 248 nm yielded rough margins and an abnormal zone of densely staining collagen 2 to 3µm wide. If collagenous tissue is produced with an irregular structure, it forms a scar, scatters light, and decreases visual acuity. However, most corneas studied develop a persistent haze that last up to 6 months without evidence of resolution (104). Haze after the healing process is not the only possible reason causing the poor glare vision, but also may be due to an optical zone that is smaller than dilated pupil. Halo refers to a situation where the peripheral cornea creates a blurred image concentric to the sharp image of the corrected (flatter) control cornea. Larger optical zones will help to overcome the halo problem. However, greater optical zones leads to greater excision depths and deeper ablation may increase the potential for corneal opacification.

Controversy still exists as to whether PRK will produce a surface with good resultant optical properties and how the healing process will influence the stability of the induced changes over time. Marshall et al (103) created straight-walled ablations in rabbit and monkey corneas with the 193nm excimer laser, producing well-healed regions with good optical quality, but the epithelium was hyperplastic over the ablated area. Square-edged discs produced by Tuft et al (105) in rabbit eyes revealed that the epithelium migrated rapidly over the wound edges and covered the base, producing leveling effect. In a one-year follow up Seiler et al (106) concluded

that PRK is an efficient procedure to correct myopia up to -7D and the stability between 6 and 12 months was excellent for only two third of the patients (8% of the treated eyes showed fluctuations of more than 1D). One important requisite for stability of regenerated epithelium is tight adhesion of the underlying stroma. Anchoring fibrils are thought to help establish this adhesion via its basement membrane (107).

Generally, the clinical application of laser refractive keratectomy depends on the ability to create a surface with good resultant optical properties that are stable over time. When the corneal surface is altered, it responds by attempting to re-create a new smooth surface by a combination of epithelial regeneration and stromal regrowth. By producing a smoothly contoured profile with excimer laser in the animal models Goodman et al (108) observed that the epithelial regeneration creates a smooth corneal surface without hyperplasia. In 1991, Sher et al (109) used a 193nm laser to ablate the cornea and to remove opacities and other corneal disease in a procedure called phototherapeutic keratectomy and reported that after surgery, the majority of patients had eye pain, sometimes severe. In general, this procedure is more painful than radial keratectomy and patients had to take narcotic analgesia during 24 to 48 hours after surgery.

For clinically useful laser refractive keratectomy the following points are suggested by Hanna et al (112):

1 - Acceptable lasers with defined wavelengths and energy parameters must be identified, for example ArF (193nm), HF (2.9μm).

2 - A delivery system must be developed that creates an accurate ablation profile and is flexible enough for different types of refractive corneal surgery.

3 - A method of coupling the laser and delivery system to the eye to compensate for ocular and body movements must be devised if the potential accuracy of laser surgery is to be realized.

4 - There must be demonstration of acceptable tissue response and control of corneal wound healing, specifically the prevention of subepithelial fibrosis causing light scattering and of epithelial hyperplasia that may neutralize the newly created curvatures of the corneal surface.

5 - There must be accurate calculation of the refractive outcome after wound healing using computer models of the cornea.

6 - Methods must be developed to measure the results of such corneal surgery, including complete measurements of corneal thickness and topography.

It must be noted that there is a big difference between measurements of non living and living tissues. For example, the effect of cornea age on ablation rate as well as the short and long term response after healing process are among other important issues.

Other applications of excimer lasers in ophthalmology

So far, the ocular application of excimer lasers have been concentrated on corneal surgery with a certain amount of success. It is, therefore, natural to utilize the advantages of these lasers in other parts of the eye. However, the

optical properties of a particular part of the eye should be thoroughly studied with respect to given laser parameters. The concept that exposure of human and animal lenses to UV wavelengths of sunlight is a factor in the formation of cataracts has existed for many years. It was mentioned in section 2.3.1 that the perfect physicochemical arrangement of the lens proteins gives transparency to the lens, and that the lens aging and opacification (cataract formation) are induced by the formation of protein aggregates which disturbs the molecular organization of the crystallines.

Generally, the UV wavelengths are designated as near (UV-A) 400-315nm, mid (UV-B) 315-280nm, and far (UV-C) 280-100nm. The cornea is a very efficient filter for blocking the UV-C, whereas the lens in the UV-A has low transmission and high absorption. The high absorption of the lens in the UV-A is due to a pigment which accumulates throughout life, and apparently shields the retina from this radiation. In comparative studies of excimer laser ablation of the cornea and lens using 193nm and 248nm radiation, Puliafito et al (111) observed a higher threshold fluence for cornea and lens using 248nm. At 193nm they (111) found the values of 46mJ/cm^2 and 20mJ/cm^2 for human and bovine corneas, whereas at 248nm values of 58mJ/cm^2 and 71 mJ/cm^2 were measured respectively. For bovine lens fluence of (1-3.8) J/cm^2 at 193nm and (2.2-3.8) J/cm^2 at 248nm were used. The reasons for greater tissue damage and irregular incisions in the case of 248nm are likely due to the greater penetration depth at this wavelength than 193nm. Following these experiments Naneviez et al (112) performed similar experiments with lens tissue

using all four excimer laser wavelengths. The highest ablation rate was observed at 248nm with lower rates at 193nm and 308nm. No ablation was observed at 351nm. In ref. (112) the ablation thresholds of lens at three excimer laser wavelengths were found as follows: 248nm > 308nm > 193nm whereas in this thesis the order is as 308nm > 248nm >193nm. In 1987, Bath et al (113) demonstrated the use of pulsed UV radiation for removal of cateractous lenses. Although they (113) used a 308nm laser for lens ablation, the main difference with previous (111, 112) experiments was the use of optical fibre. Up to 20mJ of XeCl laser (17ns) output was coupled to quartz optical fibre. In 1988, Bath et al(114) reported another experiment in which 308nm laser was used to ablate lens tissue. The ablation threshold for bovine lens was approximately 0.6J/cm^2 for cortex and 1J/cm^2 for nucleus. In the same year Muller (115) carried out an endocapsular cataract operation in which the lens nucleus was fragmented by the 308nm pulses and aspirated. The lens cortex was aspirated in a similar manner to a phaco-emulsification procedure. Fluences around 50mJ/mm^2 were applied and the endocapsular ablation of human lens nuclei could be performed without major damage to the anterior and posterior lens capsule (116). In 1990, Li et al (117) used calf lens and UV wavelengths of 308nm, 337nm and 350nm and exposure time of 10 minutes to 5 hours at 2, 0.2 and 2 watts respectively. They concluded that lenses exposed to 308nm UV radiation for 10-30 minutes showed significant yellow-brown pigmentation and colourless opacification compared with dark control lenses by photographic record. Lenses exposed to 337nm light

showed primarily colourless opacity with little pigment production. Lenses exposed to 350nm radiation for 1 hour were visibly indistinguishable from dark controls. Lens damage can be initiated by 280-310nm UV radiation which is absorbed directly by the lens proteins, (mainly by tryptophan residues (118)), by longer wavelengths of UV radiation where it maybe absorbed by some other chromophore (eg. N-Formylkynurine-NFK), or even by visible light absorbed by photo-sensitizors such as riboflavin (119).

Excimer lasers have been used in other medical research fields such as angioplasty (120-123) where 308nm radiation coupled to optical fibre can be used to unblock the coronary arteries. Perhaps, the most important issue in this case is identification of healthy and atheroma tissues. This has recently been approached by using laser induced fluorescence spectroscopy (LIFS). In urology, the 308nm-fibre combination has also been used to photoablatively decompose rather than fragmenting kidney or gall stones (124, 125). Recently, interest in using UV lasers in dentistry has grown and two different wavelengths ie, 308nm and 193nm are used. The 308nm-fibre combination was used to remove residual organic tissue from the canals (126), and 193nm to study the ablation of dentin and enamel tissues (127). Finally, by combining 308nm radiation and tappered fused silica fibres Dressel et al (128) were able to achieve output fluences up to 32 J/cm^2 and ablation rate of 3μm per pulse of hard tissue (Bone). This enables bone and cartilage cutting in a real accident surgery.

Limitations of excimer lasers

These limitations are related to a number of factors: (1) - optical properties of the laser radiation, (2) - safety considerations, (3) - type of application and delivery system, (4) - optical and physical properties of the target in different media. Ideally, one would prefer to use 193nm radiation outside and inside the eye because of its clean and controllable incisions. However, its uses invivo are severly restricted by the delivery system ie, lack of suitable optical fibre. Since the energy of a photon at this wavelength is 6.4ev, no fibre at present time can withstand high fluence radiation for prolonged exposure. Additionally some researchers believe that even if a suitable 193nm optical fibre were developed it would still need to be immediately adjacent to the target tissue to avoid absorption of radiation by physiologic saline - Na^+Cl^- (129). The absorption mechanism of 193nm light in physiologic saline is considered as a charge transfer from chloride (Cl^-) to water (H_2O). The energy of 193nm photon is theoretically sufficient to detach an electron from chloride (129, 130). This process has a resonance absorption maximum at 190nm wavelength, which would explain why 193nm light is absorbed more readily than 308nm in saline. As far as 193nm radiation safety is concerned, there are number of contradictory results, but perhaps the overall view is that this laser wavelength is not a serious problem. Loree et al (131) in an experiment with 193nm, 248nm and 308nm simply concluded that for laser ablation of the cornea, ArF seems to be both the best and the most interesting. Ablation of rabbit cornea with 193nm (132)

and mouse fibroblasts (133) did not produce a significant amount of mutagenic effects. On the other hand, irradiation of saccharomycas cervisiae using this wavelenght has shown DNA lesions, a result which has been interpreted to be due to secondary fluorescence light rather than direct excitation by this wavelength (134). In 1991, Rimildi et al (135) reported that a low level of unscheduled DNA synthesis could be detected following irradiation at 193nm with 70J/cm^2, and both the 193nm and 248nm radiation were able to induce chromosomal aberrations.

According to Kochevar (136) there are at least two reasons which could explain the lower cytotoxicity of 193nm radiation; (i) the radiation is absorbed by proteins of the cell membranes and cytoplasm ie, the proteins effectively shield the nucleus from the damaging effects of 193nm radiation. (ii) if photons of this wavelength reach the nuclear DNA and induce DNA photoproducts these are either not cytotoxic or are readily repaired by the cells. Because absorption of 193nm radiation produces a higher excited state of DNA than 254nm radiation, the latter is a likely possibility. A model is suggested by Forster et al (137) for testing the excimer laser radiation mutagenicity in ophthalmology.

Gactitis et al (138) have proposed use of a solid-state laser that produces a wavelength near 193nm (ie 213nm) which could eliminate many of 193nm excimer lasers disadvantages, eg. use of a fluorine gas mixture which is toxic and potentially hazardous to patients, had a short 'sealed' life, and a corrosive effect on laser cavity and resonator. In an

experiment (138) it was shown that these disadvantages are overcome and damage zone for the 213nm laser was less than 1μm and for 266nm light less than 10μm for corneal tissue.

Studies using 248nm laser radiation have shown that this wavelength is highly mutagenic (132, 133). UV-C (eg.193nm) wavelengths are most photochemically active due to their energetic photons and therefore are strongly absorbed in certain amino acids and proteins. UV-B (eg.308nm) wavelengths are less photochemically active but penetrate more in most tissue. UV-A (eg.351nm) wavelengths are the least photochemically active radiations and penetrate tissue more than UV-B and UV-C. More importantly because 308nm radiation lies on the edge of most protein absorption spectra it makes this wavelength the most hazardous radiation causing possible carcinogenic effects (139). Some believe that the development of fibre optic delivery systems and the use of XeCl laser on the lens tissue would be a useful adjunct to current surgical technologies such as those 308nm lasers used in refs. (115-117). Other advantages of this laser include lower potential risk to patients and clinic personnel to toxic gas, as HCl rather than fluorine is used.

However, Keates et al (140) observed blue flourescent emission at the posterior pole in the aphakic eyes exposed to 308nm radiation. In the visible part of the spectrum such radiation can travel through the entire eye experiencing little absorption. Keates et al (141) in previous experiments suggested the orientation of the fibre tip and the surgical approach could limit the dose to other structures. For example, ablation of nucleus first would limit the

retinal exposure by taking advantage of the absorption of scattered radiation by the cortex. In any case, exposure of the ciliary body would more likely be greatest. Another safe approach in the endo-capsular cataract operation is to keep the UV exposure of the retina below the critical value of 1.7J/cm^2. However, in real phacoemulcification procedures it is very probable that capsule rupture occurs, hence allowing leakage of some radiation. One method of reducing such leakage to the retina would be to inject a UV absorbing drug in the vitreous humour, but more research is required to allow the best approach to be determined.

Strictly speaking, one does not wish to suggest that all ultraviolet laser wavelengths would be undesirable in endo-capsular or other surgical operations in the eye. However, the choice of wavelength should be made with regard to the absorption by target tissue and the potential for injury to adjacent tissues by scattered radiation or pretarget absorption.

Infrared lasers

Knowledge of the interaction of IR radiation with ocular structure is of considerable importance and a variety of surgical procedures have been developed eg. keratectomy, cataract surgery, cutting vitreous membrane, retina photocoagulation and glaucoma. In this section a brief review of interaction mechanisms and applications of near (IR-A) 0.7-1.4μm, mid (IR-B) 1.4-4μm, and far (IR-C) 4-30μm is given.

An early infrared laser application made use of Nd:YAG in ophthalmology. The development of the Q-switched laser led to an interaction where there was no apparent burning of bio-

logical tissue (142).

An example of the application of YAG laser is the removal of a cloudy posterior capsule following cataract surgery. The normal lens is contained in a sack called the capsule. After removal of a cloudy lens, the posterior wall of the capsule often opacifies. In conventional cataract surgery an opening is provided by puncturing the capsule. However, this invasive method carries with it the potential for infection or damage to other ocular membranes. YAG ophthalmic surgery involves focusing a short, high-power pulse of radiation on the membrane to produce optical breakdown and thus mechanical rupture, due to the associated shock wave. The result is a hole in the capsule without the potential side effects of invasive surgery. The ultimate objective of the laser design is to produce individual pulses of uniform energy, pulse width and spatial mode. Detailed considerations are given by Lerman (143) and Puliafito (144).

Another clinical example of IR laser is the application of Nd:YLF (1.053μm) in radial keratectomy. Plasma mediated ablations were performed on human donor corneas with a short pulsed Nd:YLF laser with a pulse duration of 60psec. operating at 1KHz (145). The walls of the laser excisions were reported to be smooth with distortions of less than 1μm. An important and possibly hazardous problem when the eye is irradiated by pulsed IR-A light is second harmonic generation (SHG) by the cornea, lens and retina. Although, Hochheimer (146) reported a small conversion efficiency ($6x10^{-9}$) using a pulsed YAG laser with an average pulse width of 30μsec when irradiated cornea, these results did not rule out the

possibility that there would be a similar effect occuring in the retina. The possible mechanisms responsible for these SHG are discussed in detail in references 146 and 147.

The last example of near-IR lasers is the application of semiconductor diode lasers for treatment of different ocular diseases. Despite relative successes of current laser therapy with argon and krypton lasers, the retinal vascular operation, for example, is complicated by recurrence, haemorrhage, pain, visual loss and treatment failure. Work continues on developing new diode laser systems with the hope to overcome these problems. Light scattering is a phenomenon inversely proportional to the wavelength of light to the fourth power (Rayleigh scattering) so that short wavelength blue light is scattered much more than longer wavelength red light. Macular photocoagulation with blue light can cause direct heating and thermal damage to the inner retina, but this can be avoided by using longer wavelengths. The light emitted by currently available laser diode is in the near infrared with wavelength from 780 to 840nm. At this comparatively long wavelength, light penetration through cataract and haemorrhage is improved compared with shorter wavelengths (148).

Balles et al (149) performed retinal photocoagulation using a GaAlAs diode laser emitting at 805nm. The operation was performed using 300 to 1300 mW and exposure durations of 0.2 to 0.5 seconds with a 200μm spot diameter. Jacobson et al (150) also used a 805nm wavelength with power levels of 500 to 700 mW in iridectomy. Absorption of diode or argon laser energy is dependent on tissue pigmentation. The principal

1. Halldorsson T.L., Langerhok J.C.
Thermodynamic analysis of laser irradiation of biological tissue.
Appl. Opt. 17:3948:1978.

2. Goldman L.
Lasers in Medicine - Vol. 1:1971

3. Mccord R., Weinberg W. et al.
Thermal effects in irradiated biological tissue,
Proceedings of lasers in med. and biology symposium,
Neuherber. pp.91-99, 1977.

4. Carslaw and Jaegar J.C.
Conduction of heat in solids.
Oxford University press - p.259 - 1959.

5. Walsh, J., Flotte T.,
Pulsed Co_2 laser tissue ablation: effect of tissue type and pulse duration on thermal damage.
Lasers in Surg. and Med.
8:108:1988.

6. Ippen, E.P. Shank V.
Techniques for measurements in ultrashort light pulses
springer-verlag, Berlin, p.83, 1977.

7. Salin, F. et al.
Single-shot measurement of a 52 fs-pulse,
Appl. Opt. Vol.26, No.21, 1987.

8. Kaminow I.P., Wiesenfeld J.M.
Argon laser disintegration of Thrombus and atherosclerotic plaque.
Appl. Opt. 23:1301:1984.

9. Srinivasan R., Mayne-Banton.
Self-developing photoetching of PET-Laser radiation.
Appl. Phys. Lett.
41:576:1982.

10. Müller G., Schaldach B.
Basic laser-tissue interaction,
Proceedings of first planary workshop on safety and laser tissue interaction. Berlin - November 1988.

11. Lune R.J., Wynne J.J.
Ultraviolet laser ablation of skin: healing studies and a thermal model.
Lasers Surg. Med. 6:504:1987.

12. Isner J.M., Clerk R.H.
The paradox of thermal ablation without thermal injury
Lasers in Med. Sci. Vol.2, No.3, 1987.

13. Bown S.G.
Phototherapy of tumours
World J. Surgery. 7:719:1983.

14. Matthewson K., Coleridge-Smith P. et al.
Comparison of CW and pulsed excitation for interstial Nd:YAG laser induced hyperthermia.
Lasers in Med. Sci. 1:197:1986.

15. Dowdern J.M., Davis M., et al.
Heat flow in laser treatment by local hyperthermia.
Lasers in Med. Sci. 2:211:1987.

16. Whiting P., Dowden J.M., Kapadia P.
A mathematical anlaysis of results of experiments on rats livers by local laser hyperthermia.
Lasers in Med. Sci. 4:55:1989.

17. Mordon S.R., Cornil H., et al.
Nd::YAG laser thermal effect,
Lasers in Med. Sci. Vol.2, No.4, 1987.

18. Driver I., Feuther J.W., et al.
Coagulation of blood at the tip of optical fibres used for light delivery in P.D.T.
Lasers in Med. Sci. Vol.4, No.2, 1989.

19. Rubinstein E.
Condylomatous ulcerative lesions in the Vulva and introitus: Effects of Carbon dioxide laser vapourization.
Lasers in Med. Sci. 1:175:1986.

20. Dougherty T.J.
Hematoporplyrin as a photosensitizer of tumours.
Photochem. Photobiol. 38:377:1983.

21. Weishaupt K.R., Gomer C.J., et al.
Identification of singlet oxygen as the cytotoxic agent in photoactivation of a murine tumour.
Cancer Res. 36:2316:1976.

22. Hayata Y., Kato H., et al.
HPD and Laser photoradiation in the treatment of lung cancer.
Chest, 81:269:1981.

23. Hayata Y., Kato H., et al.
HPD and photoradiation therapy in early stage lung cancer.
Lasers in Surg. Med. 4:39:1984.

24. Spinelli P., dalFante M.
Endoscopic photodynamic therapy in lung cancer.
Lasers in Med. Sci. 5:181:1990.

25. Cohen A.M., Wood W.C., et al.
Cytotoxicity of human brain tumours by HPD,
J. Surg. Res; 41:81:1986.

26. Muller P.J., Wilson B.C.
Photodynamic theroapy of malignant brain tumours,
Lasers in Med. Sci. 5:245:1990.

27. Stamp J.M., Fowler G., et al.
The use of photodynamic therapy (PDT) for treatment of superficial tumours on the bladder wall.
Lasers Med. Sci. 5:5:1990.

28. Stamp J.M., Williams J.L.
Photodynamic therapy in the bladder: can the light dose be easily quantified?
Lasers Med. Sci. 6:147:1991.

29. Wilson B.C., Patterson M.S.
Dependence of laser-induced breakdown field strength on plasma duration.
Appl. Phys. Lett., 22:635:1973.

30. Boulnois J.L.
Photophysical procession in recent medical laser developments: a review.
Lasers Med. Sci., 47:1:1986.

31. Fradin D.W., Bloembergen N., et al.
Dependence of laser-induced breakdown field strength on plasma duration.
Appl. Phys. Lett., 22:635:1973.

32. Steinert R.F., Puliafito C.A., et al.
Plasma formation and shielding by three Nd:YAG lasers
AM.J. Ophthal. 96:427:1983.

33. Fleix M.P., et al.
Laser-induced liquid breakdown. A step-by-step account
Appl. Phys. Lett. 19:484:1971.

34. Gaby Sh., Kremer I., et al.
The retinal effects of copper vapour laser exposure.
Invest. Ophth/vis Sci. 29:528:1988.

35. Stern D., Schoenlein R.W., Puliafito C.
Corneal ablation by nanosecond, Picosecond, and Femto-second lasers at 532 and 625nm.
Arch. Ophth. 107:587:1989.

36. Srinivasan R., Mayne-Benton V.
Self-developing photoetching of PET films by far U.V. excimer laser radiation.
Apl. Phys. Lett. 41:576:1982.

37. Dyer P.E., Srinivasan R.
Nanoseconds photoacoustic studies on U.V. laser ablation of organic polymers.
Appl. Phys. Lett. 48:445:1986.

38. Srinivasan R., Dyer P.E.
Far-ultraviolet ablation of the cornea: photoacoustic studies.
Lasers in Surg. Med. 6:514:1987.

39. Taylor R.S., Singleton D., et al.
Effect of optical duration on the XeCl laser ablation of polymers and biological tissue.
Appl. Phys. Lett. 50:1779:1987.

40. Srinivasan R.
Etching Plymide films with continous wave U.V. Lasers
Appl. Phys. Lett. 58:2895:1991.

41. Pettit G.H., Saverberg R.
Fluence-dependent transmission of polymide at 248nm under laser ablation conditions.
Appl. Phys. Lett. 58:793:1991.

42. Müller G., Dorschel K., Kar H.
Biophysics of photoablation process
Lasers in Med. Sci. 66:241:1991.

43. Srinivasan R.
Science, 234:559:1986.

44. Sartori M.P., et al.
Proceedings of SPIE 908:34:1988.

45. Sutcliffe E., Srinivasan R.
J. Appl. Phys. 60:3315:1986.

46. Srinivasan R.
Ablation of polymers and tissue by ultraviolet lasers
SPIE 1064:77:1989.

47. Wolbarsht M.L.
Laser surgery:Co_2 or HF.
J. QE. 20:1427:1984.

48. Walsh J.T., Flotte T.J., Deutsch T.E.
Er:YAG laser ablation of tissue: effect of pulse duration and tissue type on thermal damage.
Lasers Surg. Med. 9:314:1989.

49. Charlton A., Dickenson M.R., et al.
Er:YAG and Ho:YAG laser ablation of bone.
Lasers in Med. Sci. 50:365:1990.

50. Kopchok G., White R., et al.
Ho:YAG laser ablation of vascular tissue.
Lasers in Surg. Med. 10:405:1990.

51. Charlton A., Dickenson M.R., et al.
The interaction of Ho:YAG laser radiation with soft tissue.
Lasers in Med. Sci. 1991.

52. Kuwabara T., Gorn R.A.
Retinal damage by visible light on electron microscopic study.
Arch. Ophthal. 79:69:1968.

53. Kuwabara T.
Retinal recovery from exposure to light.
Am. J. Ophthal. 70:187:1970.

54. Pomerantzeff O., et al.
Effect of the ocular media on the main wavelength of argon laser emission.
Invest. Ophthal. Vis. Sci. 15:70:1976.

55. Marshall J., Bird A.C.
A comparative histopathological study of argon and krypton laser irradiations of the human retina.
Br. J. Ophthal. 63:657:1979.

56. Karmon G., Savir H.
Retinal damage after argon laser iridotomy.
Am. J. Ophthal. 101:554:1986.

57. Schwartz A.L., Martin N.F., et al.
Corneal decomposition after argon laser iridotomy.
Arch. Ophthal. 106:1572, 1988.

58. Rosenblatt M., Luntz M.H.
Intraocular pressure rise after argon laser trabeculoplasty.
Br. J. Ophthal. 71:772:1987.

59. Finley J., Barsky S.H., et al.
Healing of portwine stains after argon laser therapy.
Arch. Dermatol. 117:486:1981.

60. Carruth J., Shakespeare P.
Toward the ideal treatment of the portwine stain with the argon laser: better prediction and an 'optimal' technique.
Lasers Surg. Med. 6:2:1986.

61. Chavoin J.P., Bonafe J.L., et al.
Large portwine stains: Continuous argon laser treatment with neuroleptanalgesia.
Lasers Med. Sci. 3:99:1988.

62. Van Germert M.J., Carrath J.A., Shakespeare P.G.
Leading article: Has the argon laser ever been used optimally for the treatment of portwine stain birthmarks?
Lasers Med. Sci. 6:371:1991.

63. Pickering J.W., Butler P.H., et al.
Copper-vapour laser treatment of portwine stains: a patient questionnaire.
Lasers Med. Sci. 5:43:1990.

64. Ashley S., Brooks S.G., et al.
Acute effects of a copper-vapour laser on atherma.
Lasers Med. Sci. 6:23:1991.

65. Prince M.R., Deutsch T.F., et al.
Preferential light absorption in athermas invitro. Implications for laser angioplasty.
J. Clin. Invest. 78:295:1986.

66. Aleinkov V.S., et al.
CO laser application in surgery.
Optics and laser tech. P.265, 1984.

67. Clement R.M., et al.
A comparison of CO and CO_2 lasers for medical applications.
IEE colloquium on: optical techniques and biomedical applications. P.6, 1991.

68. Fischburg J., Lim J.J.
Curr. Top. Eye Res. 4:201:1984.

69. Goldman J.N., Benedeck.
invest. Ophthal. 6:574:1967.

70. Benedek G.B.
Theory of transparency of the eye.
Appl. Opt., 10:459:1971.

71. Blecker J.C., Vanbest J.A., et al.
Invest. Ophth. Vis. Sci.
27:791:1986.

72. Mannier V., Cerami M.
Science, 211:491:1981.

73. Ramsey A. Ahmed, Yoo K.M., Alfano R.R.
Time resolved back scattering to monitor different stages of eye cataract.
Appl. Opt. 29:896:1990.

74. Nai-Tang Yu, Sven-Erik Bursell.
A new approach to study human cataractogensis: fluorescence/Raman intensity ratio and imaging. P.65. in "Spectroscopic and structural studies of biomaterials I:Proteins": Jacek Twardowski - Sigma.

75. Scheich T., Willis J.A., Matson G.
Exp. Eye. Res., 39:455:1984.

76. Yu N.T., Kuck J.F., Askren C.C.
Invest. Ophthal. Vis. Sci. 18:1278:1979.

77. Yu N.T., East E.J.
J. Biol. Chem. 250:2196:1975.

78. Ozaki Y., Mizuno, et al.
Structure and function of the lens proteins studied by Roman spectroscopy. P.55. in the same ref. as 76.

79. Kapany N.S., Peppers N.A., et al.
Retinal photocoagulation by lasers.
Nature - 199:146:1963.

80. Flocks M., Zweng H.
Laser photocoagulation of ocular tissues.
Arch. Ophth., 72:604:1964.

81. Srinivasan R., Mayne-Banton V.
Self-developing photoetching of PET films by far UV excimer laser radiation.
Appl. Phys. Letts. - 41:576:1982.

82. Deutsch T.F., Ceis M.W.
Self-developing UV photoresist using excimer laser exposure.
J. Appl. Phys. 54:7201:1983.

83. Rice S., Jain K.
Direct high-resolution excimer laser photoetching.
Appl. Phys. A33:195:1984.

84. Srinivasan R., Leigh W.J.
Ablative photodecomposition: action of far-ultraviolet (193nm) laser radiation on PET films.
J. Am. Chem. Soc., 104:6784:1982.

85. Srinivasan R.
Kinetics of the ablative photodecomposition of organic polymers in the far ultraviolet (193nm).
J. Vac. Sci. Tech. B., I:923:1983.

86. Trokel S.L., Srinivasan R., Braren B.
Excimer laser surgery of the cornea.
Am. J. Ophthal. 96:710:1983.

87. Marshall J., Trokel S., Rothery S., Schubert H.
An ultrastructural study of corneal incisions induced by an excimer laser at 193nm.
Ophthal. 92:749:1985.

88. Srinivasan R., Dyer P.E., Braren B.
Far-ultraviolet laser ablation of the cornea: photo-acoustic studies.
Laser in Surg. Med. 6:514:1987.

89. Puliafito C.A., Steinat T.F., et al.
Excimer laser ablation of the cornea and lens.
Ophthal, 92:741:1985.

90. Dyer P.E., Al-Dhahir R.K.
Transient photoacoustic studies of laser tissue ablation.
SPIE 1202:46:1990.

91. Puliafito C.A., Kai Wong, Steinert R.
Quantitative and ultrastructural studies of excimer laser ablation of the cornea at 193 and 248 nanometers.
Lasers in Surg. Med. 7:155:1987.

92. Taylor R.S., Singleton D.L., Paraskevopolons G.
Effect of optical pulse duration on the XeCl ablation of polymers and biological tissue.
Appl. Phys. Lett. 50:1779:1987.

93. Srinivansan R.
Ablation of polymers and tissue by ultraviolet lasers.
SPIE 1064:77:1989.

94. Marshall J., Trokel S., Rothery S., Krueger R.
A comparative study of corneal incisions induced by diamond and steel knives and two ultraviolet radiations from an excimer laser.
Br. J. Ophthal. 70:482:1986.

95. Thomson K.P., Trentacoste J., et al.
Corneal photoablation by far ultraviolet lasers.
Arch. Ophthal. 105:312:1987.

96. Andrew J.E., Dyer P.E., Forster D., Key P.
Direct etching of polymeric material with XeCl laser.
Appl. Phys. Lett., 43:717:1983.

97. Murphy-chutorian D., Aselzer P.M., Kosek J., et al.
The interaction between excimer laser energy and vascular tissue.
Am. Heart. J. 112:739:1986.

98. Singleton D., Paraskevopulous G., Taylor R., et al.
Excimer laser angioplasty: Tissue ablation, arterial response and fibreoptic delivery.
IEEE J. QE. 23:10:1987.

99. Keates R.H., Pediotti C.S., et al.
Co_2 laser beam control for corneal surgery.
Ophthalmic Surg. 12:117:1981.

100. Puliafito C.A., Stern D., et al.
High-speed photography of excimer laser ablation of the cornea.
Arch. Ophthalmol. 105:1255:1987.

101. Dehm E.J., Puliafito C.A., et al.
Corneal endothelial injury in rabbits following excimer laser ablation at 193nm and 248nm.
Arch. Ophthalmol. 104:1364:1986.

102. Schroder E., Dardenne M., et al.
An ophthalmic excimer laser for corneal surgery.
Am. J. Ophthal. 472:3(II):1987.

103. Marshall J., Trokel S.R., et al.
Photoablative reprofiling of the cornea using an excimer laser: photorefractive keratectomy.
Lasers in Ophthal. 1:21:1987.

104. Steinart R.F., Puliafito C.A.
Laser corneal surgery.
int. Ophthal. Clinics. 28:2:1988.

105. Tuft S., Marshall J., Rothery S.
Stromal remodelling following PRK.
Lasers Ophthalmol. 1:177:1987.

106. Seiler T., Wollensak J.
Myopic photorefractive keratectomy with the excimer laser: one year follow up.
Ophthalmol. 98:1156:1991.

107. Gibson I.K., Spurr-Michaud S.J., Tisdale A.S.
Anchoring fibrils from a complex network in human and rabbit cornea.
J. Invest. Ophthal. Vis Sci. 28:212:1987.

108. Goodman G.L., Trokel S., et al.
Corneal healing following laser refractive keractomy.
Arch. Ophthal. 107:1799:1989.

109. Sher N.A., Bowers R., Zabel R., et al.
Clinic use of the 193nm excimer laser in the treatment of corneal scars.
Arch. Ophthal. 109:491:1991.

110. Hanna K.D., Chastang J.C., et al.
Excimer laser keratectomy for myopia with a rotating-slit delivery system.
Arch. Ophthal. 106:245:1988.

111. Puliafito C.A., Steinert R.F., et al.
Excimer laser ablatiion of the cornea and lens: experimental studies.
Ophthalmol. 92:741:1985.

112. Naneviez T., Prince M., et al.
Excimer laser ablation of the lens.
Arch. Ophthalmol. 104:1825:1986.

113. Bath P., Mueller G., et al.
Excimer laser lens ablation.
Arch. Ophthalmol. 105:1164:1987.

114. Bath P., Muller G., et al.
Excimer laser application for cataract surgery.
SPIE 908:72:1988.

115. Muller-Stolzenberg N.
Application of 308nm excimer laser radiation for ocular surgery: safety consideration.
Proceedings of safety and laser-tissue interaction (European laser Assoc). P.1290, 1988.

116. Muller-Stolzenberg N., Muller G., et al.
Second int. workshop on laser corneal surgery. (Oct.1988).
light in Ophthalmol. 1989.

117. Dong-Yun Li., Borkman R.
Photodamage to calf lenses in vitro by excimer laser radiation at 308, 337, and 350nm.
Invest. Ophthal. Vis Sci. 31:2180:1990.

118. Borkman R., Tassin J., Lerman S.
The rate of photodestruction of tryptophan residues in human and bovine ocular lens proteins.
Exp. Eye Res. 32:747:1981.

119. Borkman R., Hibbard L., Kirk N.
Lens damage from 337.1nm laser radiation.
Lens Research 2:109:1985.

120. Fracasso A., Campnile F., et al.
Coronary laser angioplasty
lasers Med. Sci. 6:335:1991.

121. Baumbach A., Hasse K., et al.
Improved results of coronary excimer laser angioplasty by the use of advanced transmission devices.
Lasers Med. Sci., 6:317:1991.

122. Taylor R.S., Gladysz D., Brown D.
Laser induced fluorescence imagining of coronary arteries for open heart surgery applications.
SPIE. 1420:183:1991.

123. Baraga J., Rava R.P., et al.
Laser induced fluorescence spectroscopy of normal and atherosclerotic human aorta using 306-310nm excitation.
Lasers in Surg. Med., 10:245:1990.

124. Mitchell N.F., Novak R., Lunney G.
Ablation of gallstones using excimer laser pulses.
J. Appl. Phys. 65:286:1989.

125. Shi W., Papaioannou T., et al.
Fragmentation of biliary stones with a 308nm excimer laser.

126. Pini R., Salimbeni R., Vannini M., et al.
Laser Dentistry: A new application of excimer laser in root canal therapy.
Lasers in Surg. Med. 9:352:1989.

127. Neev J., Lih-Huie L., Raney D.V., et al.
Selectivity, efficiency, and surface characteristics of hard dental tissues ablated with ArF pulsed excimer lasers.
Lasers Surg. Med. 11:499:1991.

128. Dressel M., Jahn R., Neu W., et al.
Studies in fibre guided excimer laser surgery for cutting and drilling bone and meniscus.
Laser Surg. Med. 11:560:1991.

129. Lane R.J., Linsker R., et al.
Ultraviolet laser ablation of skin.
Arch. Dermatal. 121:109:1985.

130. Rabinowitch E.
Electron transfer spectra and their photochemical effect.
Rev. Mod. Phys. 14:112:1942.

131. Loree T., Johnson T., Birmingham B.
Fluorescence spectra of corneal tissue under excimer laser irradiation.
SPIE 908:65:1988.

132. Nuss R.C., Puliafito C., Dehn E.
Invest. Ophthalmol Vis Sci. 28:287:1987.

133. Trentacoste J., Thompson K., et al.
Ophthalmol. 94:125:1987.

134. Winckler K., Golz B., et al.
Photochem. Photobiol. 47:225:1988.

135. Rimoldi D., Alexandra C., et al.
DNA damage in cultured human skin fibroblasts exposed to excimer laser radiation.
J. Invest. Dermatol. 96:898:1991.

136. Kochevar I.E.
Cytotoxicity and mutagenicity of excimer laser radiation.
Lasers Surg. Med. 9:440:1989.

137. Forster W., Scheid W., et al.
A model for testing the mutagenicity of excimer laser radiation in ophthalmology.
Acta Ophthalmol. 69:533:1991.

138. Gailities R., Ren Q., Thompson K., et al.
Solid-state UV laser (213nm) ablation of the cornea and synthetic collagen lenticules.
Lasers Surg. Med. 11:556:1991.

139. Cole C.A., Forbes D.F., Davis P.D.
An action spectrum for UV photocarcinogensis.
Photochem. Photobiol. 43:275:1986.

140. Keates R., Bloom R.T., Schneider R., et al.
Absorption of 308nm excimer laser radiation by balanced salt solution, sodium hyalaronate and human cadvar eyes.
Arch. Ophthal. 108:1611:1990.

141. Keates R., Genstler D.E., Tarabuchi S.
Ultraviolet light-transmission of the lens capsule.
Ophthalmic Surg. 13:374:1982.

142. Krasnov M.

Am. J. Ophthalmol. 75:674:1973.

143. Lerman S.

Observations on the use of high-power lasers in ophthalmology.

J.QE. 1465:20:1984.

144. Puliafito C.A., Steinert R.

Short-pulsed Nd:YAG laser micro-surgery of the eye: Biological considerations.

J.QE. 1442:20:1984.

145. Niemz M.H., Klancnik E.G., et al.

Plasma-mediated ablation of corneal tissue at 1053nm using a Nd:YLF oscillator/regenerative amplifier laser.

Lasers Surg. Med. 11:426:1991.

146. Hochheimer B.F.

Second harmonic light generation in the rabbit cornea.

Appl. Optics. 21:1516:1982.

147. Zaidi Q., Pokorny J.

Appearance of pulsed IR light: second harmonic generation in the eye.

Appl. Optics. 27:1664:1988.

148. Mainster M.A.

Wavelength selection in macular photocoagulation: tissue optics, thermal effects and laser systems.

Ophthalmol. 93:952:1986.

149. Balles M., Puliafito C.A., et al.
Semiconductor diode laser photocoagulation in retinal vascular disease.
Ophthalmol. 97:1553:1990.

150. Jacobson J., Schuman J., et al.
Diode laser peripheral iridectomy.
Int. Ophthal. Clinics. 30:120:1990.

151. Watts G.K.
Retinal hazards during laser irradiation of the iris.
Br. J. Ophthalmol. 67:55:1971.

152. Peyman G.A., Naguib K.H., Gaasterland D.
Transscleral application of a semiconductor diode laser.
Lasers Surg. Med. 10:569:1990.

153. McHugh J.D., Marshall J., et al.
Diode laser trabeculoplasty for chronic simple glaucoma.
Invest. Ophthal. Vis. Sci. 4:1676:1990.

154. Brancato R., Carassa R., Trabucchi G.
Diode laser compared with argon laser for trabeculoplasty.
Am. J. Ophthal. 11:50:1991.

155. Walsh J.T., Flott T.J., Anderson R., et al.
Co_2 laser tissue ablation: effect of tissue type and pulse duration on thermal damage.
Lasers Surg. Med. 8:108:1988.

156. Hale G.M., Query M.R.
Optical constants of water in the 200nm to 200μm wavelength region.
Appl. Optics. 12:555:1973.

157. Robertson C.W., Williams D.
Lambert absorption coefficients of water in the IR.
J. Opt. Soc. Am. 61:1316:1971.

158. Margolis T.I., Farnarth D.A., Puliafito C.
Er:YAG laser surgery on experimental vitreous membranes.
Arch. Ophthalmol. 107:424:1989.

159. Borivakehanyavat S., Puliafito C.A., Kliman G., et al.
Ho:YAG laser surgery on experimental vitreous membranes.
Arch. Ophthalmol. 109:1605:1991.

160. Domankevitz Y., Nishioka N.
Measurement of laser ablation threshold with a high-speed framing camera.
J.QE. 26:2276:1990.

161. Lin C.P., Stern D., Puliafito C.A.
High-speed photography of Er:YAG laser ablation in fluid.
Invest. Ophthal. Vis. Sci. 31:2546:1990.

162. Carts Y.
Holmium laser treats glaucoma patients.
Laser Focus, p.42.

163. Seiler T., Marshall J., et al.
The potential of an infrared HF laser (3μm) for corneal surgery.
Lasers in Ophthalmol. 1:49:1986.

164. Loertscher H., Mandelbaum S., et al.
Preliminary report on corneal incision created by a HF laser.
Am. J. Ophthalmol. 102:217:1986.

165. Dyer P.E., Khosroshahi M.E., Tuft S.
Optical fibre delivery and tissue ablation studies using a pulsed HF laser.
Lasers Med. Sci. 7:331:1992.

Part II: Excimer lasers experiments

There are a growing number of situations where high peak power laser light must be delivered through an optical fibre, eg. in industrial and medical applications. For medical applications based on the photo-ablation of tissue, the fibres must be capable of transmitting high peak power without substantial change to the fibre transmission and without damage. Three main advantages of fibre delivery of laser light are: (i) - it gives greater maneouvering freedom to the surgeon than mirrored reflector systems, (ii) - it allows power to be delivered endoscopically through natural body canals without more invasive surgery, and (iii) - it may allow the laser to be located outside the operating room.

There are, however, limitations to power transmission arising from the onset of optical nonlinearities and physical damage to the fibre core. Damage can arise from a number of factors such as laser power density, fibre surface quality and impurities and is dependent on wavelength and pulse duration. Also, the effect of fibre optic tips should be taken into account when studying problems concerning heat damage to the fibre and tissue,(1,2).

This section (II) is mainly concerned with studying optical fibre transmission properties in the ultraviolet region using different excimer laser wavelengths. Chapter 3 reports optical fibre preparation, laser-fibre coupling and the transmission capabilities of different types of fused silica fibres using XeCl, KrF, and ArF lasers under various conditions. This is followed by a study of the interaction of fibre-delivered UV light with some organic materials such as

polymers and lens tissue in Chapter 4.

Chapter 3

Fused silica fibre studies

3.1 - Basics of optical fibres

An optical fibre consists of a central part called the 'core' surrounded by a material called the 'cladding' as shown in Fig. 3.1

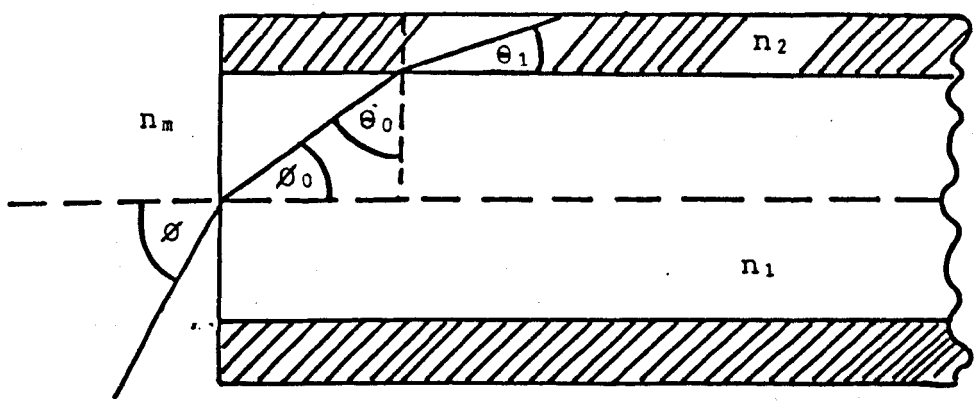

Fig. 3.1 - Light transmission in an optical fibre

There are two possibilities for light behaviour:

i. If $n_1 < n_2$, then the refraction angle follows Snell's law,

$$n_1 \sin \theta_0 = n_2 \sin \theta_1 \qquad 3.1$$

where n_1 and n_2 are the core and cladding refractive indices respectively, and a ray is transmitted at the boundary.

ii. If $n_1 > n_2$, and $\theta_0 > \theta c$, the critical angle, electromagnetic waves can be confined to in the core region by total internal reflections taking place at the boundary between the core and cladding. The critical angle is given by $\theta c = \mathrm{Sin}^{-1}\, n_2/n_1$.

The fundamental parameters describing the characteristics of optical fibres are the relative refractive index difference Δ, the numerical aperture N.A, and the maximum external acceptance angle, ϕ_{max} defined as:

$$\Delta = \frac{n_1 - n_2}{n_1} \qquad 3.2$$

$$N.A = (n_1^2 - n_2^2)^{1/2} \qquad 3.3$$

$$\phi_{max} = \mathrm{Sin}^{-1} \frac{N.A}{n_m} \qquad 3.4$$

n_1 and n_2 govern the value of N.A. which is determined by the difference in refractive index between the core and the cladding. It is a measure of the light acceptance capability of the optical fibre and as the N.A increases so does the ability of the fibre to couple light into the fibre over a wider range of input angles.

Coupling efficiency also increases as the fibre diameter increases, since the larger fibre can collect more light. Thus, the maximum light collection efficiency occurs for large diameter and large N.A fibres. On the other hand fibres with large N.A have high losses. Throughout these experiments multimode step-index fibres have been used having a constant core refractive index surrounded by constant cladding refractive index. The optical fibres and lasers used are listed in table 3.1 and more details given in the following sections.

Table 3.1 - Optical fibres used in these experiments.

Type	Core diameter (μm)	N.A	λ (nm)	Supplier
PCS	600	0.4	308,248	Quartz and Slice
PCS	1000	0.4	308,248	TSL group plc
HCN	600	0.37	248	Optronics plc
HCG	550	0.22	248	
sup. PCS	1000	0.4	308	Tech. optics LTD.
sup. G	600	0.22	248,193	

3.2 - Fibre preparation

3.2.1 - Polishing.

Before an optical fibre is used it must be cut and polished very carefully. An attempt was made at the beginning to cut a PCS 600μm core diameter fused silica fibre with pulsed TEA CO_2 laser. The laser had 100mJ output energy focused through a 100mm focal length NaCl lens. Although, this energy was selected arbitrarily, it resulted in clear and sharp core cutting but left molten buffer and cladding (see Fig. 3.2).

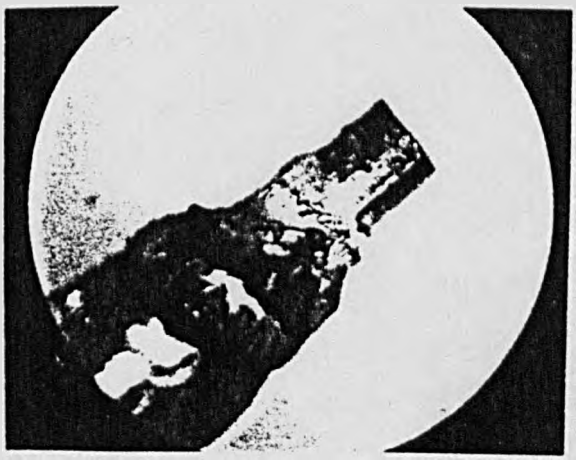

Fig. 3.2 - PCS 600μm fibre cutting with CO_2 laser

The above procedure was repeated with an excimer laser. The 60mJ output energy of an ArF laser (193nm) was focused through a 150mm focal length quartz cylindrical lens giving a sharp line image on the fibre, but the interaction produced no visible cutting of the buffer or silicone cladding.

The second attempt was to cut the fibre with a sapphire blade provided by Fibre - DATA Ltd. This was done by placing the fibre inside a disc with different size of holes to suit different fibre diameters and then scoring slowly until a flat end was achieved. However, since the blade was designed

for use with core diameters $\leq$250μm, only an irregular surface was obtained, although no fracturing occured along the fibre during the preparation. The final approach was to use a scalpel, and although, unlike the sapphire blade, it produced side fracturing, it proved more suitable for cutting 600μm and 1000μm core diameter fibres.

On the basis of these findings a combination of sapphire blade and scalpel was used to score and cut the fibre. The fibre surface had then to be made flat using a set of different grades (600, 800 and 1200) of emery papers. The last step was to use an aerosol cutting polish compound (RS-556-34) in order to achieve a smooth surface. At later stages of the polishing procedure, an air-jet blower was used to get rid of the particulates left on the surface during the polishing. Alternatively, a cleaning solvent (FDCF 1000, Fibre - DATA) was also used for the same purpose. Figure 3.3 shows an example of fibre before (a) and after (b) polishing process.

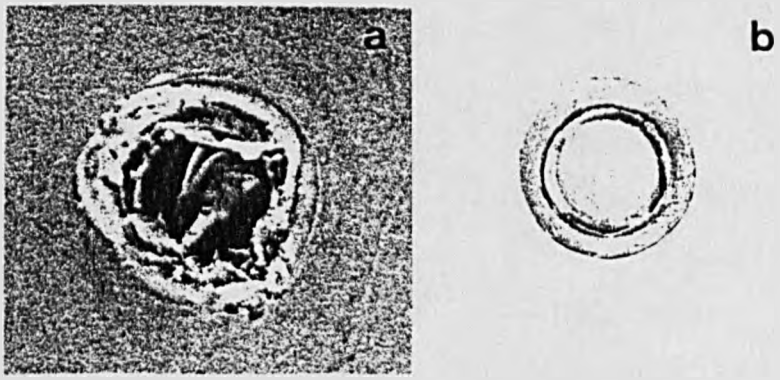

Fig. 3.3 - optical fibre before (a) and after (b) polishing.

3.2.2 - Laser-fibre coupling

Once the fibre is polished, the laser light must be coupled to it as efficiently as possible. Four important steps were employed for all the experiments throughout this work which are equally applicable to all types of lasers and fibres. However, here only one example is given for clarity ie, PCS 600μm core diameter and the KrF (248nm) laser.

Step 1 - Illumination of fibre.

A circular aperture was used to select of region of uniform fluence from the output beam and a suitable lens was then used to image this aperture on to the fibre core. A thin wire placed across the aperture was used to assist image focussing. The required demagnification was calculated knowing the lens focal length. The numerical aperture was also checked against the acceptance angle of fibre so that the light enters within its limit.

Step 2 - Measurement of the lens-aperture loss.

The transmission loss of the lens and aperture were measured separately and combined to give a net transmission which for all the excimer lasers used in these experiments was between 80 and 90%. The lowest transmission corresponded to the ArF laser at 193nm where the lens started to exhibit increased absorption.

Step 3 - Measurement of required spot size.

In these experiments the input beam to the fibre was chosen to cover 85% of the core diameter to avoid the core-cladding interface damage. The spot size was measured as follows: A thin mylar film was placed at the focal plane of the lens and

irradiated by the laser. The smallest spot was obtained at this position but by gradually moving the film backward using a micropositioner, the spot could be recorded in different planes as shown in Fig. 3.4. The spot sizes were then measured using a stereo microscope and once the required spot was selected, the fibre was moved to that particular position.

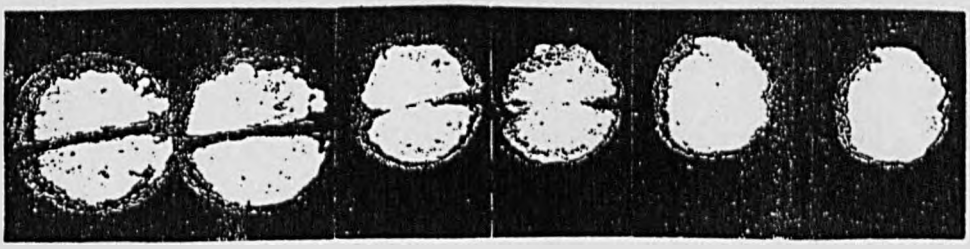

Fig. 3.4 - Image of aperture recorded using unexposed, developed polaroid. The line is produced by a wire on the aperture that was used to assist focussing. The lens-target distance and spot size increases from R —L.

Step 4 - Optimization of the fibre position

Once the fibre was positioned to achieve the required spot size a thin transparent film was placed in front of the fibre so that the fibre input and irradiated area could be observed simultaneously using a stereo microscope. When the fibre had been positioned behind the irradiated area the film was removed and the laser beam was attenuated to avoid fibre damage during its final adjustment. At this stage the transmitted beam was monitored using a pyroelectric joulemeter whilst adjusting the micropositioner in the X-Y directions. When the maximum signal was obtained, the fibre was kept in that position for the subsequent experiments. Finally, the actual experiment began when the film was removed and the fluence set to a required value using the attenuators.

3.3 - UV lasers and fibre experiments

The object of these experiments was to investigate some of the physical characteristics of different types of fused silica fibres for various excimer laser wavelengths. These characteristics were mainly the transmission capability, flexibility, and damage thresholds which are important parameters in clinical applications of lasers. The type of optical fibres used in these experiments are given in table 3.1. Since these fibres were not all available at the same time, only a limited amount of work could be carried out with each type of fibre and laser. These results are discussed in detail in section 3.4.

3.3.1 - Method and results - XeCl laser

Fig. 3.5 illustrates the experimental set up for measurement of the 308nm laser pulse duration. The output beam was diverted by a quartz beam splitter to a vacuum photodiode (FD 125). The signal was displayed on a Tektronix 7834 oscilloscope with its given output recorded using a digitizing camera. The pulse duration was measured approximately as 5ns (FWHM) as shown in Fig. 3.6.

Fibre experiments

For experiments with the 308nm laser, two types of fibres were used: PCS 1000μm core (w) and Superguide PCS with a 1000μm core. The PCS 1000μm (w) has a silica core with 3000 ppm OH^- content, a silicone resin cladding and Ethylene-Tri-Fluoroethylene (ETFE) jacket. The Superguide PCS has a pure fused silica core , plastic cladding; and Tefzel jacket. The first set of these experiments were to study the

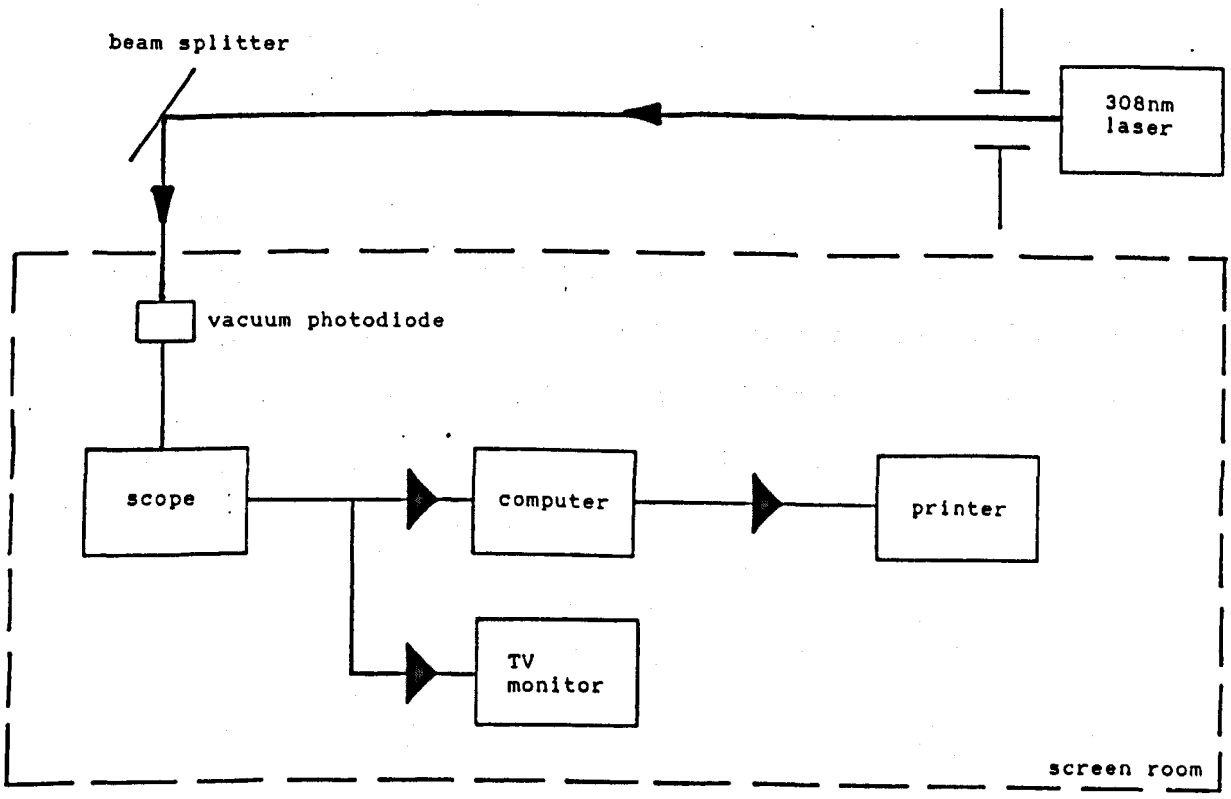

Fig. 3.5 - Experimental set up for measurement of 308nm laser pulse duration.

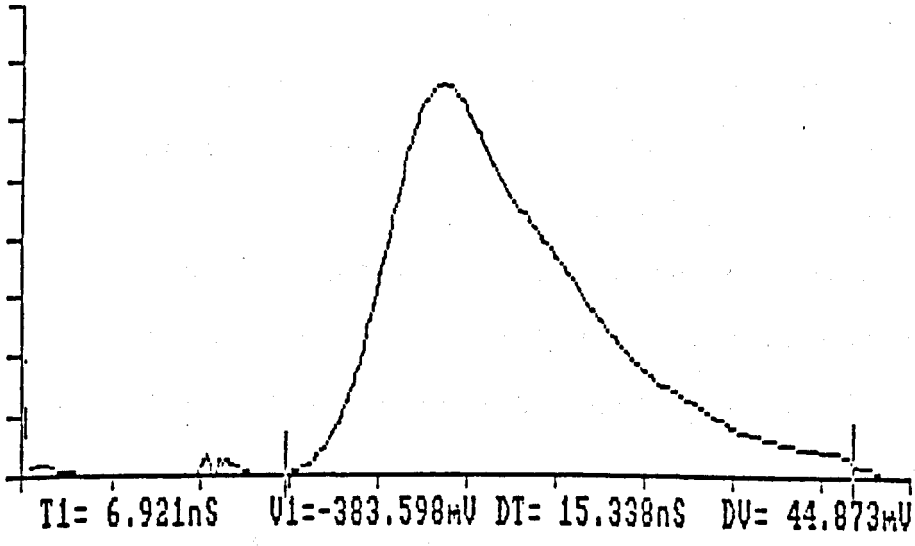

Fig. 3.6 - Pulse shape of XeCl laser, τ = 5ns.

fibre transmission for various fibre lengths in order to derive the attenuation coefficient for the 308nm laser.

Transmission properties

The fibre jacket from the input end was first stripped for approximately 5mm so that the core surface could remain free of possible contamination from debris produced during the experiment. An example is shown in Fig. 3.7.

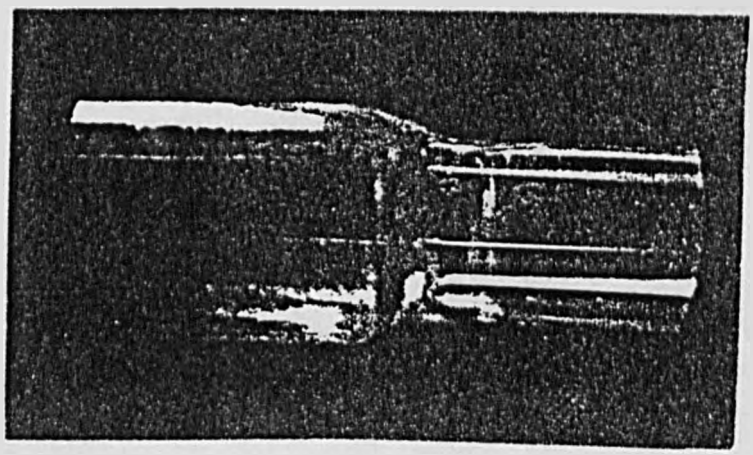

Fig. 3.7 - An example of stripped fibre

This was then followed by the '4-steps' procedure described in section 3.2.2 for laser-fibre coupling. The output beam passed through a circular aperture (6mm) to select a region of uniform fluence and a quartz lens of 30mm focal length was used for imaging. The experiment began with the longest fibre and the laser operating at 1Hz. Transmission was measured as the ratio of output energy to input energy within $\pm$ 5% accuracy.

In order to avoid possible cumulative effects on the surface and bulk of the fibre, energy transmission was measured using one pulse only. Once a measurement was recorded, the fibre was cut to a smaller length, polished and the above procedure was repeated. It can be seen from Figs.

3.8 and 3.9 that the fibre transmission decreases as the length of fibre increases and the comparison between PCS 1000μm and Superguide PCS 1000μm shows that both fibres essentially have the same transmission at very short distance ie, about 80% at 15cm. However, as the length increases, the latter shows higher transmission. This may be due to having less impurities in its core and better quality of cladding material.

The distributed loss coefficient, K (cm^{-1}) for a fibre can be calculated from the ratio of output energy E_o to input E_{in} using:

$$E_T = \frac{E_o}{E_{in}} = T_i \, T_L \, T_o \qquad 3.5$$

where $T_L = e^{-KL}$ 3.6

describes the distributed loss, L being the fibre length, and T_i and T_o the input and output transmission.

Rearranging eqn. 3.5 gives:

$$\text{In } E_T = \text{In } (T_i \times T_o) - KL \qquad 3.7$$

so that values of $T_i \times T_o$ and K can be found from the intercept and slope of a plot of In E_T versus L.

From Figs. (3.8b) and (3.9b), $T_i \times T_o \simeq 0.82$ and assuming that for relatively low fluence $T_i \simeq T_o$, the input and output coupling efficiency becomes $T_i \simeq T_o = 91\%$. This corresponds to a loss of 9%, part of which is due to Fresnel reflection at fibre face given by:

$$R = \left[\frac{n-1}{n+1}\right]^2 \qquad 3.8$$

where n is the core refractive index. For pure fused silica, $n \simeq 1.458$ giving $R \simeq 3.5\%$. From the slopes in Figs. 3.8b and

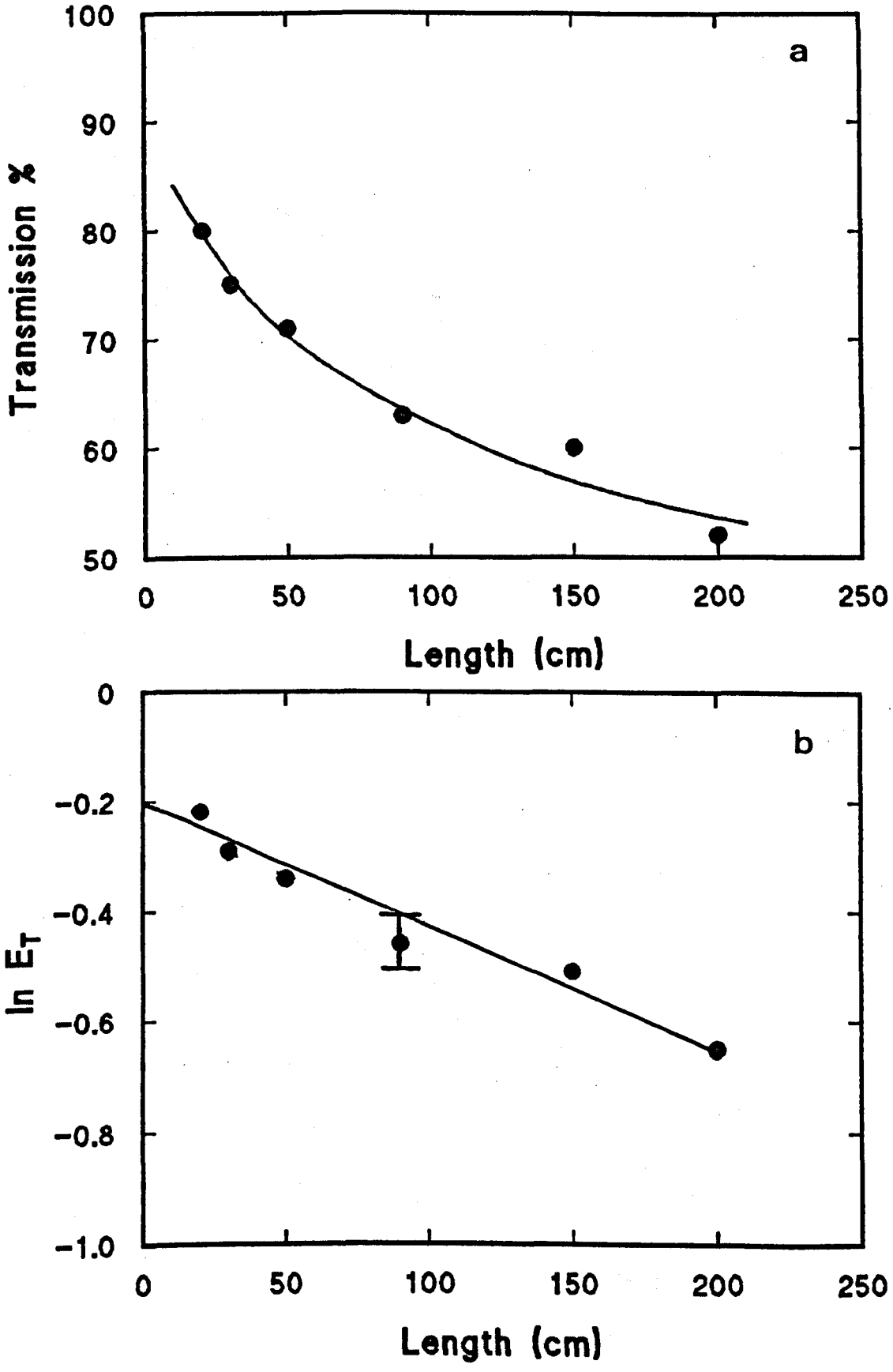

Fig. 3.8 - Variation of energy transmission (a) and its logarithm (b) with the length of PCS 1000μm fibre, F~440mJcm^{-2} using 308nm.

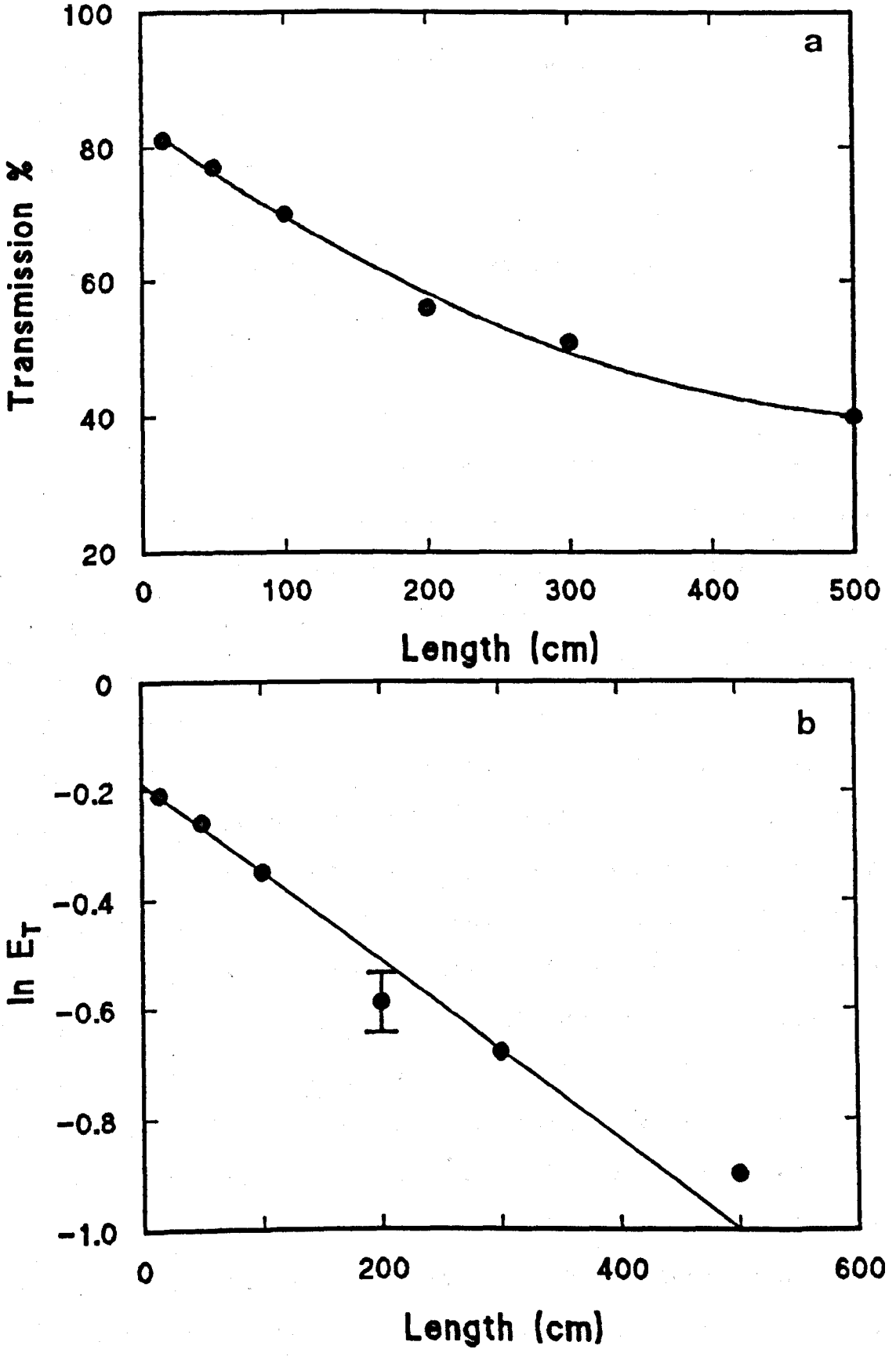

Fig. 3.9 - Variation of energy transmission (a) and its logaorithm (b) with the length of superguide PCS 1000μm fibre, F~500mJcm^{-2} using 308nm.

3.9b values of $K = 2 \times 10^{-3}$ cm^{-1} (0.86dB m^{-1}) for PCS 1000μm and $K = 1.60 \times 10^{-3}$ cm^{-1} (0.69dB m^{-1}) for Superguide PCS 1000μm are obtained. For comparison, data sheets provide values of (0.3-0.4)dB m^{-1} and 0.3dB m^{-1} respectively for low power transmission at 308nm. This descrepancy might be due to additional losses that are incurred under high power, pulsed laser conditions.

In a clinical environment the transmission capability of laser light in a liquid environment such as saline is important. To study this a perspex container (50 x 40) mm incorporating a fibre was made (Fig. 3.10a) and filled with saline (9g salt: 1 lit. distilled water). One meter of PCS 600um fibre was used, with the laser operating at 1Hz and an input fluence of about 500mJ cm^{-2}. The position of joulemeter was kept constant above the container while the fibre was gradually pulled downward hence increasing the separation, L. Fig. 3.10b shows that the energy transmission decreased by more than 50% at d=4cm which corresponds to a loss of ~ 220 $mJcm^{-2}$ compared with when the fibre tip is just below the saline level. This reduction is mainly due to absorption of radiation by saline and by using the data in Fig. 3.10 a value for absorption coefficient of saline of 0.27cm^{-1} was deduced which is somewhat larger than the value reported in 3.

Another important factor is the bending loss of the fibre. To test this a two meters length of Superguide PCS 1000μm was used to produce different diameters of bending. The geometry is shown in Fig. 3.11 where the fibre is held in position by a disc in such a way as to produce a single loop (360^{o}) bend. The laser was operated at 1Hz with input fluence

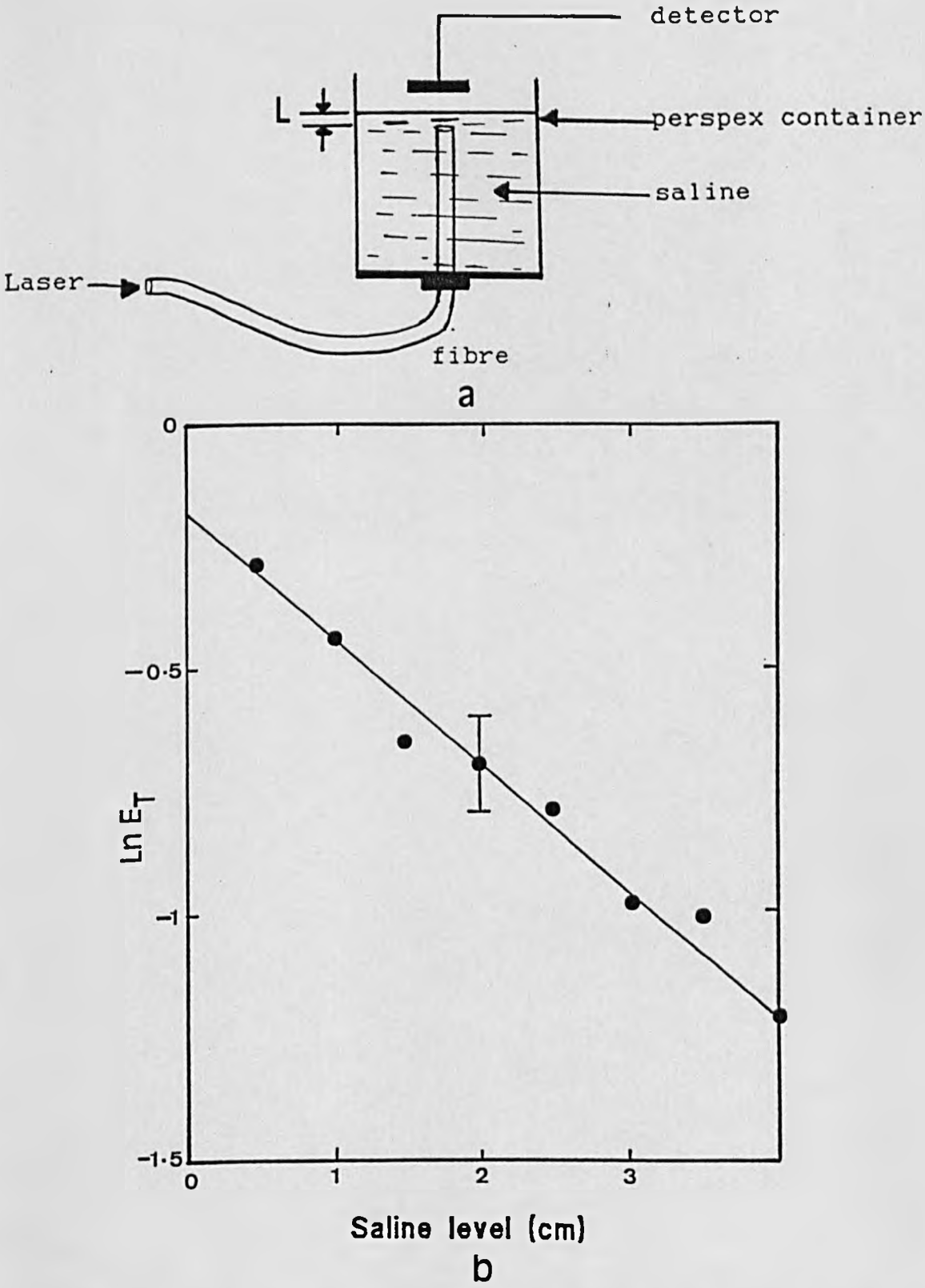

Fig. 3.10 - The experimental set up for energy transmission measurement in saline (a) and its variation with distance, L, in saline (b), using PCS 600μm at 308nm.

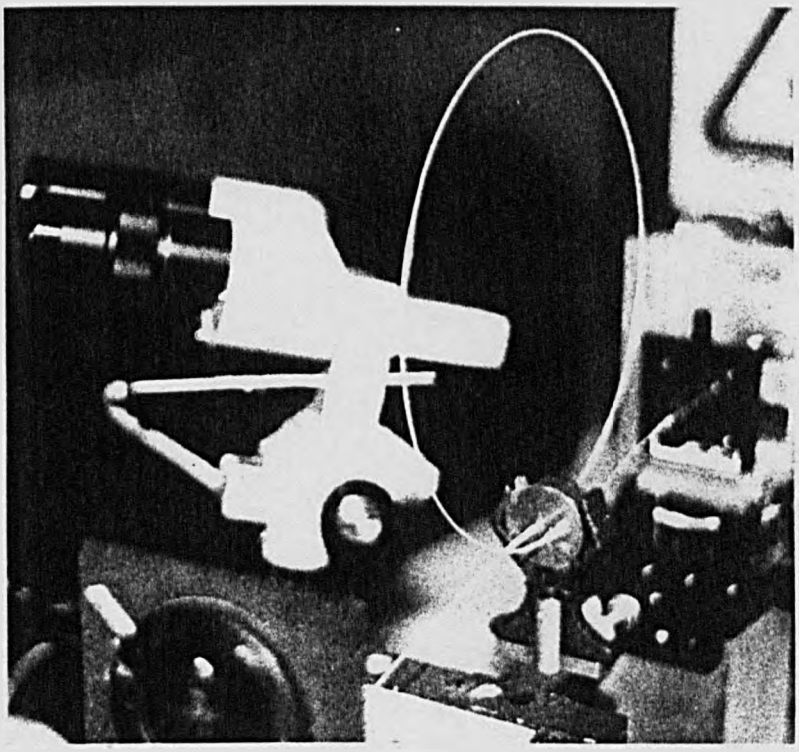

(a)

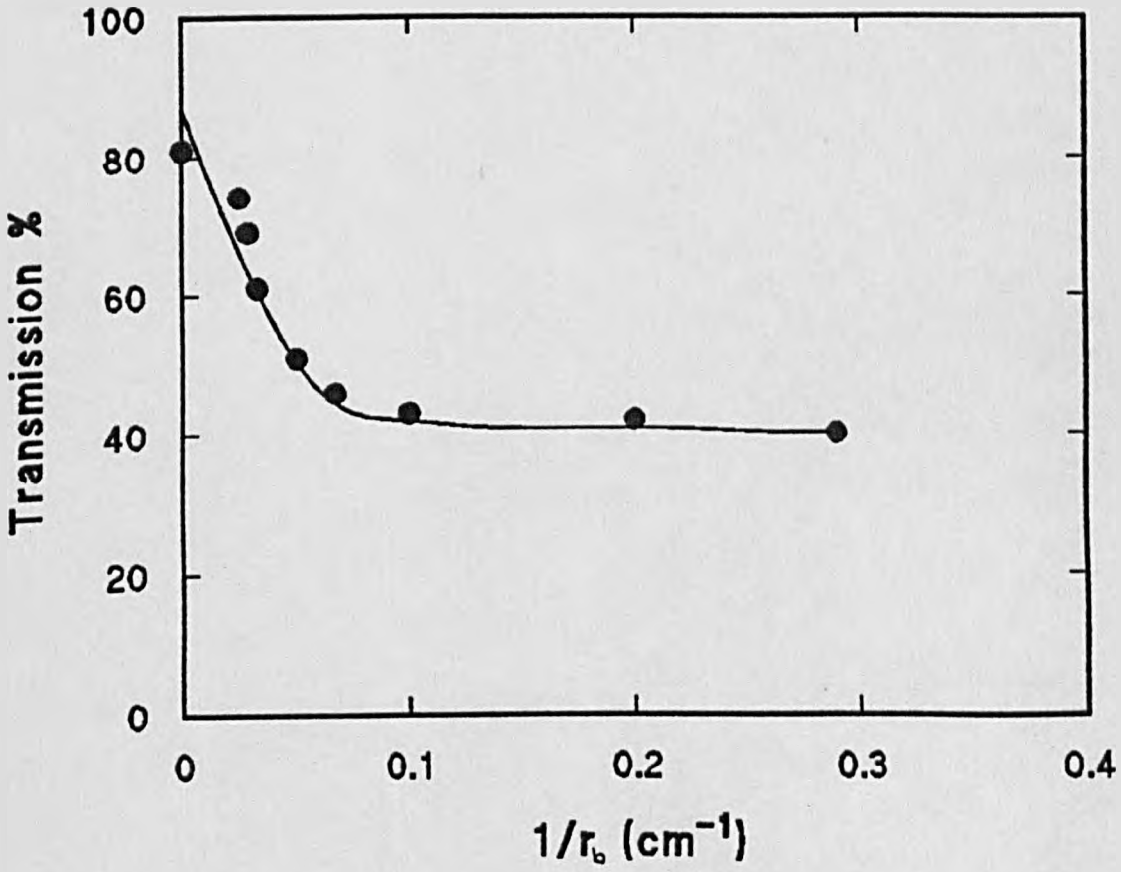

(b)

Fig. 3.11 - An example of PCS 1000μm fibre bending (a), and variation of transmission with the inverse bend radius $^{1}/r_{b}$ (b) at F~500mJcm^{-2} at 308nm.

of about 500mJcm^{-2}.

As can be seen in Fig. 3.11b a transmission of $\simeq$ 81% was achieved for the straight fibre (ie, $^1/r_b = 0$) this decreasing steadily as the bending radius r_b decreased to around 10cm, beyond which ($^1/r_b \geq 0.1cm^{-1}$) transmission remained approximately constant.

3.3.2 - Method and results - KrF laser

The laser used in these experiments was a Lambda Physik-EMG 50E (248nm) device. Prior to experiments the pulse duration of the laser was measured as 15ns at FWHM(Fig. 3.12).

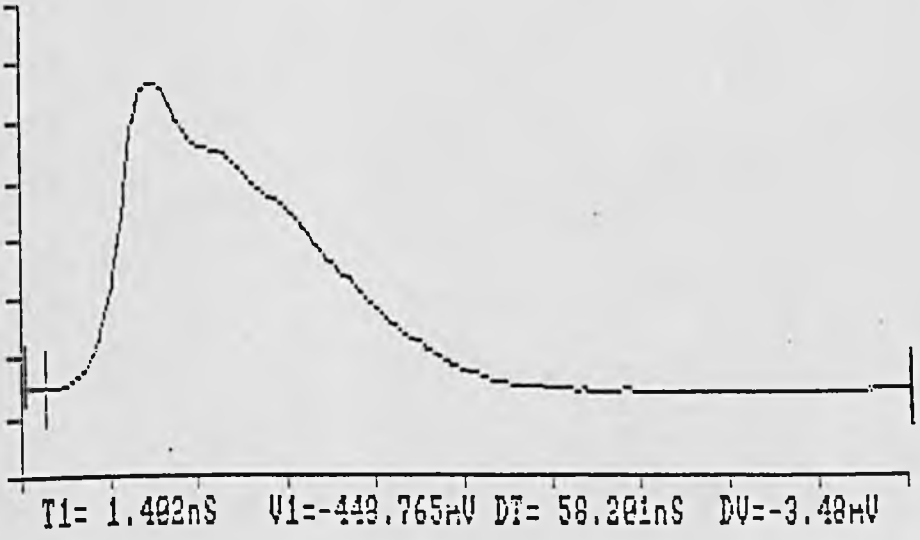

Fig. 3.12 - The pulse shape of KrF laser

An energy of 29mJ was achieved using a fresh gas mixture and, under sealed-off conditions and a PRF of 1Hz, the energy remained constant for in the excess of 30 minutes which was sufficient for performing the experiments. Measurement of the coupling and transmission loss of a Superguide-G 600μm fibre were carried out using similar procedures as discussed above. The laser output was passed through a 6mm diameter aperture and imaged on to the fibre face using a 30mm focal length

quartz lens. At a relatively low fluence (85mJcm^{-2}) a transmission of more than 90% was achieved using a 15cm long fibre, this decreasing to 24% at 4 meter (Fig. 3.13a). However, when the fluence was increased to about 460 mJcm^{-2} and 2800 mJcm^{-2} the transmission decreased to just below 70% and 60% respectively. The distributed loss coefficient K, and the coupling efficiency were derived from Fig. 3.13b using equation (3.5). A mean value of K=3.63 x 10^{-3} cm^{-1} (or 1.6dBm^{-1}) was obtained for 85 and 465mJcm^{-2} which is very close to the data sheet value of about 1.5dBm^{-1}, and a value of 6x10^{-3} cm^{-1}(2.6dBm^{-1}) at 2800mJcm^{-2}. At 85mJcm^{-2} the coupling efficiency $T_i x T_o$ was measured to be 0.9, giving $T_i \simeq 95\%$ assuming $T_i \simeq T_o$ ie. an input and output loss of only 5%. By the same argument, T_i values of 82% and 72% were measured at fluence of 465 mJcm^{-2} and 2840mJcm^{-2} respectively. This confirms that the transmission loss at high fluences is due to a decrease in coupling efficieny, although at the highest fluence the distributed loss is also higher.

The effect of fluence on the energy transmission was studied as follows: One meter of PCS 600μm fibre was prepared and irradiated at various energies for an input spot area to the fibre of $A_{in} \simeq 2x10^{-3}$ cm^2 (Fig. 3.14). It can be seen that whilst a transmission of 29% was obtained at relatively low fluence ($\simeq$ 0.24Jcm^{-2}) this fell to $\simeq$ 15% when the fluence reached $\simeq$ 6Jcm^{-2}. Similarly a transmission of about 90% was obtained for a 0.5m PCS 1000μm fibre at low fluence (20mJcm^{-2}) but this fell to just below 40% at about 2Jcm^{-2} (Fig. 3.15a). For HCN 1000μm fibre the transmission was also above 80% at low fluence (130mJcm^{-2}) but reduced to about 40% at higher

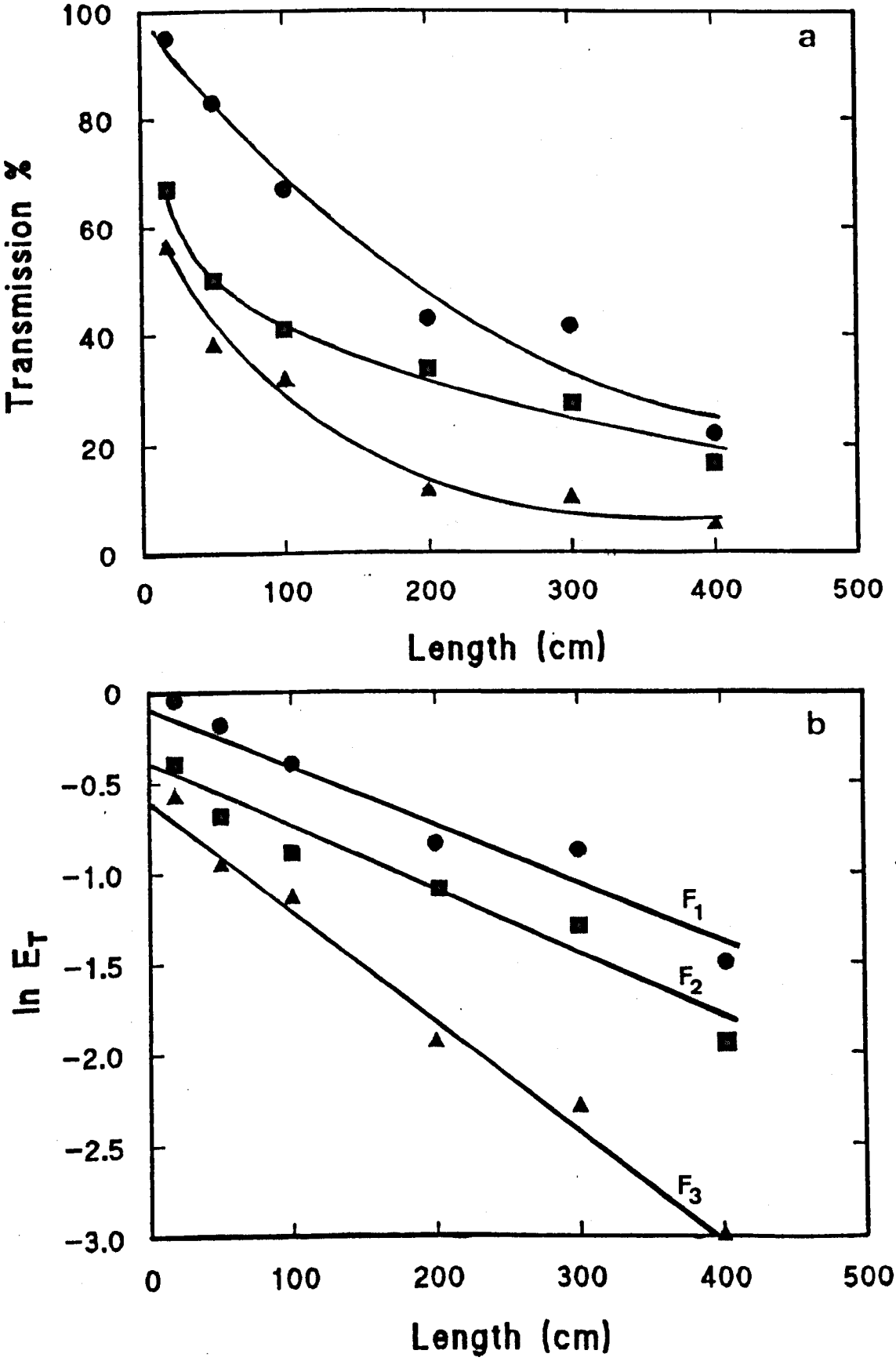

Fig. 3.13 - Variation of energy transmission (a) and its logarithm (b) with the length of superguide-G 600μm fibre, $F_1 \tilde{=} 85 mJcm^{-2}$, $F_2 \tilde{=} 465 mJcm^{-2}$, $F_3 \tilde{=} 2840 mJcm^{-2}$ using 248nm.

values (Fig. 3.15b). This decrease in energy transmission with increasing fluence can probably be attributed to a

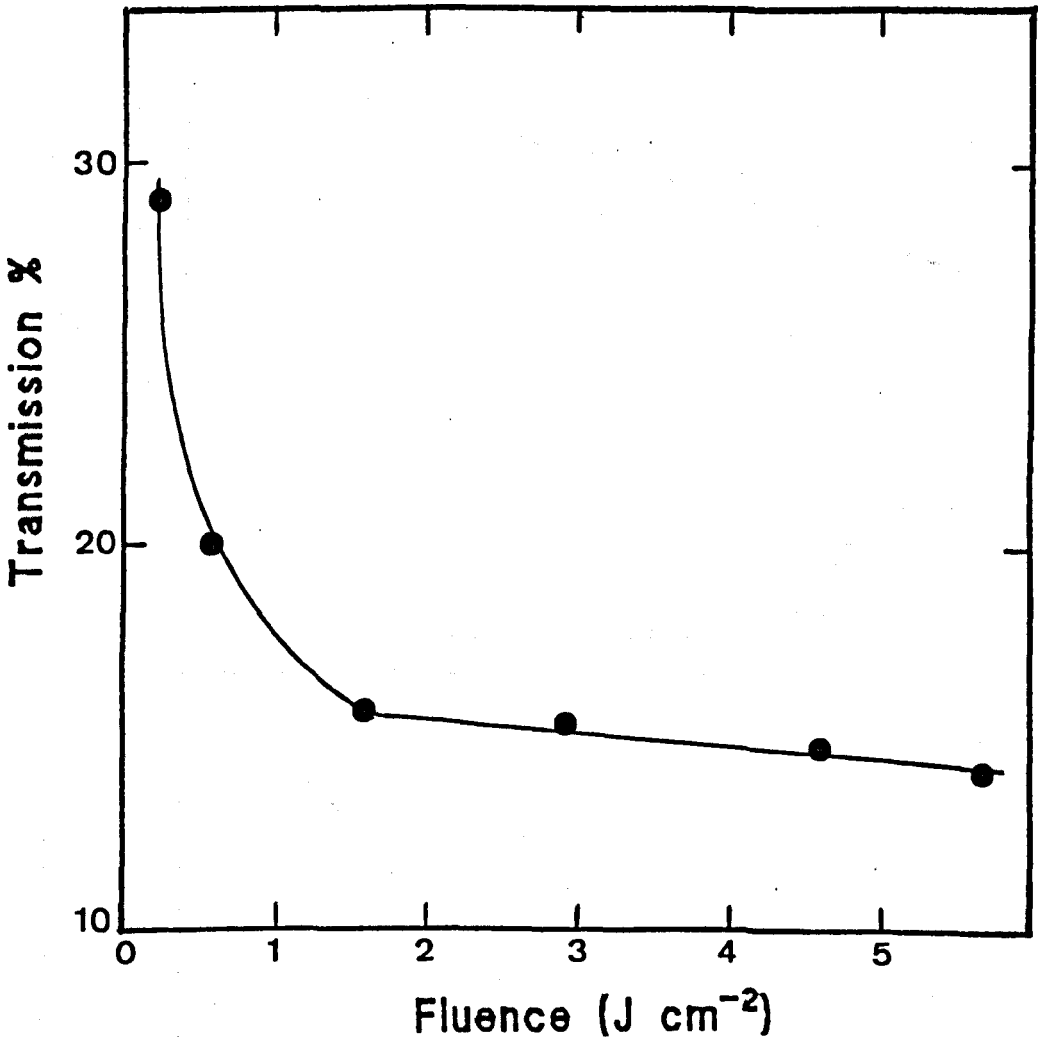

Fig. 3.14 - Energy transmission of PCS 600μm, L=1m as a function of fluence at 248nm.

reduced coupling efficiency because of non-linear absorption and possible surface damage. Also, the cumulative effect of previous shots at different fluences can be important even though only one pulse was used for each point shown.

The next experiment was concerned with the multishot exposure effect at a constant fluence on transmission. One meter of PCS 600μm was prepared and set up as before and

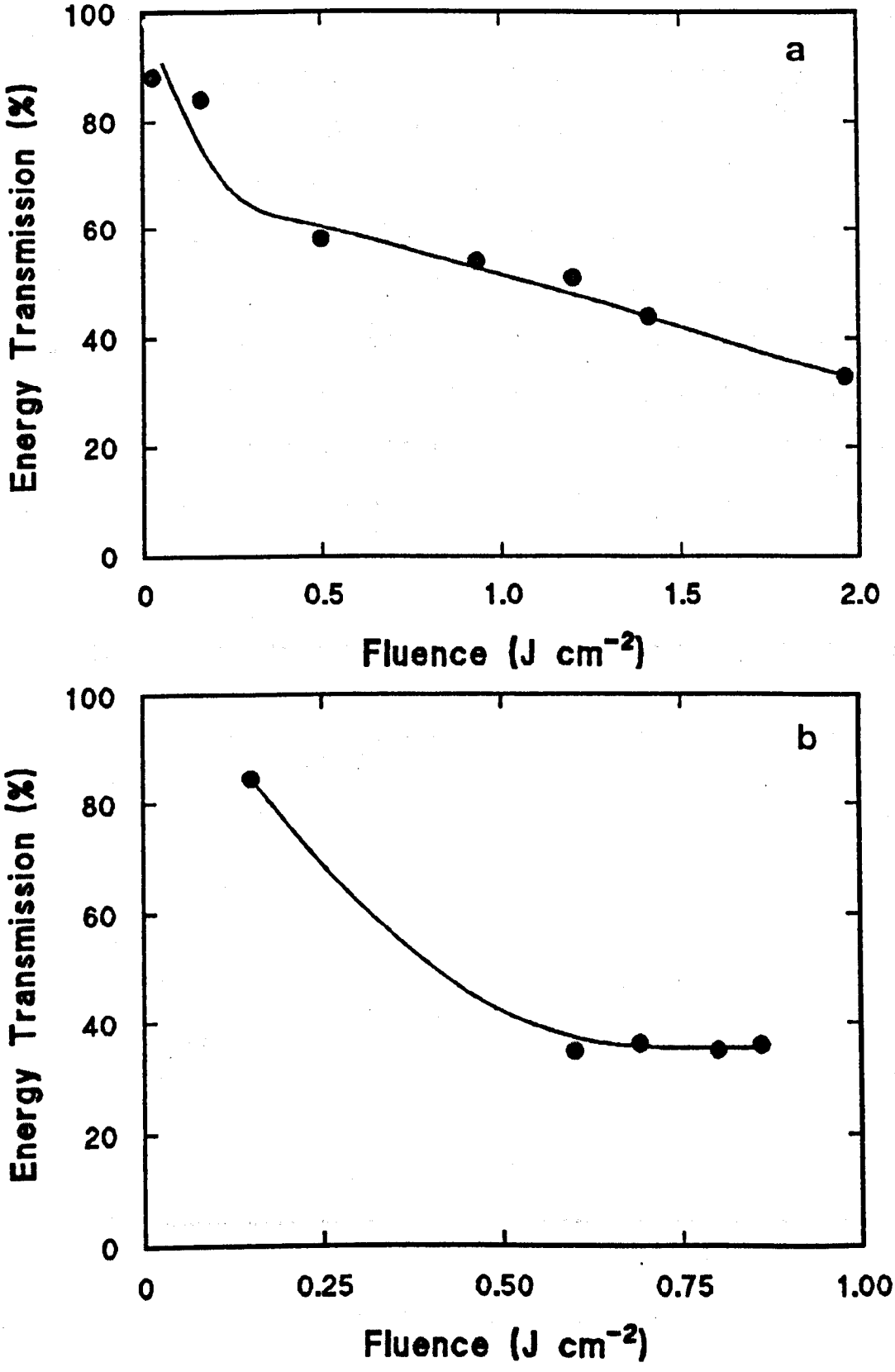

Fig. 3.15 - Energy transmission of PCS 1000μm, L=0.5m (a) and HCN 1000μm, L=0.5m (b) as a function of fluence at 248nm.

irradiated at the fluence ~3Jcm^{-2}. Fig. 3.16 shows the results of this experiment where, after 60 pulses, the energy transmission has fallen from its initial value of 19% which was measured after 2 pulses to about 16% and then remains more or less constant up to 200 pulses. After this the transmission falls rapidly reaching a value of 3.5% after 900 pulses. An important observation during the experiment was the formation of a white region around the fibre input end as the exposure time increased. This region appeared as 'ring-like' lines which were thicker near the fibre tip and became thinner further away. No spark (plasma) was observed during the experiments.

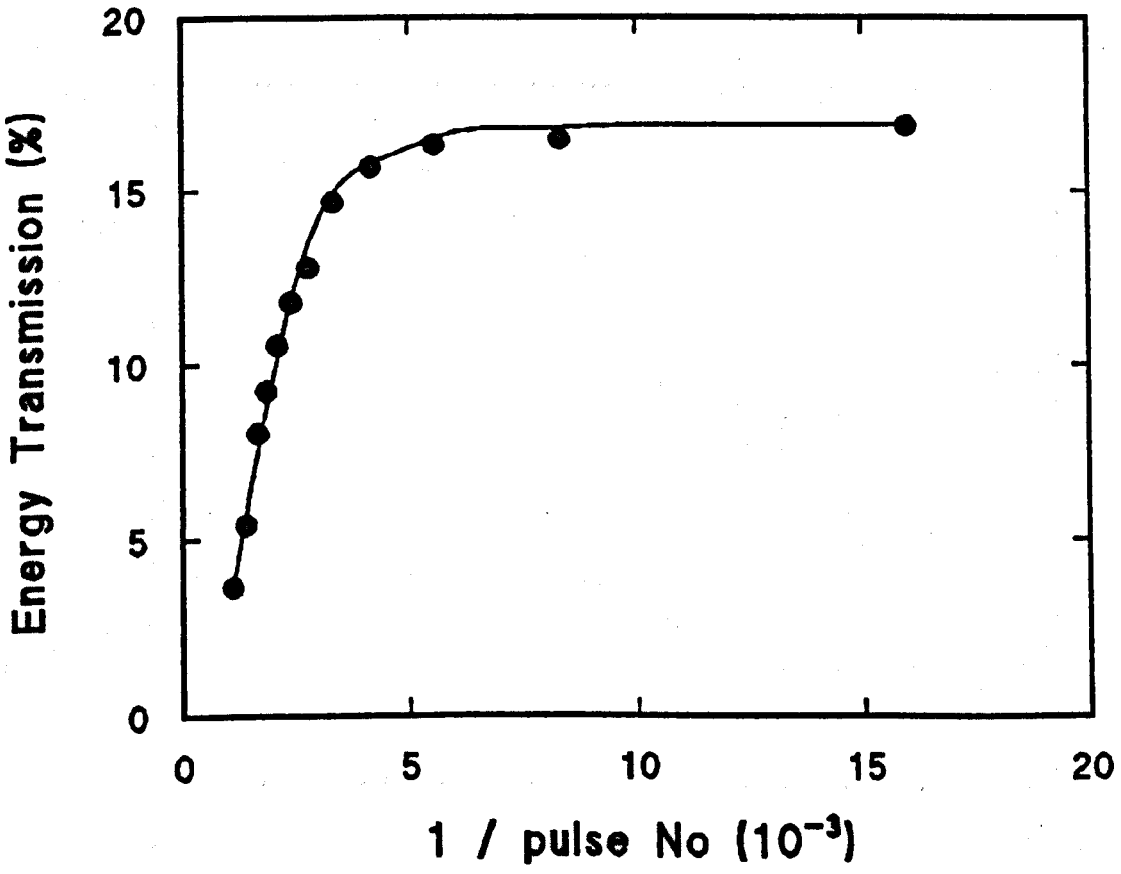

Fig. 3.16 - Cumulative effect of multishots on transmission at constant fluence of 3Jcm^{-2} using PCS 600μm at 248nm.

The transmission decrease in this particular case is mainly due to prolonged exposure time and hence relatively large number of pulses. As no catastrophic damage due to plasma formation was observed the cause of the limitations to power transmission probably mainly arise from non-catastrophic physical damage to the fibre core. It is known that multishot laser-induced absorption bands at 210 and 265nm limits the fibre transmission, with the latter associated with a non-bridging oxygen hole centre (NBOHC).

Fig. 3.17 shows the energy transmission of PCS 1000μm (L=0.5m) and PCS 600μm, (L=1m) as a function of input irradiance. The irradiance was calculated by dividing the input energy by the product of the laser pulse duration and 70% of the fibre core area.

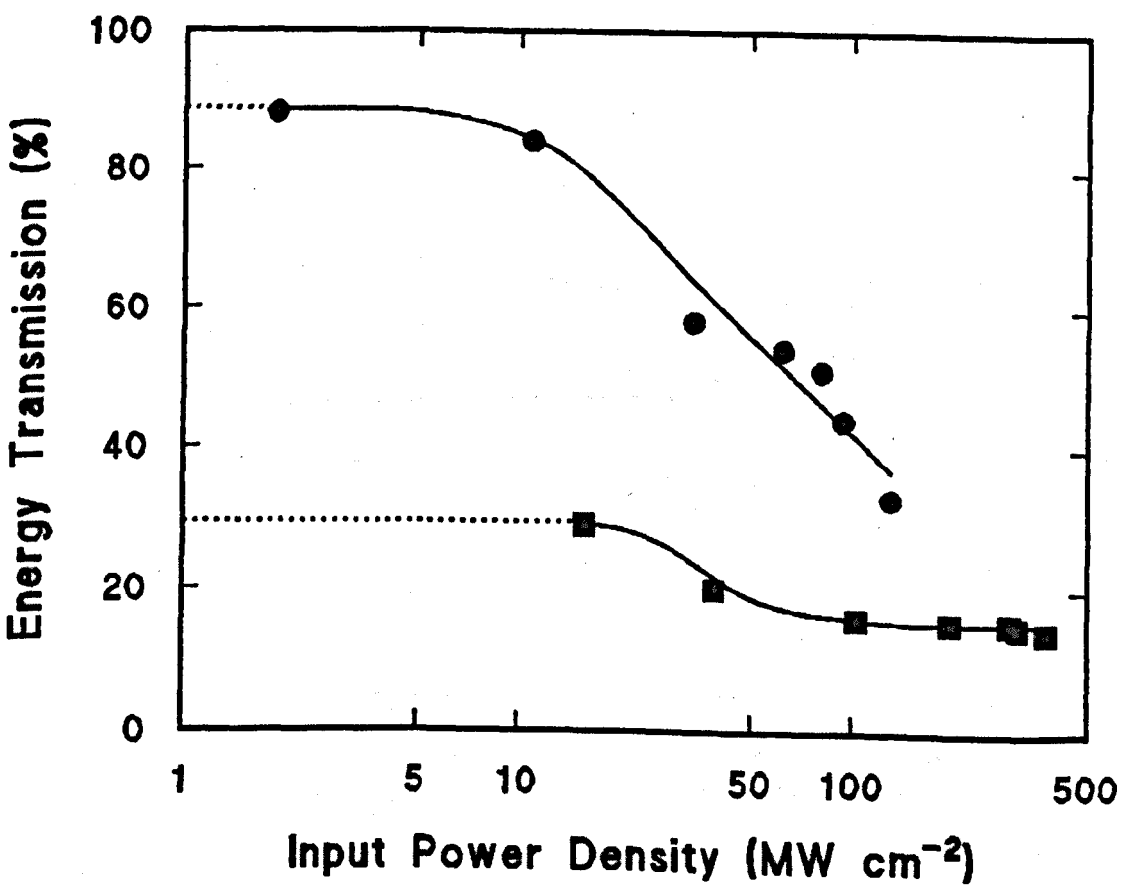

Fig. 3.17 - Non-linear transmission of PCS 1000μm, L=0.5m(●) and PCS 600μm, L=1m(■) at 248nm.

As the single-shot laser irradiance level at the fibre surface was increased considerable non-linear attenuation was observed. The onset of increased loss occurs at values of 10 and 13 $MWcm^{-2}$ (Fig. 3.17) for PCS 1000μm and PCS 600μm fibres respectively.

The last experiment in this section was to test the fibre bending loss. Fig. 3.18 shows the transmission of

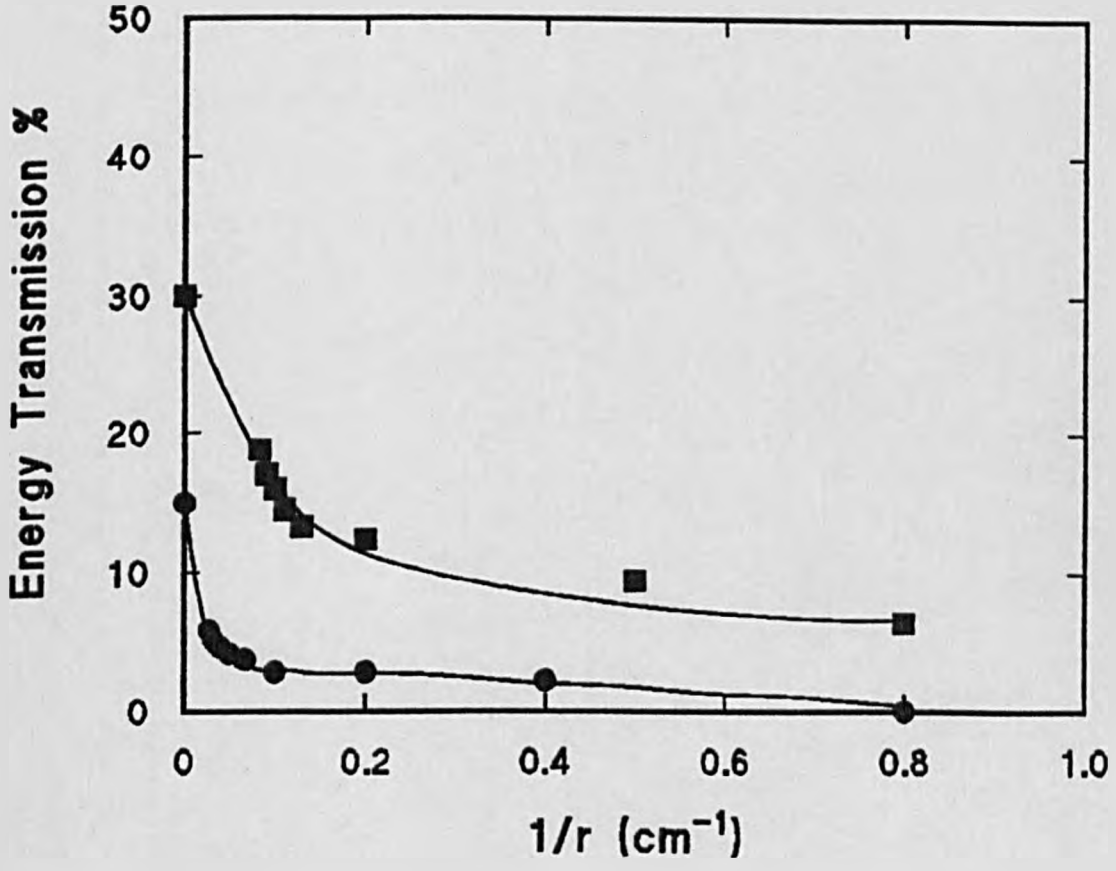

Fig. 3.18 - Energy transmission of PCS 600μm (●) and HCG 550μm (■) as a function of fibre bend radius at F≃3.5Jcm^{-2} and F≃2Jcm^{-2} respectively using 248nm.

energy as a function of fibre bend radius for PCS 600μm at constant fluence of 3.5Jcm^{-2} and HCG 550μm at a fluence of 2Jcm^{-2}. The initial transmission for a straight section of

HCG 550μm was measured as about 30%; the transmission then fell quite rapidly as the diameter of bend decreased such that this was below 10% at the minimum radius of 1.25cm just before it broke. For PCS 600μm, the initial value of transmission was measured to be 15% for a straight sample and this transmission likewise decreased with increased bending though somewhat more abruptly than for the smaller core fibre. The results are consistent with the principle that losses due to fibre bending decrease as the core radius decreases.

Fig. 3.19 shows three different examples of fibre damage. It can be seen in Fig. 3.19(1a) that when the fibre was placed very close to the focal point of the input lens even at relatively low fluences, catastrophic damage due to breakdown occured. When the fibre was positioned behind the lens focal plane so as to produce an input spot size filling $\sim$ 70% of the fibre core area, prolonged exposure at high fluences also led to permanent mechanical damage which is illustrated in Fig. 3.19(1b). Here linear fracturing along the core surface can be seen. Figs 3.19-2(a),(b),(c) show different types of bulk damage, and the misalignment damage caused by the fibre being off-axis hence resulting in severe damage of cladding and jacket, Fig. 3.19-(3a,b).

(1) Surface damage

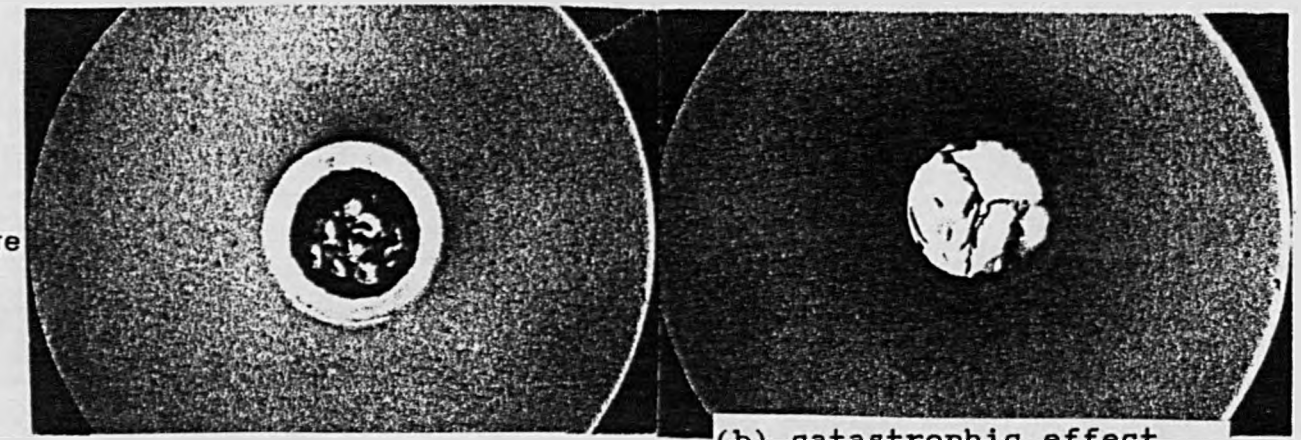

(x50) (a) multishot effect
λ = 248nm, PCS 600µm

(b) catastrophic effect
λ = 248 nm, HCN 600µm
irradiation time ~ 15mins (x50)

(2) Bulk damage

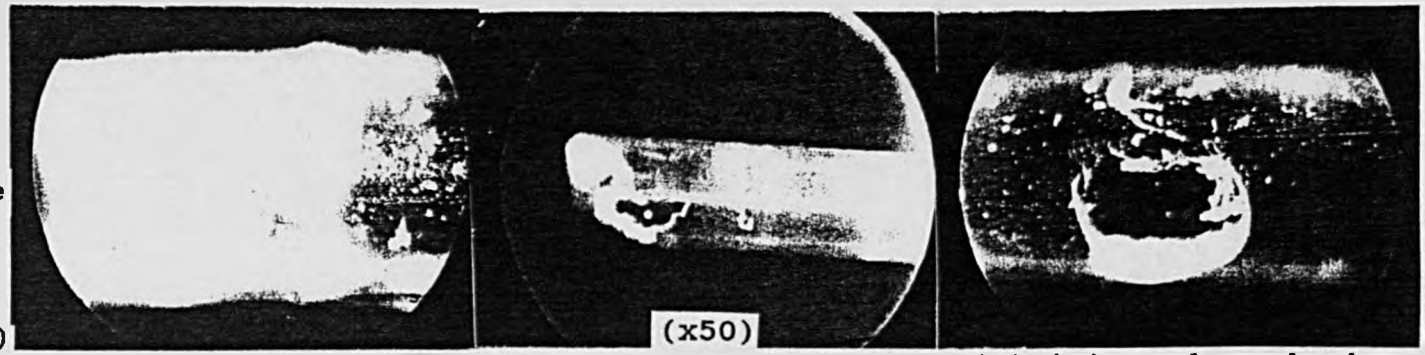

(x100)

(a) cumulative damage
length ~ 3mm
λ = 248nm, PCS 600µm
damaged length ~ 3mm

(x50)

(b) Fractured
length ~ 10mm
λ = 248nm, HCN 600µm
damaged length ~ 10mm

(c) internal explosive
effect, inside focused
length ~ 15mm
λ = 248nm, PCS 600µm. (x100)

Fig. 3.19 - Examples of surface damage (1), bulk damage (2) and misalignment damage (3) of PCS 600µm using 248nm.

(3) misalignment damage

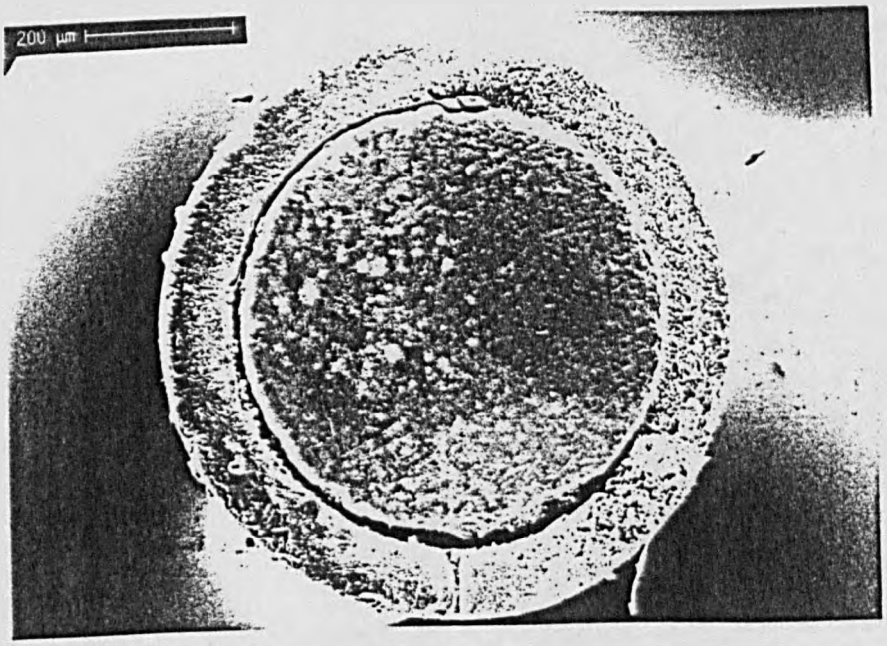

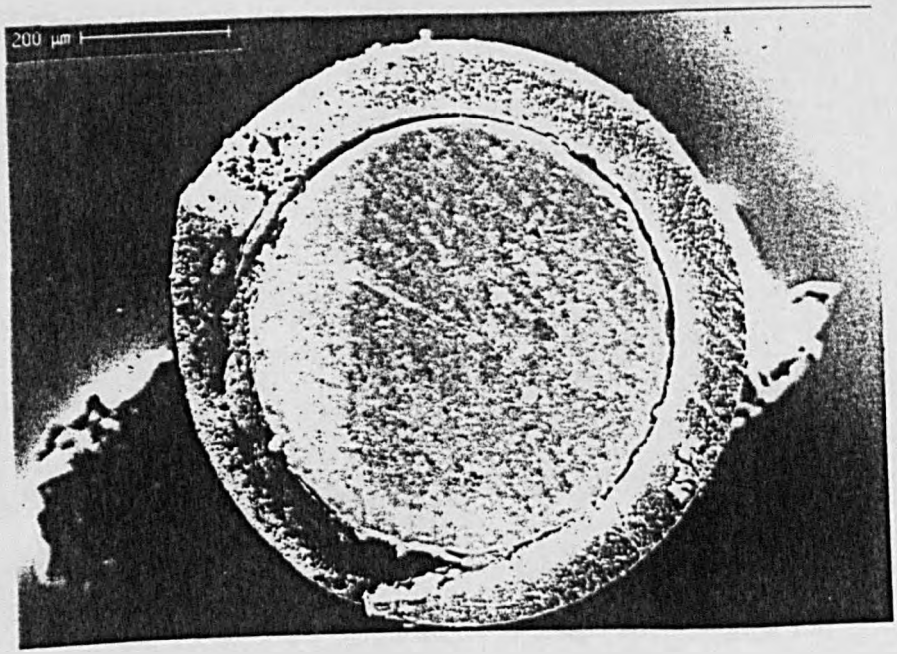

3.3.3 - Method and results - ArF laser

Fig. 3.20 shows the variation of transmission with fibre length for three input fluences (60, 470 and 4700 $mJcm^{-2}$). The maximum radiation transmission was just below 50% at a fluence of $60mJcm^{-2}$ and fibre length of 20 cm. From these results a mean value for the attenuation coefficient of $K=7x10^{-3}cm^{-1}$ (ie. $3dBm^{-1}$) was obtained. The data sheet value is about 2.5 dBm^{-1} which is slightly lower than measured value.

The coupling efficiency at 60, 470 and 4700 $mJcm^{-2}$ was calculated as 53%, 37% and 5% respectively; assuming $T_i \simeq T_o$ corresponding values of 72%, 60% and 22% are obtained for T_o, (Fig. 3.20b). It can be seen (Fig. 3.20) how rapidly the transmission reduces with increasing fluence. It is reasonable to assume that losses at the fibre input are higher than the output end and the likely mechanism of damage caused by 193nm radiation is due to colour-centres formation.

Figure 3.21a shows the variation of transmission as a function of fluence where each point shown on the graph represents a new piece of fibre (L=20cm) and the transmission at each fluence was measured after 1 pulse only. The data shown in Fig. 3.21a were used to plot the transmission versus input irradiance (Fig. 3.21b) in order to evaluate the onset of non-linearity of Superguide-G fibre. However, this was not possible due to lack of sufficient data at low fluences.

The final experiment in this section was to study the bending loss of a 1m fibre long sample. A maximum energy transmission of 16% was obtained when the full length of the fibre was in the straight position. Transmission fell to less

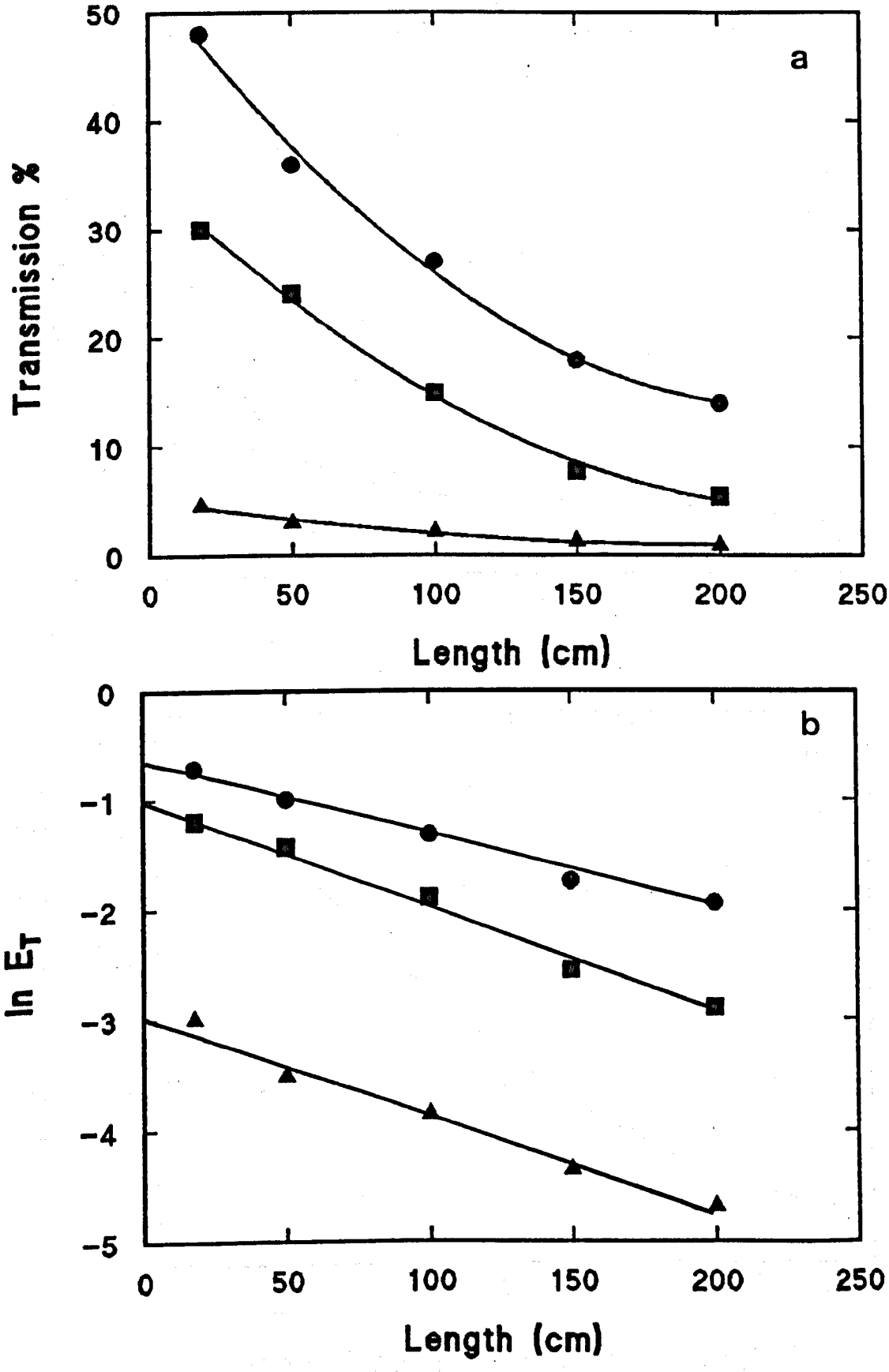

Fig. 3.20 - Measurement of energy transmission of Superguide-G 600μm fibre as a function of distance at fluences of 0.06Jcm^{-2} (●), 0.470Jcm^{-2}(■) and 4.72Jcm^{-2}(▲), using 193nm.

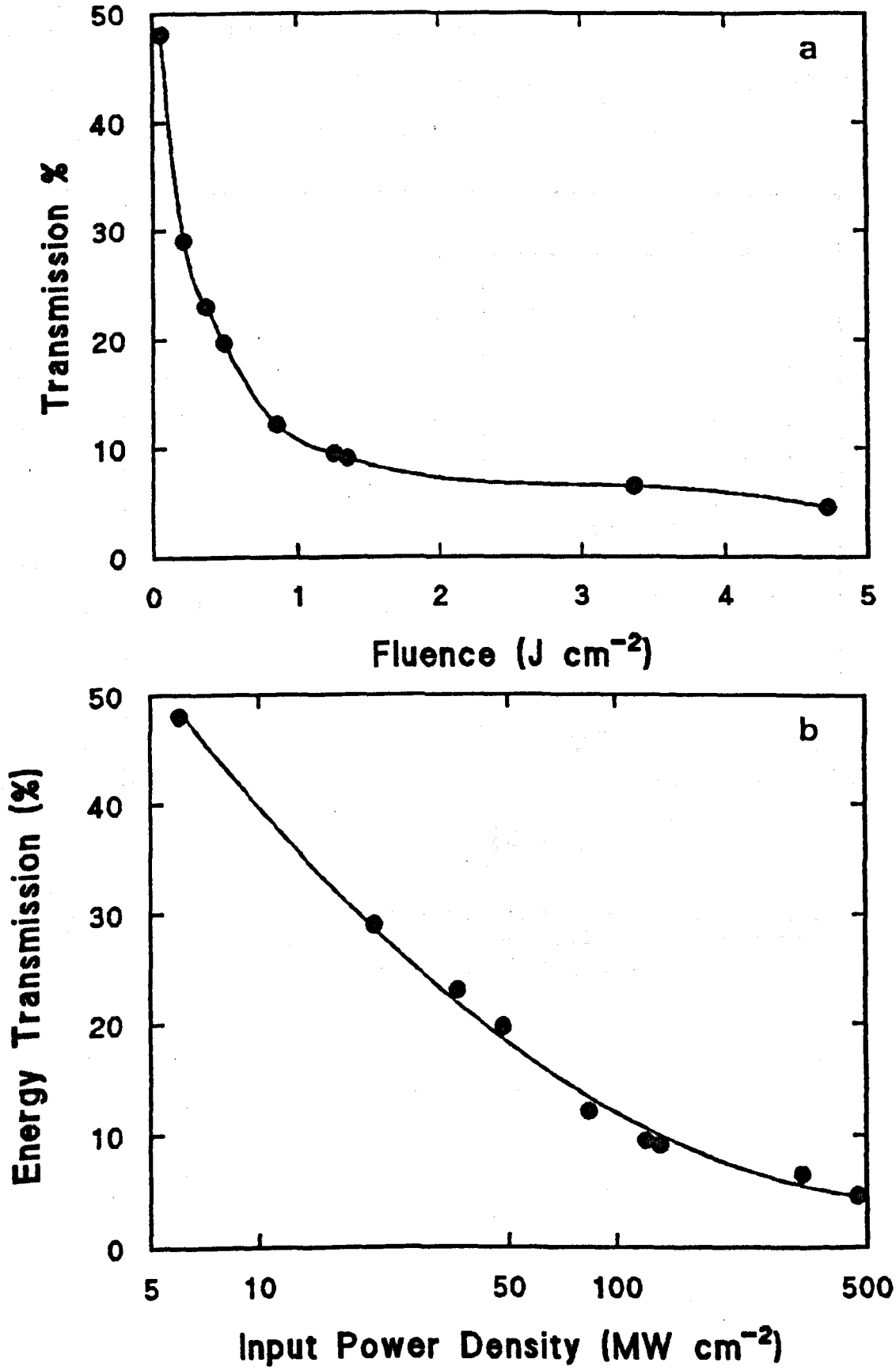

Fig. 3.21 - Measurement of energy transmission of Superguide-G 600μm fibre as a function of input fluence (a) and input power density (b) at 193nm.

than half a percent at a radius of 18cm and at a radius of 6cm was essentially zero. A very rapid energy loss was therefore inccured at relatively large bending diameters.

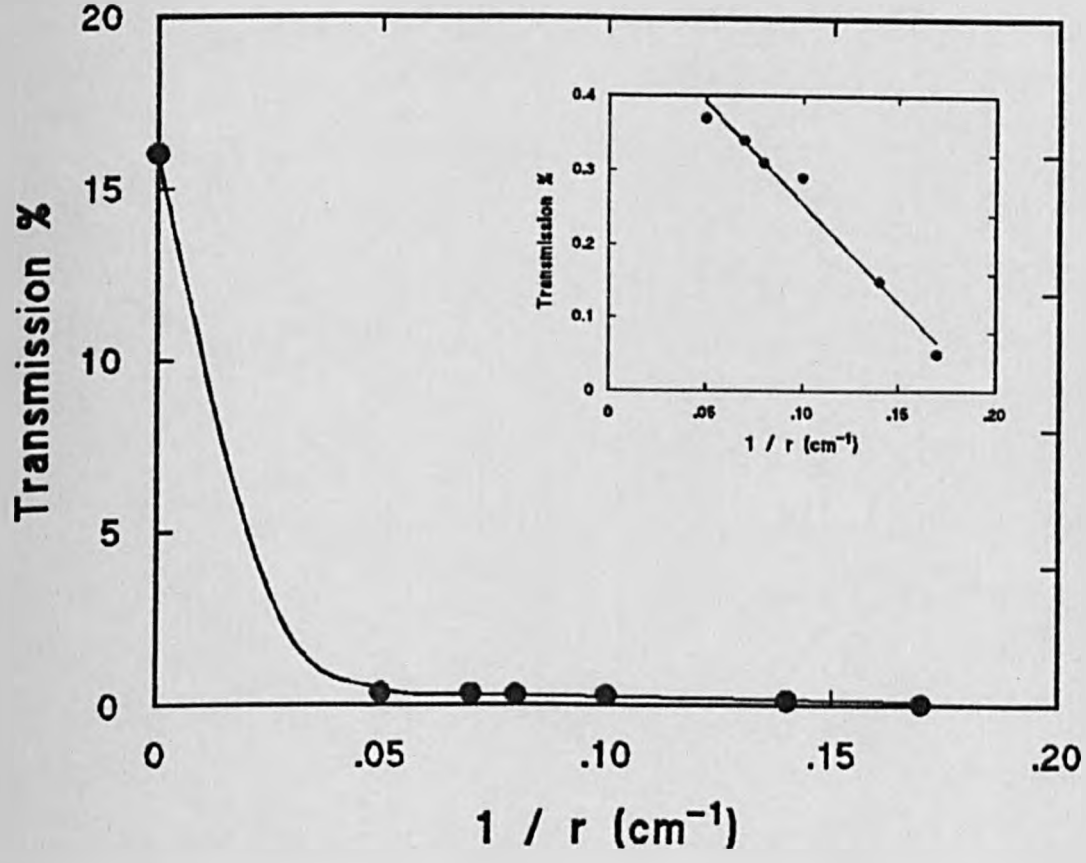

Fig. 3.22 - Plot of energy transmission as a function of Superguide-G 600µm fibre bend radius at $F_{in} \sim 420$ mJcm^{-2}, (L=1m), using 193nm.

Discussion

The interaction of high power UV laser pulses with fibre material causes specific problems which have been studied recently by several groups (4-10). The maximum amount of excimer laser energy which can be transmitted is limited by the onset of optical non-linearities and physical damage to the fibre. Laser damage is influenced by laser power density, wavelength, pulse duration, fibre surface quality, and impurities. By surface damage, it is normally meant the formation of a plasma at a dielectric surface due to, for example, electron avalanche. Generally the surface damage threshold is much lower than the bulk for two reasons: First due to the fact that a mechanically finished surface exhibits many defects, eg. cracks and imbedded polishing materials and secondly due to contamination by air borne particles, finger prints or impurities such as H_2O.

Transmission loss is one of the important parameters that must be taken into account when evaluating the effectiveness of ultraviolet high power delivery through optical fibres. Loss of transmission with increasing length of fibre can be described using equation 3.6 where the energy transmission exhibits an exponential decrease with length due to distributed loss. These losses are produced by absorption at impurities and defects and also by scattering. Improved transmission of 308nm XeCl laser radiation was obtained using Superguide PCS rather than ordinary PCS fibre; this was shown by the smaller distributed loss coefficient of 1.4×10^{-3} cm^{-1} for Superguide PCS compared with 2×10^{-3} cm^{-1} for ordinary PCS. This improvement is attributable to the purer core

material of Superguide.

Since some of the medical applications take place in a liquid environment, a simple experiment was performed to study the effect of energy transmission in saline. It was shown (Fig. 3.10b) that the 308nm transmission decreases rapidly with distance. This decrease is due to UV absorption in saline. Another cause of transmission loss is fibre bending which in most practical clinical applications is unavoidable. An example is shown in Fig. 3.11 where the transmission was 81% using PCS 1000μm fibre in a straight position but fell to $\simeq$ 40% at a bend radius of 10cm, beyond which the transmission remained fairly constant.

Variation of energy transmission with length using Superguide-G fibre was studied with the 248nm KrF laser at three fluences (Fig. 3.13). A transmission of more than 90% at 85mJcm^{-2} for a 15cm long fibre was achieved but as the fluence was increased to 460mJcm^{-2} and 2800mJcm^{-2} this decreased to just below 70% and 60%, respectively. This is probably due to non-linear absorption at the front surface of the fibre which results in increased end losses associated with coupling energy into and out of the fibre. All fibres investigated at 248nm exhibit a rapid decrease in transmission with increasing fluence (Fig. 3.14, PCS 600μm; Fig. 3.15a PCS 1000μm; Fig. 3.15b 1000μm), restricting efficient transmission to fluences $<<0.25$Jcm^{-2}. The lower transmission of HCN fibre (Fig. 3.15a) compared with PCS fibre is due to its higher core impurities which was confirmed by the manufacturer (Optilas).

The object of energy transmission measurements versus

pulse number was to study the fibre lifetime under the cumulative effect of multishot exposure at a constant fluence ($3Jcm^{-2}$). The results, shown in Fig. 3.16, indicate that the fibre output remained constant for the first 200 pulses and then began to decrease. Since no audible sound or plasma formation was noted, it is conjectured that the transmission loss is due to laser-induced absorption bands at 210 and 265nm which are associated with colour-centre formation and NBOHC defects (15).

There are a number of other non-linear effects such as stimulated Raman scattering (SRS), stimulated Brillouin scattering (SBS), and multiphoton absorption which can reduce the fibre transmission at high irradiance levels. SRS and SBS can be neglected in these experiments because of the very short lengths of fibre used. However two-photon absorption can be important and has been observed at 248nm by Itoh et al (11) in short (1-2) metre lengths of fused silica fibres at irradiance levels in the range of $10^{6} - 10^{8}$ W/cm^2.

By plotting the measured values of inverse transmission versus the product of irradiance and the fibre length, a two-photon absorption coefficient is then given by slope of the line. In these experiments the values of $0.3x10^{-4}$ cm/MW for PCS 600μm and $3.3x10^{-4}$ cm/MW for PCS 1000μm were evaluated which are in close agreement with those reported by Taylor et al (5,6).

Different types of fibre damage are shown in Fig. 3.19(2a) shows an example of fibre damage following multishot irradiation which was discussed for PCS 600μm and shown in Fig. 3.16. However, when the fluence exceeded $6Jcm^{-2}$ the

surface was badly damaged after a few pulses due to breakdown and plasma formation. Fig. 3.19(1b) shows the effect of catastrophic breakdown of the fibre surface. If one continued to irradiate the fibre at such a high fluence level the surface would be completely shattered and fractured along the bulk of the fibre as shown in Fig. 3.19(2b). Finally, fragments of the fibre core would disintegrate leaving an irregular surface and seriously decreasing beam transmission. One last type of fibre damage which could seriously affect the transmission is 'off-centre' or 'misalignment' of the laser as shown in Fig. 3.19(3a,b). This damage is caused by interaction of the UV beam with the cladding-core interface as the diverging beam comes into contact with the core circumference just inside the input face.

The surface damage threshold was measured by Pini et al (7) as 2.1Jcm^{-2} for a PCS 600 μm fibre using 249nm, although Allison et al (8) believe that the damage threshold varies widely, eg. (0.7-3.5)Jcm^{-2} at the input face. Taylor et al(5) showed that the surface damage threshold varied as $A^{-1/4}$ where A is the laser beam area at the core. Although this dependency is weak, it points to the necessity of using similar laser beam areas when comparing damage threshold data.

Results obtained with the ArF laser (Figs.3.20 and 3.21) show the severe limitation on transmission at moderately low fluences. For examples, the transmission through a 20cm fibre was only about 50% at 0.06Jcm^{-2} and at 0.47Jcm^{-2} the transmission dropped to $\simeq$5%. Therefore, for ablation of targets using fibre-delivered ArF laser it is best to use fluences as low as possible.

Unlike the KrF laser experiment with Superguide-G where the non-linearity began at $\geq$ 10MWcm^{-2}, with the ArF laser no value can be calculated from Fig. 3.21b for the onset of non-linearity due to lack of sufficient experimental data at low irradiance. This is because no 'turning point' was observed in the present data, (Fig. 3.21b), although Taylor et al (6) have measured a value of (0.6-0.7) MWcm^{-2} for the inception of non-linearity. This shows there is a need for more data at lower irradiance levels than used in this present experiment. However, the two-photon absorption coefficient for ArF-fused silica fibre is an order of magnitude greater than if the KrF is used (6).

The final experiment with the ArF laser was to study the fibre bending loss by measuring its transmission at different bend radii, Fig. 3.22. The initial transmission of a 1 metre fibre at 0.42Jcm^{-2} was measured to be about 16% which is consistent with Fig. 3.20, but it rapidly approached zero at a bend radius of 20cm ie, a loss of 98%.

Distributed loss in fibres is made up of intrinsic and extrinsic components. The intrinsic losses involve i - absorption due to electronic transition and lattice vibration and ii - Rayleigh and Raman scattering. Extrinsic losses, however, mainly arise through i - impurity absorption because of transition metal and OH vibration, and ii - scattering due to structural imperfections. Perhaps two of most important factors for fused silica are the absorption loss due to electronic transition and Rayleigh scattering. A fundamental absorption due to electronic band gap transitions results in an UV absorption tail which varies exponentially with the

photon energy E according to

$$\alpha = \exp\ [(E-E_g)/kT] \qquad 3.9$$

where E_g, k, T are the band gap energy ($\simeq$8eV), Boltzmann constant, and temperature respectively. Thus the most suitable materials for use would be those with higher energy band gap in order to reduce the effect of the UV absorption tail.

Rayleigh scattering on the other hand is caused by small particles and inclusions in the material which result in microscopic variation of local dielectric constant. The scattering coefficient is proportional to λ^{-4} which means the amount of scattered light increases as the wavelength decreases. According to Pinnow (12) the contribution of Rayleigh scattering to the attenuation coefficient is about 30% for fused silica.

Another factor which should be taken into account when considering the damage is the type of fibre ie, 'wet' or 'dry' depending upon the concentration of OH doping. This is of interest because the presence or absence of OH has a significant effect on the types of point defects present in fused silica. Low-OH material have a higher concentration of defects such as Si-Si bonds and Si-O-O-Si bonds, whereas in the high-OH material defects such as Si-OH are more common (13). These defects in turn affect the fibre response to radiation including the generation of electron centres (E' centres) and other defects by ultraviolet light at energies below the band gap (14). Therefore, the dry silica fibre is better suited for IR transmission because of removal of OH absorption at 1.35μm and wet fibres much better suited for UV transmission since the inclusion of water in the lattice

helps to reduce stress in the silica during annealing. This is because hydrogen atoms have finite mobility at room temperature, allowing them to seek out and attach to dangling bonds. A well known colour centre in fused silica is related to an absorption band at 4.8eV at 260nm (15,16) which corresponds to a red luminescence band of 1.9eV at 650nm (15,17,18). The centre is undesirable for KrF laser optics since the photon energy of the absorption band is close to that of the laser ie, 5eV at 248nm.

Some comments on the use of optical fibres with excimer lasers are given in table 3.2. Briefly, the experiments showed that PCS 600um has a satisfactory flexibility and relatively a good transmission for 308nm radiation. The flexibility of this fibre reduced when a larger core diameter (1000μm) was used but still maintained a high transmission at moderate fluences using this wavelength. When using shorter wavelengths (248nm, 193nm) its transmission capability was greatly reduced as explained before.

HCN fibre showed a poorer transmission at both 308nm and 248nm mainly due to high core impurity. It is also less flexible compared with the PCS fibre. With a smaller core diameter fibre such as HCG, a much better flexibility and very good transmission was observed using the 308nm wavelength, and it was also possible to transmit 248nm radiation for relatively long periods of time.

The transmission of 308nm and 248nm wavelengths was improved when a Superguide PCS fibre was used because of its higher core purity. However, Superguide-G 600μm proved to be by far the best fibre compared with the others investigated.

It exhibited sufficient flexibility and a much better transmission at all wavelengths particularly at 193nm where other fibres failed to transmit any useful level of ArF laser radiation.

Table 3.2 - Summary of the fibres performance in these experiments.

Fibre (core diameter)	Transmission (nm)	Flexibility
PCS 600	308 good 248 poor 193 ——	v. good
PCS 1000	308 good 248 poor 193 ——	good
HCN 1000	308 poor 248 v.poor 193 ——	poor
HCG 550	308 v.good 248 good 193 poor	excellent
Sup. PCS 1000	308 v.good 248 good 193 v.poor	good
Sup. G. 600	308 excellent 248 v.good 193 good $<0.5 Jcm^{-2}$	v.good

For the XeCl laser which is the most attractive for medical applications such as angioplasty, the induced absorption in fused silica fibres is negligible because of the small photon energy. The use of KrF laser radiation is very doubtful in medicine due to its carcinogenic effects, but the study of fibre transmission at this wavelength (248nm) should give additional information regarding the nature of photoinduced colour centres in fibres.

1. Royston D., Waynant R., et al,
Optical properties of fibre optic surgical tips,
Appl. Opt. 28:799:1989.

2. Ward H.
Modeling of laser energy by shaped optic fibre tips.
Lasers Surg. Med., 7:405:1991.

3. Al-Dhahir R. (PhD thesis),
Development and interaction of excimer laser with tissue.
Hull Univ. - 1989.

4. Hata K., Watanabe M., et al,
Non-linear processes in UV optical material at 248nm.
Appl. Phys. B., 50:55:1990.

5. Taylor R.S., Leopold K., et al,
Dependance of the damage and transmission properties of fused silica fibres on the excimer laser wavelengths.
Appl. Opt., 27:3124:1988.

6. Taylor R.S., Leopold K., Birmacombe R.
Dependance of the non-linear transmission properties of fused silica fibres on the excimer laser wavelengths.
J. Appl. Phys., 66:4035:1989.

7. Pini R., Salimbeni R., Vannini, M.
Optical fibre transmission of high power excimer laser radiation.
Appl. Opt., 26:4185:1987.

8. Allison, S.W., Gillies T., et al,
Pulsed laser damage to optical fibres.
Appl. Opt., 24:3140:1985.

9. Artjushenko V.G., Kenovkvi, et al,
Fused silica fibres for the delivery of high power UV radiation.
SPIE., 1420:149:1991.

10. Hillrichs G., Dressel M., et al,
Transmission of XeCl excimer laser pulses through optical fibres: dependence on fibre and laser parameters.
Appl. Phys. B., 54:208:1992.

11. Itoh Y., Kunitomo K., et al,
High power KrF Laser transmission through optical fibres and its application to the triggering of gas switches.
J. Appl. Phys., 54:2956:1983.

12. Pinnow D.A., Rich T.C., et al,
Fundamental optical attenuation limits in the liquid and glassy state with application to fibre optical waveguide materials.
Appl. Phys. Lett., 22:527:1973.

13. Griscom D.L.
Defect structure of glasses.
J. Non-cryst. Solids, 73:51:1985.

14. Stathis J., Kastner M.
Photoionized paramagnetic defects in amorphous silicon dioxide.
Phys. Rev. B., 29:7079:1984.

15. Tohmon R., Shimogaichi Y., et al,
Relation between the 1.9 eV luminescence and 4.8eV absorption bands in high purify silica glass.
Appl. Phys. Lett., 54:1650:1989.

16. Nakamura Y., Yamushita H., et al,
Excitation and decay mechanisms of the intra-4f luminescence of Yb^{3+} in epitaxial InP:Yb layers.
Appl. Phys. Lett., 52:114:1988.

17. Tanimura K., Tanaka T., et al,
Creation of quasistable lattice defects by electronic excitation in SiO_2.
Phys. Rev. Lett., 51:423:1983.

18. Stathis J.H., Kastner M.A.
Vacuum - ultraviolet generation of lunimescence and absorption centrs in a-SiO_2.
Philos. Mag. B., 49:357:1984.

Chapter 4

Interaction of excimer lasers with organic material

4.1 - Introduction

Following the discovery by Srinivasan and Mayne-Banton (1) in 1982 that polymers could be etched with sub-micron resolution and without apparent thermal damage using the 193nm ArF laser, many research groups began to study the medical and electronic applications of photoablation. In order to efficiently utilise excimer lasers for the ablation of biological material and for use in related microsurgery applications it is desirable to have a clear understanding of the ablation process. The mechanism(s) by which the interaction between excimer lasers and materials takes place will be discussed in detail later.

In Chapter 3 the UV transmission of different types of fused silica fibres was studied, and consideration given the limitations imposed by each of the main UV excimer laser wavelengths. In this chapter the application of fibre delivered UV radiation to the ablation of organic polymers such as polyetheylene terephthalate (PET; Mylar) and polyimide (Kapton), and to biological lens tissue ablation is reported.

This tissue was chosen as there was a specific interest in evaluating the potential for using the fibre delivered excimer laser for ophthalmic applications such as phaeco-emulsification, lens capsulatomy and vitreous surgery (See chapter 2). The main interest in ablating organic polymers is that they are easy to work with, and provide a useful 'model' to study biological tissues. However, there are significant

differences, notably that organic polymers have excellent homogeneity which is not the case for biological tissue. In addition the saline content of tissue is likely to lead to modified interaction mechanisms. The chemical structure of PET and polymide repeat units are shown in Fig. 4.1. The weakest bonds in the former are O-C and C-H and in the latter the N-C bond. The dissociation energies for these bonds are estimated to be about 5eV.

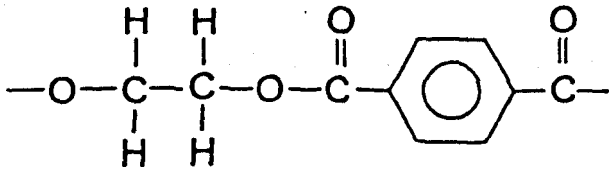

(a)

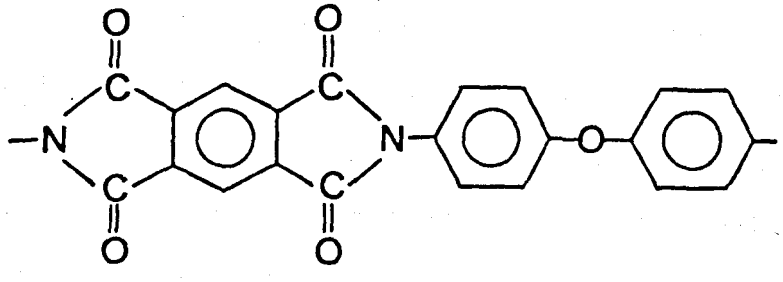

(b)

Fig. 4.1 - Schematic diagram of (a) PET and (b) Polyimide monomers.

4.2 - Ablation of organic polymers with KrF and ArF lasers

Ablation experiments were performed using a Lambda-Physik EMG-50E KrF (248nm) laser with a 15ns (FWHM) pulse duration. The films used were 70μm thick PET (Melinex) and 90μm thick polyimide provided by ICI and DuPont respectively. The experimental setup is shown in Fig. 4.2 where a 6mm diameter aperture was used to select a region of uniform fluence from the laser output operating at 1Hz. The aperture was imaged onto the input of the fibre using a 30mm focal length quartz lens. A 1 meter long PCS 1000μm fibre was employed, that had been polished and optimized as described in chapter 3.

The output fluence from the fibre was measured as the ratio of output energy from the fibre to the full core area. Attenuators placed before the aperture were used to vary the fluence and energy measurements were made using a calibrated pyroelectric joulemeter. During the experiment a small fan was placed at a distance of 30cm from the fibre output. This fan-fibre distance was chosen so that no vibration occured at the fibre. The purpose of the fan was to gently blow away ablation products generated during the experiment which could have otherwise been deposited on the surface of fibre causing absorption and possibly damaging it.

For the second part of the experiment a home-built ArF (193nm) laser with a pulse duration of ~10ns (FWHM) was used. The laser operated at 1Hz and the output beam from the laser was imaged onto a 15cm long Superguide-G 600μm fibre using a 50cm focal length quartz lens. The same experimental set up as in Fig. 4.2 was used for the ablation of 23μm thick PET.

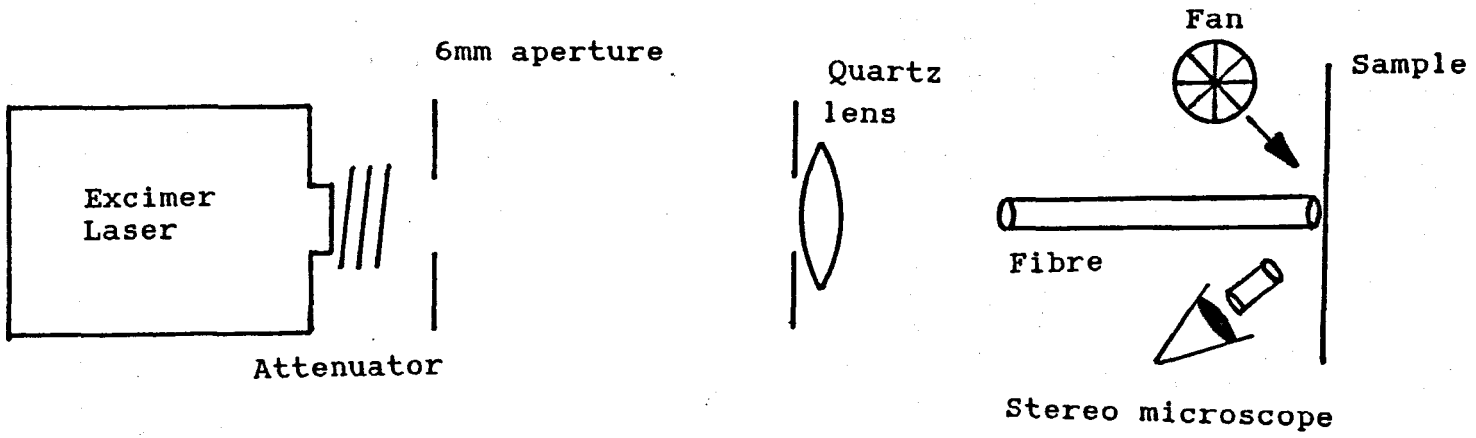

Fig. 4.2 - Experimental setup for polymer ablation with KrF and ArF lasers

Material removal measurements were made by exposing the polymers to a predetermined number of laser pulses, n, and measuring the depth of material removed, Δ , using a high resolution microscope (Olympus BHM $\pm$ 2μm depth resolution). The average etch depth per pulse was then calculated from Δ/n.

Results

Useful information about the material can be derived from removal rate measurements by applying Beer's-Lamberts law (Eq.4.1A) to describe the etch depth per pulse D_e according to(2):

$$D_e = \frac{1}{\alpha} \ln \frac{F}{F_{th}} \qquad 4.1A$$

Here α, F and F_{th} are effective absorption coefficient, fluence and threshold fluence respectively. The law in its simplest form states that no material is actually removed until the absorbed photon energy per unit volume has reached a critical value known as energy density, and the plume retains the same absorption coefficient as the condensed phase. Fig. 4.3 shows the removal rate measurements for PET in air using the fibre delivered laser. The etching began at fluence of $\sim$ 20mJcm^{-2} and then increased quite rapidly as the fluence was increased. In the range 25-300mJcm^{-2} (low fluences: L_F) a fit to the data using equation 4.1A gives $\alpha \sim 12 \times 10^4$ cm^{-1}. Beyond this the etch rate increases more rapidly possibly as a result of increasing plume transparency. Under these conditions (transparent plume) the etch rate is described by (3):

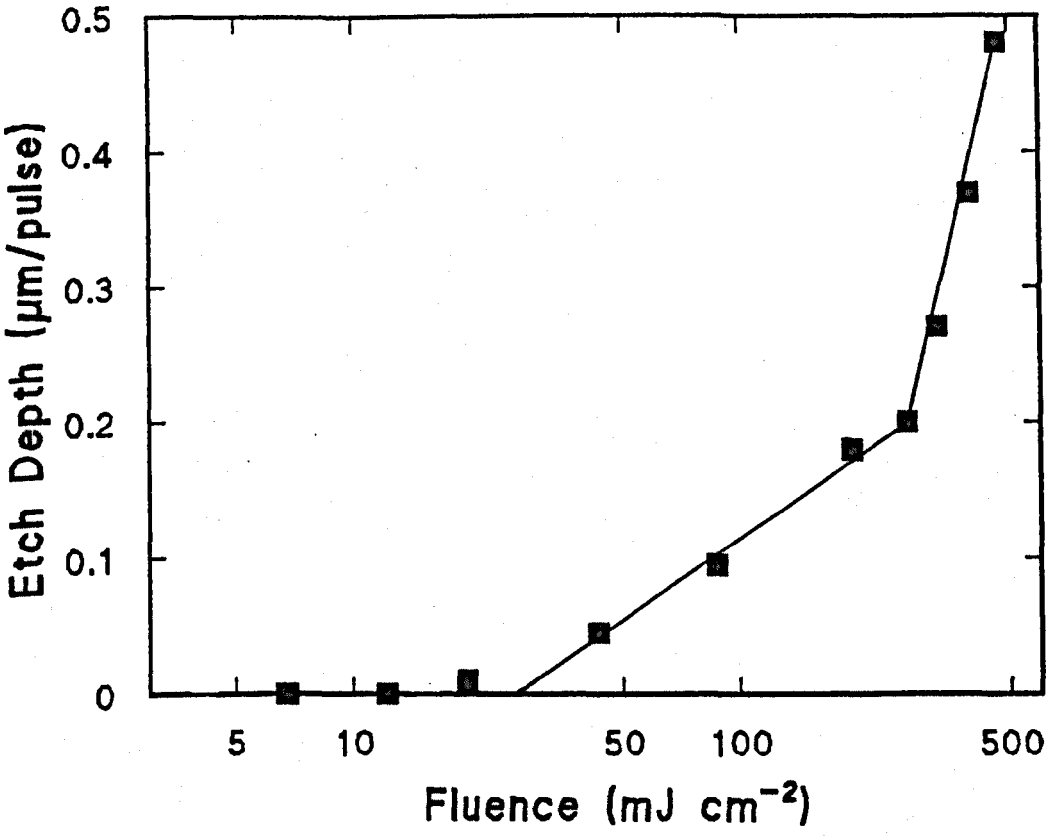

Fig. 4.3 - Ablation of 70μm PET with fibre in air using KrF laser.

$$D_e = \frac{F - F_{th}}{\alpha F_{th}} \qquad 4.1B$$

and D_e becomes linearly dependent on fluence. The increased transparency of plume is probably due to strong heating of the ablation products formed in the early stages of the laser pulse at high fluence and resulting in their degradation to lower mass species which absorb less strongly. In this experiment an assumed linear fluence dependence beyond $\sim$300mJcm^{-2} (high fluence: h_f) in Fig. 4.3 yields from eq. 4.1B $\alpha F_{th} \sim 7 \times 10^{3}$ Jcm^{-3} and with $F_{th} \sim$25mJcm^{-2} a value of $\sim 28 \times 10^{4}$ cm^{-1} for the effective absorption coefficient. This is broadly consistent with that derived from eq. 4.1A.

When the fluence exceeded the threshold the ablation was

accompanied by a weak audible noise which became stronger at higher fluences. The acoustic sound is thought to originate from the ablation products moving at supersonic speeds. In addition to this, the polymer surface in the vicinity of ablation site was covered with a light brown colouration which according to Srinivasan et al (4) is due to carbon-containing species. An SEM of ablation sites on PET are shown in Fig. 4.4 where (a) shows an etched area without the fibre at 58 $mJcm^{-2}$ after 150 pulses. The beam is penetrated the film at the centre of the spot indicating that the fluence is slightly higher on the axis. Fig. 4.4(b) shows a fibre ablated region at 204 $mJcm^{-2}$ with 90 pulses. A close up of this in (c) illustrates that there is some irregularity at the base of the crater.

Etch rate data for Kapton obtained using the fibre delivered KrF laser are shown in Fig. 4.5. For these results eq. 4.1A gives values of $15x10^{4}$ cm^{-1} for effective absorption coefficient and 19$mJcm^{-2}$ for the threshold fluence. During the ablation of Kapton with the KrF laser (Fig. 4.5) it was observed that a soot-like deposit formed around the interaction zone which became darker as the fluence increased. These black regions are thought to be formed mainly by solid carbon products such as C_2, although other volatile materials were shown to be present in the ablation plume (5).

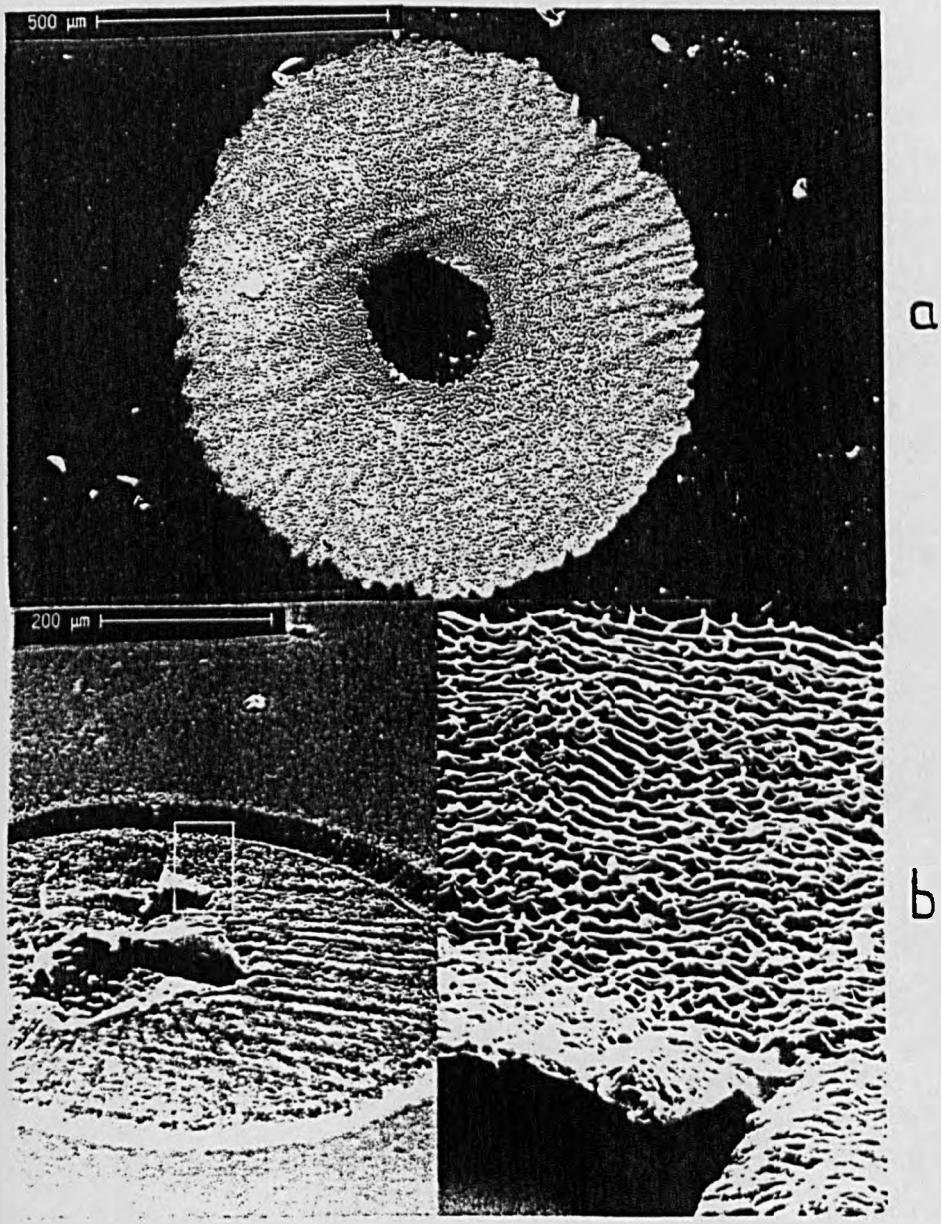

Fig. 4.4 - SEMs of PET ablation with the KrF laser
(a) without fibre at 58 mJcm-2, 150 pulses
(b) with fibre at 204 mJcm-2, 90 pulses,
(c) close up of (b).

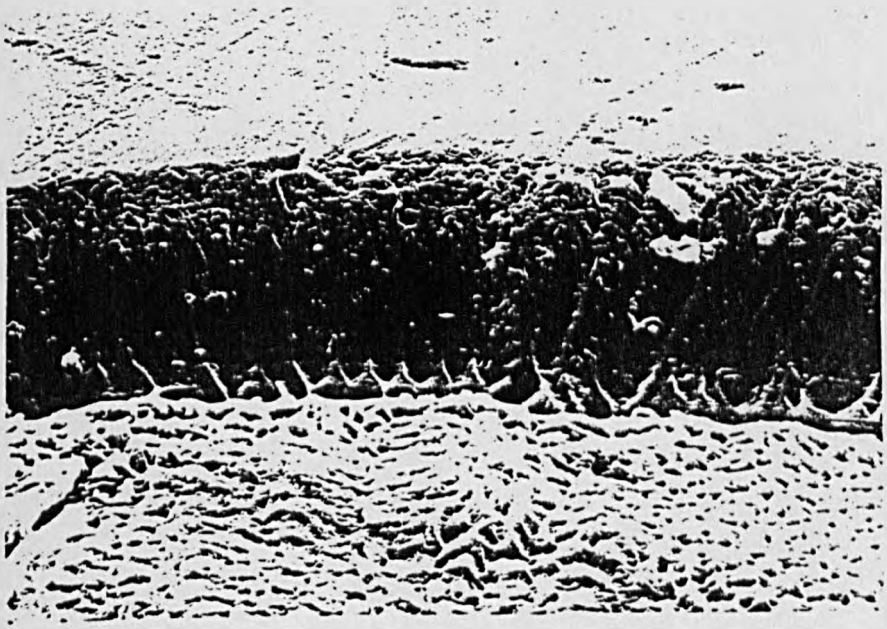

C

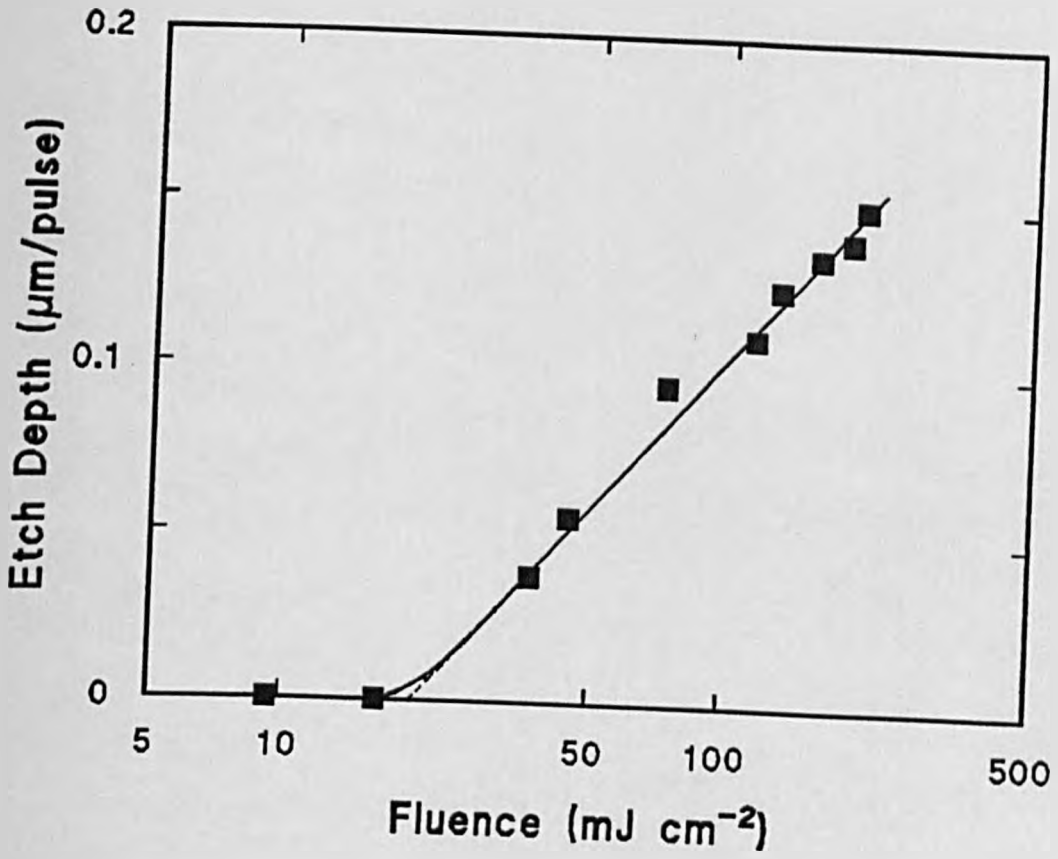

Fig. 4.5 - Ablation of polyimide (Kapton) with fibre using KrF laser.

The SEM photographs in Fig. 4.6 show some examples of Kapton film ablated without (a) and with (b,c) the optical fibre at different fluences and pulse numbers.

SEM photographs showed that the KrF laser produced smoother etching of polyimide (Fig. 4.6a) than PET (Fig. 4.4c). This is mainly due to the higher effective absorption coefficient α_e of the polyimide at this wavelength (ie 15×10^4 cm^{-1} which leads to a cleaner cut. Fig. 4.6c shows the laser-induced surface modification of polyimide by KrF radiation. The conical features have previously been observed (6) in seeded and unseeded Kapton irradiated at 308nm and 157nm

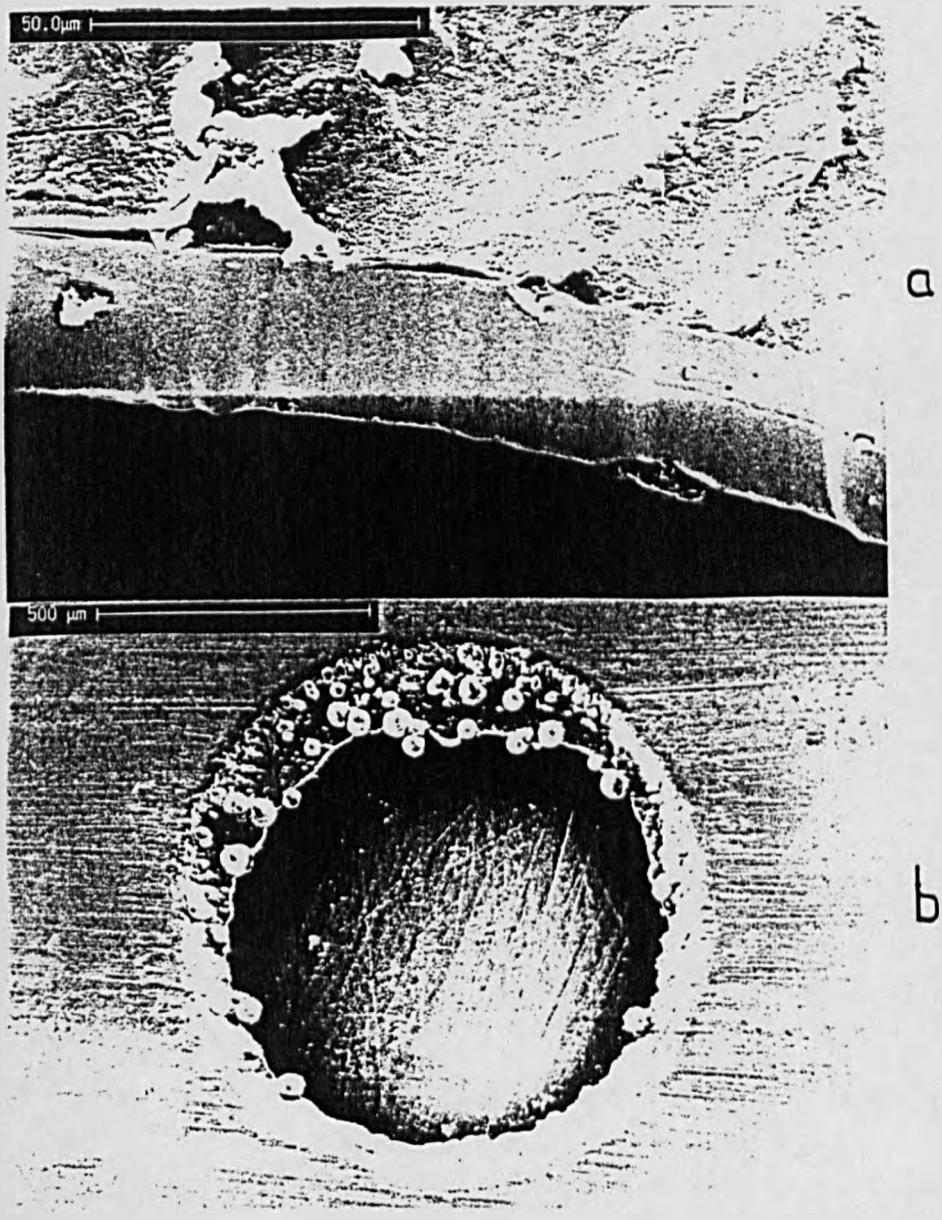

Fig. 4.6 - SEMs of Kapton ablation with the KrF laser
(a) without fibre at 1200 mJcm^{-2}, 115 pulses,
(b) with fibre at 204 mJcm^{-2}, 600 pulses,
(c) close up of edge region in (b).

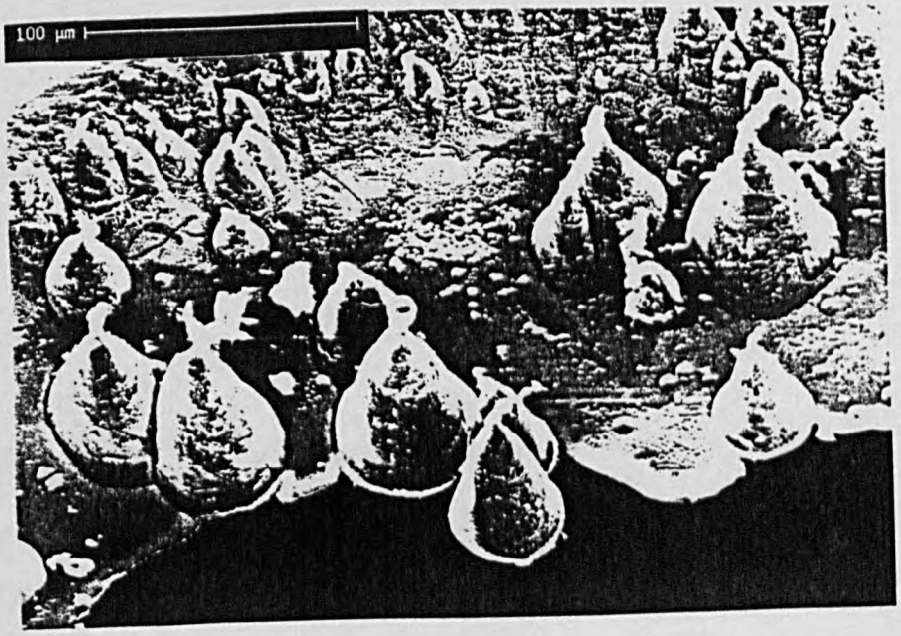

C

and attributed to particulate contamination produced during the polymer preparation or through redeposition of the ablation products. Recently it was observed (7) that nap-type and wall-type structures can also develop on non-melting polymer surfaces such as Kapton with the KrF laser.

The final experiment was the ablation of PET with the fibre-delivered ArF (193nm) laser. It was found that this polymer could be ablated using the fibre system at relatively low output fluences $\leq$0.5 Jcm^{-2} thus avoiding catastrophic fibre damage. The entire experiment used 1500 pulses with 88% of those below 243 $mJcm^{-2}$ and 12% between 243-307 $mJcm^{-2}$. An important observation during the experiment was the red fluorescence of fibre which covered the entire 15cm length of superguide G fibre, particularly being more intense at the ends. As shown by the results in Fig.4.7 the etching began at a fluence just above 15$mJcm^{-2}$ and in the range 15-100$mJcm^{-2}$ a fit to the data using equation 4.1A gave $\alpha_e \tilde{=} 21 \times 10^4 cm^{-1}$. Beyond 100$mJcm^{-2}$ the curve steepens (Fig. 4.7) and the slope yields a value of $\alpha_e \tilde{=} 12 \times 10^4 cm^{-1}$.

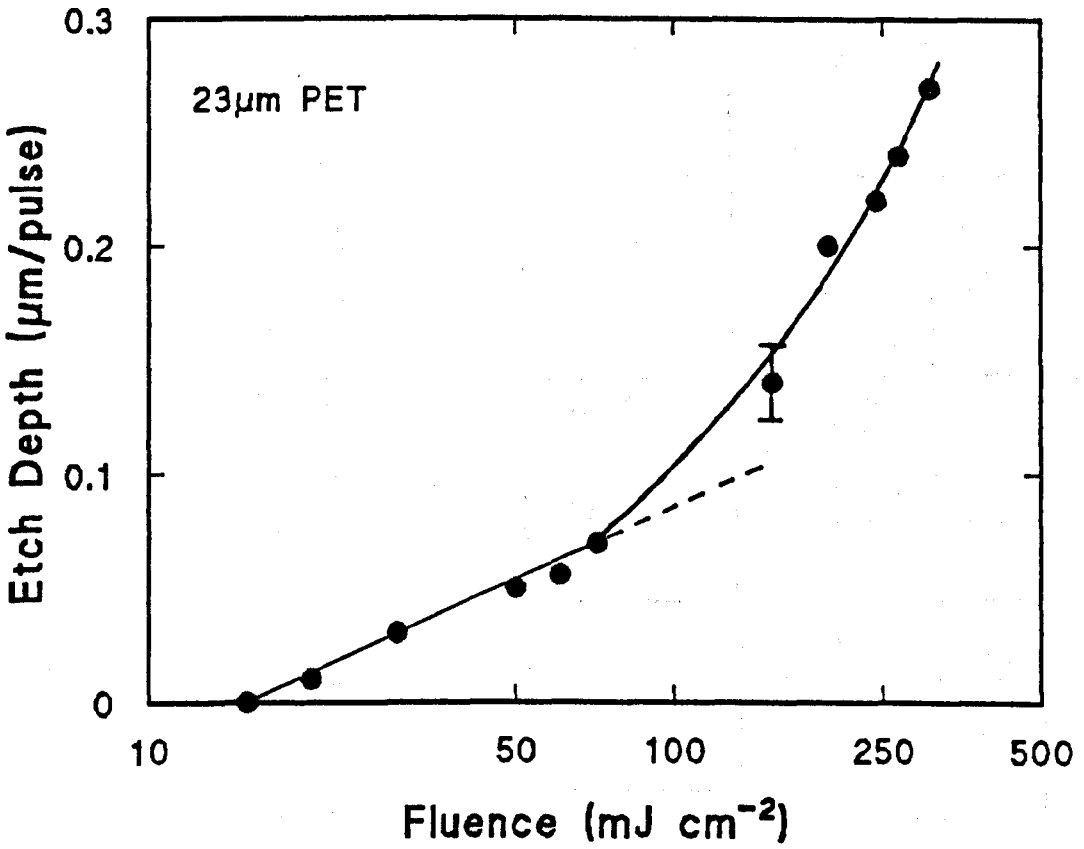

Fig. 4.7 - Ablation of 23μm PET polymer with fibre using ArF laser.

	PET					Polyimide (Kapton)			
λ(nm)	Thickness (μm)	F_{th} (mJ cm^{-2})		$\alpha_e(10^4)$ (cm^{-1})	αF_{th} kJ cm^{-3}	Thickness (μm)	F_{th} (mJ cm^{-2})	$\alpha_e(10^4)$ (cm^{-1})	αF_{th} kJ cm^{-3}
248	70	25	l_F	12	3	90	19	15	2.8
			h_F	28	7				
193	23	16	l_F	21	3.3				
			H_F	12	2				

l_F : low fluence

h_F : high fluence

Table 4.1 - Experimental results of polymer ablation with optical fibre-delivered excimer lasers.

4.3 - Ablation of biological lens tissue

There are numerous clinical applications of excimer lasers where the laser beam may and may not need to be delivered through a fibre. Ophthalmology is one such example where 193nm radiation can be used to produce precise incisions and reshaping the surface of the cornea without recourse to fibre delivery as was mentioned in Chapter 2. However, other applications such as vitreous surgery or diabetic retinopathy and phaecoemulsification would necessitate fibre delivery to gain access to intraocular structures.

In this part of the work an attempt was made to study the possibility of using 193nm, 248nm and 308nm wavelength radiation for ablation of lens tissue. A comparison was drawn between their etch rates in different media (air and saline).

4.3.1 - Removal rate measurements with XeCl, KrF and ArF lasers

In these experiments a bovine lens was cut from its equator in to slices 500μm thick and then stored in Glutaraldehyde Formaldehyde (GF) fixative solution to allow later use. It should be pointed out, however, that as preserving tissues in fixative may alter their structure, the results are likely to vary from those applicable 'in-vivo' to the clinical situation.

The experimental set up was essentially similar to that in Fig. 4.2 except that a 0.5cm thick cell with a quartz entrance window was constructed in order to facilitate the ablation of tissue in saline. Ablation of lens in air was carried out by imaging the beam of the XeCl laser with a 50mm focal length quartz lens onto a 50cm long polished 600μm PCS fibre. Throughout the experiment the laser operated at 4Hz and the tissue was kept damp to prevent dehydration during the ablation process. In the case of ablation without the fibre the required spot size (500±10) μm was measured prior to filling the cell with saline, and once the cell was filled the experiment began.

The experimental fluence was corrected for transmission loss in the quartz window and in saline. As quartz exhibits good bulk transmission at 308nm the primary loss is due to Fresnal reflections at its interfaces. For saline at 308nm a value of the transmission coefficient of $0.18cm^{-1}$ was used (8) to correct for transmission loss. No such correction was necessary for saline absorption with the fibre since the fibre output end was brought in to contact with the surface

of sample. The fluence in this case was calculated as the ratio of output energy known from separate experiment to the full core area (2.8×10^{-3} cm^2). The depth of tissue ablated was measured using an Olmypus (BHM) microscope with $\pm$ 2μm depth resolution.

The removal rate measurement of lens tissue with the KrF (248nm) laser operating at 2Hz was carried out in an essentially similar way except that in this case a 50cm long PCS 1000μm fibre was used. For saline at 248nm a value of the transmission coefficient of $0.51 cm^{-1}$ was used (8) to correct for transmission loss. The fluence was measured by using areas of 7.85×10^{-3} cm^2 (1000μm spot size) and 5.67×10^{-3} cm^2 (850μm spot size) for the fibre in air and for direct beam delivery in saline respectively.

The last experiment made use of the ArF (193nm) laser without and with the fibre. In the former case an 850μm diameter spot size was produced at the tissue using a 50mm focal length lens, and in the latter the beam was transmitted by a 20cm long Superguide-G 600μm fibre. In both cases the laser operated at 1Hz.

SEM Sample preparation

The samples were prepared by technical staff of the biology department as follows:
The tissue was immersed in (GF) fixative in a 0.1m phosphate buffer (PH 7.2) for 2 hours at room temperature. This was then followed by immersion in phosophate buffer overnight. Post fixation was carried out in 1% osmium tetroxide in a 0.1m phosphate buffer for 2 hours. Samples were dehydrated following fixation to remove water using increasing strengths

of acetone diluted in water as follows: 30% acetone 30 mins, 50% acetone 30 mins, 70% acetone 30 mins, 90% acetone 30 mins, 100% acetone 60 mins, 100% acetone 60 mins, 100% acetone dried 30 mins. The samples were finally critical point dried (CPD) using an E300 CPD apparatus (Polaron Equip. Ltd.). Detail of the drying process can be found in ref. (8).

Results

Ablation of lens tissue in air with the fibre delivered XeCl laser showed a higher etch rate compared with those in saline. Fig. 4.8 shows that the etch rate reached about 5μm per pulse at 500 mJcm^{-2} compared with only 0.5μm per pulse in saline. This difference is most likely related to the fact that saline acts to impede the ejection of material from the surface.

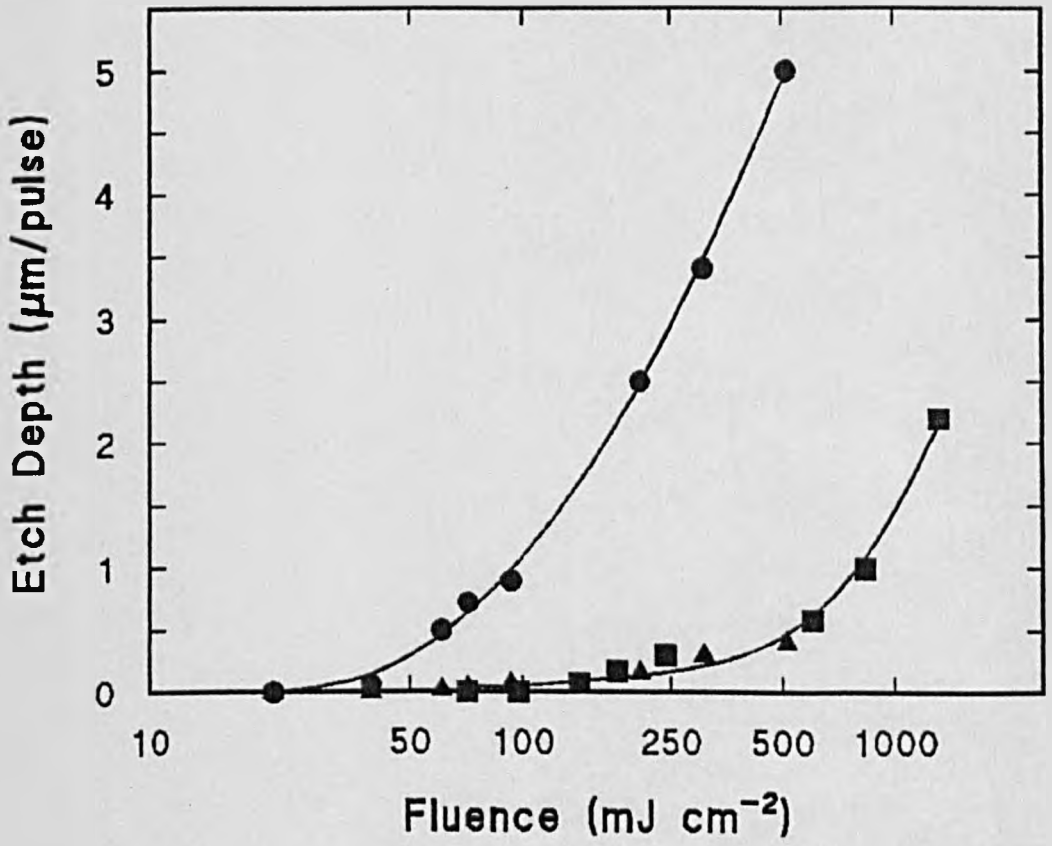

Fig. 4.8 - Ablation of lens tissue with XeCl laser in air with fibre (●), in saline with fibre (▲) in saline without fibre (■).

It can be seen from Fig. 4.8 that the significant ablation in air occurs at about 50 mJcm^{-2} where as in saline, this begins at a considerably higher value of 200mJcm^{-2}. The SEM photograph in Fig. 4.9(a) indicates that the lens surface is only weakly ablated at 135 mJcm^{-2} without any deep incision being

produced and superficial fibrous material is evident. However, at higher fluences (eg. 830mJcm^{-2} Fig. 4.9b) a very smooth and clean crater was produced. Fig. 4.9c shows a part of tissue after being ablated in saline at 220mJcm^{-2} (300 pulses). Details of the results are summarised in table 4.2.

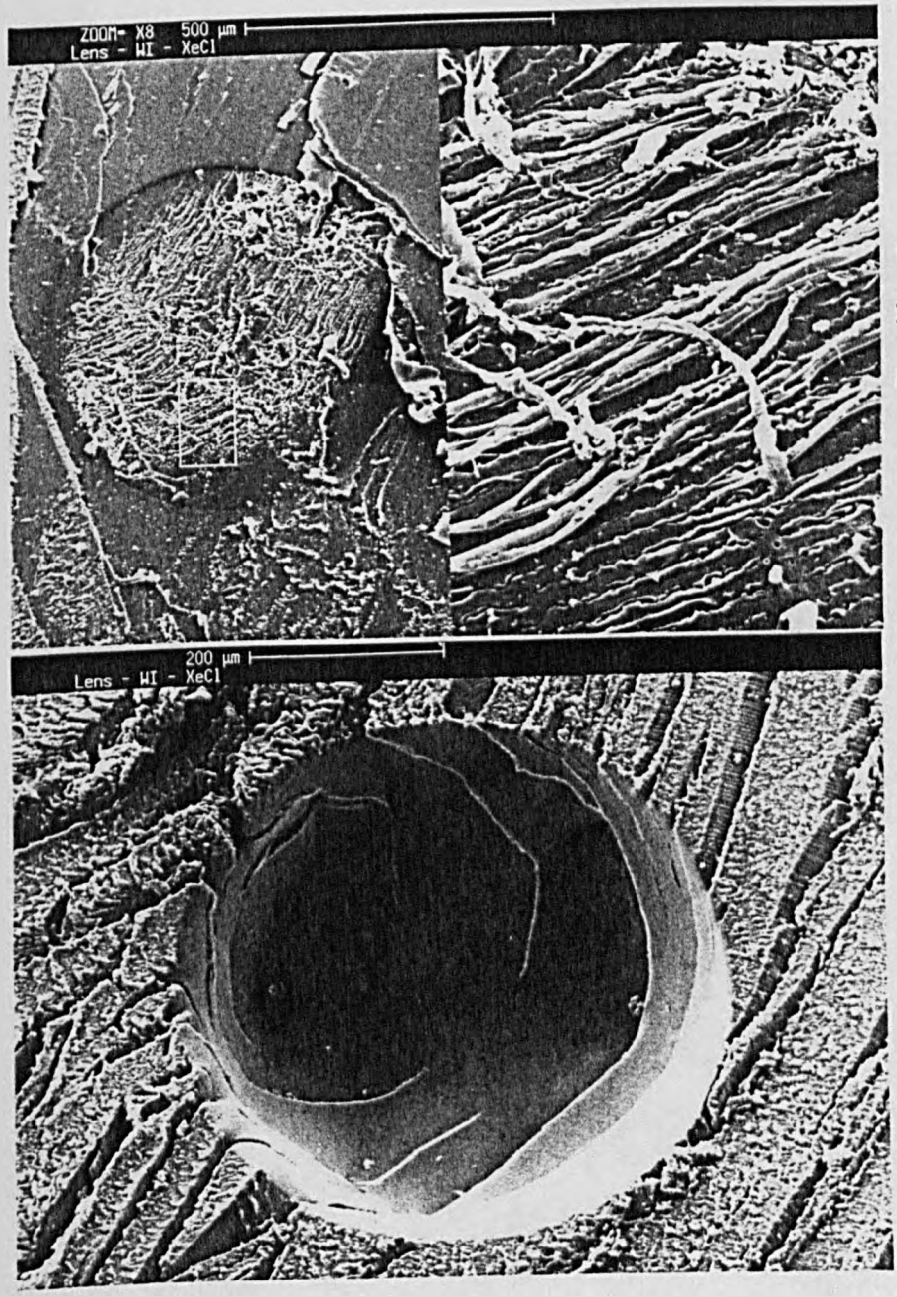

(a)

$F \sim 135\ mJcm^{-2}$

84 pulses

(b)

$F \sim 830\ mJcm^{-2}$

90 pulses

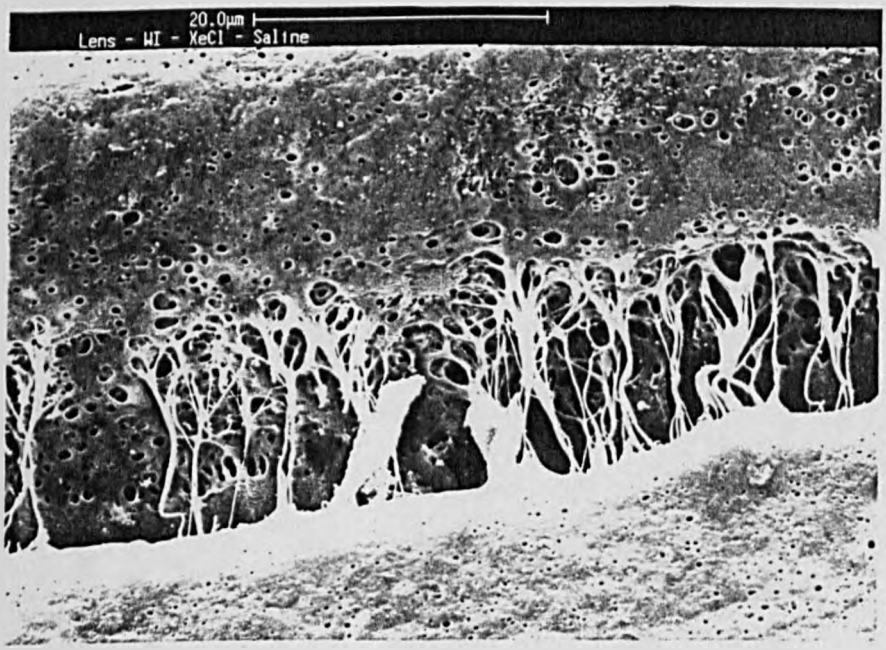

(c)

F≃ 220 mJcm^{-2}

300 pulses

Fig. 4.9 - XeCl laser ablation of lens tissue with fibre in air (a,b) and saline (c)

The ablation of lens tissue with the KrF laser in air and saline (Fig. 4.10) using the fibre, produced submicron etch rates which are much smaller than those attained with the XeCl laser (Fig. 4.8) at similar fluences.

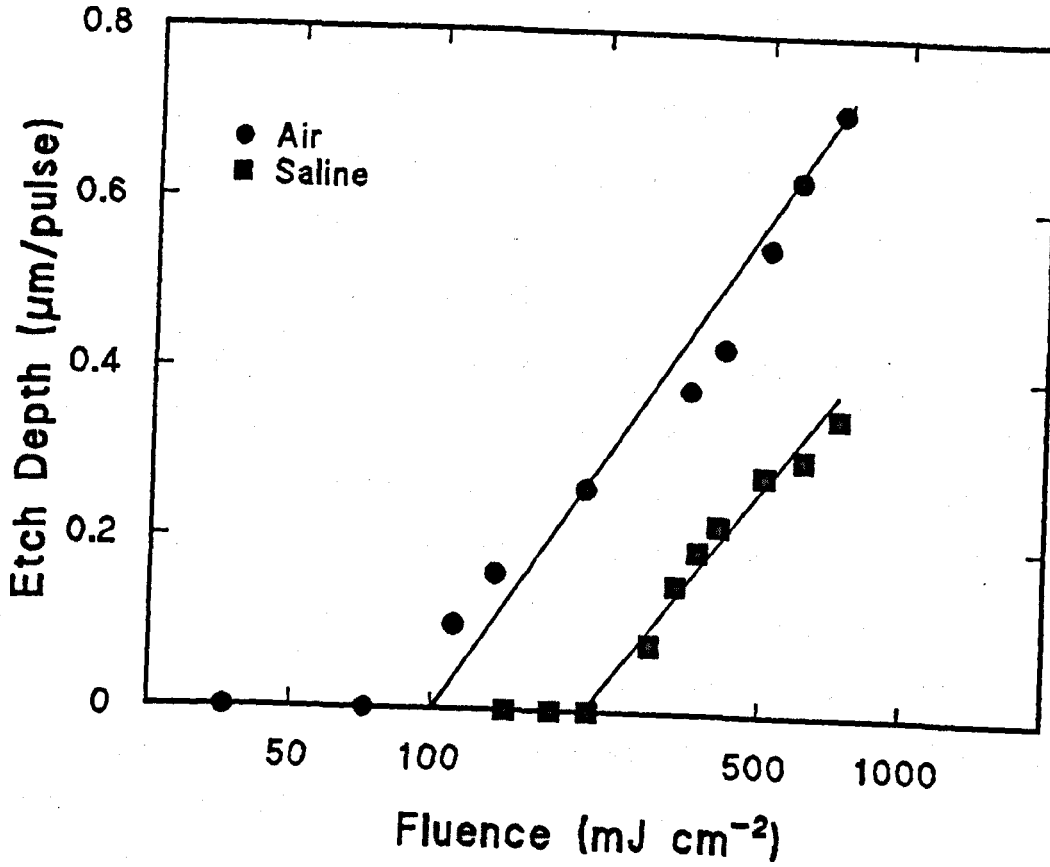

Fig. 4.10 - Ablation of lens tissue with fibre using KrF laser.

This is mainly because of the higher absorption coefficient for the KrF laser which implies lower etching rate due to lower transmission (eq. 4.1A). Again saline apparently has the effect of raising the ablation threshold, although the effective absorption coefficient derived from the slope of the data remain approximately the same ($\sim 3 \times 10^{4}$ cm^{-1}.) A strong smell from the tissue was noted during the laser-tissue interaction above 70 $mJcm^{-2}$. At approximately 400$mJcm^{-2}$ a luminescent plume was formed whose size gradually became larger in the direction of the target normal with fluence,

reaching an estimated size of about $\simeq$ 0.5 cm in the region of 1000mJcm^{-2}. A strong blue laser-induced fluorescence was also evident from the tissue.

Fig. 4.11 shows SEM photographs of the ablation site from which it is evident that ablation produces a relatively smooth but undulating surface in the cortex and nucleus with some vacuoles in the latter. In both cases the lens surface had some cracks which are artefacts related to the handling and processing steps for the SEM.

Removal rate experiments were also carried out with the ArF (193nm) laser in air and saline and both with and without the fibre. No results could be obtained for ablation in saline probably because of strong saline absorption at this wavelength and possibly insufficient number of delivered pulses. A threshold fluence for ablation of lens tissue in air (Fig.4.12) was estimated about 34mJcm^{-2} with an effective absorption coefficient of 5x10^{4} cm^{-1}.

The fibre output fluence was measured by recording the fibre initial output energy after one pulse and the final output energy after a certain number of laser pulses. The final reading is then given by their average value. However, it must be noted that the fluence difference between without and with fibre can never be avoided since fibre multishot damage during the experiment is inevitable, and that the fibre can not be removed during the experiment for polishing purpose unless between two consecutive fluences.

An attempt to compensate the output energy loss by increasing the input energy must be avoided because the fibre degradation and hence transmission loss increases with

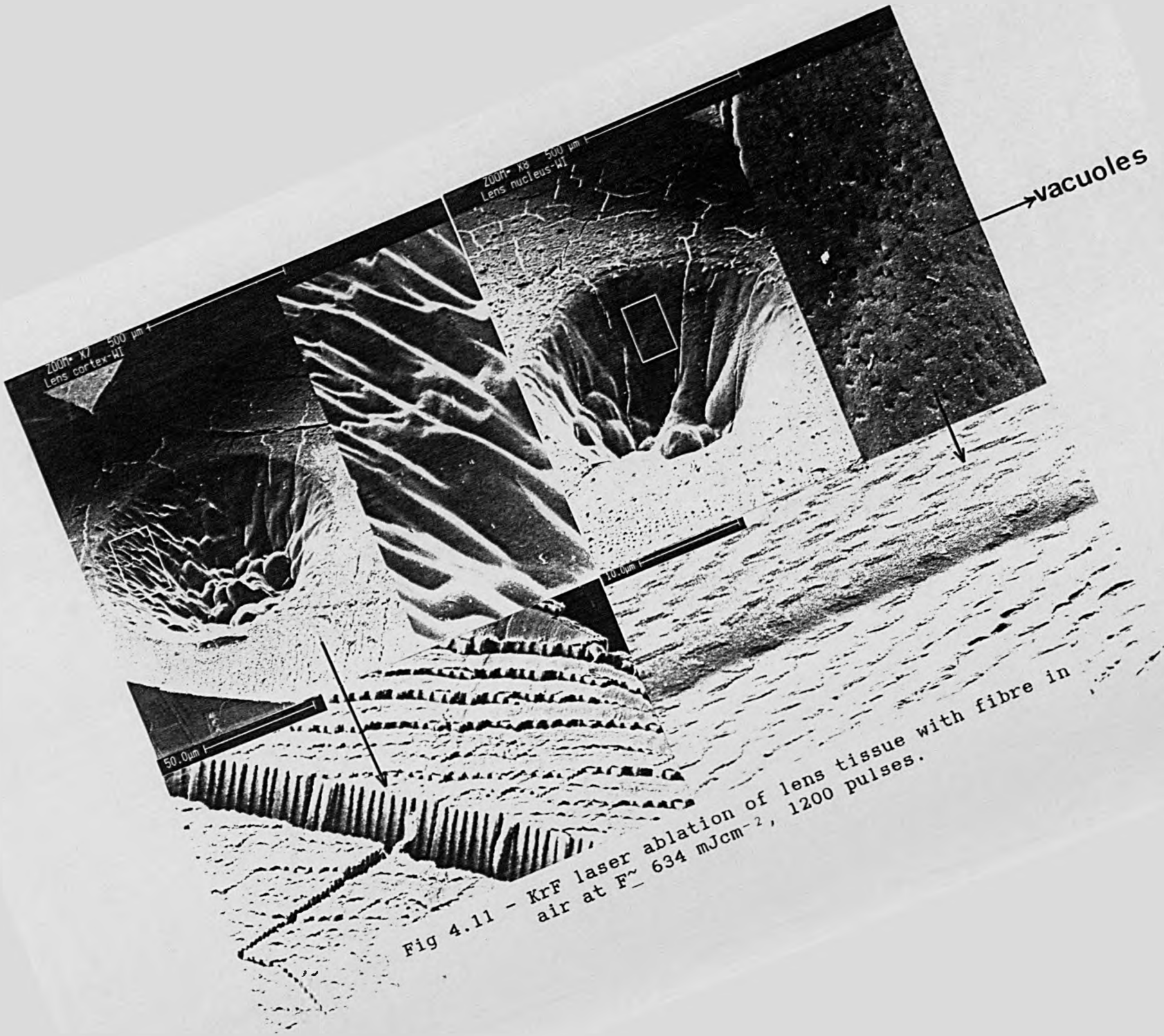

Fig 4.11 - KrF laser ablation of lens tissue with fibre in air at F~ 634 mJcm^{-2}, 1200 pulses.

increasing input fluence. Indeed as the experiment continued the red fluorescence of both ends of the fibre became stronger with fluence as well as with irradiation time. It is essentially the colour-centre damage which decreases the transmission capability of the fibre. Fig. 4.13 shows an example of broken fibre input surface after being irradiated with many laser pulses at different fluences (Fig. 4.13a) and an example of lens tissue ablated by fibre delivered ArF laser (Fig. 4.13b).

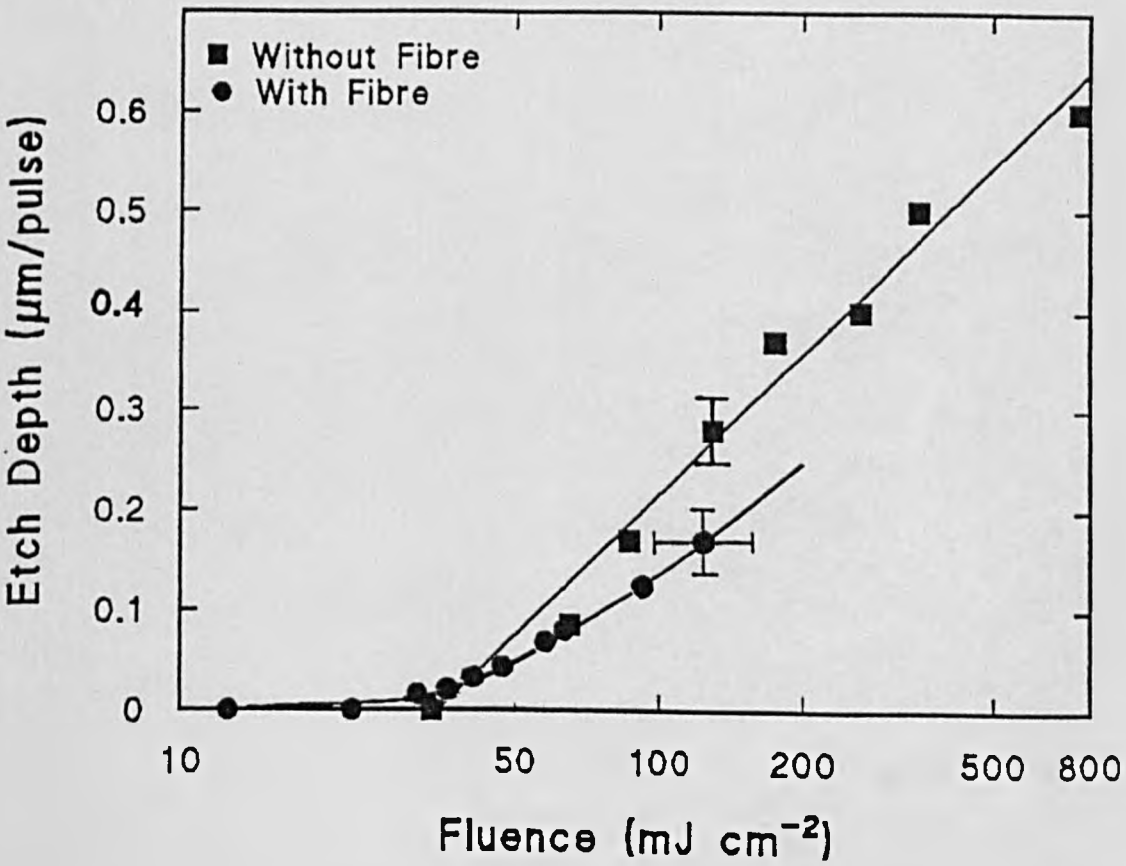

Fig. 4.12 - Ablation of lens tissue in air with (●) and without (■) fibre using ArF laser.

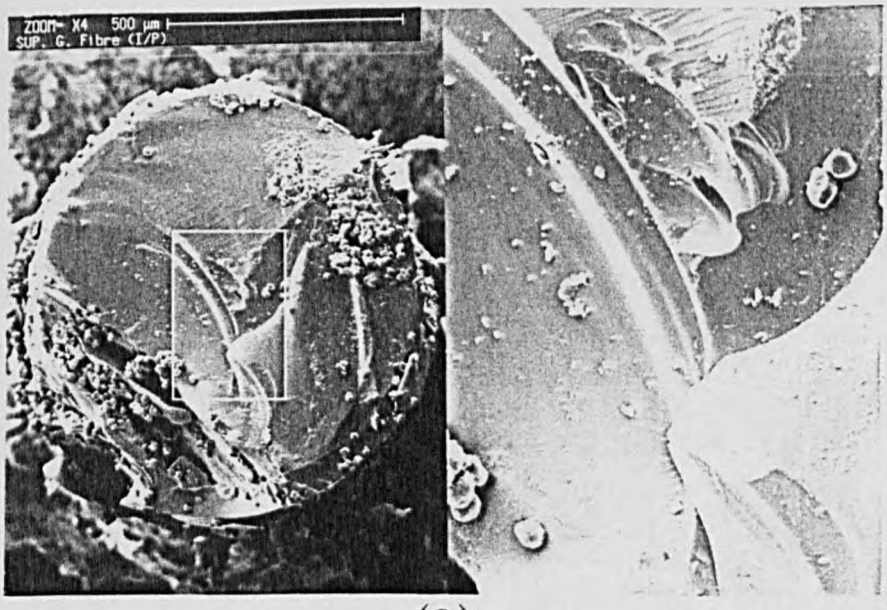

(a)

(b)

Fig. 4.13 - (a) An example of input surface damage of 600µm superguide-G fibre by ArF laser at various fluences, (b) - Ablation of lens tissue with fibre at $F_o \tilde{=}$ 150 mJcm^{-2} after 800 pulses.

4.3.2 - Photoacoustic studies: Theory

Photoacoustic refers to the generation of acoustic waves by modulated optical radiation. It finds important applications in areas such as spectroscopy, monitoring of deexcitation processes, and probing the thermoelastic as well as other physical properties of materials (eg. acoustic velocity, elasticity, temperature, specific heat and thermal diffusivity).

The generation of sound by the absorption of laser radiation in transparent and absorbing liquids was first proposed by Askaryan (9) using a 1μs pulse width ruby laser. An acoustic wave can be generated by three main mechanisms. First, if the absorbed laser energy during the interaction is smaller than the boiling threshold of the liquid no evaporation takes place, but there may still be a large acoustic wave generated in the medium by the thermoelastic effect. The observed generation of high-frequency acoustic waves shows that the thermoelastic effect is a very fast process (10), such that the reaction force from the surrounding medium against this rapid expansion may be very large due to inertia of the medium.

Under this large reaction force, the medium may be extensible and compressible. In association with this extension-compression action, an acoustic wave is produced. According to Carome et al (11) when the laser pulse is absorbed in the liquid the temperature of the absorbing layer increases within its duration and the temperature rise should fall off exponentially with increasing depth. The gradients of the resulting thermal stress would then act as a source of

acoustic waves. The stress transient consists of a compression pulse (positive component) followed by a rarefaction pulse (negative component). In the range where the absorbed laser fluence is near the vapourization threshold then both thermoelastic and vapourization may be present simultaneously (10).

A second source of acoustic waves arises if the absorbed energy is well above the vapourization threshold; the associated stress transient then becomes purely compressive which reflects the onset of the vapourization process. The third mechanism for producing an acoustic wave is by the electrostriction effect which is important only for transparent media and for laser intensities with electric field strengths of about 10^7 Vcm^{-1}. This high electric field may generate a significant stress wave in the medium by means of electrostriction coupling if the electrostriction coefficients are high.

Theoretical models for the thermoelastic generation of acoustic waves are readily available (10-15) but only Hu (13) and Sigrist (15) described a three-dimensional analytical model for spherical geometry. Their model predict a symmetric pressure signal with respect to the time axis, peak amplitudes proportional to the laser power and inversely proportional to the radius, r, of the acoustic wave.

Similarly, studies with non-biological (16-20) and biological (21-23) materials have shown that the laser can produce acoustic waves in the material by two distinct mechanisms: Thermal expansion at low laser fluence (thermoelastic effect), and by vapourizing surface material at high

laser fluence (ablation effect). Further theoretical and experimental considerations can be obtained from references (24-26). For biological tissues which can be strong absorbers, depending on the wavelength, the main source of acoustic waves at relatively low fluences where vapourization of tissue is negligible is due to thermoelastic effect. This according to White (12) is caused by thermal expansion due to rapid heating and hence rise in temperature of the medium which is unable to quickly adjust itself to the new thermal equilibrium condition. The magnitude of force produced by the absorption of radiant energy of laser pulses depends on the absorbed energy density and the pulse duration.

The form and magnitude of acoustic waves generated as a result of rapid heating of tissue in the sub-threshold regime and by ablation can provide useful information on the tissue attenuation coefficients, ablation thresholds and ablation time scales. The magnitude of these acoustic waves is particularly important as they can penetrate deeper in tissues than the laser photons or thermal waves and possible tissue damage due to acoustic stress can extend to large distances from the irradiation site. For example shocks associated with intense stress wave can result in mechanical rupturing of tissue well beyond the range of energy deposion. Acoustic signatures may also hold promise for 'in vivo' monitoring of the ablation process allowing, for example, differentiation between healthy and atheroma arterial tissue in laser angioplasty procedures.

Experimental arrangement

The photoacoustic response of lens tissue exposed to excimer laser pulses was studied in both air and saline using the set up shown in Fig. 4.14. The main part of this is a 9μm thick polyvinylidene fluoride (PVDF) piezoelectric film (Metal Box-UK) which was cut to dimensions of 10x20mm^2. Each side of PVDF was bonded to a pair of thin copper contacts using silver loaded epoxy adhesive (RS. 567-604). This was then bonded onto a 4mm thick perspex impedance matching stub using cyanoacrylate adhesive (RS. 567-159). The perspex stub minimized acoustic reflection at the rear film interface, giving a response time of $x/V_a \simeq 4$ns where x (=9μm) is the thickness of transducer and V_a (=2250ms^{-1}) is the longitudinal acoustic velocity in PVDF.

A 50Ω resistor was connected to the detector output to absorb reflected pulses from the high impedance termination of the 300mm coaxial cable connecting the transducer to the 7A16A plug-in in a Tektronix 7834 oscilloscope. The whole device was then placed inside a metal can to provide noise shielding. When amplified using a high impedance oscilloscope plug-in (1 MΩ), the transducer output voltage gives a direct measurement of the time-resolved normal force at the transducer according to.

$$F(t) = \frac{(C_t+C_L)V(t)}{d_t} \qquad 4.2$$

where C_t and C_L are transducer capacitance ($\simeq$2.7nF) and load capacitance ($<<C_t$) respectively, d_t is the thickness-mode strain constant (20 pCN^{-1}) for PVDF, and V(t) the time-dependent voltage. If, for a thin tissue section, the

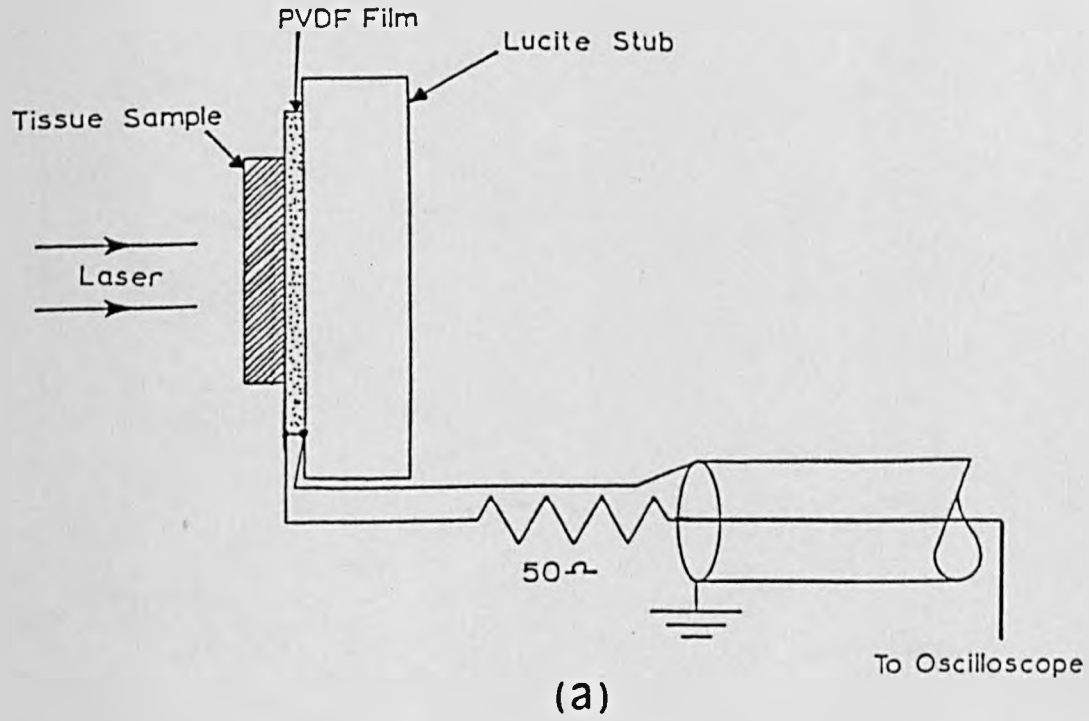

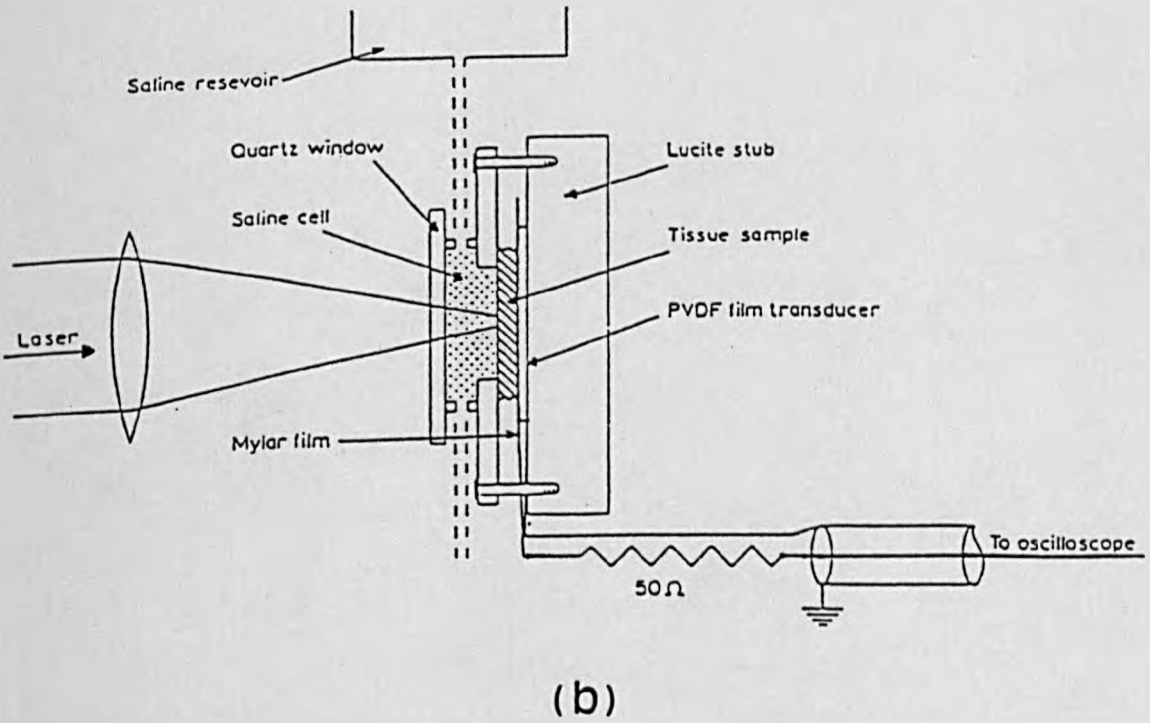

Fig. 4.14 - Experimental set up for photoacoustic studies of lens tissue with KrF laser in (a) air and (b) saline

acoustic stress wave is assumed to propagate as a plane wave between the surface and transducer, the stress can be found using

$$\sigma = \frac{F(t)}{A} \qquad 4.3$$

where A is the laser-irradiated area. When the tissue was placed in saline, Fig. 4.14b, a 19μm thick mylar film was bonded to the front of transducer to prevent its contact with saline.

For these experiments bovine eye lenses were cut from their equators into slices of about 500μm thick. The saline solution was prepared by using distilled water and salt (1 lit: 9g) and was introduced into the cell by means of an inlet pipe connected to a reservoir (Fig. 4.14b). It was important to maintain a slow flow of saline solution through the cell in order to flush out dissolved or suspended ablation products. In the absence of flow the ablated products may attenuate the beam, hence decreasing the laser fluence at the tissue surface and possibly giving irreproducible results.

The KrF laser output beam was passed through a 6mm diameter aperture to select a region of uniform fluence. A quartz lens of 50mm focal length was used to produce a spot size of approximately 800μm diameter which corresponds to an irradiated area of 5×10^{-3} cm². This area was assumed to be small enough so that any variations in tissue thickness over the irradiation zone can be ignored. To assume that a plane acoustic wave propagates between the tissue surface and transducer, the following equation should be satisfied.

$$Z < Z_R = \frac{\phi^2}{4\lambda_{ac}} \qquad 4.4$$

where Z and Z_R are the propagation distance and near field range respectively, Φ is the beam diameter (800μm) and λ_{ac} the characteristic acoustic wavelength which is given by

$$\lambda_{ac} \simeq 2l \simeq 2c\Delta t \qquad 4.5$$

where l is the beam penetration depth, c is the acoustic velocity in tissue (~1600 ms^{-1}) and Δt (~50ns) the width of pressure pulse (Fig. 4.15). Thus, a value of Z_R = 1.1mm can be found for both in air and saline which is almost twice the thickness of tissue (ie. ~500μm).

Results

Results for the peak stress generated in lens tissue irradiated in air and saline using the KrF laser are shown in Fig. 4.16a. For fluences between 0.05 and 0.7Jcm^{-2} the stress varies approximately linearly with the logarithm of fluence and similar results are obtained for both air and saline environments. A peak stress of 9MPa was recorded when the tissue was ablated in air at fluence of ~2.3Jcm^{-2} and similarly a value of just below 6MPa was evaluated for tissue ablation in saline at ~1Jcm^{-2}. The higher values of stress signals produced in saline than in air at a given fluence is primarily due to acoustic waves generated by the rapid thermal expansion of surrounding liquid and possibly pressure exerted by microbubbles against the surface of the tissue.

The experimental acoustic waveforms were used to determine the attenuation coefficient, α, of the sample by

plotting the logarithm of the amplitude versus time (Fig. 4.16b) for the early stages of the compressive curve in the subablation regime (11) (Appendix I).

From the slope of the line in Fig. 4.16b given by:

$$\tau_R = \frac{T_2 - T_1}{\ln A_2 - \ln A_1} \qquad 4.6$$

a characteristic time constant $\tau_R \simeq 11ns$ is found which can be related to using (23):

$$\tau_R = \frac{1}{\alpha V_a} \qquad 4.7$$

where $V_a \simeq 1600ms^{-1}$ is the acoustic velocity in the tissue. For ablation in air this yields $\alpha \simeq (550\pm50)cm^{-1}$ for lens tissue at the KrF laser wavelength, indicating that this is a relatively weakly absorbing material even at this wavelength. A similar procedure for irradiation in saline gave $\alpha \simeq (370\pm20)cm^{-1}$.

It was observed that in the thermoelastic regime the stress signal was increased with the laser irradiance and hence fluence. However, with the inception of ablation the signal increased more rapidly which probably is due to recoil momentum transferred to the surface by the ablation products. The transition from thermoelastic region to ablative was accompanied by a change in the shape of the acoustic signal (Fig. 4.15) ie, the signal became purely compressive once the fluence exceeded $700mJcm^{-2}$.

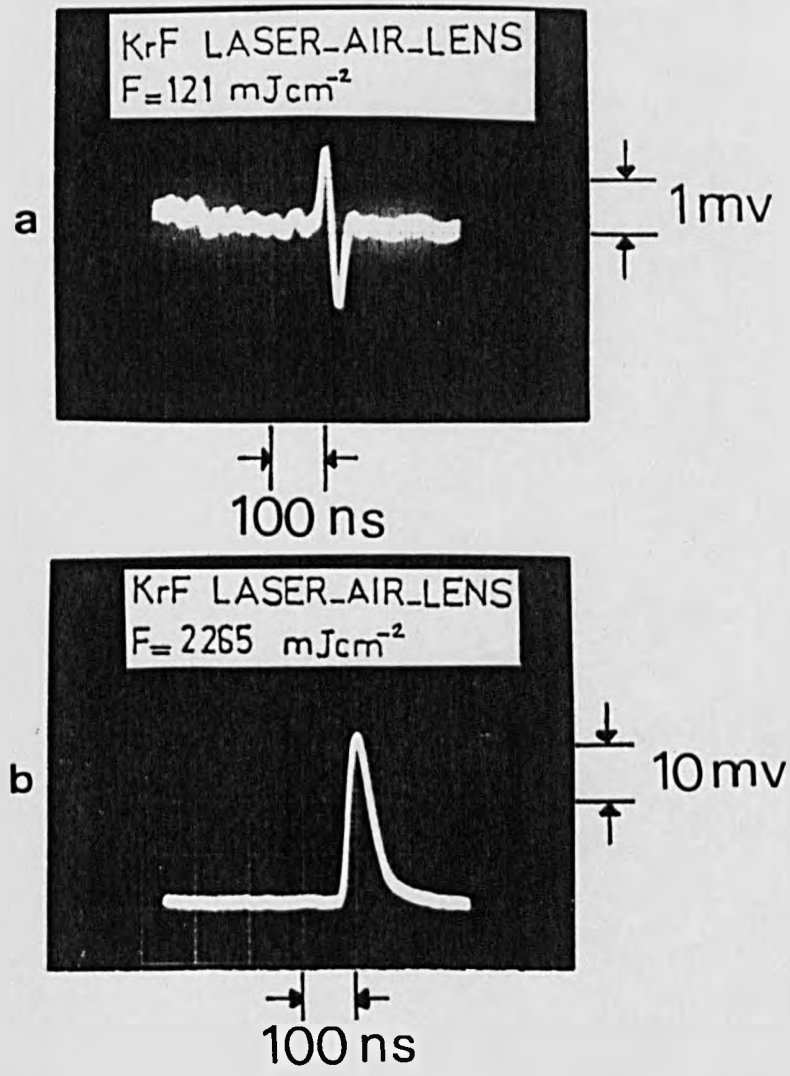

Fig. 4.15 - KrF laser generated thermoelastic and ablative stress waveforms for lens tissue in air (a,b) and saline (c,d).

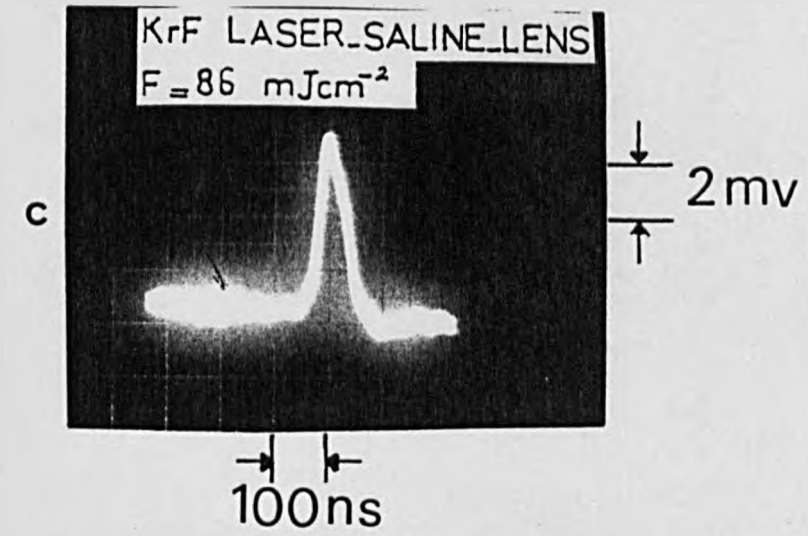
KrF LASER-SALINE-LENS
F = 86 mJcm⁻²
c
2mv
100ns

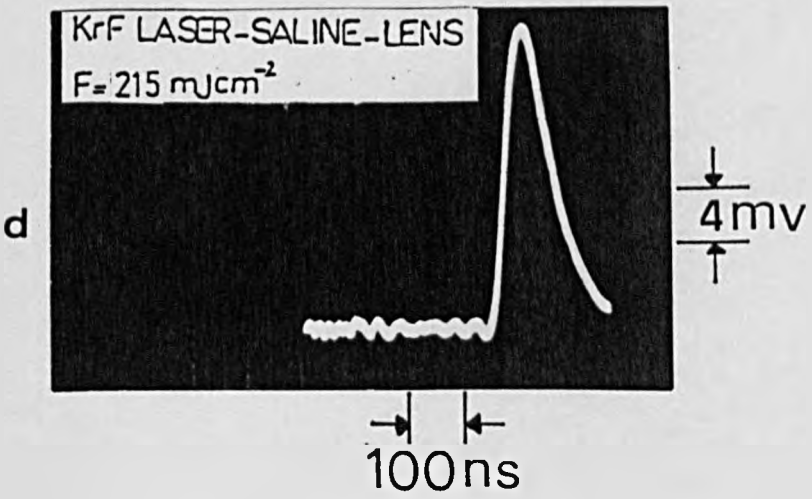
KrF LASER-SALINE-LENS
F = 215 mJcm⁻²
d
4mv
100ns

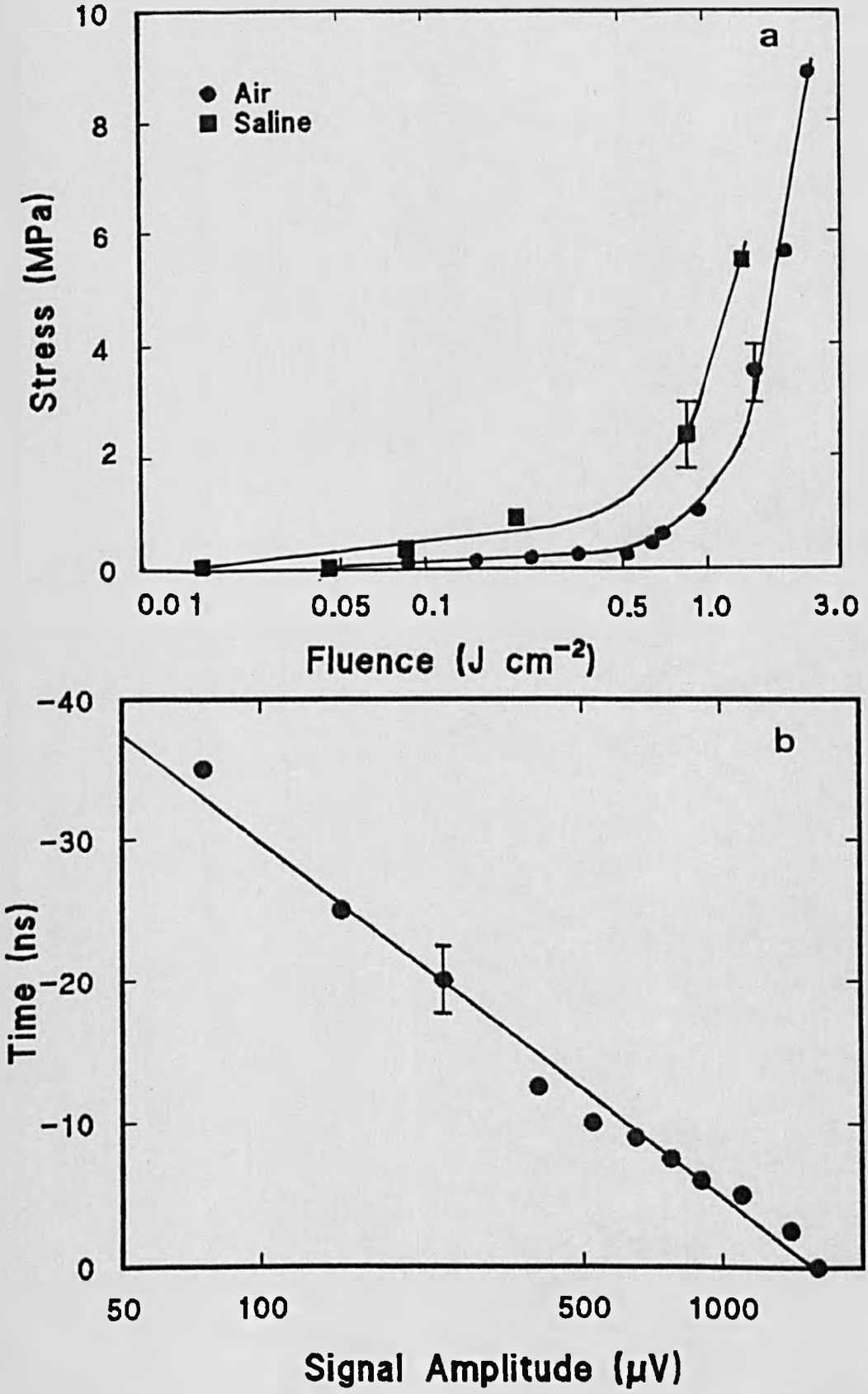

Fig. 4.16 - (a) stress amplitude Vs fluence for lens tissue, (b) logarithmm of the amplitude of rising portion of stress waveform Vs time in air using 248nm laser.

λ(nm)		Air			Saline				
		$F_{th}(mJcm^{-2})$		$\alpha_e(cm^{-1})(10^4)$	$F_{th}(mJcm^{-2})$		$\alpha_e(cm^{-1})(10^4)$		
308	Removal rate	32		2	WO	100	l_F	5	
							h_F	3	
					Wi	100	3		
248	Removal rate	100		2.8	220		3.4		
	Photoacoustic	$V_a(ms^{-1})$	$\tau_R(ns)$	$\alpha(cm^{-1})$	$V_a(ms^{-1})$	$\tau_R(ns)$	$\alpha(cm^{-1})$		
		1600	11	545	1600	17	367		
193	Removal rate	Wi	23	5.5					
		WO	34	5					

Table 4.2 - Experimental results of lens tissue ablation with excimer lasers

4.3.3 - Fluorescence spectroscopy

The experimental arrangement used to study the fluorescence emission from tissue below and above the ablation threshold in a darkened room is shown in Fig. 4.17. Bovine lens tissue was irradiated by either the 248nm or 193nm laser operating at 4Hz with and without the fibre in air. The emission was imaged onto a UV-visible monochromator (Bentham, U.K) with a slit width set at 300μm using a 50mm focal length fused silica lens which was oriented at approximately at 45° to the tissue surface. The monochromator was equipped with a 1200 lines/mm holographic diffraction grating and an EMI 9813QB photomultiplier detector (operating voltage $\leq$ 1.8KV) with a bi-alkali photo-cathode (EMI, U.K). The detector was powered by a Brandenburg (model 475R) power supply. The photo multiplier current pulse was passed through an integrating amplifier in order to achieve time integrated spectra. The output voltage was displayed on a CR 600 chart recorder (JJ instrument) and the monochromator scanned using a stepper motor drive (Bentham - SMD 3D) from 190 - 150nm for the KrF laser and from 170-400nm for the ArF laser. The circumference of lens tissue and slit was covered by black cardboard so that radiation scattered and reflected from the optics were not imaged onto monochromator.

Results

Figs. 4.18(a,b) show the fluorescence spectra obtained from the lens tissue using the 248nm laser at low (125mJcm^{-2}) and high (1850mJcm^{-2}) fluence with peaks of 280-285nm. There is also, a very broad continuum band between 320-480nm.

The fluorescence spectra of lens tissue using the 193nm laser (Fig. 4.19) was quite different to the results obtained with the 248nm KrF laser. When the tissue was irradiated at 10 and 310mJcm^{-2} two distinct peaks were observed at 216 $\pm$ 2nm and 250 $\pm$ 2nm respectively. In a separate experiment (not shown) the 193nm laser was used without the fibre to irradiate commercially available serium albumin which mainly contains proteins. The solution was prepared by using 0.1mg of serium albumin crystals mixed with 100mg diluted Nacl (1:10) according to instruction provided by the manufacturer. A cell with UV-grade quartz window was then filled with the solution and irradiated with the ArF laser at 300mJcm^{-2} and 1Hz. Two peaks in the spectrum appeared at 258nm and 310nm respectively.

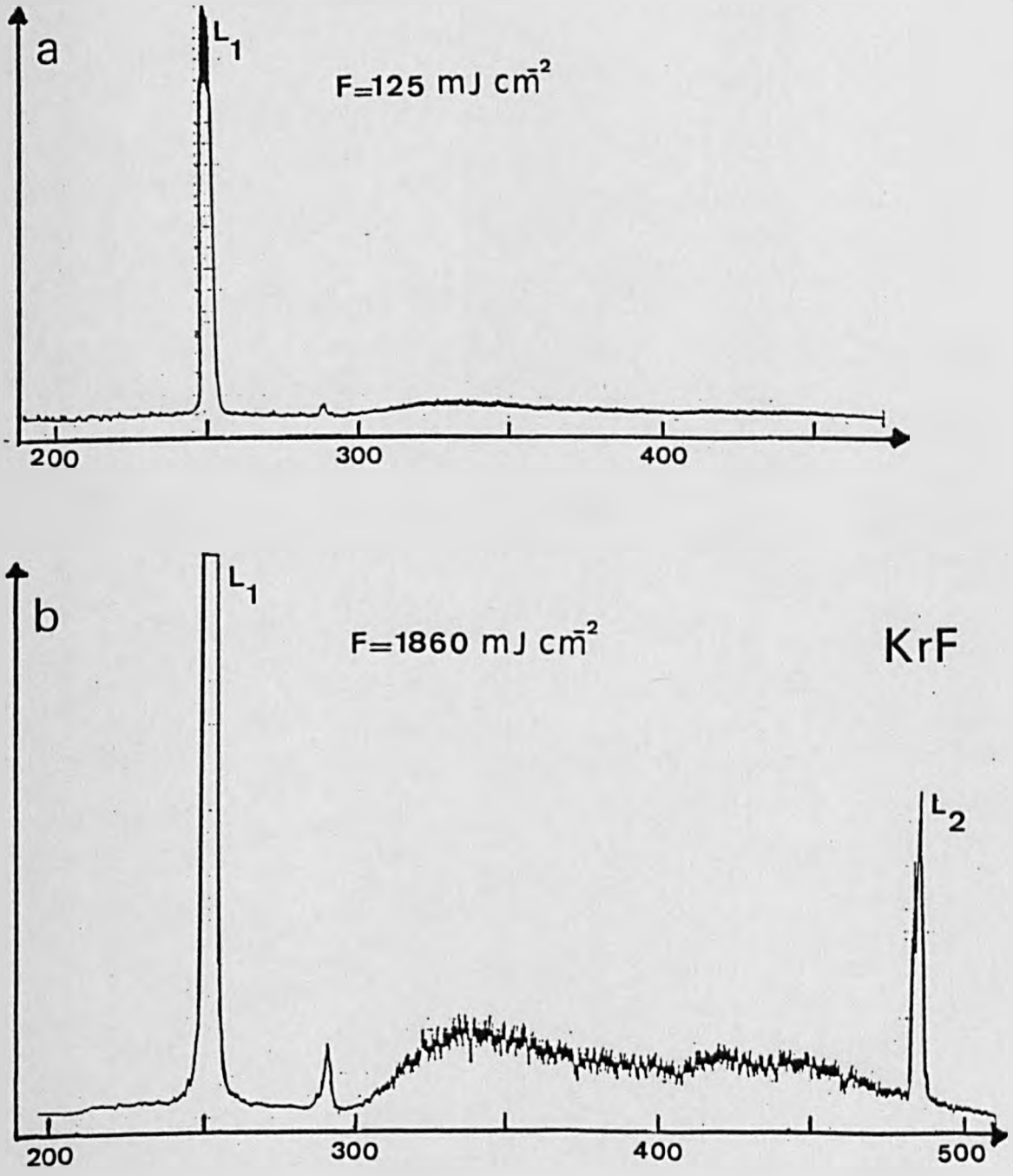

Fig. 4.18 - Fluorescence spectra of lens tissue using 248nm laser at (a) 125 and (b) 1860mJcm^{-2} respectively. L_1 and L_2 are the Laser first and second order lines.

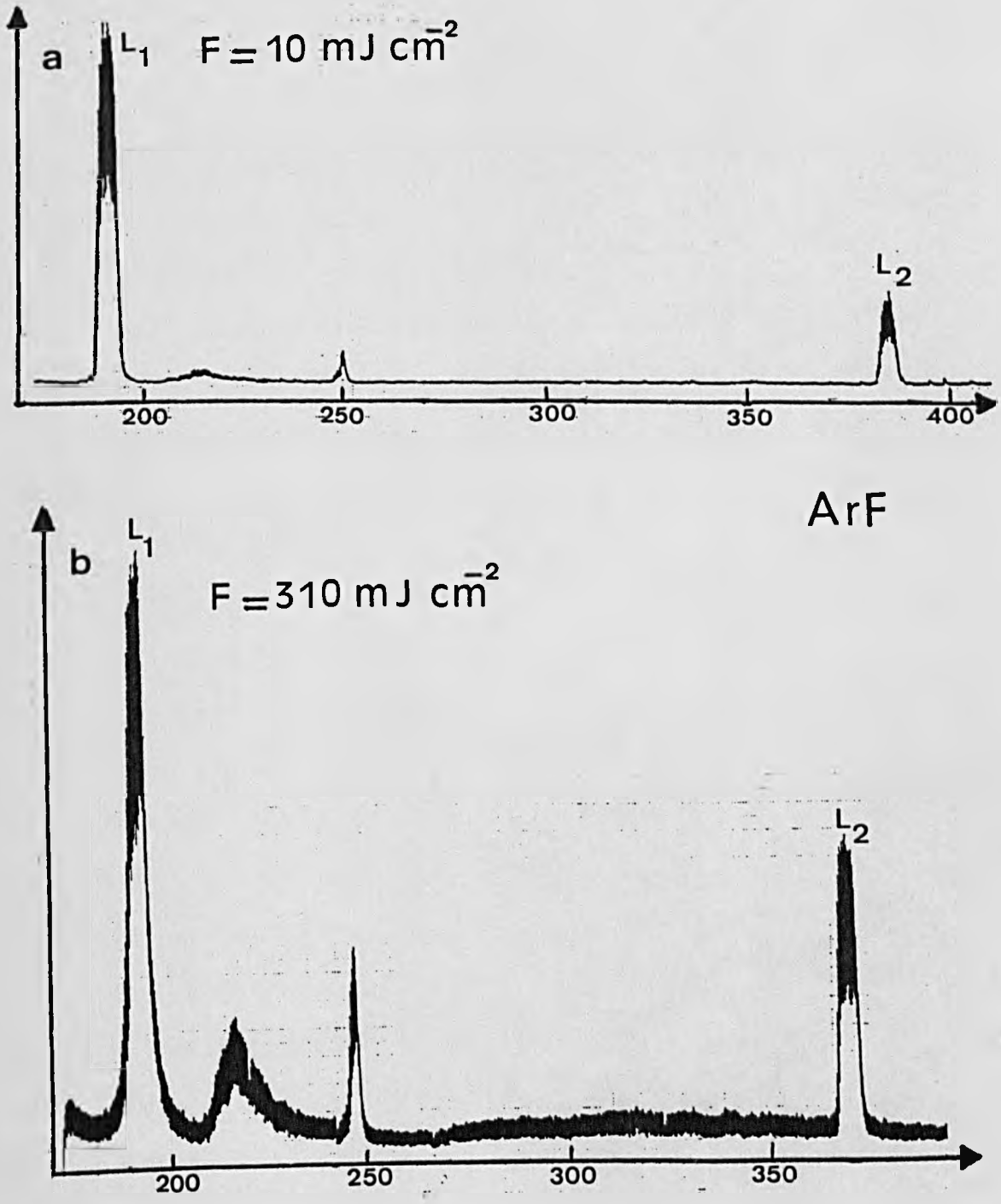

Fig. 4.19 - Fluorescence spectra of lens tissue using 193nm laser (a) below and (b) above ablation threshold respectively.

Discussion

In the past few years a number of reports have dealt in detail with pulsed excimer laser ablation of polymers and biological tissue (1-6 and 89-95 in chapter 2). The purpose of this chapter was to study and demonstrate the capability of UV optical fibres for delivering excimer lasers for such applications. A summary of the results for polymers and lens tissue are given in tables 4.1 and 4.2 respectively and there are number of points worthy of note.

For example, using equations 4.1A and 4.1B to study the variation of the ablation rate at low and high fluences, values of the effective absorption coefficient can be obtained as given in table 4.1. Dyer and Srinivasan(22) have shown that the ablation of polymers actually starts within several nanoseconds of the start of the laser pulse which means the rest of pulse energy can enhance the heating effect. In fact, Dyer et al (27) used a small thermocouple to measure the temperature rise of PET and polyimide at 193nm, 248nm, and 308nm, and Gorodetsky (28) used a pyro-electric crystal for the same purpose. Both groups concluded that below or near the threshold fluence almost all the laser energy is converted to thermal energy and that at higher fluences the temperature increase was small. Most of the excess energy ($F-F_{th}$), was believed to be carried away as kinetic energy of the ablation products. In 1982, Srinivasan et al (1) used the term photodecomposition to describe the ablation of polymers by high power UV radiation where the photochemical process directly leads to the photodissociation of the polymer molecules in to all sizes of fragments.

Ablation is the result of repulsion between fragments which carries the energy remaining after bond breaking.

When a polymer molecule is replaced by a number of such fragments of much lower molecular weight, the products may occupy a much larger specific volume under the same pressure-temperature conditions. In 1983 Andrew et al(96 - Chapter 2) and Brannon et al (29) suggested that the ablation process can be considered as a result of ultrafast thermal events. In this case, the initial electronic excitation caused by absorption of the ultraviolet radiation is converted to ground state vibrational energy by rapid relaxation, and thermal decomposition of the polymer occurs.

Excimer laser-tissue interaction can also be studied in a similar manner except that in the UV region, the principal coupling of the laser wavelength is to chromophores in the structural proteins. Basically proteins form a major constituent of most cells and tissues. Each protein is composed of amino acids linked by 'peptide bonds' which are also called amide bonds. A chain of many amino acids linked by such bonds forms a polypeptide chain and an individual amino acid in such a peptide chain is called a 'residue'. The occurence of differing electrical charges on a protein molecule are brought about by ionization phenomena which are in fact properties of the amino acid residues of the proteins concerned.

In simple terms, the ability of a target to absorb radiation energy is expressed by Beer's law. $I=Ie^{-\gamma x}$ where $\gamma=\alpha+\beta$, is the attenuation coefficient, and α and β are the absorption and scattering coefficients respectively. The

latter is given by $\beta = (\frac{\alpha V}{D})^{1/2}$ where V and D are the speed of light in the tissue and diffusion coefficient for photons in the tissue respectively. The etch rate of material is given by equation (4.1A) where at low fluences the etch rate varies with logarithm of fluence according to Beer's law and the plume retains the same absorption coefficient as the condensed phase so that $\alpha = \alpha_p$, where α_p is the plume absorption coefficient. However, for the limiting case of a transparent plume ($\alpha_p \rightarrow o$), equation 4.1B shows that etch depth per pulse is linearly dependent on fluence. The transition to a transparent plume is probably due to strong heating of the ablation products produced in the early stages of the laser pulse at high fluence and their degradation to low mass, relatively transparent, species.

In order to study the feasibility of using excimer lasers to ablate lens tissue in air and saline with and without using fibre, a number of experiments were carried out using 308nm, 248nm and 193nm lasers. Some experiments regarding the lens tissue ablation with 308nm have been reported (30-35) but none at 248nm and 193nm using optical fibre delivery. Despite the fibre delivery capability of 308nm radiation with good operating fibre lifetime compared with other wavelengths, it is a very hazardous radiation since it deeply penetrates tissue, lies within the very narrow UV-B wavelength band and has a relatively high degree of scattering inside the eye.

It was shown in the present experiments that 248nm radiation can also be transmitted through a fibre in air and saline to ablate the lens tissue provided the input fluence

is $\leq 2 Jcm^{-2}$ to avoid fibre damage. However, its clinical usefulness seems very doubtful due to mutagenic effects.

193nm radiation provides energetic photons and is strongly absorbed by protein and, with its low absorption depth, it can produce very smooth photoablation. However, it is also strongly absorbed by physiological saline which is clearly a disadvantage in terms of 'in vivo' delivery. The use of the ArF laser is further limited by the lack of suitable optical delivery system for tissue ablation. In the present experiment it was shown that at an output fluence of $(50-60) mJcm^{-2}$ 700 pulses were transmitted to produce a crater of 14μm which corresponds to 0.02μm/pulse (Fig. 4.12).

As far as the cytotoxicity of this radiation is concerned recent results indicate that 193nm radiation is not mutagenic in a mammalian cell mutagenesis assay (36). At least two reasons could explain the lower cytotoxicity of this radiation. First, the number of 193nm photons reaching the nuclear DNA may not be sufficient to cause cytotoxicity because the radiation is absorbed by proteins of the cell membranes and cytoplasm. Therefore, the protein shields the nucleus from the damaging effects of 193nm radiation. Secondly, the photons of this wavelength reaching the nuclear DNA induce DNA photo products that are either not cytotoxic or are rapidly repaired by the cells (37).

Another aspect of the present work was a determination of the effective absorption coefficient of lens tissue from etch rate and acoustic measurement. When the tissue was immersed in saline (Figs. 4.8, 4.10), fluence thresholds were moved to a higher value and it required more pulses to ablate

the material than in air. This is likely due to the impedance to expansion presented by the liquid environment. The SEM photograph in Fig. 4.9a shows the heating effect of 308nm laser at low fluence on the lens fibres. As the fluence increased the quality of etching improved (Fig. 6).
At 248nm there were vacuoles and non-uniformities in the crater wall whereas a smooth, well defined crater was produced by fibre-delivered ArF laser.

Photoacoustic techniques can be useful in providing some information regarding the material attenuation coefficients, ablation thresholds and ablation time scales. The technique has already extensively been used in industry (38,39), spectroscopy (40, 41) and biomedicine (21, 23, 25, 42-46). In general, below a threshold fluence thermoelastic stress occurs due to the absorption of laser energy and heating in the absence of any change in state of the irradiated medium. Thus, thermal expansion due to rapid heating and consequent rise in temperature results in the generation of an acoustic waveform. For a free surface the final waveform consists of a compression followed by rarefaction propagating at the sound speed (Fig. 4.15a).

The absence of a bipolar signal below threshold in saline (Fig. 4.15c) is due to impedance matching at the boundary and a significant lengthening of the ablative stress at high fluence. The experimental acoustic waveforms were used to determine the attenuation coefficient of the sample by plotting the logarithm of the amplitude versus time for the early stages of the compressive curve (Fig. 4.16b). For a flat, parallel and homogenous tissue sample the maximum

attenuation coefficient that can be measured by the acoustic technique is set by the response time of the detection system.

Fluorescence emission of lens tissue irradiated by the KrF laser (Figs. 4.18a,b) shows a peak arising at about 280-285nm at 125 and 1860mJcm^{-2}. At 1860mJcm^{-2}, however, the amplitude of the peak increased and a broad spectrum appeared covering a range between 300-480nm(b). This change could be due to plasma formation which gives rise to luminous ablation products. The fluorescence emission of lens with the ArF laser at well below and above ablation threshold (Figs. 4.19a,b) exhibited two distinct peak at 215-218nm and 240-250nm with higher amplitude.

The absorption of protein in the wavelength range of 240-310nm is determined by the amino acid residues particularly tryptophan and tyrosine both of which show absorption in the 280nm region. At 248nm, possible chromophores are nucleic acid which in the cornea absorb well between 230-290nm due to the 260nm absorption peak of the purines and pyrimidines (47). At 190nm DNA is the main absorber and ArF laser radiation produces single-strand breaks in aqueous solution of isolated DNA at 50mJcm^{-2} (48-50). The peak at 240-250nm in these experiments mentioned above was also observed by Tuft et al (51) and was thought to be due to small level of occasional fluctuation and noise in the detection system.

It is not wished to suggest that all UV laser wavelengths are undesirable for 'in vivo' and 'in vitro' experiments and ophthalmic surgery. However, the choice of

wavelength should be made with due regard to the absorption by target tissue and the potential for injury to adjacent tissues by radiation. Table 4.3 summarizes some of the comments on fibre delivery of excimer laser wavelengths for ablation of a target material.

Table 4.3 - Some comments on the fibre delivery of excimer lasers for ablation.

Wavelength (nm)	comment
308	- very good transmission through Superguide PCS fibres - very long laser - fibre exposure time above an input fluence of $3Jcm^{-2}$ - high etch rates - good transmission in saline - high scattering therefore hazardous - phaecoemulsification possible if scattering confined
248	- moderate transmission through Superguide 'G' fibre up to 55% at $F_{in}(1.5\text{-}2)Jcm^{-2}$ - relatively long fibre delivery period ($\geq$400 pulses) at F_{in} $(1.5\text{-}2)Jcm^{-2}$, $F_o \leq 1Jcm^{-2}$ - Smaller etch rate than 308nm wavelength - lower transmission in saline - possible mutagenic effects
193	- moderate transmission through Superguide 'G' fibre up to 30% at $F_{in} \leq 0.5Jcm^{-2}$ - very short fibre delivery period - practical output fluences $\leq$ $(0.1\text{-}0.2)Jcm^{-2}$ ($\sim$100 pulses) - very small (submicron) etch rates - strong absorption in saline - lack of sufficient evidence for its mutagenicity - well-controlled phaecoemulsification if delivered more suitably at higher pulse rates

Appendix I

Below the ablation threshold the acoustic transients can be modeled using thermoelastic theory in which the stress generated by rapid heating and thermal expansion of the sample surface is related to the thermomechanical and optical properties of the sample. In this experiment the acoustic impedances of the liquid (saline) and tissue are closely similar. The acoustic reflection coefficient at the boundary is then $R \tilde{} 0$ in saline and R=1 in air. A solution for the thermoelastic stress wave can be found using an extension of the Carome et al (11) or Bushnell and McCloskey's (16) formulation. For a laser irradiance I,

$$I = I_o (1 - e^{-K\tau}) e^{-m\tau} \qquad (1)$$

where k and m are the rates of rise and fall of the laser pulse respectively and I_o is given by,

$$I_o = \frac{m(m+K)F}{K} \qquad (2)$$

where F is the fluence, the stress becomes,

$$\sigma = \frac{1}{2} \Gamma \alpha I_o \frac{Ke^{at'}}{(m+a)(K+m+a)} \qquad t' \leq o$$

$$\sigma = \frac{1}{2} \Gamma \alpha I_o \left[\frac{e^{-mt'}}{(m+a)} - \frac{e^{-(K+m)}}{(K+m+a)} \right] \qquad t' > o \qquad (3)$$

Here $t' = t - 1/V_a$, with $(1/V_a)$ being the acoustic transit time from the sample to the transducer plane (Fig. 1), α is the laser attenuation coefficient in the sample, and $a = \alpha V_a$,

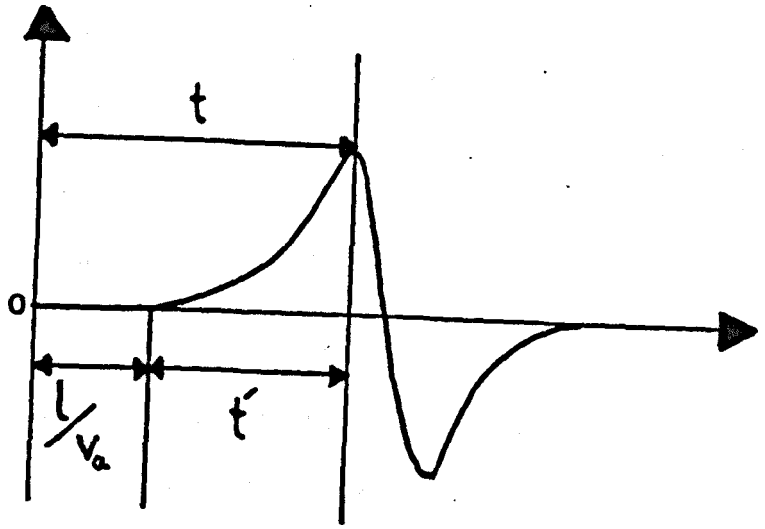

Fig. 1 - Stress waveform for exponential absorption after laser pulse incident on the sample in air from L-R.

$$\Gamma = \frac{\beta V_a^2}{C_p} \qquad (4)$$

where V_a is the acoustic velocity in tissue. The term, Γ, is the Grüneisen constant of the absorbing medium, where β is the thermal volume expansion coefficient, and Cp the specific heat capacity. In deriving the expressions for σ, thermal conduction within the absorbing sample or between the sample and liquid layer can be neglected on the scales involved because of the low thermal diffusivity. It is also assumed that absorbed energy is instantaneously transformed to heat.

It can be seen from Eq.(3) that in the early stages of the stress wave ($t'<0$), the leading edge is exponential, reflecting the assumed exponential fall-off of laser irradiance in the sample, with a characteristic rise time given by $(\alpha V_a)^{-1}$. Thus the acoustic transient can provide information on the attenuation coefficient for radiation in the sample.

1. Srinivasan R., Mayne - Banton V.
Self-developing of photoetching of PET film by far UV excimer laser radiation.
Appl. Phys. Lett., 48:445:1982.

2. Andrew J.E., Dyer P.E., et al
Direct etching of polymeric materials using a XeCl laser.
Appl. Phys. Lett., 43:717:1983.

3. Schildbach K., in "proceeding of SPIE International congress on optical science and Engineering",
The Hague, 1990 paper 1279-07.

4. Srinivasan R., Leigh W.
Ablative photodecomposition: Action of far-UV (193nm) laser radiation on PET films.
J. Am. Chem. Soc., 104:6784:1982.

5. Srinivasan R., Braren B., et al.
Ultraviolet laser ablation of polyimide films.
J. Appl. Phys., 61:372:1982.

6. Dyer P.E., Jenkins S., Sidhu J.
Development and origin of conical structures on XeCl laser ablated polyimide.
Appl. Phys. Lett., 49:453:1986.

7. Arenholz E., Wagner M., et al.
Structure formation in UV-laser-ablated polyimide foils.
Appl. Phys. A., 55:119:1992.

8. Al-Dhahir R.
Development and interaction of excimer laser with tissue.
Hull Univ. - 1989.

9. Askaryan G.A.
The effects of a laser beam in a liquid.
Sov. Phys. JETP., 17:1463:1963.

10. Sigrist M., Kneubuhl F.
Laser-generated stress waves in liquids.
J. Acoust. Soc. Am., 74:1652:1978.

11. Carome E., Clark N., Moeller C.
Generation of acoustic signals in liquids by ruby laser-induced thermal stress transients.
Appl. Phys. Lett., 4:95:1964.

12. White R.M.
Generation of elastic waves by transient surface heating.
J. Apply. Phys., 34:2123:1963.

13. Hu C.L.
Spherical model of an acoustical wave generated by rapid laser heating in a liquid.
J. Acoust. Soc. Am., 46:728:1969.

14. Bushanam G., Barnes F.
Laser-generated thermoelastic shock wave in liquids.
J. Appl. Phys., 46:2074:1975.

15. Sigrist M., Kneubuhl F.
Spherical model on thermoelastic generation of acoustic waves.
Rapport de la societe suisse de physique. 29:353:1978.

16. Bushnell J.C., McClosky D.J.
Thermoelastic stress production in solids.
J. Appl. Phys., 39:5541:1968.

17. Scruby C.B., Dewhurst R., et al.
Quantitative studies of thermally generated elastic waves in laser-irradiated metals.
J. Appl. Phys., 51:6210:1980.

18. Dewhurst R., Hutchins D., et al.
Quantitative measurements of laser-generated acoustic waveforms.
J. Appl. Phys., 53:4064:1982.

19. Bourkoff E., Palmer C.H.
Low-energy optical generation of acoustic pulses in metals and non-metals.
Appl. Phys. Lett., 46:143:1985.

20. Aussel J., Le Brun A., Baboux J.
Generating acoustic waves by laser: theoretical and experimental study of the emission.
Ultrasonics, 26:245:1988.

21. Cleary S.F.
Laser pulses and the generation of acoustic transients in biological material in
"laser applications in medicine and biology", Vol.3., ed M.L. Wolbarsht, Plenum press, New York, 1977.

22. Dyer P.E., Srinivasan R.
Nanosecond photoacoustic studies of UV laser ablation of organic polymers.
Appl. Phys. Lett., 48:445:1986.

23. Cross F.W., Al-Dhahir R., Dyer P.E.
Ablative and acoustic response of pulsed UV laser-irradiated vascular tissue in a liquid environment.
J. Appl. Phys., 64:2194:1988.

24. Rosencwiag A., Gersho A.
Theory of photoacoustic effect with solids.
J. Appl. Phys., 47:64:1976.

25. Dyer P.E.
Nanosecond photoacoustic studies of UV laser ablation of polymers and biological materials.
In "photoacoustic and photothermal phenomena"
eds., Hess P., Pelzl J., P. 164, 1987.

26. Scruby C.B., Drain L.
"Ultrasonic generation by laser" in laser ultrasonics.
Adam Hilger - 1990.

27. Dyer P.E., Sidhu J.
Excimer laser ablation and thermal coupling efficiency to polymer films.
J. Appl. Phys., 57:1420:1985.

28. Gordotesky T., Kazyak R., et al.
Calorimetric and acoustic study of ultraviolet laser ablation of polymers.
Appl. Phys. Lett., 46:828:1985.

29. Brannon J., Lankard J., et al.
Excimer laser etching of polyimide.
J. Appl. Phys., 58:2036:1985.

30. Puliafito C.A., Steinert R., et al.
Excimer laser ablation of the cornea and lens: experimental studies.
Ophthalmol., 92:741:1985.

31. Naneviez T., Prince M., et al.
Excimer laser ablation of the lens.
Arch. Ophthal., 104:1825:1986.

32. Bath P., Mueller G., et al.
Excimer laser ablation.
Arch Opthal., 105:1164:1987.

33. Muller, Stolzenburg.
Application of 308nm excimer laser radiation for ocular surgery: safety consideration.
Proceedings of first planary workshop on safety and laser-tissue interaction (ELA). p.129, 1988.

34. Bath P., Muller G., et al.
Excimer laser application for cataract surgery.
SPIE., 908:72:1988.

35. Li D., Borkman R.
Photodamage of calf lenses in vitro by excimer laser radiation at 308, 337 and 350nm.
Invest. Ophthal Vis. Sci., 31:10:1990.

36. Green H., Boll J., et al.
Cytotoxicity and mutagenicity of low intensity, 248, 193nm excimer laser radiatiion in mammalian cells.
Cancer Res., 47:410:1987.

37. Kochevar I.E.
Cytotoxicity and mutagenicity of excimer laser radiation.
Lasers in Surg. Med., 9:440:1989.

38. Biswas A., Ahmad T., et al.
Thermal characterization of coal using piezolectric photoacoustic microscopy.
Can. J. Phys., 64:1184:1986.

39. Hutchins D.A., Young R.
Rock property assessment using laser-generated acoustic waves.
Rev. Sci. Inst., 62:1995:1991.

40. Ponomarev Yu.
Photoacoustic investigation of the interaction of laser radiation with molecules and inter-molecular interaction in gases.
Infra. Phys., 32:377:1991.

41. P. Hess, J. Pelzl.
Part I in "photoacoustic and photothermal phenomena". Spring-verlag 1987.

42. Oehler O., Seifert, et al.
Detection of gases produced by biological systems with an enzyme-photoacoustic sensor.
Infra. Phys., 25:319:1985.

43. Balasubramanian D., Mohan C.H.
Application of photoacoustics to biology: some specific systems and methods.
Can. J. Phys., 64:1132:1986.

44. Guy M., Banengo J.
Designing a differential cell for in vivo photoacoustic measurement of skin absorbance.
Can. J. Phys., 64:1142:1986.

45. P. Hess, J. Pelzl.
Part VI in "photoacoustic and photothermal phenomena". Spring-verlag 1987.

46. Dyer P.E., Al-Dhair R.
Transient photoacoustic studies of laser tissue ablation.
SPIE., 1202:46:1990.

47. James J., Tas J.
"Detection of proteins by means of their photochemical properties" in: Histochemical protein staining methods. Microcscopy handbooks 04-1983,

48. Preiss J.W., Setlow R.
Spectra of some amino acids, peptides, nuclei acid, and proteins in the vacuum ultraviolet.
J. Chem. Phys., 25:138:1956.

49. Ito A., Ito T.
Absorption spectra of deoxyribose, ribose-phosphate, ATP and DNA by direct transmission measurements in the vacuum-UV (150-190nm) and far-UV (190-269nm) regions using synchrotron radiation as a light source.
Photochem., Photobiol., 44:355:1986.

50. Johnson, Thompson M., Halpern J.B., et al.
Vacuum UV laser interactions as probes for vacuum-ultraviolet radiation damage and repair.
Photochem., Photobiol., 44:359:1986.

51. Tuft S., Al-Dhair R., Dyer P., Zhu. Z.
Characterization of the fluorescence spectra produced by excimer laser irradiation of the cornea.
Invest. Ophthal. Vis. Sci., 31:1512:1990.

Chapter 5

Construction of pulsed HF laser

5.1 - Introduction

Chemical lasers are those in which a chemical reaction excites an atom or molecule to the upper laser level. The first experimental chemical laser emission was observed in 1965 by Kasper et al (1), in a photolytically initiated hydrogen-chlorine explosion. Chemical reactants can store energy quite efficiently and release it rapidly in a suitable chamber; thus one of their prime attractions is their potential to generate high powers. Most chemical lasers operate on infrared vibrational transitions of diatomic molecules, mainly hydrogen halides. There are number of chemical lasers such as hydrogen fluoride (HF), deuterium fluoride (DF) and iodine. The HF laser emits between 2.5-3μm in the infrared, but by substitution of hydrogen by deuterium emission shifts to a range between 3 - 4.7μm where the atmosphere is more transparent. The iodine laser emits in the region of 1.3μm based on an electronic transition which can be pumped by excited molecular oxygen produced by a chemical reaction.

A great deal of experimental and theoretical research on pulsed HF/DF chemical lasers has been carried out, since the first observation of HF laser action produced in electrical discharges by Deutsch (2). Applications of such lasers are varied and include military, spectroscopy, chemistry, telecommunication and medical. It is the medical application that this work will concentrate on since there is a considerable interest in studying the ablation of tissue using lasers in

the 2.5-3μm region where water shows a peak in its infrared absorption spectrum. Cutting quality comparable to that with the deep UV ArF excimer laser might be achieved in this way, with the added advantages of being able to use fibre delivery and avoiding possible mutagenic threat (3).

This chapter deals with the construction of a pulsed HF laser and the subsequent chapters will address fibre delivery of this laser and its application in tissue ablation related to opthalmology.

5.2 - Physical principles of chemical lasers

The operation and hence output of gas lasers are based on various types of molecular and atomic energy level transitions. The most important high-power infrared lasers are those using vibrational-rotational transitions in molecules. This class includes the important chemical lasers such as HF, DF, CO_2 and CO which can be pumped either electrically or photolytically.

A classical 'billiard ball' model can be used to understand how a chemical reaction can lead to population inversion and hence laser action. Fig. 5.1 shows the reaction between a fluorine atom and a hydrogen molecule. The fluorine atom approaches the hydrogen molecule, and sometimes during the collision the electronic orbits change in such a way that

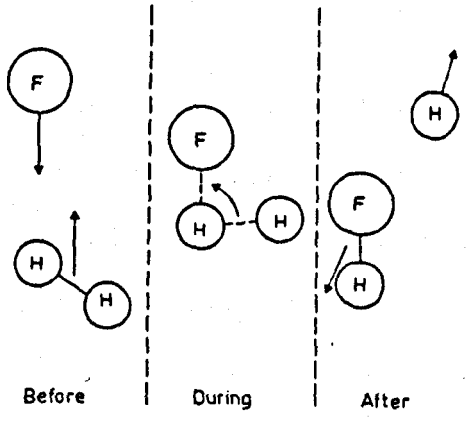

Fig. 5.1 - Schematic of a reactive collision

the chemical bond is shifted. After the collision, the fluorine is bonded to one of the hydrogen atoms, and the other hydrogen atom departs. It is known from the chemical bond energies that this leads to a release of vibrational energy. This is because the electron jump occurs when the hydrogen and fluorine atoms are further apart than they would

be in equilibrium in the HF molecule. Thus, the HF molecule is formed with a 'stretched' molecular bond containing potential energy. When the HF and H separate, this stretch is converted into vibration in the newly formed bond.

Each vibrational level has a large number of rotational sublevels and when the molecule decays radiatively from one vibrational level to another, (Fig. 5.2) a broad range of wavelengths is emitted.

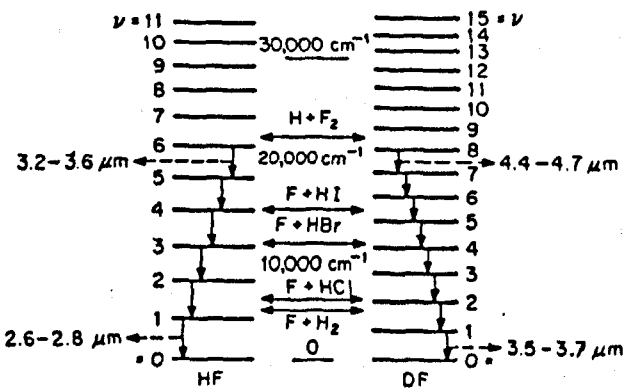

Fig. 5.2 - Vibrational energy levels of HF/DF molecules

Various methods are available for initiating the chemical reactions including flashphotolysis (4-7), electrical discharge (2, 8-11), electrical beam (12-16) and nuclear pumped (17-22). Of these the pulsed self-sustained discharge technique ie. electrical discharge is probably the simplest and most commonly used and was chosen here as a convenient means of providing submicrosecond laser pulses at useful output energy levels. In the discharge scheme dissociation due to electron collisions produces the required reactive species (F) from a fluorine donor subsequently reacts with a hydrogen donor to produce HF. Various fluorine/hydrogen donor combinations can be employed, the most common reactions being

as set out in 1-4 below.

1. $F_2 + e^- \rightarrow F + F + e^-$
   $F + H_2 \rightarrow H + HF(V) + 32$ K cal mol^{-1}
   $H + F_2 \rightarrow F + HF(V) + 98$ K cal mol^{-1}

2. $SF_6 + e^- \rightarrow SF_5 + F + e^-$
   $F + H_2 \rightarrow H + HF(V) + 32$ K cal mol^{-1}

3. $SF_6 + e^- \rightarrow SF_5 + F + e^-$
   $F + C_2H_6 \rightarrow C_2H_5 + HF(V) + 38$ K cal mol^{-1}

4. $SF_6 + e^- \rightarrow SF_5 + F + e^-$
   $F + C_3H_8 \rightarrow C_3H_7 + HF(V) + 38$ K cal mol^{-1}

where V designates vibrationally excited HF.

Of these (1) is based on H_2-F_2 mixtures are explosive but yield highly energetic species via the 'hot' reaction $F_2 + H \rightarrow HF + F$. The others utilizing F atom reactions are less energetic but more convenient in terms of safe handling in the laboratory. Here use was made of C_3H_8 or H_2-SF_6 mixtures excited in a transversely excited, medium pressure, discharge. Discharges involving SF_6 tend to be highly unstable to arc formation because of the high electron attachment rate of SF_6. It is thus necessary to use special techniques such as resistive pin (8, 9, 23-25) or fast ultraviolet (UV) preionized (26-31), discharges to produce the required volume excitation. Here use was made of a UV preionized discharge.

5.3 - Laser construction

5.3.1 - Electrodes

The construction of laser began by choosing an appropriate pair of uniform field electrodes among different types. The well known Rogowski profile is actually made up of three unsmoothly joined segments taken from an infinitely wide analytic profile. The Bruce profile, on the other hand, is a purely empirical approximation, and the Harrison profile is a numerical compromise between Rogowski and Bruce profiles. According to Chang (32) it is very difficult to improve any of these profiles from its state of approximation.

For this reason, a pair of aluminium Chang profile electrodes were chosen because of their capability of producing a uniform, smooth discharge area at high pumping energy. This uniformity is due to their equi-potential surface which takes a form of a smooth curve without any flat region. Other types of electrodes have a flat region at the centre which causes a strong discharge at the flat-curve boundary and a weaker discharge at the centre, ie. the discharge is confined to that portion of the electrodes closer to pre-ionization (PI) source. Consequently, the overall discharge at high pumping energy becomes non-uniform. Fig. 5.3 shows the schematic diagrams of Rogowski and Chang electrodes with their gain profiles.

The length of electrodes was 82cm, and at their design spacing of 2.1cm produced a nominal discharge width of 1.5cm, giving a total discharge volume of 258cm^3.

In order to assist uniform avalanche discharge formation the electrode surfaces were polished thoroughly and kept

free of possible contamination. The presence of dust or other particles can cause field emission due to localized enhancement of electric field by the surface imperfections and non-uniformities. Also positive ions can come temporarily to rest on an insulating oxide layer on the cathode surface and hence create locally a great enhancement of the applied electric field (33).

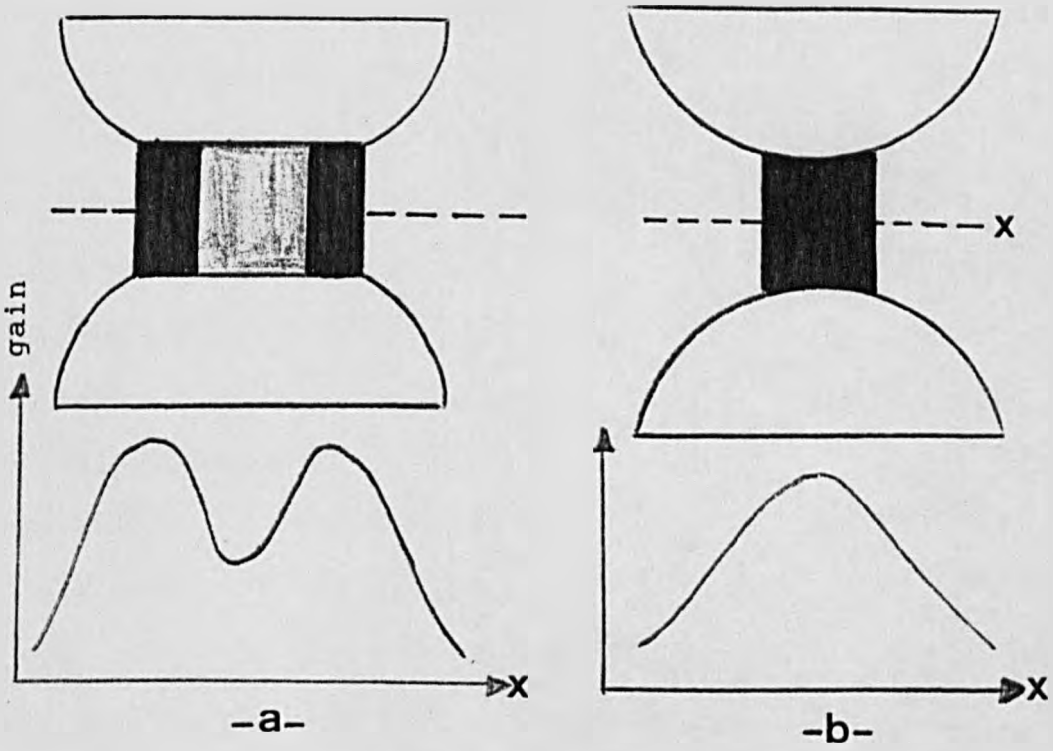

Fig. 5.3 - Schematic diagram of (a) Rogowski and (b) Chang electrodes and mid-plane gain profile.

5.3.2 - Preionization (PI)

The electrical breakdown in gases is usually characterized by the generalized parameters E/P and Pd where p is the pressure and d the electrode spacing. In transverse discharge geometries where d is small compared to the extension of the electrodes perpendicular to the field direction, increasing values of the parameters E/P and Pd may lead to the formation of an inhomogeneous discharge mode. The discharge can then transform into spark channels.

A common problem associated with chemical HF lasers is the electronegativity of sulphur hexafluoride (SF_6) which through attachment makes the attainment of a uniform electron 'background' density difficult. As a result inhomogeneities and instabilities in the plasma develop leading to the formation of filmamentary streamers and arcs. The latter are deterimental both to laser operation and electrode life. Arc formation can be reduced by keeping the duration of the discharge short by the use of low inductance, low capacitance pulsers and careful circuit design. The limitation on current pulse duration, however, limits the energy that can be deposited in the gas unless high charging voltages are employed.

These inhomogeneities are largely caused by boundary effects and statistical fluctuations in the starting conditions ie. background electron density. Techniques to overcome such difficulties have included resistively ballasted pin discharges (8, 9, 23-25), UV-preionization (26-31), semiconductor preionizers (34-37), and X-ray preionizers (11, 38, 39).

In this experiment UV-preionization was used which generally has two forms: (a) volumetric pre-ionization and (b) photoemission of electrons from the cathode. In the former case, the geometric positioning of the PI source with respect to the discharge volume is important, and it can be located so as to illuminate the discharge either transverse or longitudinal to the electric field. In the transverse geometry the main gradient of the photoionization electron density is perpendicular to the main field direction. The electron density shows a $1/r^2$ dependency, where r is the distance between the PI source and point at which the density is measured (40). This implies a higher preionization electron density at the edge of the electrodes nearest to PI source, which effectively would result in preferential development to the discharge in such areas. One solution suggested by Tallman (41) is the use of an identical PI source in the mirror image position of the first PI source.

One main advantage of the longitudinal geometry is that during the avalanche phase, space-charge effects enhance the electric field and ionization rate in the low density regions. This leads to a decrease of field in the dense region and as a result a more homogeneous and smoother electron density profile can be achieved. In addition to electronegativity and possible inhomogeneity of discharge there are other problems associated with the HF lasers namely: gas contamination, spark erosion and optics degradation, all of which can decrease the life time of a sealed-off system.

In the present design transverse preionization was

employed based on a total of 48 peaking capacitors (Murata-272Z/40kV) each of 2.7nF. The capacitors were arranged in two rows on either side of the electrodes (Fig. 5.4) and each disconnected series-pair defined 12 sparks uniformly distributed down each side (Fig. 5.6).

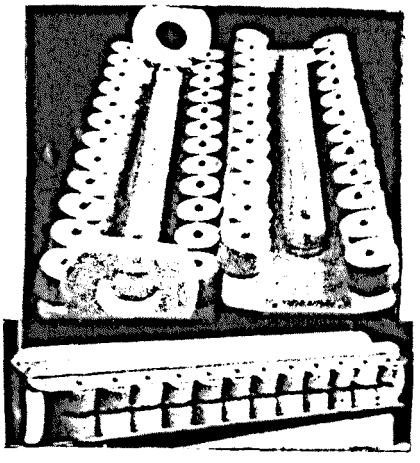

Fig. 5.4 - Assembly of laser electrodes and UV pre-ionizers

When 'connected' by the sparks each pair of capacitors produced an effective capacitance load of ~1.35nF giving a total 1.35x24 = 32.4nF in parallel with the gap. Each spark was formed by steel 'tag' electrodes screwed onto the capacitor terminals, and the gaps were located ~20mm from the centre of the discharge electrodes. The array was sufficiently large (~90cm compared with 82cm electrode length) to ensure quasi uniform UV illumination along the electrodes, thus minimizing end effects associated with field enhancement at the roll-off point of the flat portion.

An advantage of using the preionization scheme in Fig. 5.6 is that it provides automatic synchronization of the sparks with the main discharge. The small gap and strongly non-uniform field associated with each preionizers ensures

employed based on a total of 48 peaking capacitors (Murata-272Z/40kV) each of 2.7nF. The capacitors were arranged in two rows on either side of the electrodes (Fig. 5.4) and each disconnected series-pair defined 12 sparks uniformly distributed down each side (Fig. 5.6).

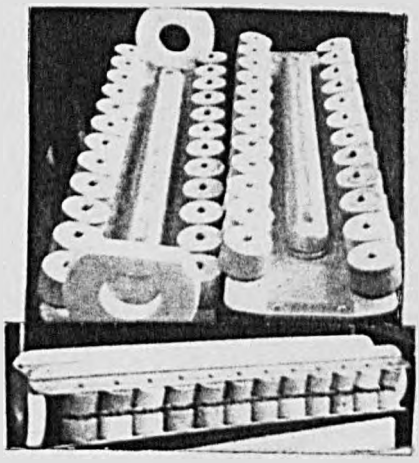

Fig. 5.4 - Assembly of laser electrodes and UV pre-ionizers

When 'connected' by the sparks each pair of capacitors produced an effective capacitance load of ~1.35nF giving a total 1.35x24 = 32.4nF in parallel with the gap. Each spark was formed by steel 'tag' electrodes screwed onto the capacitor terminals, and the gaps were located ~20mm from the centre of the discharge electrodes. The array was sufficiently large (~90cm compared with 82cm electrode length) to ensure quasi uniform UV illumination along the electrodes, thus minimizing end effects associated with field enhancement at the roll-off point of the flat portion.

An advantage of using the preionization scheme in Fig. 5.6 is that it provides automatic synchronization of the sparks with the main discharge. The small gap and strongly non-uniform field associated with each preionizers ensures

that it breakdowns before the applied voltage is sufficient to breakdown the main, uniform field, gap. This introduces a time delay between the appearance of a background electron density produced by the sparks firing and the onset of the main discharge. This is advantageous since no additional external circuitary is necessary to power the preionizers and to time the firing of the sparks and main discharge. The closely coupled 'peaking' capacitors formed by the preionizers also help produce a fast rising discharge current pulse.

The final assembled form of electrodes and the peaking capacitors is shown in Fig. 5.5 where they are placed inside a steel chamber. In the circuit in Fig. 5.6 the main discharge is initiated automatically after a fixed time delay, t_d, with respect to preionizer initiation. This is advantageous as no external circuit is needed to separately time the preionizers and main discharge. A spark gap was triggered using a pulse transformer to switch the discharge network shown in Fig. 5.7.

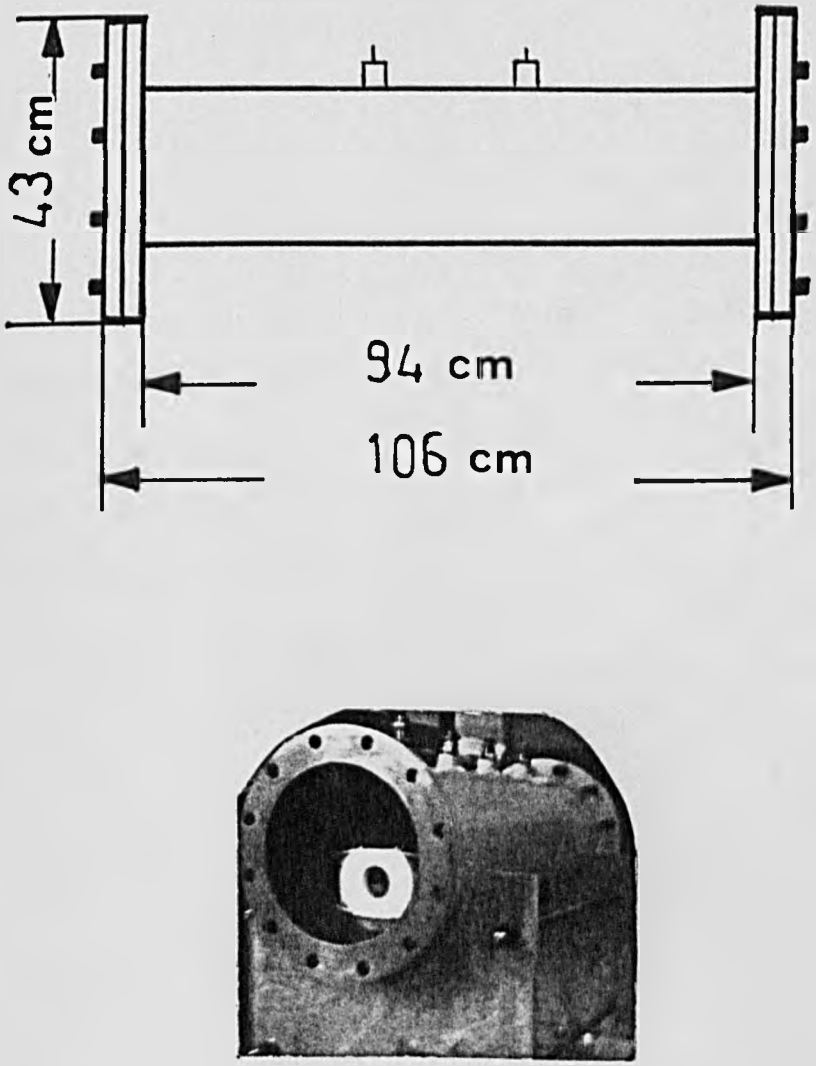

Fig. 5.5 - Schematic diagram of the chamber (a) inside which the laser head is positioned (b).

5.3.3 - Main discharge circuit

The pulser circuit used for excitation is shown in Fig. 5.6. The value of the main discharge capacitor, C_s was estimated assuming a required output energy of 1J, and laser efficiency of 2%, giving an input energy of E_s=50J. This corresponds to an energy density of 0.194Jcm^{-3} (194J lit^{-1}) which is given by the ratio of stored energy to discharge volume. Using

$$E_s = {}^1/_2 \, C_s \, V^2 \qquad 5.1$$

and a discharge voltage of V$\simeq$ 50kV, a value of 40nF was obtained. This was provided by connecting two 20nF rapid discharge capacitors (Hivotronic LTD - UK) in parallel.

A high voltage dc power supply (50kV-5mA) was used to charge the main capacitor which was then discharged to the laser electrode gap by triggering a home-built spark gap. The triggering circuit for spark gap is shown in Fig. 5.7. As far as the main discharge circuit is concerned a 20MΩ charging resistor, R_c, and a 134Ω pulsed resistor, R_p, (RS:156:923) were incorporated in the circuit where the latter allowed charging of the capacitor and provided damping in the discharge phase. In the trigger circuit Fig. 5.7 a 500pF capacitor was used in series as a safety precaution and also a 10kΩ resistor was connected to the spark gap in order to reduce the electrical noise.

The main electrical discharge circuit was mounted on a (58x36)cm steel plate and was then connected to the laser electrodes via two electrical leads running through the chamber wall (Fig 5.8). The circuit was then completely and

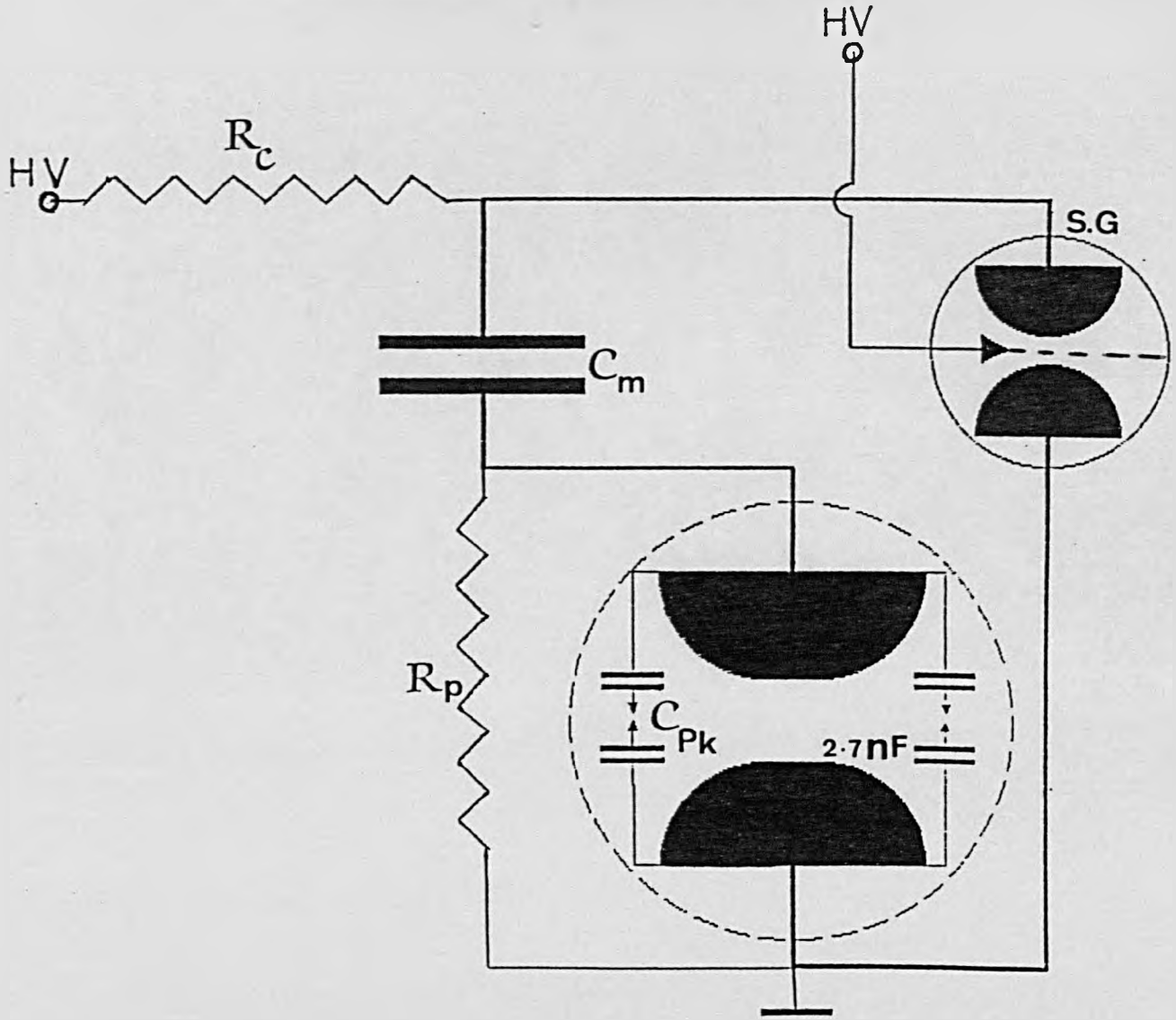

Fig. 5.6 - Laser Main electrical discharge circuit.

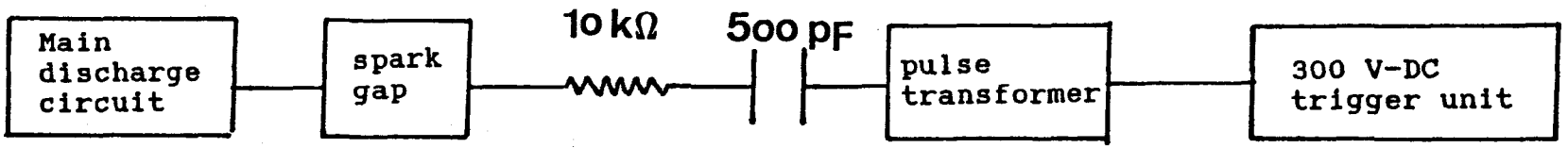

Fig. 5.7 - Block diagram of laser triggering circuit.

tightly covered by (58x30x28)cm tin plate box to reduce radiative noise (Fig. 5.9).

When the spark gap closes, the voltage across the electrode rise to a value of V_1 in time t_1 ie, $V_1 = V(t_1)$, which is small compared with the voltage breakdown of the laser electrode, $V_B = V(t_B)$, where t_B is the time taken for the voltage pulse to reach the breakdown voltage (V_B) of the laser electrodes. During this period ($t_1 < t_B$) the UV radiation emitted by the preionizer gaps has a high intensity which preionizes the laser medium and hence provides the laser gases with a suitable background electron density. The main laser gap becomes conductive when the $t_1 \geq t_B$ and the electron multiplication process dominates production from the UV source.

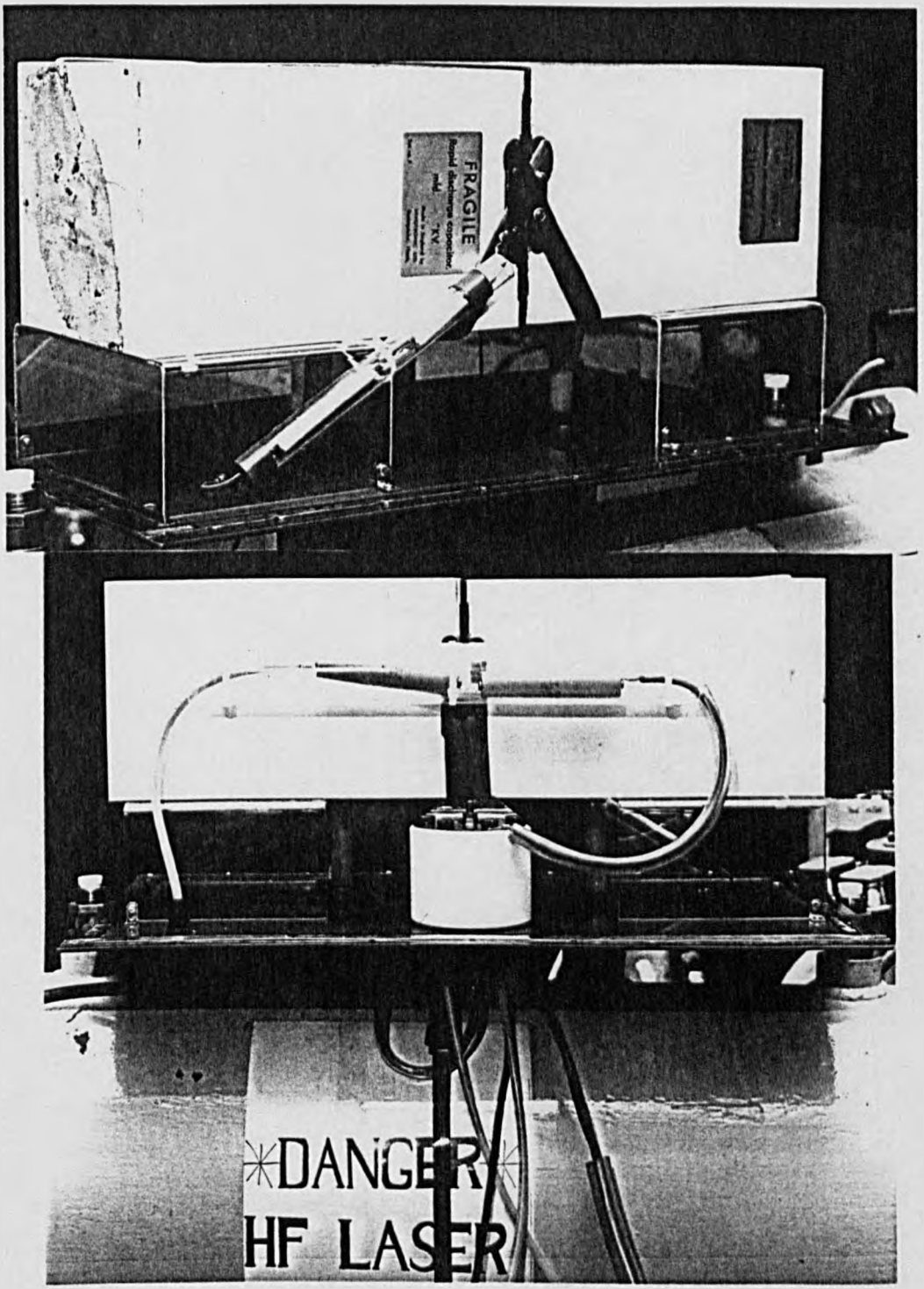

Fig. 5.8 - The photograph of completed excitation circuit.

Fig. 5.9 - Photograph of the completed laser.

All the experiments were performed with low inductance home made spark gap switch pressurized with N_2 gas. Fig. 5.10 shows the optimization of the spark gap breakdown at different applied voltages.

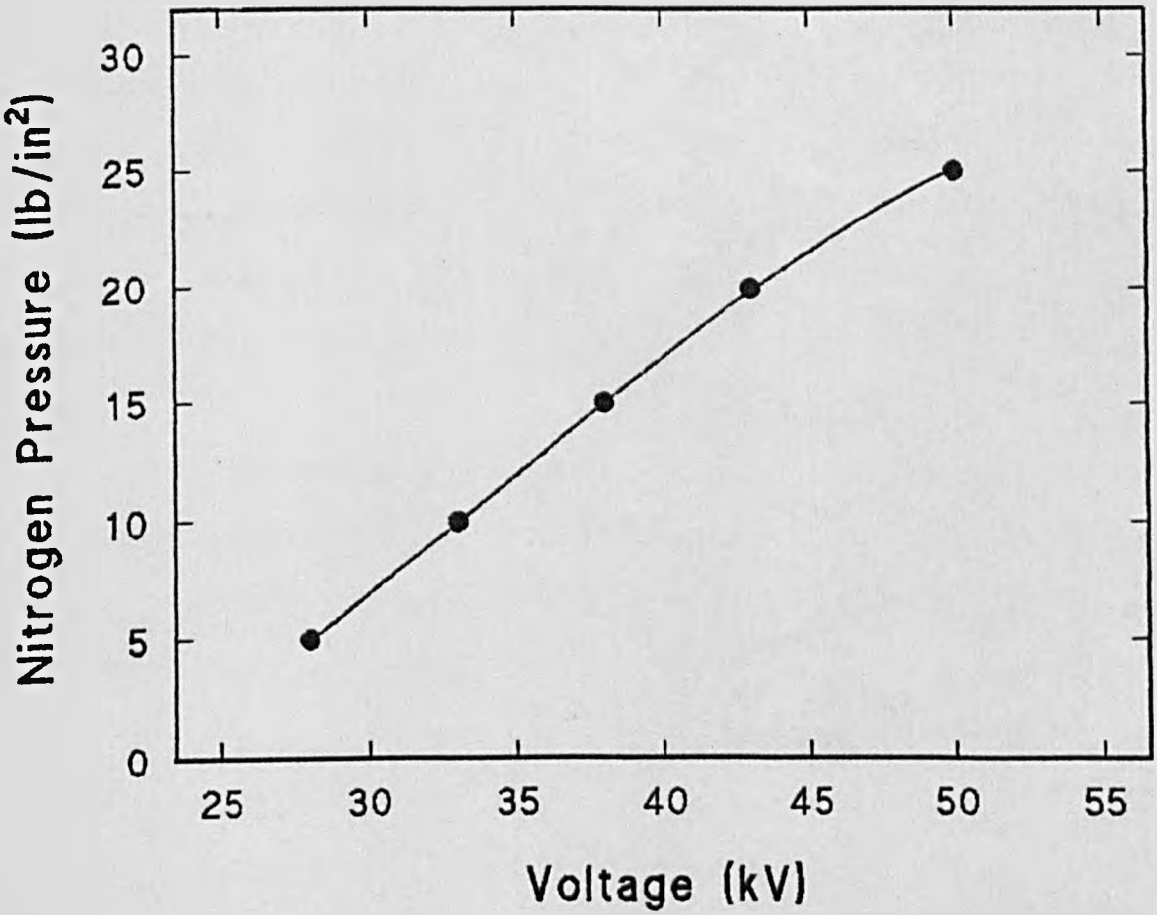

Fig. 5.10 - Variation of spark gap pressure with applied voltage.

5.3.4 - Resonator

For these experiments a stable resonator was used to form the optical cavity consisting of a spherical (concave) Au coated mirror with R1 = 10m and a 7.5cm diameter NaCl flat output coupler of 2.5cm thickness separated by 1m. The Au coated mirror was later changed to a brass mirror (R=10m) whose surface was covered by a thin salt window to protect it from gas corrosion. The end plates and mirror cells were sealed to the laser chamber using viton O-rings (Edwards - U.K) to provide compatibility with HF.

5.3.5 - Gas-handling system

This is an important part of a laser construction and should not be underestimated particularly when using hazardous gases such as C_3H_8. Nylon pipe was used for the gas lines and copper pipes for the pump lines. To ensure high vacuum integrity Viton O-rings (Edwards) were used throughout the system and were coated with fluorinated vacuum grease. The gas pressure was monitored using an Edwards 0-100 torr guage and prior to gas filling the chamber was pumped for at least 1 hour.

At the end of experiments the sealed gas mixture was pumped out to help reduce damage to the optics due to HF corrosion. As the exhaust gas contained HF it was passed through a solid-pellet NaOH trap to convert HF to NaF and H_2O.

5.4 - Laser characterization

5.4.1 - Optimization of gas mixture

The variation of laser output energy at 0.2Hz with the charging voltage and the partial SF_6 pressure was measured using a pyroelectric joulemeter. Fig. 5.11 shows that the energy increases with increasing charging voltage and that maximum energy ($\simeq$ 500mJ) was obtained at $V_c \simeq$ 45kV and 55 torr of SF_6 using a fixed amount ($\simeq$ 3torr) of propane (C_3H_8). The same procedure was repeated to obtain the optimum value of C_3H_8 partial pressure at constant (55 torr) SF_6 partial pressure. Fig. 5.12 shows that at V_c = 45kV an optimum value of 4 torr of C_3H_8 is obtained. On this basis, by varying the pressure for a fixed ratio of SF_6:$C_3H_8 \simeq$ 14:1, the optimum pressure was found to be $\simeq$ 60 torr at 45kV and $\simeq$ 40 torr at 30kV (Fig. 5.13). The maximum output energy at 45kV was $\simeq$ 500mJ

The laser pulse duration for the optimum SF_6 + C_3H_8 gas mixture was recorded by scattering the incident beam by steel wool and detecting a portion of this beam by an InAs photovoltaic detector (EG-G Judson, J12 series). The photodetector output was amplified using a 7A19 plug-in and displayed using a 7834 Tektronix storage oscilloscope. The pulse shape is shown in Fig. 5.21 from which a width of ~ 400ns (FWHM) was obtained for the multiline HF emission (SF_6: $C_3H_8 \simeq$ 14:1, 60 torr.

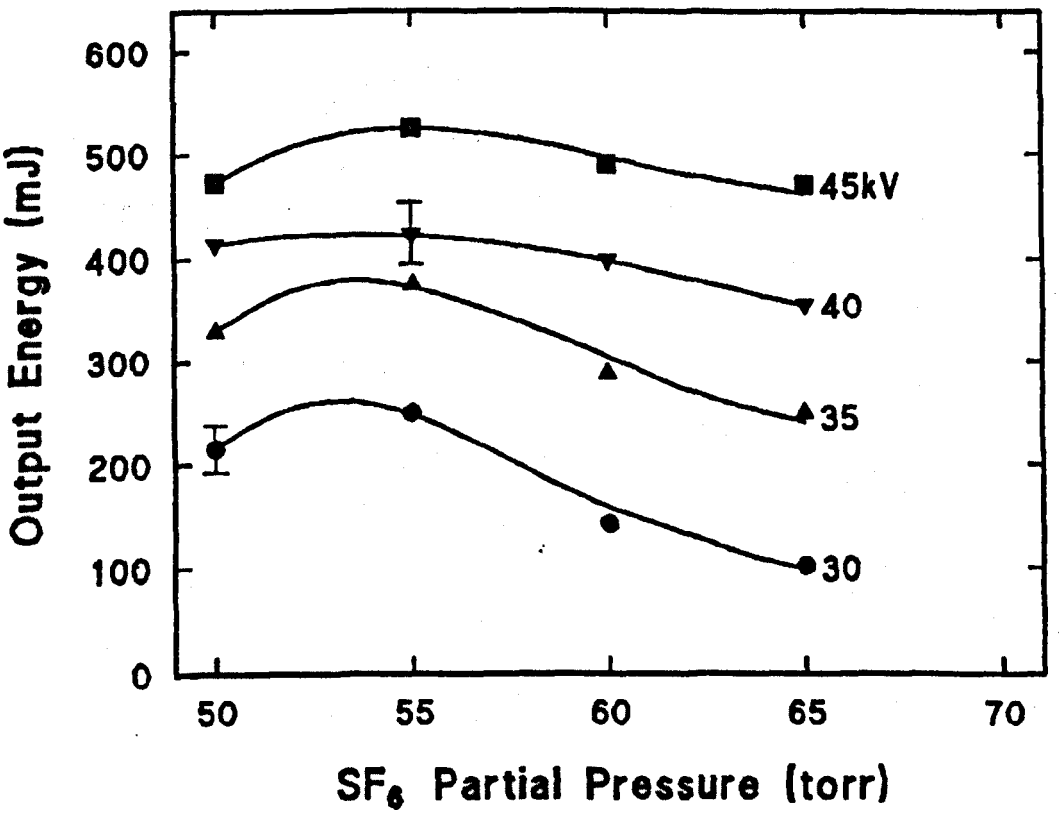

Fig. 5.11 - Variation of the laser output energy with the charging voltage and partial SF_6 pressure, (C_3H_8 = 3 torr).

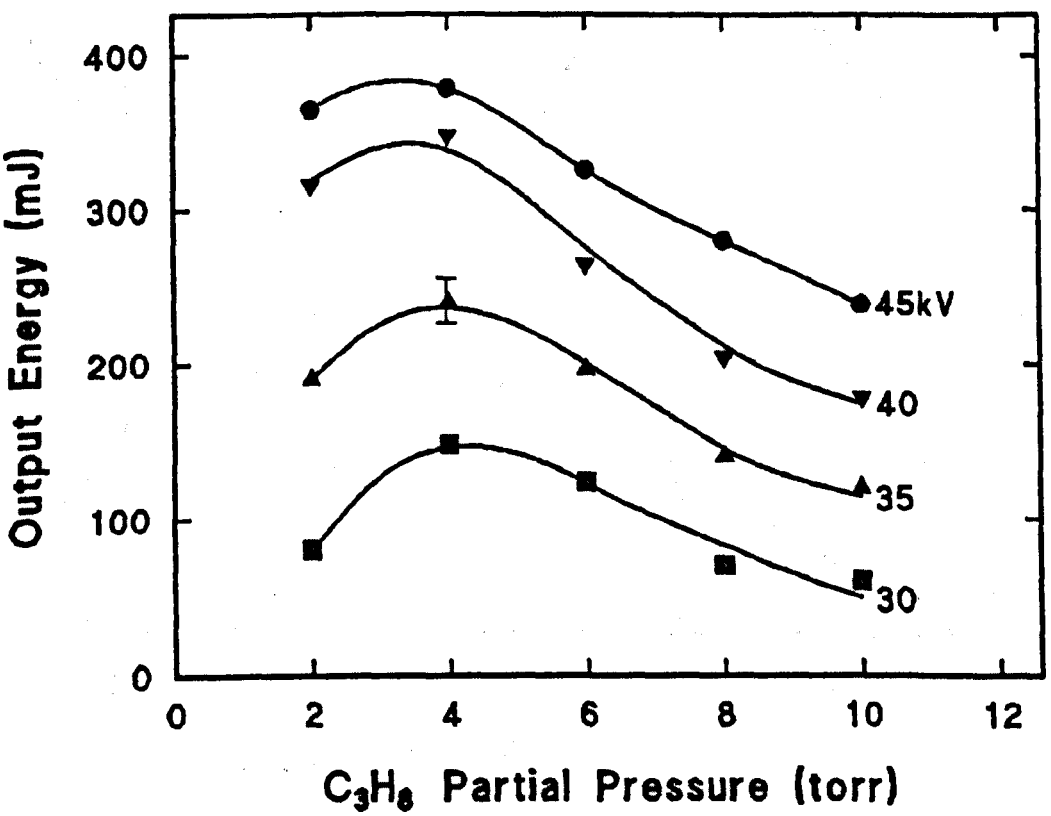

Fig. 5.12 - Variation of the laser output energy with the charging voltage and partial C_3H_8 pressure, (SF_6 = 55 torr).

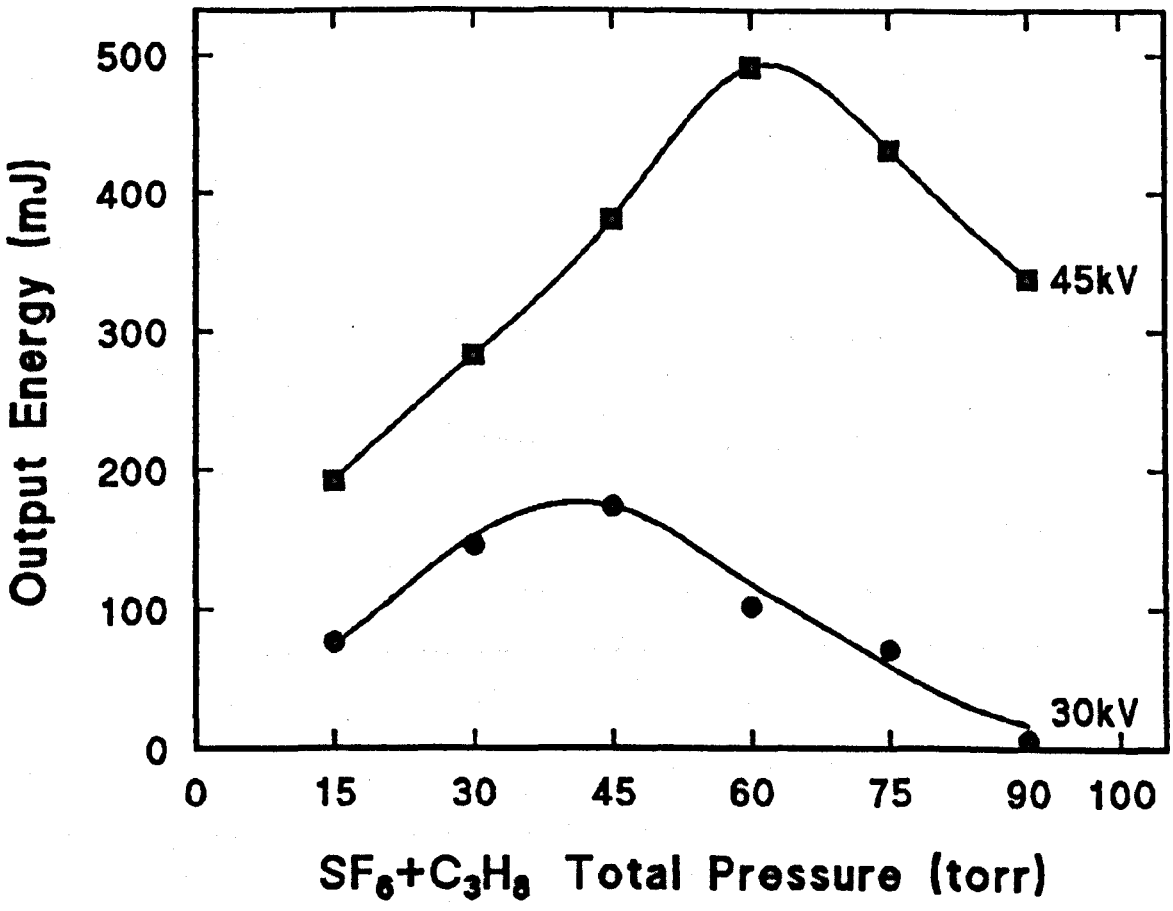

Fig. 5.13 - Variation of HF laser energy with (SF_6+C_3H_8) total pressure.

The occurence of different optima for energy is related to the fact that maximum energy is obtained when the HF production is maximized during the excitation pulse (42).

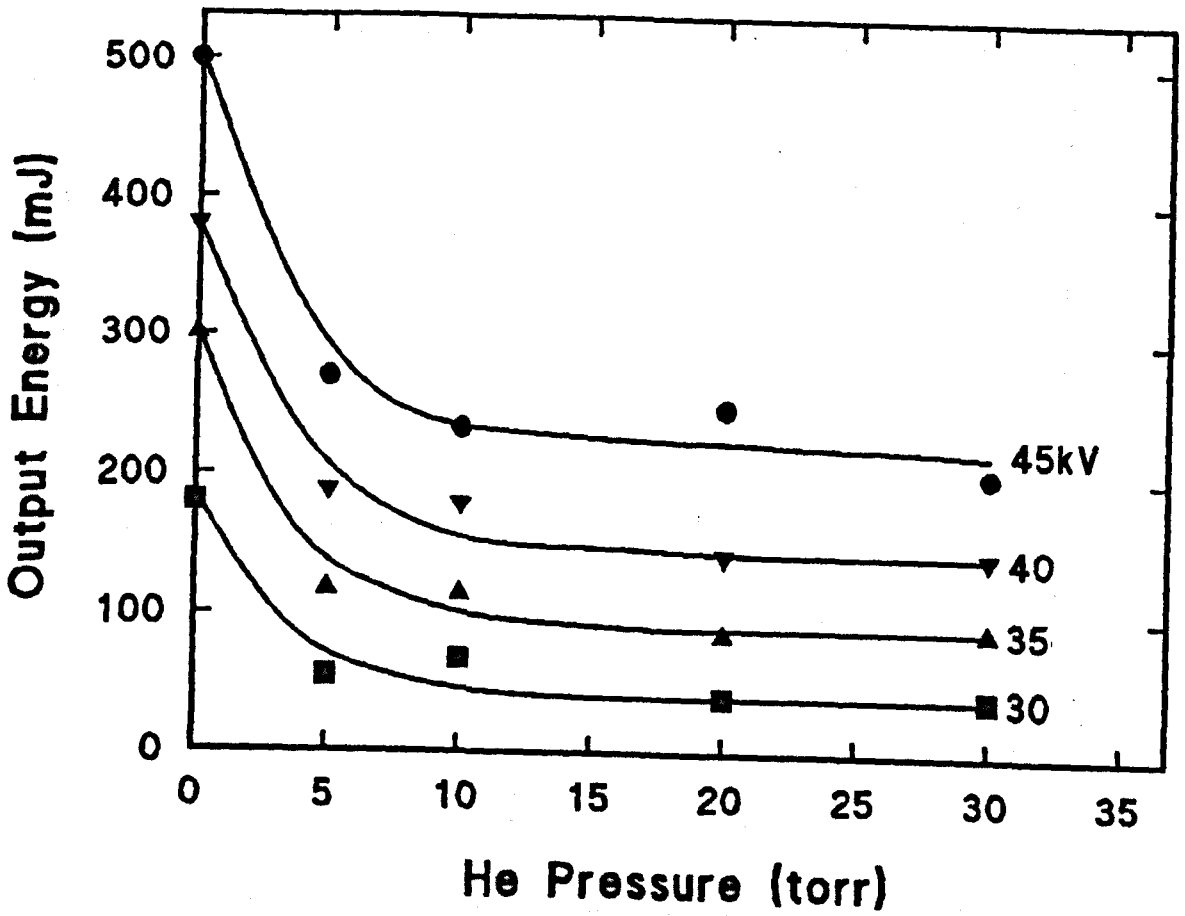

Fig. 5.14 - Variation of HF laser energy with He gas added to optimum (SF_6+C_3H_8) total pressure.

The effect of He gas on the output energy of the laser was studied by adding a fixed amount of He ($\geq$5torr) to the optimum (SF_6+C_3H_8) gas mixture at different charging voltages. As seen in Fig. 5.14, He addition led to a reduction in output energy over the entire range of values investigated. Similar results were obtained by Jacobson et al (8) at pressures from 30-60 torr; however, they found He addition was necessary at pressures above 100 torr in order to obtain laser oscillation.

The effect of replacing C_3H_8 by H_2 as a H-donor is shown in Fig. 5.15. To investigate the origin of the decrease in output energy with (SF_6+H_2) compared with (SF_6+C_3H_8) Puech et al (43) changed the initial electron density by more than an order of magnitude. Whichever the H atom donor was, the

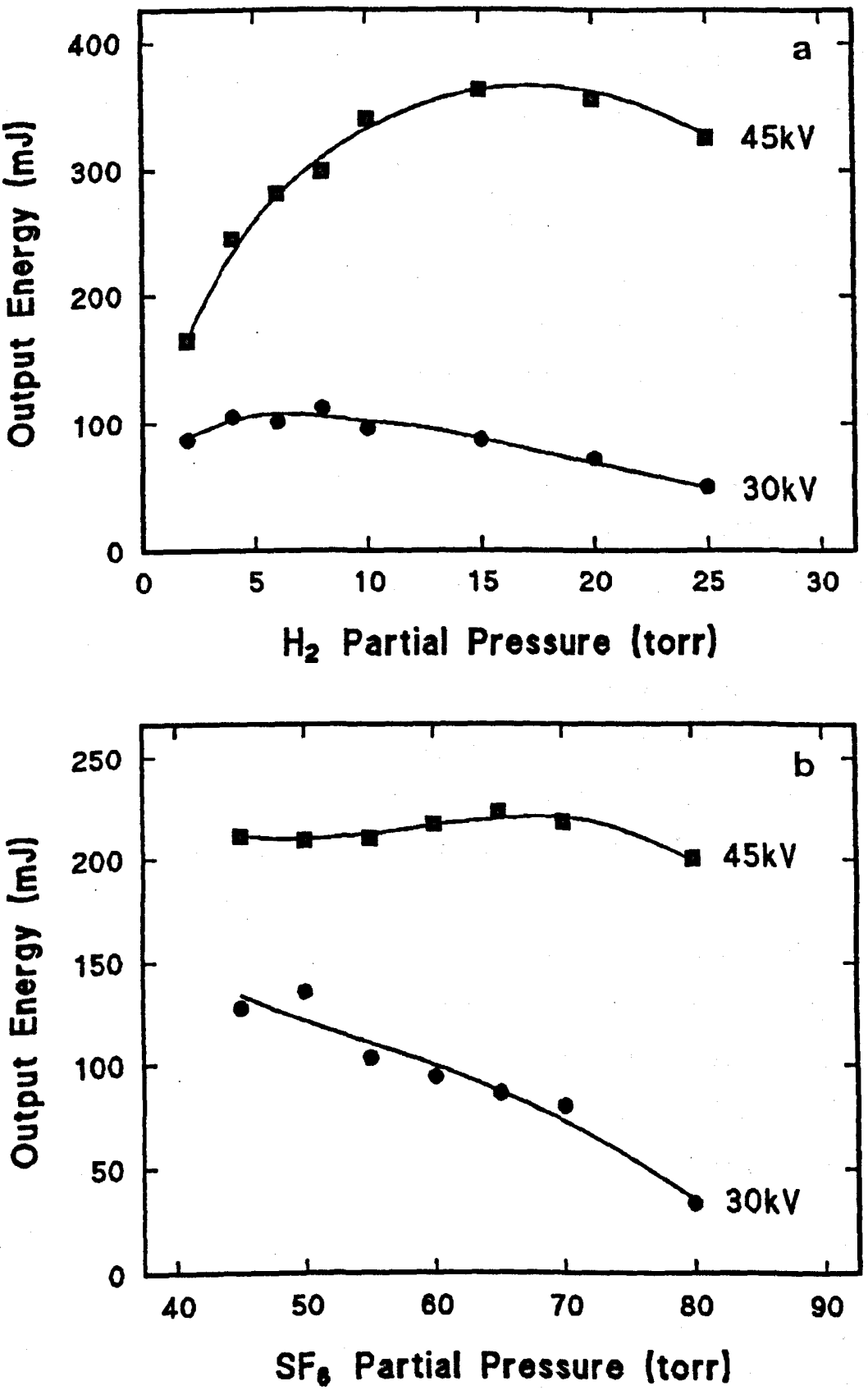

Fig. 5.15 - Variation of laser output energy with (a) H_2 (SF_6~ 65 torr) and (b) SF_6 (H2~ 3 torr) partial pressures.

laser performance proved insensitive to the value of the initial electron density. Therefore, they concluded it is not due to ineffective preionization but lies in a dramatic shortening of the laser pulse which suddenly ends when the discharge voltage drops to zero. In propane based mixtures, the final collapse of the discharge voltage occurs at later times for which the laser action is already completed (43). Therefore, the HF laser operates more efficiently with an (SF_6+C_3H_8) gas mixture.

The final experiment was to monitor the gas lifetime of the static mixture under repetitively pulsed conditions. This was carried out by recording the pulse energy using a Gen-Tec joulemeter and chart recorder (JJ-instrument). Fig. 5.16 shows the variation of laser output energy with operating time for charging voltage of 45 and 40kV. The rate of decay per min using 45kV is much faster (steeper slope) than using 40kV, which means the gas consumption is lower at lower charging voltage.

The effect of injecting a small fraction of the fuel gases during the experiment was also investigated. Fig. 5.16c shows the effect of adding C_3H_8 (1 torr at three intervals) to (SF_6+C_3H_8) mixture at 40 kV. This did not increase the energy but rather appeared to accelerate the decay rate. In contrast when 4 torr of SF_6 was injected the energy increased slightly and more importantly the decay rate decreased. Unfortunately, the duration of this improved stability can not be discussed due to the short period ($\sim$2mins) of observation. A similar experiment was performed at higher repetition rate of 0.5Hz (Fig. 5.17) and it was observed that

the energy loss ($\simeq$ 87%) was substantially higher at 45kV than that at 40kV (64%).

Finally, the above procedure was repeated for a SF_6+H_2 mixture operated at 40kV and 0.2Hz. Fig. 5.18 shows that the energy decayed from 348mJ to 207mJ within 30 minutes which corresponds to an energy loss of about 40%, which is $\simeq$ 8% lower than its corresponding value in Fig. 5.16b. Thus, although using the (SF_6+H_2) mixture at 40kV and 0.2Hz produced lower output energy than the ($SF_6+C_3H_8$) mixture under the same condition, it nevertheless produces a more stable output probably due to lower gas consumption rate.

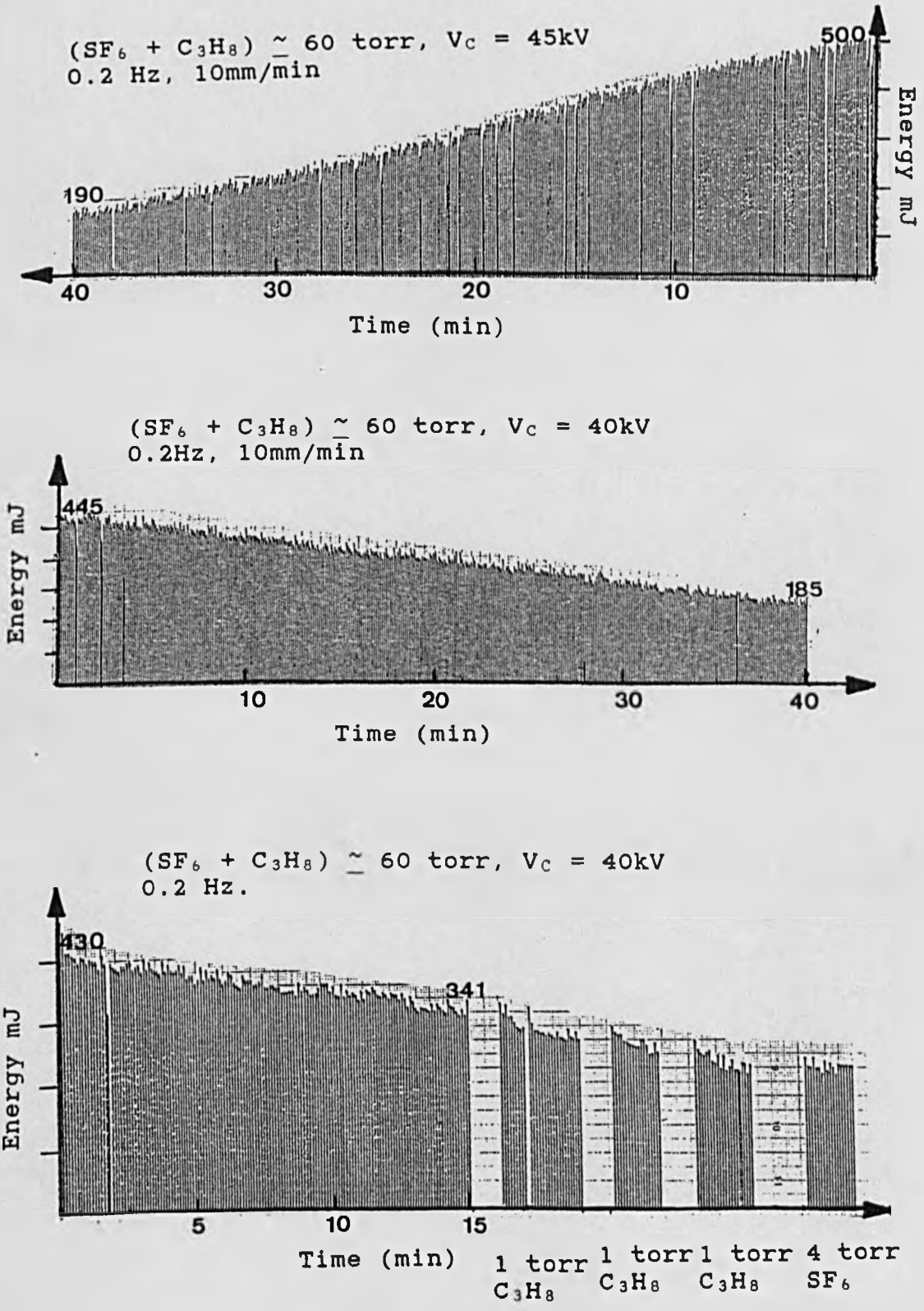

Fig. 5.16 - Monitoring of (SF_6 + C_3H_8) Lifetime at various applied voltage and constant rate.

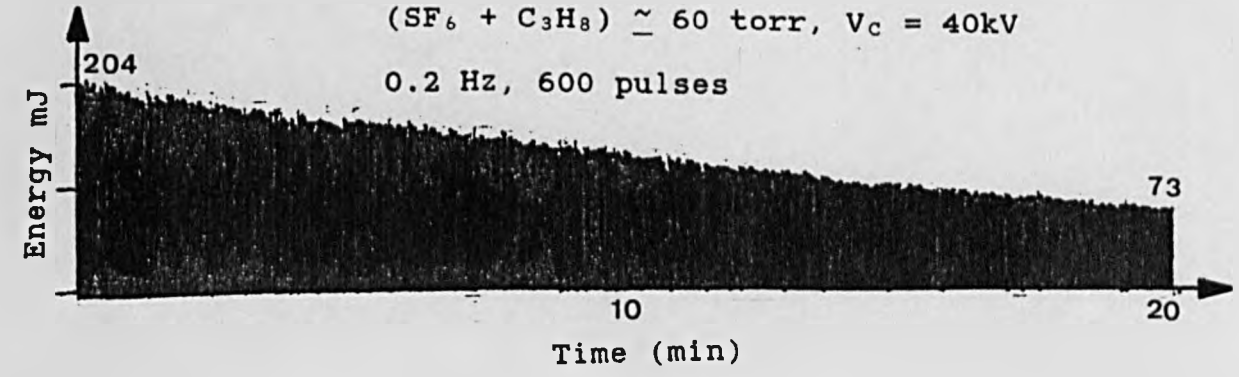

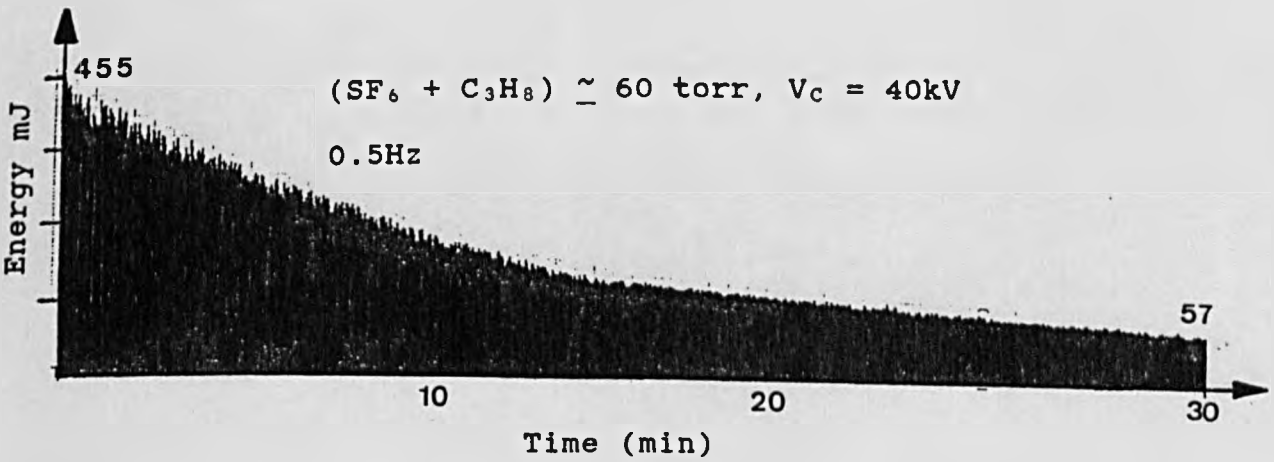

Fig. 5.17 - Monitoring of (SF_6 + C_3H_8) Lifetime at various pulse rate and constant applied voltage.

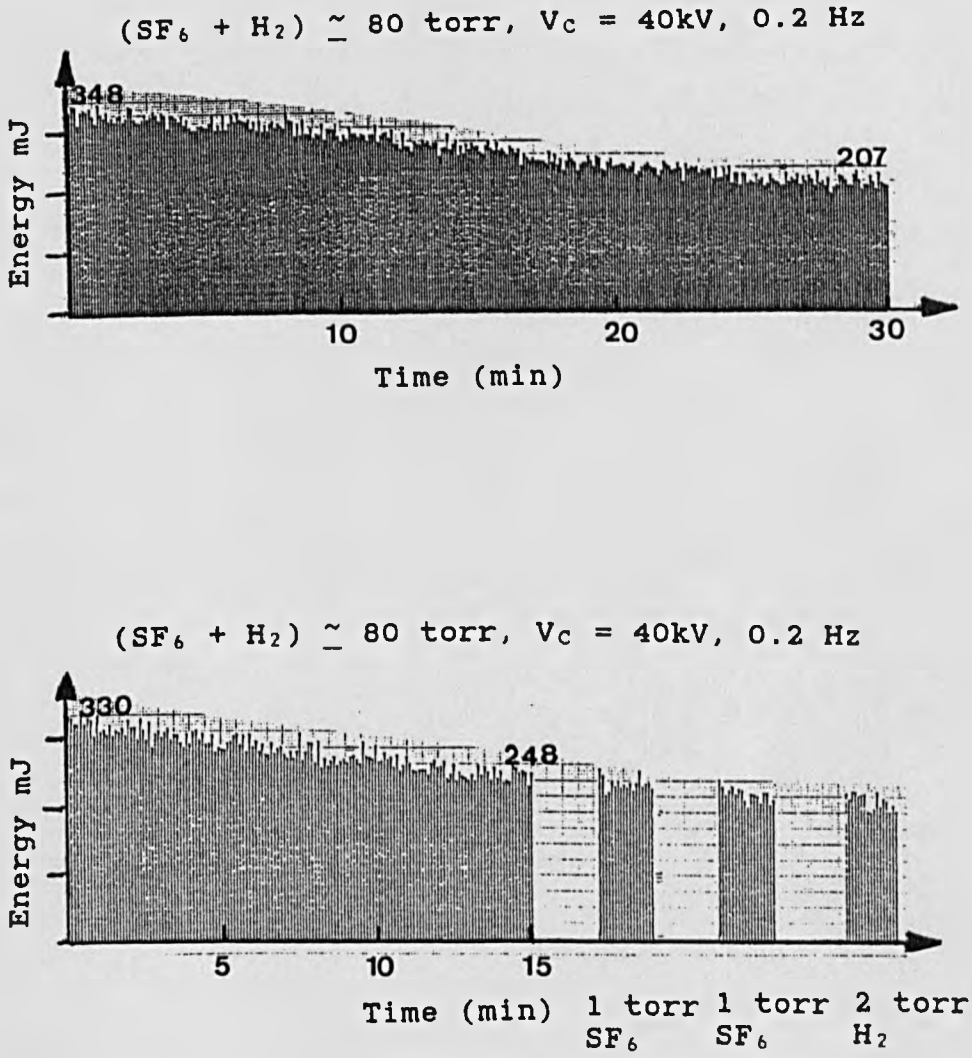

Fig. 5.18 - Monitoring of (SF_6 + H_2) Lifetime at 40kV and 0.2Hz.

5.4.2 - Divergence measurement

The laser beam divergence was measured in two different ways: (i) by scanning the beam with a Gen-Tec joulemeter covered with an 0.5mm pinhole (Fig. 5.19a), (ii) by focussing the beam onto Polaroid film using a concave mirror (R=50cm) as shown in Fig. 5.19b. In the former case the divergence was measured by obtaining the FWHM of the beam profile recorded at distances of 600 and 200mm from the output mirror. On the basis of the beam profiles shown in Fig. 5.20 a value of 3mr was obtained. In the second method the divergence was measured by dividing the spot size by the focal distances, s, and again a value of 3-4 mr was obtained.

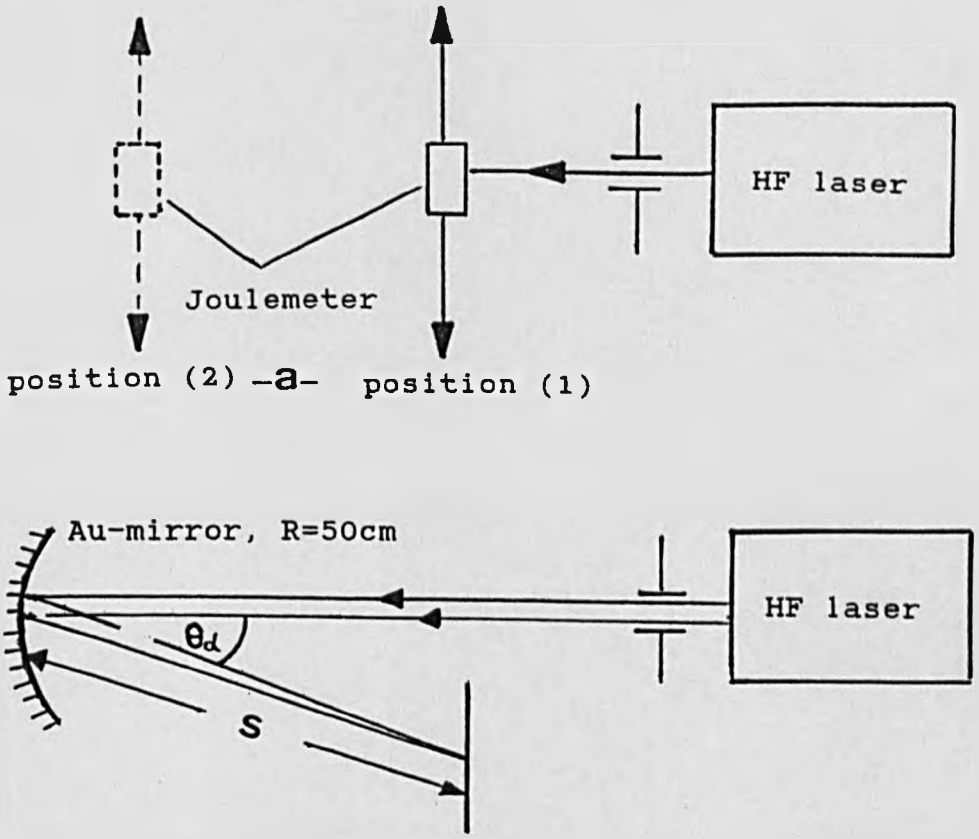

Fig. 5.19 - Measurement of HF divergence by scanning (a) and focusing (b) the beam.

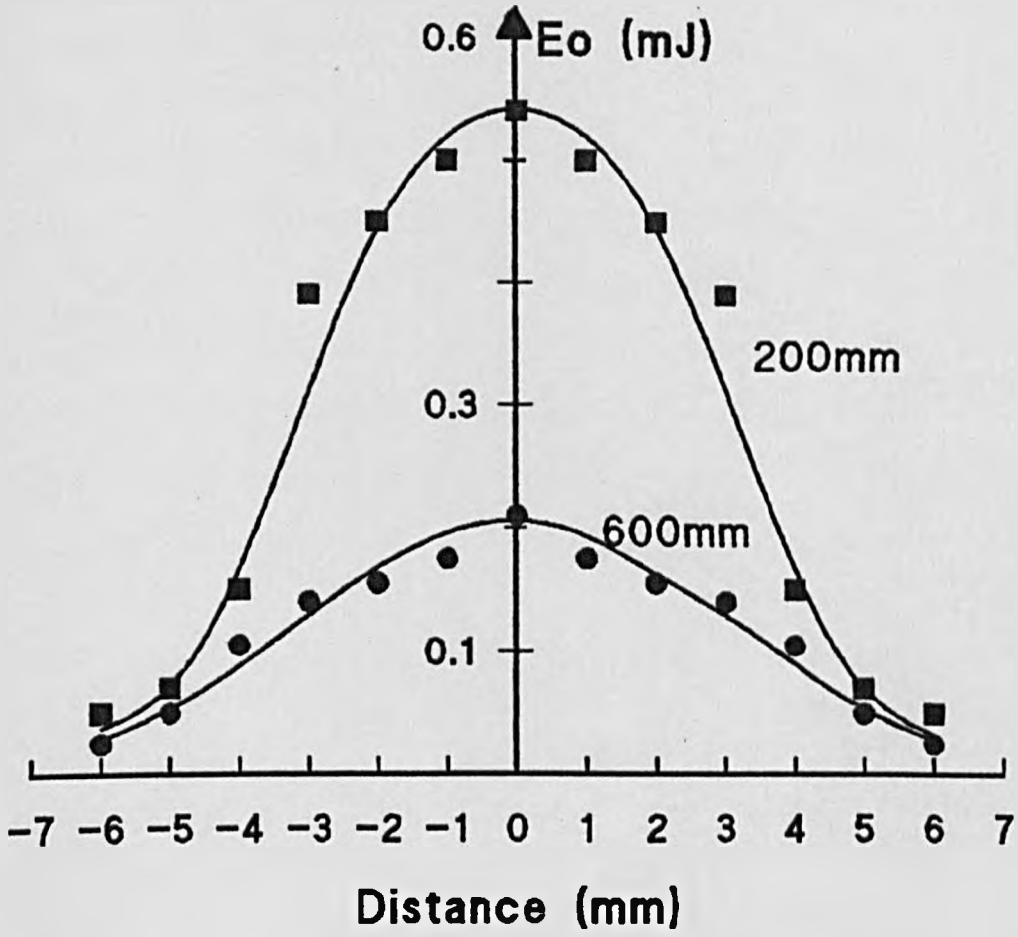

Fig. 5.20 - Evaluation of beam divergence using the scanning method.

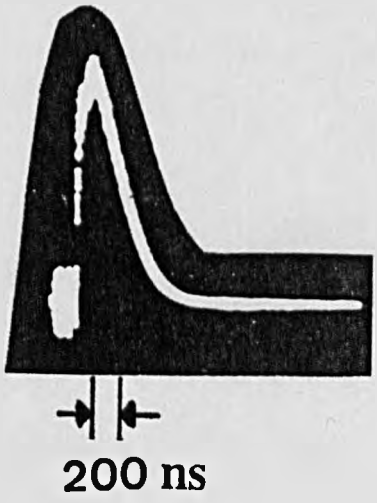

Fig. 5.21 - The pulse shape of HF at total pressure of (SF_6 + C_3H_8) $\simeq$ 60 torr, V_c = 40kV, $\tau \simeq$ 400ns.

5.4.3 - Emission spectrum

The experimental arrangement used to measure the HF laser emission is shown in Fig. 5.23 where the HF laser output was directed into a monochromator (Bentham instruments) by a 4m focal length (Fig. 5.23) gold coated mirror. The monochromator was equipped with a 300 lines/mm diffraction grating and the output detected using an SBRC gold-doped germanium IR detector cooled with liquid nitrogen. The detector was biased at 40V and its output displayed on a 7834 Tektronix oscilloscope.

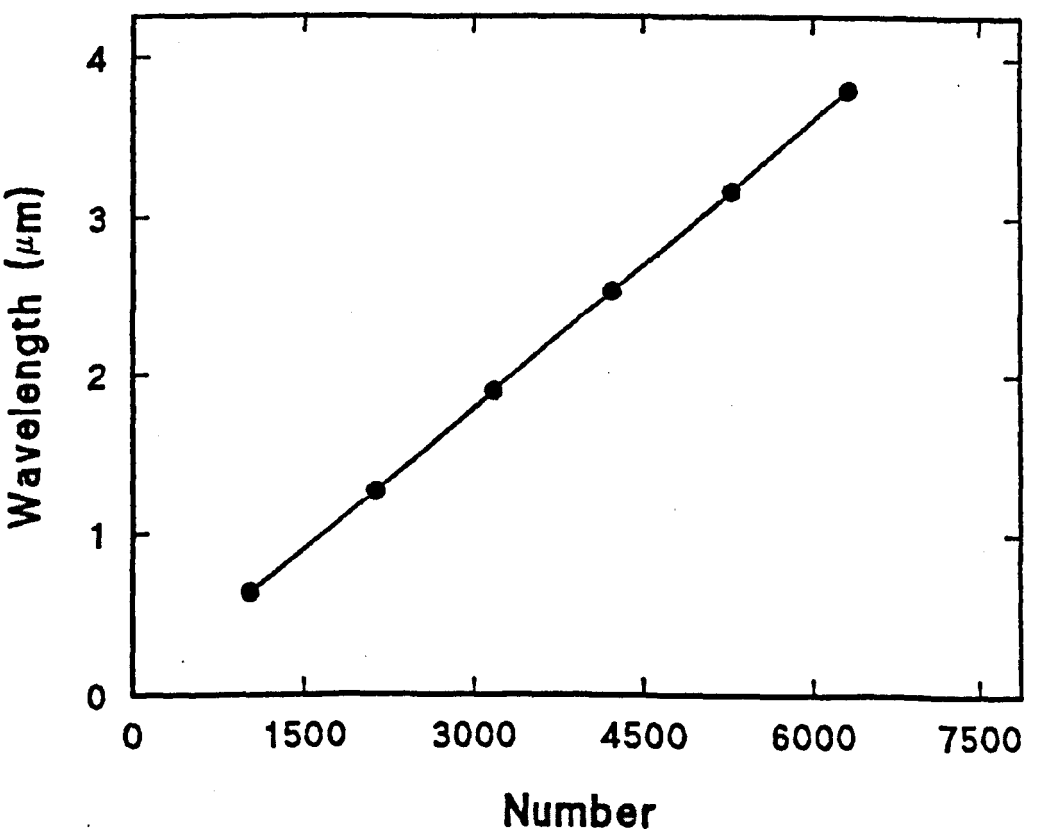

Fig. 5.22 - Calibration graph of monochromator with He-Ne.

Prior to measurement of the HF emission spectrum the monochromator was calibrated using the He-Ne laser orders between n=1 (632.82nm) and n=6 (3796.92nm) as shown in Fig. 5.22.

Table 5.2 shows that when the optimized mixture of SF_6/C_3H_8 ($\simeq$14:1) was used at Vc = 40kV, the HF laser emission spectrum consisted of 20 P-branch transitions in the 1→0, 2→1 and 3→2 bands of HF covering the wavelength range 2.678 - 2.925 μm. Fig. 5.24 shows the distribution of energy in the various lines. The dominant emissions were at 2.76, 2.78, 2.82, 2.85 and 2.92 μm. The selective transition lines of HF lasers are given in table 5.1 (44).

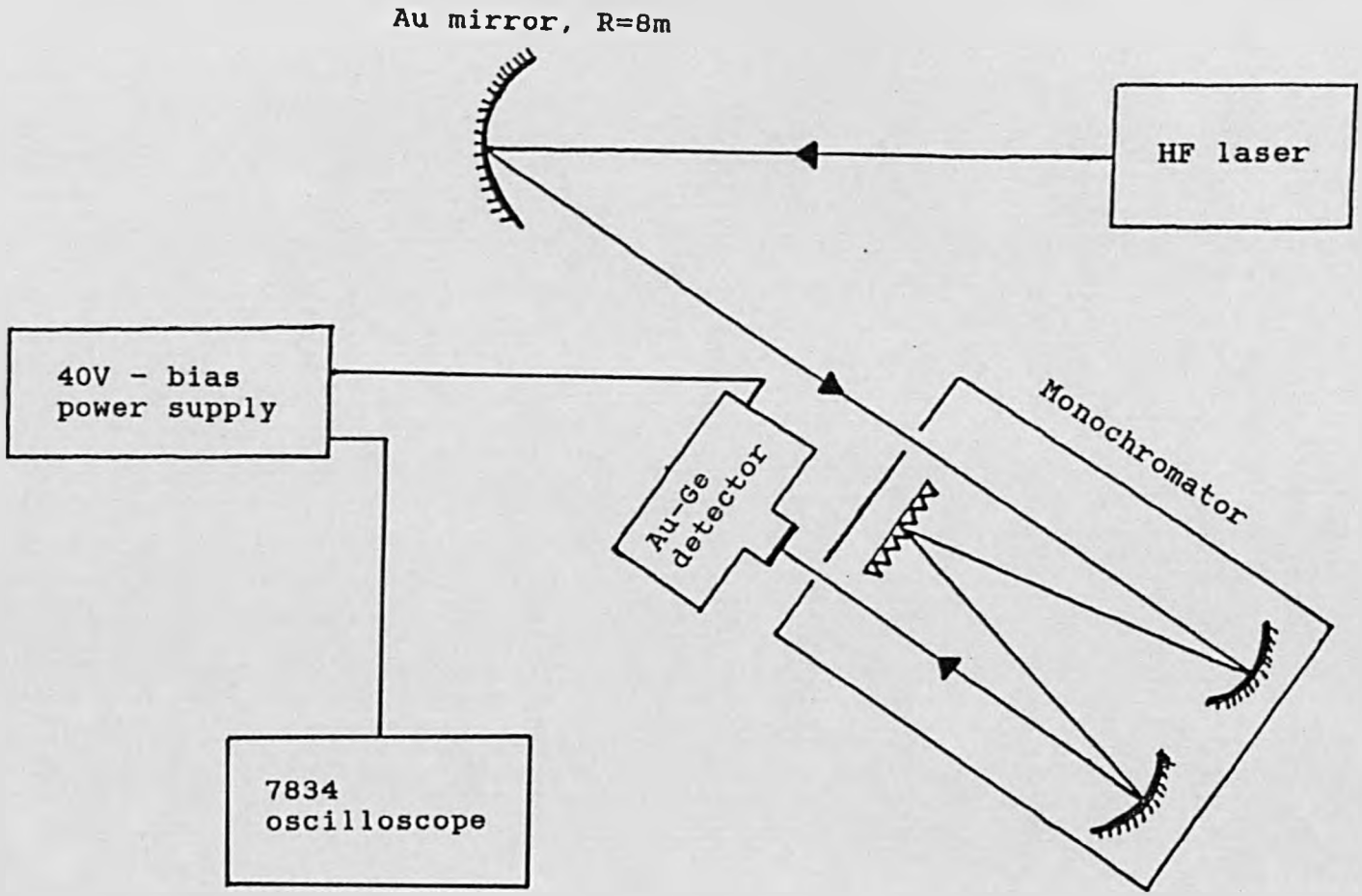

Fig. 5.23 - Experimental set up for measurement of HF emission spectrum

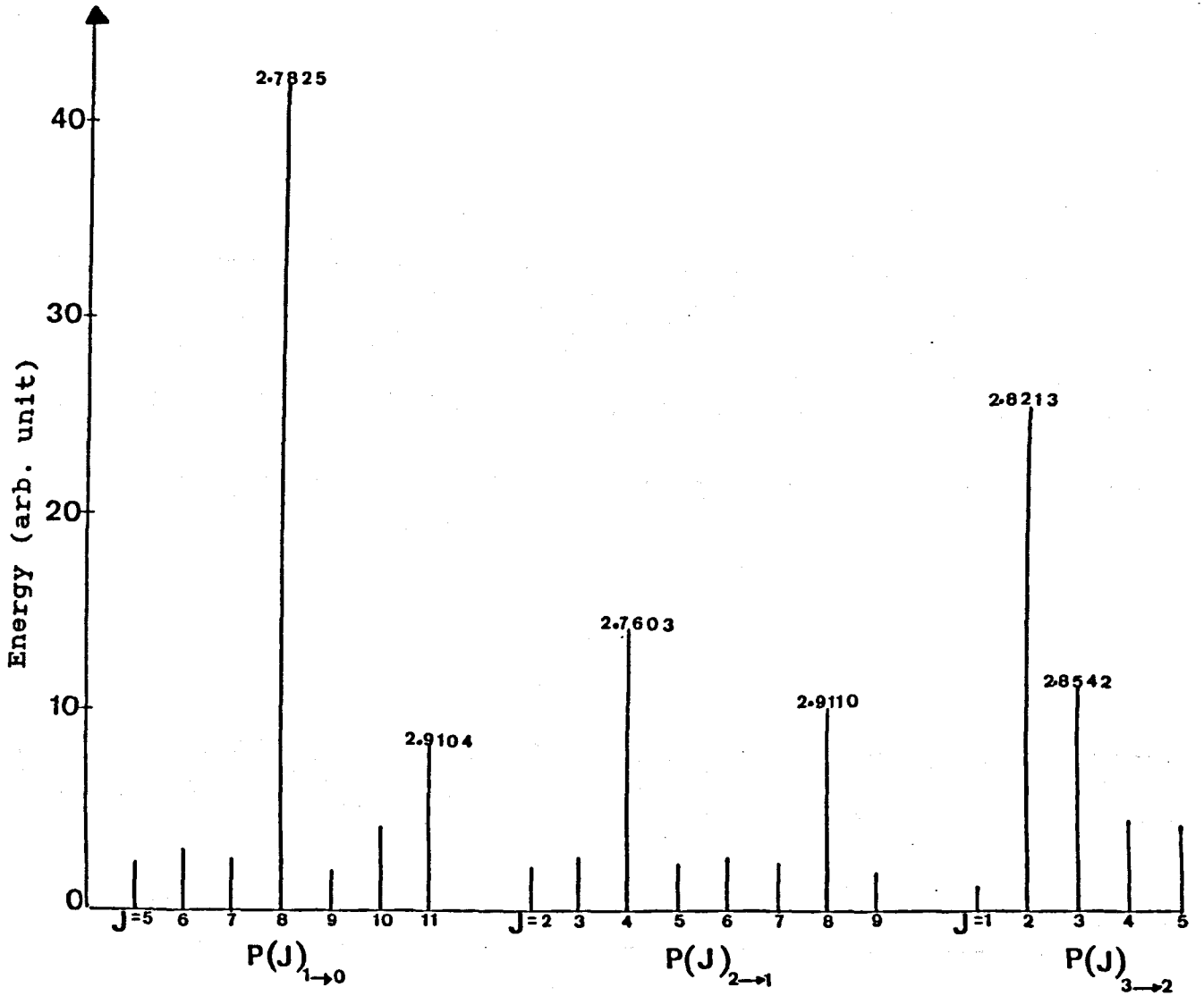

Fig. 5.24 - Energy distribution of HF emission lines.

Table 5.1 - The selective transition lines of HF lasers (44).

	WAVELENGTH IN VACUUM [MICROMETER]	TRANSITION
HF	2.41	1- 0 R(4)
HF	2.43	1- 0 R(3)
HF	2.45	1- 0 R(2)
HF	2.48	1- 0 R(1)
HF	2.551	1- 0 P(1)
HF	2.579	1- 0 P(2)
HF	2.6064	1- 0 P(3)
HF	2.6396	1- 0 P(4)
HF	2.6726	1- 0 P(5)
HF	2.7075238	1- 0 P(6)
HF	2.7440	1- 0 P(7)
HF	2.7826	1- 0 P(8)
HF	2.8231	1- 0 P(9)
HF	2.8657	1- 0 P(10)
HF	2.9103	1- 0 P(11)
HF	2.9573	1- 0 P(12)
HF	3.0064	1- 0 P(13)
HF	3.0582	1- 0 P(14)
HF	3.1125	1- 0 P(15)
HF	3.1695	1- 0 P(16)
HF	3.2292	1- 0 P(17)
HF	3.2919	1- 0 P(18)
HF	2.6608	2- 1 P(1)
HF	2.6963	2- 1 P(2)
HF	2.7275	2- 1 P(3)
HF	2.7604	2- 1 P(4)
HF	2.7952	2- 1 P(5)
HF	2.8319	2- 1 P(6)
HF	2.8705	2- 1 P(7)
HF	2.9111	2- 1 P(8)
HF	2.9539	2- 1 P(9)
HF	2.9989	2- 1 P(10)
HF	3.0461	2- 1 P(11)
HF	3.0958	2- 1 P(12)
HF	3.1480	2- 1 P(13)
HF	3.2029	2- 1 P(14)
HF	3.2603	2- 1 P(15)
HF	3.2206	2- 1 P(16)
HF	2.7902	3- 2 P(1)
HF	2.8213	3- 2 P(2)
HF	2.8542	3- 2 P(3)
HF	2.8890	3- 2 P(4)
HF	2.9257	3- 2 P(5)
HF	2.9644	3- 2 P(6)
HF	3.0052	3- 2 P(7)
HF	3.0482	3- 2 P(8)
HF	3.0935	3- 2 P(9)
HF	3.1411	3- 2 P(10)
HF	3.1912	3- 2 P(11)
HF	3.2438	3- 2 P(12)
HF	3.2991	3- 2 P(13)
HF	2.9221	4- 3 P(1)
HF	2.9549	4- 3 P(2)
HF	2.9896	4- 3 P(3)
HF	3.026	4- 3 P(4)
HF	3.065	4- 3 P(5)
HF	3.1454	4- 3 P(8)
HF	3.1492	4- 3 P(7)
HF	3.0982	5- 4 P(2)
HF	3.1350	5- 4 P(3)
HF	3.1640	5- 4 P(4)
HF	3.2151	5- 4 P(5)
HF	3.258	5- 4 P(6)

	WAVELENGTH IN VACUUM (MICROMETER)	TRANSITION
HF	3.3044	5- 4 P(7)
HF	3.333	6- 5 P(4)
HF	3.377	6- 5 P(5)
HF	10.1978	0 (28-27)
HF	10.4578	0 (27-26)
HF	10.7439	0 (26-25)
HF	11.0573	0 (25-24)
HF	11.4033	0 (24-23)
HF	11.7854	0 (23-22)
HF	12.2062	0 (22-21)
HF	12.6761	0 (21-20)
HF	13.2009	0 (20-19)
HF	13.7841	0 (19-18)
HF	14.4406	0 (18-17)
HF	15.1744	0 (17-16)
HF	16.0215	0 (16-15)
HF	18.09	0 (14-13)
HF	19.35	0 (13-12)
HF	20.835	0 (12-11)
HF	12.2619	1 (23-22)
HF	12.7006	1 (22-21)
HF	13.1877	1 (21-20)
HF	13.7277	?1 (20-19)
HF	15.0163	1 (18-17)
HF	18.8010	1 (14-13)
HF	20.1337	1 (13-12)
HF	21.6986	1 (12-11)
HF	36.5	1 (7- 6)
HF	42.4	1 (6- 5)
HF	50.8	1 (5- 4)
HF	63.4	1 (4- 3)
HF	84.4	1 (3- 2)
HF	126.5	1 (2- 1)
HF	10.5819	2 (30-29)
HF	10.8117	2 (29-28)
HF	13.2211	2 (22-21)
HF	14.2861	2 (20-19)
HF	20.9393	2 (13-12)
HF	19.55	2 (14-13)
HF	11.5408	?3 (28-27)
HF	19.1129	3 (15-14)
HF	20.3513	3 (14-13)
HF	21.7885	3 (13-12)
HF	19.915	4 (15-14)
NUMBER OF LINES IN HYDROGEN FLUORIDE		107

Table 5.2 - HF Laser emission spectrum

measured (μm)	vibrational band	transition (J)	calculation (μm)
2.6784		5	2.6726
2.7077		6	2.7075
2.7442		7	2.7440
2.7825	1 → 0	8	2.7826
2.8232		9	2.8231
2.8656		10	2.8657
2.9104		11	2.9103
2.6969		2	2.6963
2.7274		3	2.7275
2.7603		4	2.7604
2.7962		5	2.7952
2.8321	2 → 0	6	2.8319
2.8704		7	2.8705
2.9110		8	2.9111
2.9535		9	2.9539
2.7903		1	2.7902
2.8213		2	2.8213
2.8542	3 → 2	3	2.8542
2.8890		4	2.8890
2.9254		5	2.9257

1. Kasper J.V., Pimentel C.
HCl Chemical laser.
Phys. Rev. Lett., 14:352:1965.

2. Deutsch T.
Molecular laser action in Hydrogen and deuterum halides.
Appl. Phys. Lett., 10:234:1967.

3. Wolbarsht M.L.
Laser surgery: CO_2 or HF.
IEEE J.QE., 20:1427:1984.

4. Kompa K.L., Pimentel G.
Hydrofluoric acid chemical laser.
J. Chem. Phys., 47:857:1967.

5. Kompa K.L., Parker J., et al.
WF_6 - H_2 - hydrogen fluoride chemical laser: operation and chemistry.
J. Chem. Phys., 49:4257:1968.

6. Parker J., Pimentel G.
Vibrational energy distribution through chemical laser studies. II. Fluorine atoms plus chloroform.
J. Chem. Phys., 55:857:1971.

7. Coombe R., Pimental G.
Temperature dependance of the vibrational energy distributions in the reactions $F+H_2$ and $F+D_2$.
J. Chem. Phys., 59:251:1973.

8. Jacobson T.V., Kimbell G.
WC 8 - parametric studies of pulsed HF lasers using transverse excitation.
IEEE J.QE., 9:173:1973.

9. Deka B.K., Dyer P.E., James D.
A high radiance, pulsed HF laser.
Opti. Comm., 18:462:1976.

10. Wlodarczyk G.
A photoionized atmospheric pressure HF laser.
IEEE J.QE., 14:768:1978.

11. Brunet H., Mabra M., et al.
Pulsed HF/DF chemical laser using x-ray initiated discharge.
SPIE., 1031:265:1988.

12. Gerber R., Patterson E.
Intense electron-beam initiation of a high energy HF laser.
IEEE J.QE., 10:333:1974.

13. Patterson E., Gerber R.
HF laser initiated by a 300-keV electron beam.
J. Appl. Phys., 45:1822:1974.

14. Gerber R., Patterson E.
Studies of a high-energy HF laser using an electron-beam excited mixture of high-pressure F_2 and H_2.
J. Appl. Phys., 47:3524:1976.

15. Fujioka T., Kannari F., et al.
Effect of SF_6 fluorine donor on the multikilojoule HF chemical laser initiated longitudinally by intense electron beams.
J. Appl. Phys., 58:3975:1985.

16. Inagaki H., Suda A., et al.
High-efficiency, high-energy operation of an intense electron beam initiated HF chemical laser using a mixture containing a heavy fluoride MoF_6.
Appl. Phys. Lett., 49:122:1986.

17. Miller T.G., Dezenberg G.L.
Neutron-Initiated chemical laser experiments.
Report No. RR-TR-72-2., 1972.

18. Clarke J.S., Metzger D.S.
Gamma - Initiated HF laser.
IEEE J.QE., 10:736:1974.

19. Helmick H., Fuller J., et al.
Direct nuclear pumping of a helium-xenon laser.
Appl. Phys. Lett., 26:327:1975.

20. Guyot J., Miley G., et al.
Nucl. Sci. Eng., 48:373:1972.

21. Wilson J., Deyong R., et al.
Nuclear-pumped 3He-Ar laser modelling.
J. Appl. Phys., 51:2421:1980.

22. Kushner M.J.
Characteristics of a UF_6 - H_2/HF nuclear-pumped laser.
J. Appl. Phys., 51:2421:1980.

23. Spencer D., Beggs J., et al.
Small-scale CW HF (DF) chemical laser.
J. Appl. Phys., 48:1206:1977.

24. Deka B.K., Dyer P.E.
Mode control and performance studies of a pulsed unstable resonator HF/DF laser.
IEEE J.QE., 14:661:1978.

25. Yano K., Bobitch H.
Small-signal gain measurements in a CW chemical laser.
IEEE J.QE., 14:12:1978.

26. Pearson P.R., Lamberton H.
Atmospheric pressure Co_2 lasers giving high output energy per unit volume.
IEEE J.QE., 8:145:1972.

27. Judd O.P.
An efficient electrical CO_2 laser using preionization by UV radiation.
Appl. Phys. Lett., 22:95:1973.

28. Sequin H., Tulip J., et al.
Ultraviolet photoionization in TEA lasers.
IEEE J.QE., 10:311:1974.

29. Greene A., Brau C.
Theoretical studies of UV-preionized transverse discharge KrF and ArF lasers.
IEEE J.QE., 14:951:1978.

30. Dreiling T.D., Mcgann R.L.
High-efficienty DF - Co_2 pulsed chemical laser.
Appl. Phys. Lett., 56:1397:1991.

31. Brink D.J., Hassan V.
Compact megawatt helium-free TEA HF/DF.
J. phys. E:sci. Inst., 13:553:1978.

32. Chang T.Y.
Improved uniform-field electrode profiles for TEA Laser and high-voltage applications.
Rev. Sci. Inst., 44:405:1973.

33. Slepian J., Berekey W.
J. Appl. Phys., 11:765:1940.

34. Spiers G., Vass A., et al.
The effect of sliding spark, Corona and semiconductor preionizors on the operation and output of a TEA CO_2 laser.
Opt. Comm., 62:256:1987.

35. Serafetinides A., Papadopoulos.
Investigation and comparison of preionization processes in gas laser systems.
Opt. Comm., 63:264:1987.

36. Serafetinides A., Rickwood K.
Improved performance of small compact TEA pulsed HF lasers employing semiconductor preionizers.
J. Phys. E: Sci. Inst., 22:103:1989.

37. Gorton E.K., Cross P.H., et al.
A semiconductor preionized DF laser.
Opt. Comm., 70:245:1989.

38. Lacour B., Vannier, et al.
Phototriggering of 1-J excimer laser using either UV or X-rays.
J. Appl. Phys., 62:754:1987.

39. Issa M., (Msc. thesis).
Development and studies of axial x-ray preionized TEA CO_2 laser.
Hull Univ. - 1988.

40. Salvettie G., (PhD. thesis).
Investigations of high power UV preionized Co_2 laser.
Hull Univ. - 1978.

41. Tallman C.R.
Optical society of American excimer laser meeting.
Charleston, S. Carolina, Sept. 11-13, 1979.

42. Lyman J.L.
Computer model of the SF_6-H_2 electrical discharge chemical laser.
Appl. Opt., 12:2736:1973.

43. Peuch V., Prigent P., Brunet H.
High-efficiency, high-energy performance of a pulsed HF laser pumped by phototriggered discharge.
Appl. Phys. B., 55:183:1992.

44. Beck R., Englisch W., Gürs.
Table of Laser lines in gaseous and vapours.
Springer-Verlag - 1978.

Chapter 6

Fluoride-glass fibre studies

6.1 - Introduction

The HF laser as discussed earlier (chapter 5) operates in a wavelength region (2.6-3μm) where tissue by virtue of its high water content exhibits strong absorption (1). This, as has been noted in chapter 7 helps to restrict thermal injury to a relatively small zone when the laser is used in a pulsed mode to ablate tissue. Other mid-IR lasers such as Er:YAG and Ho:YAG have also been shown to produce well defined incisions with small zones of thermal injury (2-5). For such clinical applications it is often desirable to deliver the laser using a fibre and although fibre delivery studies have been reported for Er:YAG and Ho:YAG lasers (6-9) there have not been similar investigations for the pulsed HF laser.

An advantage of the HF laser over other mid-IR lasers for carrying out basic studies on tissue ablation is that relatively short duration (<1μs) pulses can be generated using a simple TE device (chapter 5). In contrast, whilst Er:YAG and Ho:YAG can be Q-switched to produce short pulses, most tissue ablation studies reported for both fibre and direct beam delivery have involved 'normal mode' pulses having long durations (~200μs). This makes meaningful comparison of results obtained with short pulses excimer lasers difficult.

In this chapter the suitability of a fluoride glass fibre for delivering short (~400ns) pulses from the multiline HF laser at sufficiently high fluences for use in tissue

ablation is evaluated. The choice of fluoride glass was dictated by its ultralow intrinsic attenuation in the mid-IR and low toxicity compared with, for example, fused silica (high absorption in the 2-3μm region) or KRS-5 (thalium toxicity) fibres (10). Measurements reported include the distributed attenuation coefficient of the fibre for the multiline HF laser, end losses, the characteristic output beam divergence and fibre lifetime at various operating fluences. Useful output fluences ($\leq 7 Jcm^{-2}$) are shown to be obtainable making this fibre-laser system suitable for soft tissue studies as elaborated upon in subsequent chapters.

6.2 - IR laser-fibre experiments

6.2.1 - Experimental: Laser and fibre

The HF laser used in these experiments has been described in chapter 5. Measurements of the fibre energy transmission for HF laser radiation were made using the experimental setup shown in Fig. 6.1. The output from the laser was passed through a circular aperture to select a region of uniform fluence and this aperture was then suitably imaged onto the target zone (fibre face or tissue sample) using an NaCl lens of 50mm focal length. A set of glass attenuators was used to vary the fluence, energy measurements being made using a Gen-Tec pyroelectric joulemeter. A beam splitter (ir grade quartz) following the aperture directed a small fraction of the output beam onto an InAs photodiode (Judson J12) allowing the relative laser output to be monitored on a shot-to-shot basis.

A fluoride glass optical fibre (mixed metal core and cladding, with an acrylate coat) supplied by Infrared Fibre

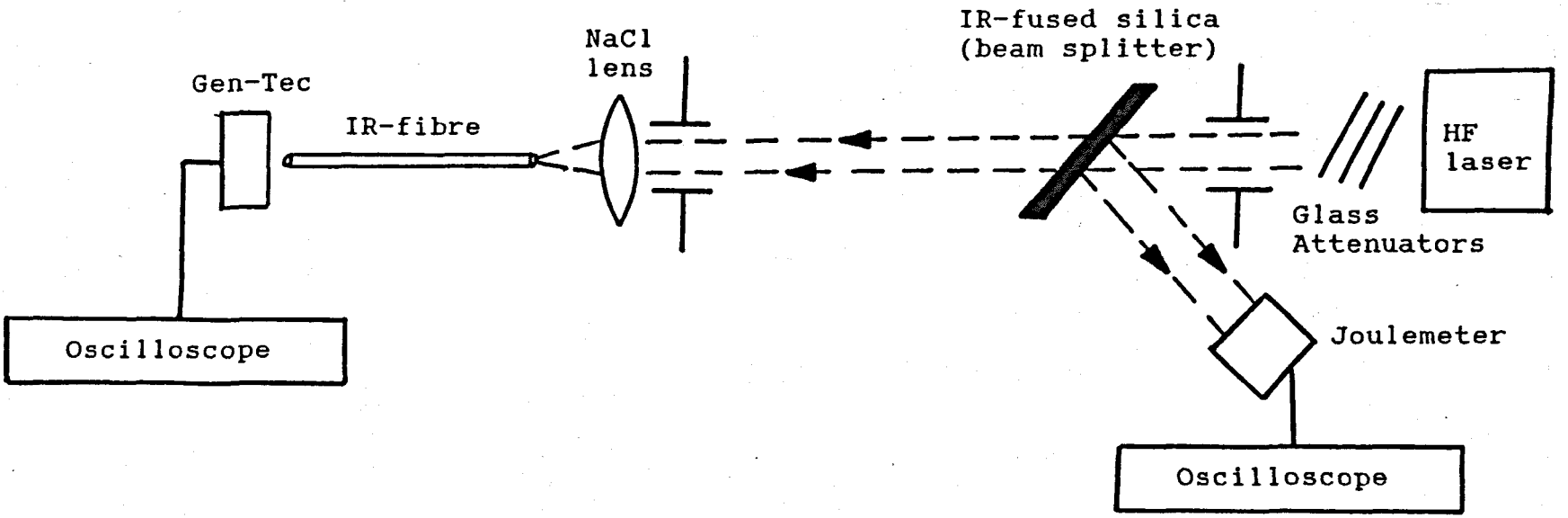

Fig. 6.1 - Experimental setup for measurement of fibre energy transmission as a function pulse numbers.

Systems (silver spring, MD, USA) was used in the experiments. The diameters of the core and core-plus cladding were 500 and 600μm, respectively. The attenuation of this fluoride glass fibre as measured by the manufacture is shown in Fig. 6.2 where the solid line indicates attenuation obtained with reagent-grade materials and the broken line the lower attenuation that can be obtained by using purer raw materials.

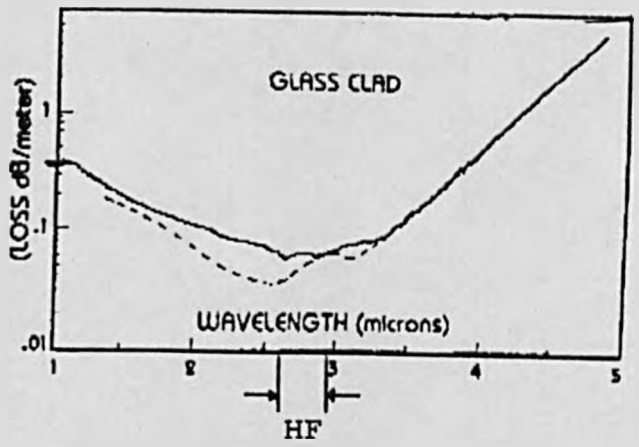

Fig. 6.2 - Attenuation curve of fluoride glass fibre. (Infrared Fibre Systems, Inc.).

It is evident that loss is minimized around 2.5-3μm where it drops to $\leq 0.1 dBm^{-1}$. A major problem associated with this large diameter fluoride glass fibre was found to be its brittleness. Great care was necessary when handling it and only very gentle bends could be tolerated without fracture.

This ruled out making measurements of the effect of bending on loss and studies were confined to essentially straight samples. Prior to all experiments the fibre ends were cleaved, polished using aerosol cutting polish (RS.556-34) and then inspected under visible light illumination using an optical microscope (Fig. 6.3a). As can be seen these steps provided a visually good quality surface and the optical illumination was able to clearly delineate the core, cladding

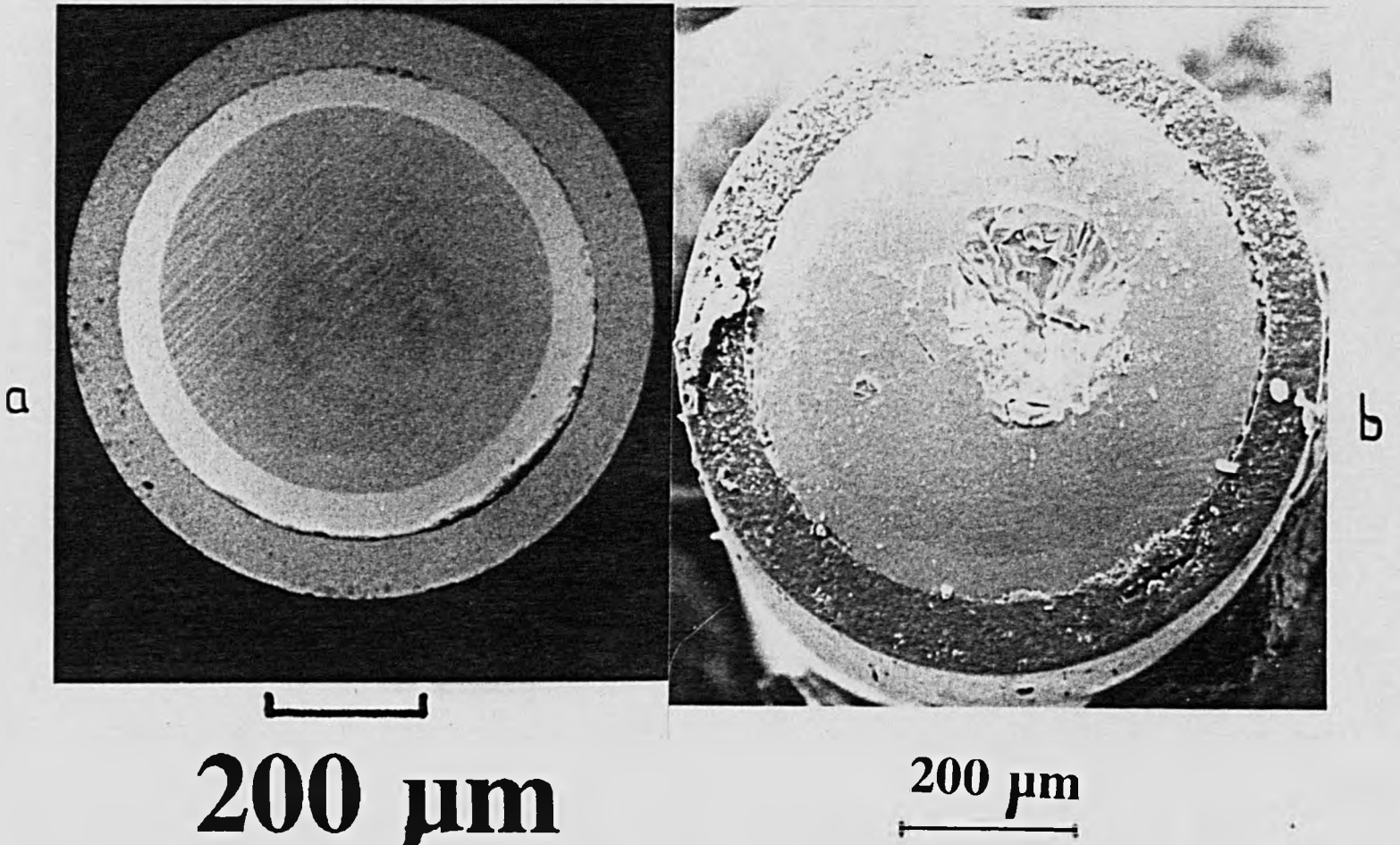

Fig. 6.3 - Fluoride glass fibre (a) Optical micrograph of polished fibre under white light transmission. The core diameter is 500µm. (b) SEM of damaged input face of fibre, 1 pulse at 35Jcm^{-2}.

and coating regions.

For studies of the fibre end-face loss a short length of fibre (~30mm) was fitted with a simple photoacoustic sensor (11) based on a PVDF piezoelectric film. This sensor, as shown in Fig. 6.4, consisted of a single layer of 9μm thick PVDF film (10x20mm^2) wrapped around a perspex cylinder through which the fibre passed. Intimate contact was maintained between the fibre and cylinder by means of silicone grease. A second cylinder of perspex was used to clamp the film in place (Fig. 6.4). Electrical contacts was made to the aluminized PVDF film using silver epoxy and the output leads taken to a 1MΩ Tektronix amplifier in a Tektronix 7834 oscilloscope. In this way thermoelastic stress waves generated by heating as a result of laser absorption at the fibre face could be detected following their propagation through the fibre and inner cylinder of the photoacoustic sensor. In addition, for some experiments a sensitive ir detector (InAs photodiode Judson J12) was employed to detect laser radiation scattered from the fibre at different positions along its length.

6.2.2 - Transmission and fibre damage measurements

Measurements of the fibre energy transmission for HF laser radiation were made by imaging the output beam on to the front face of the fibre and measuring the output energy using a pyroelectric joulemeter. The input beam was arranged to cover ~70% of the core area (12) and was input at an effective aperture ratio of 7, well within the 0.22 numerical aperture of the fibre. The cut-back technique was used to

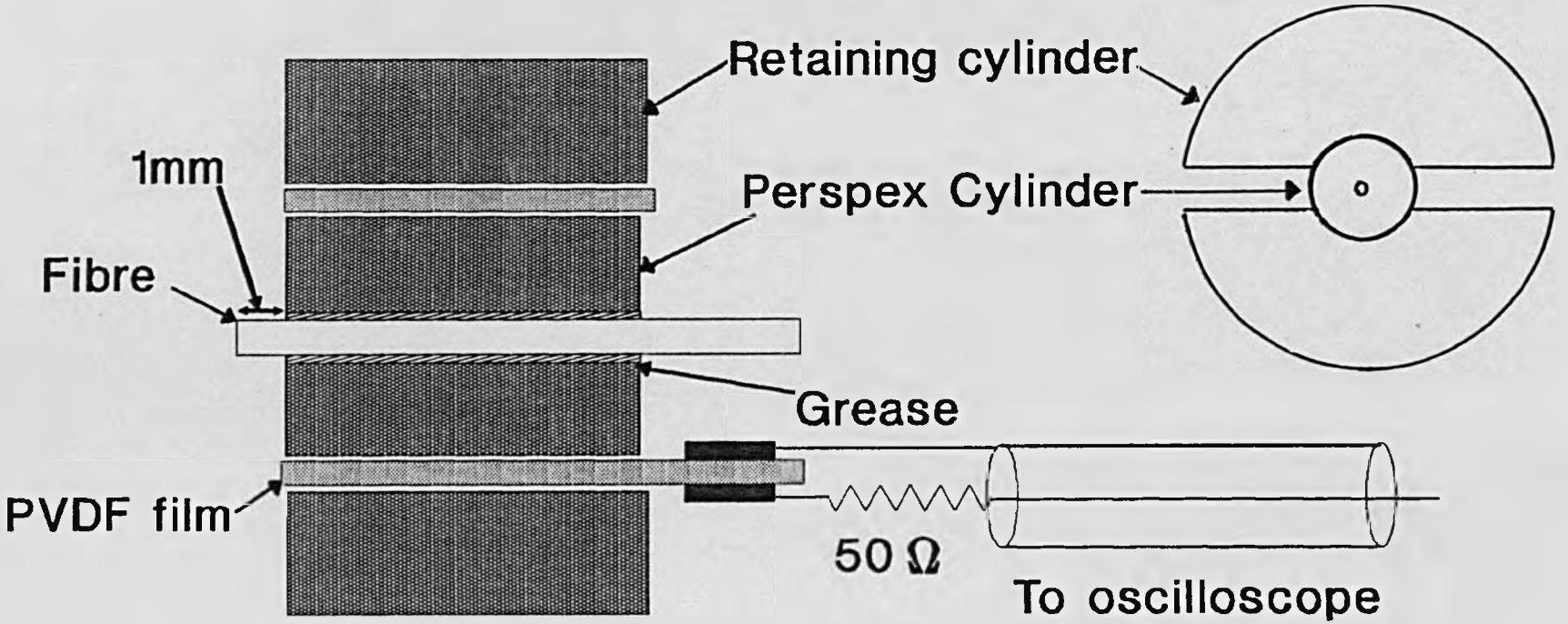

Fig. 6.4 - Schematic diagram of photoacoustic transducer used to investigate loss at the input surface of fibre.

estimate the distributed loss coefficient and the end losses of the fibre: starting with a 73cm long fibre, the transmission was measured and then the fibre progressively reduced in length, each time repolishing the cleaved end and repeating the measurements. The fibre transmission E_T, can be expressed as;

$$E_T = T_i T_o \, e^{-K(L)L} \qquad 6.1$$

where T_i and T_o are the transmission factors at the input and output faces, L is the fibre length and K(L) the distributed loss which may be length dependent.

By plotting the logarithm of the transmission, InE_T, Vs L it is thus possible to determine K(L) and also estimate T_iT_o by extrapolating to L=0. Results obtained for the fluoride glass fibre are shown in Fig. 6.5 for three input fluence levels. In each case InE_T decreases at an approximately constant rate with increasing L beyond about 20cm giving a mean value of $K = 0.15 \pm 0.03m^{-1}$ for the distributed loss. The more rapid drop in InE_T for $L \leq 20cm$ may be due to a fraction of the beam exciting cladding modes which rapidly attenuate with distance. The form of the curves in Fig. 6.5 indicates that the fall in transmission with increasing fluence can principally be attributed to increased end losses associated with coupling energy into (and out of) the fibre. Extrapolation to L=0 gives an estimated end loss of $\sim$19% per surface at $0.5Jcm^{-2}$ increasing to $\sim$24% per surface at $19Jcm^{-2}$ assuming the end loss is equally distributed between each end (ie $T_i \sim T_o$). Additional evidence for the presence of non-linear absorption at the entrance surface to the fibre was obtained from measurements using the photoacoustic transducer

described in section 6.2.1. With the fibre input surface located 1mm from front face of the transducer as indicated in Fig. 6.4, measurements of the voltage response were made as a function of the input fluence.

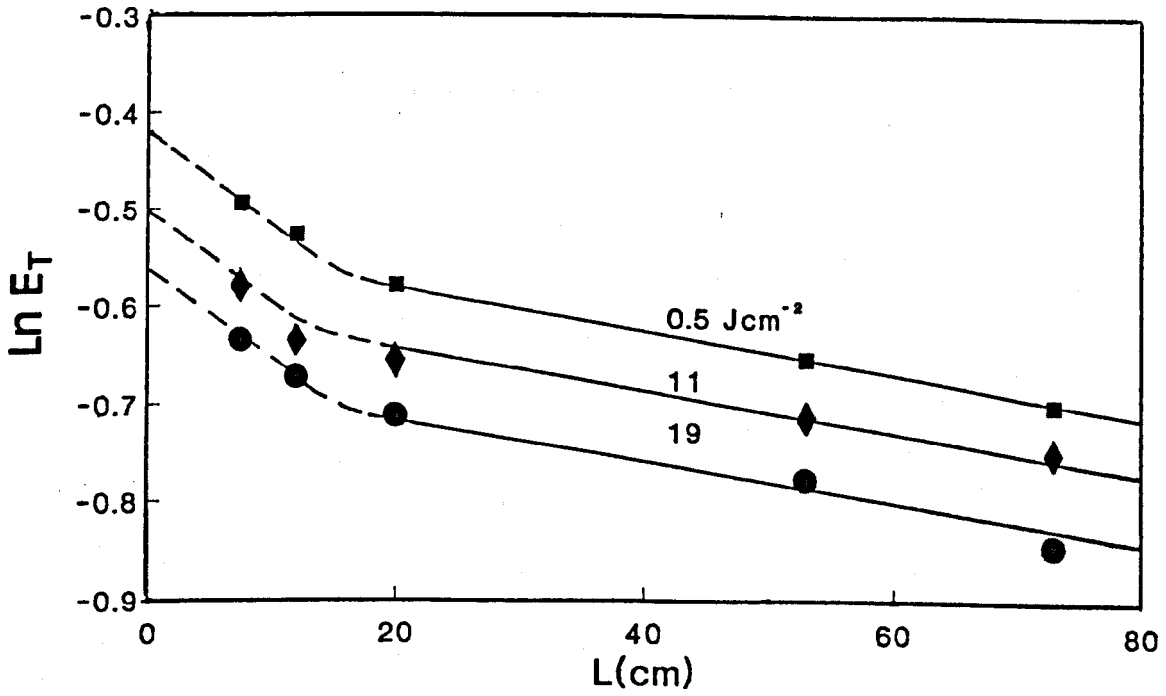

Fig. 6.5 - Plot of InE_T Vs length for fluoride glass fibre at input fluences of 0.5, 11 and 19Jcm^{-2}.

The transient voltage response shown in Fig. 6.6 (see inset) consists of an initial step delayed by ~2μs with respect to the HF laser pulse, and rising to produce a relatively large amplitude pulse peaking at ~4μs. The initial delay is consistent with the propagation time for an acoustic wave to travel through the fibre and the perspex cylinder having originated at or near the fibre surface. The maximum signal amplitude, shown in Fig. 6.6 as a function of the input fluence, exhibited a linear increase up to ~15Jcm^{-2} but beyond this increased considerably more rapidly suggesting that the absorption loss is non-linearly related to the

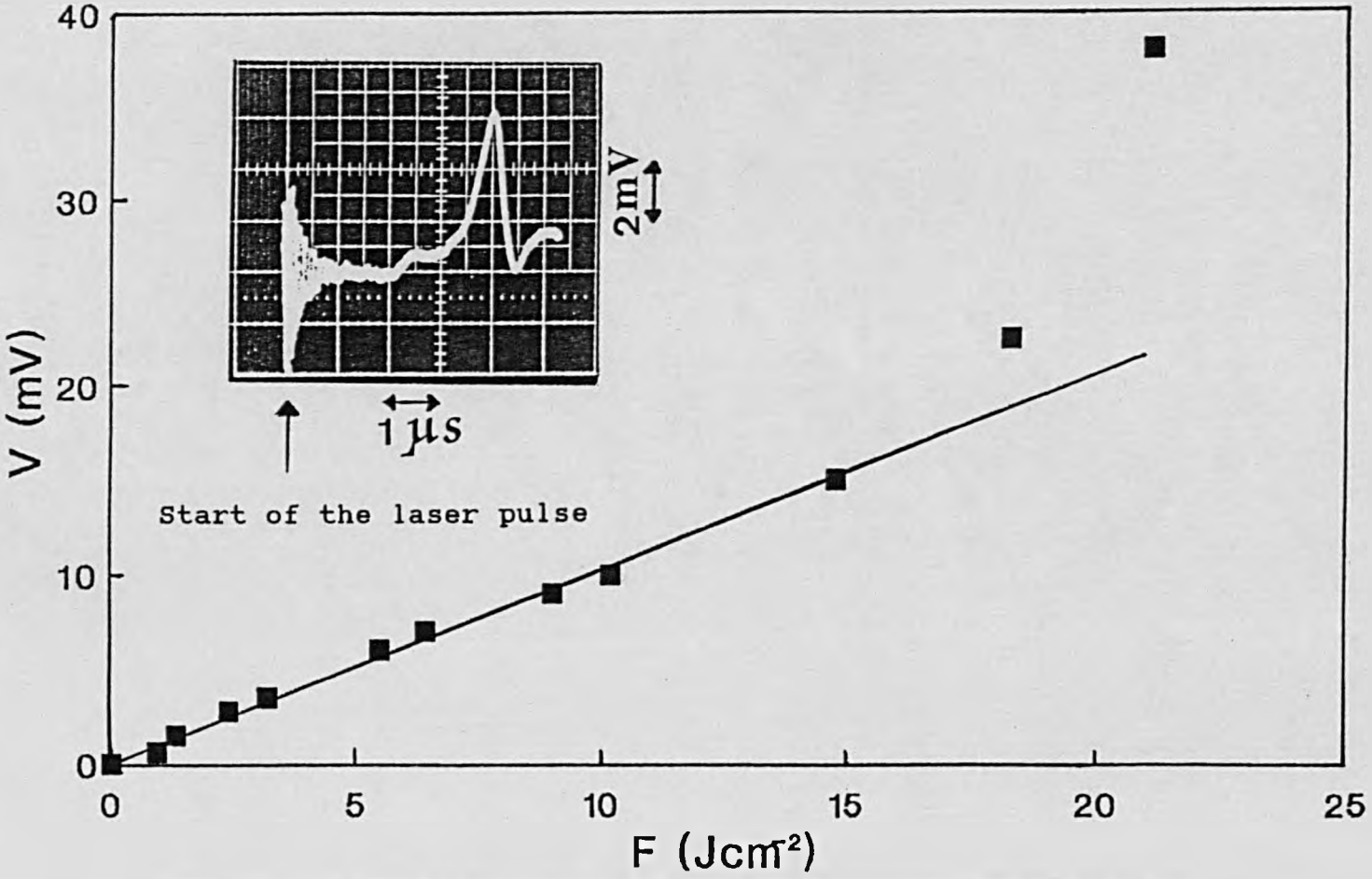

Fig. 6.6 - Peak amplitude of the photoacoustic transducer as a function of input fluence to the fibre and the transient response (inset) of transducer for fibre irradiated at an input fluence of 5.5 Jcm^{-2}.

fluence. The origin of the stress-wave signal is assumed to be the thermoelastic effect produced by the local temperature rise associated with the absorption of laser radiation at the fibre input surface and its subsequent decay to heat.

At high fluence where physical damage resulted at the fibre input face, the response of the photoacoustic transducer exhibited a relatively complicated behaviour. The first pulse caused plasma formation as evidenced by a bright spark and audible noise and the recorded photoacoustic signal was essentially unipolar (Fig. 6.7; 37Jcm^{-2}). The second pulse produced an even brighter and louder plasma response and again a unipolar, compressive photoacoustic signal but with continued exposure the plasma became progressively weaker and the signal decreased correspondingly (Fig. 6.7). This is illustrated by the steady drop in peak signal from the transducer after the second pulse which is plotted in Fig. 6.7. It is likely that the initial signals are largely dominated by contributions from the (high pressure) plasma found at the surface the signal then weakening as the surface 'conditions' and plasma formation ceases ie the fibre input face becomes cleaner and surface radiation absorption decreases. The precise mechanism leading to non-linearity is not known but it most likely relates to absorption at surface states at the fibre input (and possibly output) faces.

Measurements using the side-viewing in photodiode appeared to rule out physical damage as a contributory factor to loss. This is evidenced by the constancy of the scattered signal (Fig. 6.8) with number of laser pulses, even at fluences considerably above the value at which the photo-

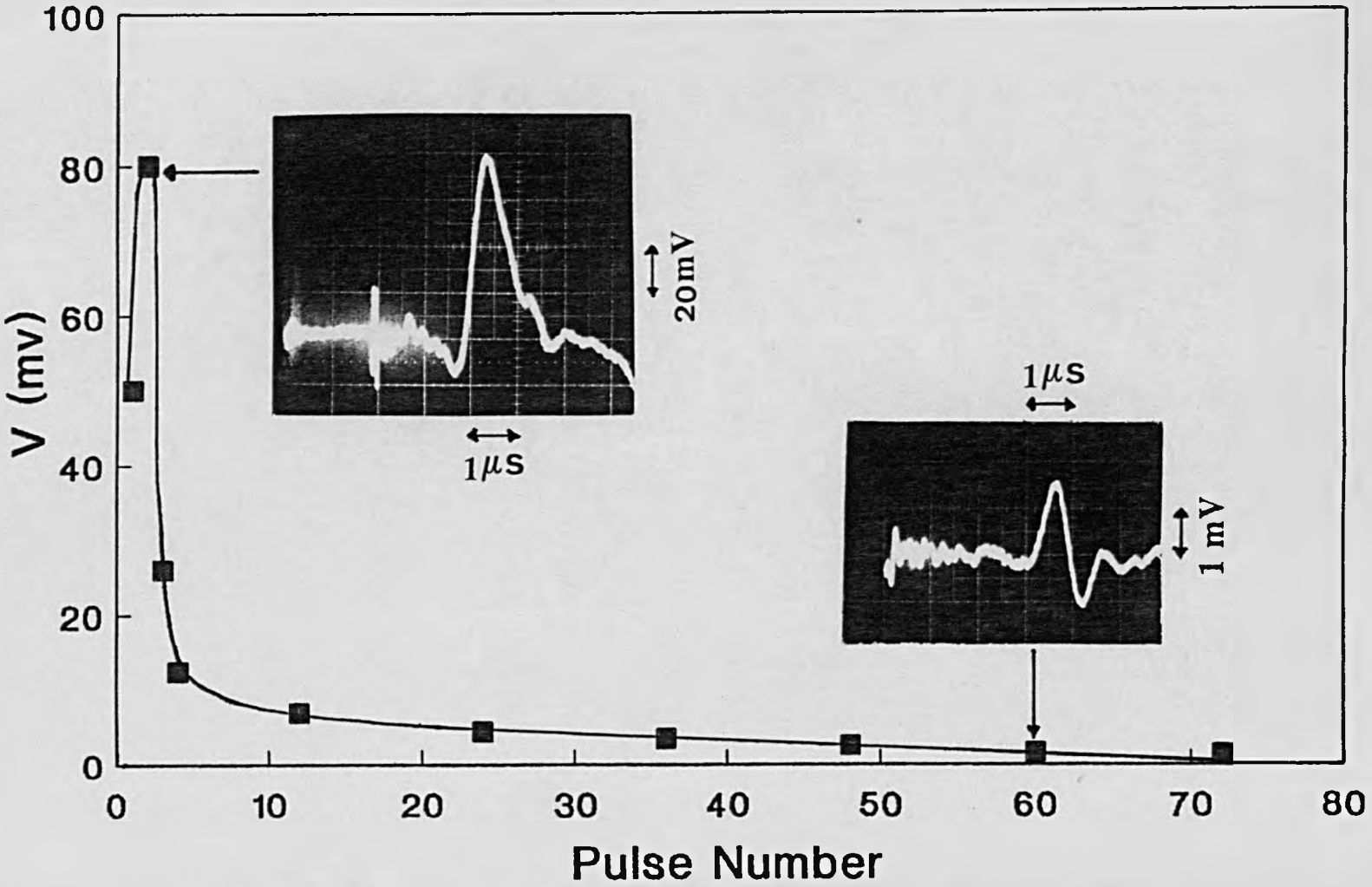

Fig. 6.7 - Peak amplitude of the photoacoustic transducer as a function of pulse number at 37Jcm^{-2}.

acoustic repsonse became non-linear (Fig. 6.6) and increased transmission loss (Fig. 6.5) occured. In contrast, at higher

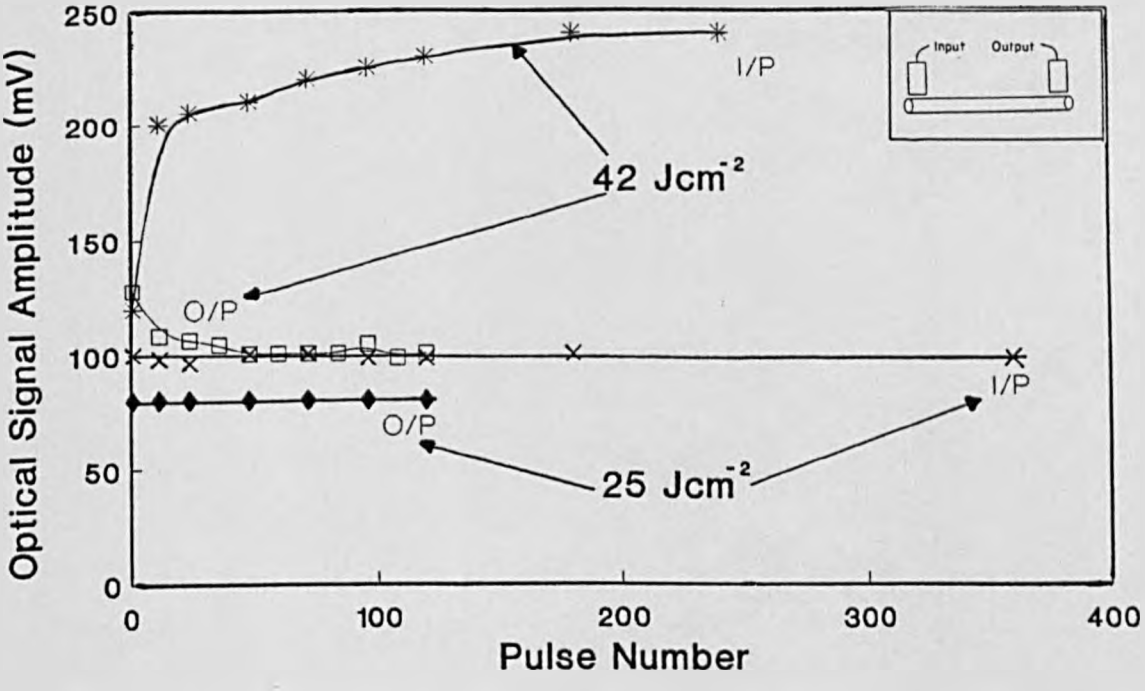

Fig. 6.8 - Amplitude of the optical signal scattered from the fibre as a function of number of pulses.

fluences ($\geq$32Jcm^{-2}) where catastrophic laser damage to the input face of the fibre occured (Fig. 6.3b), the scattered signal increased abruptly as is shown in Fig. 6.8. In this case input radiation is scattered out of the core because of the damaged end face. This is illustrated by the results in Fig. 6.9 obtained at an input fluence of 37Jcm^{-2} which show the output signal from the side viewing IR detector at various positions with respect to the input surface. The signal maximizes (a in Fig. 6.9), near the input surface where, presumably scattering, is strongest, then decreased to zero over the most of length (b in Fig. 6.9) and finally rises again due to back scattering at the output face (c and d Fig. 6.9).

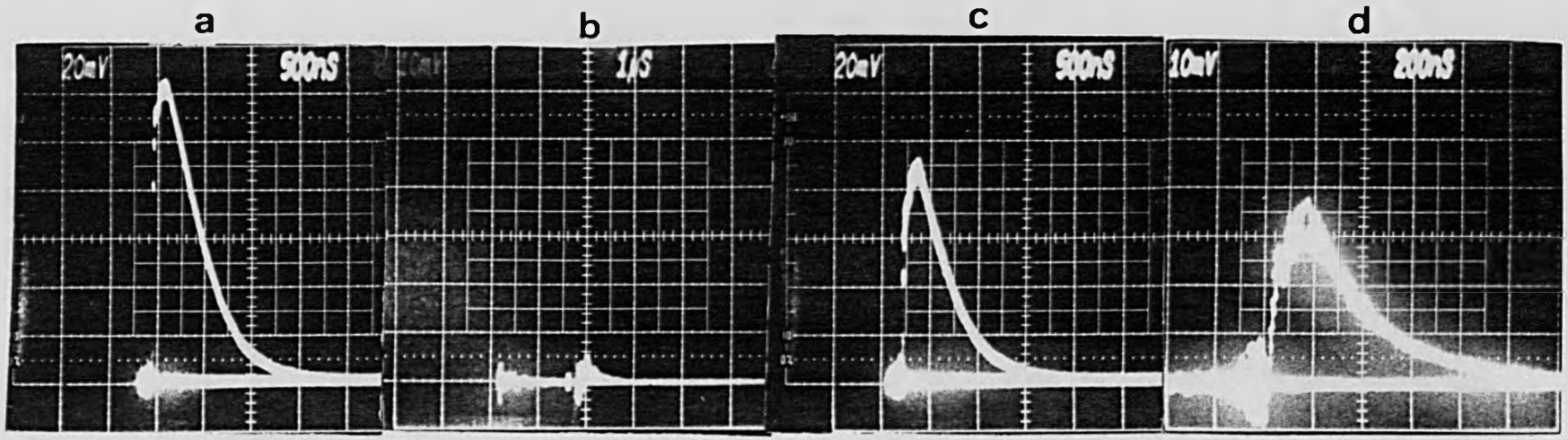

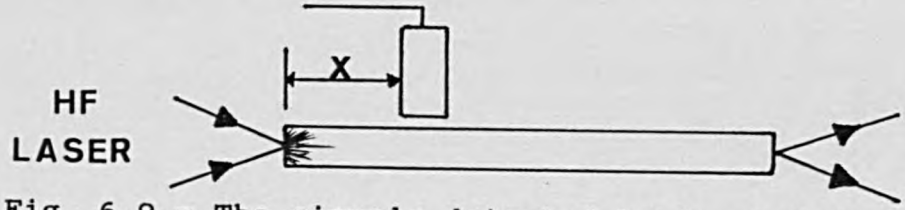

Fig. 6.9 - The signals detected by ir photodiode from different positions of the fibre at 37Jcm^{-2}. (a) x = 0 (input), (b) x = 7.5cm (middle), (c) x = 14cm, (d) x = 15cm (output).

The fibre transmission can be conveniently summarized by plotting the output Vs the input fluence as shown in Fig. 6.10 for a fibre length of L=15cm. Here the output fluence from the fibre was calculated using the core area and measured output energy and the results are based on the transmission after exposure to 100 pulses at each fluence. For input above $\sim$15Jcm^{-2} the transmission begins to fall due to increasing end losses and beyond $\sim$32Jcm^{-2} catastrophic damage is produced by the $\sim$400ns duration HF laser pulse and the output fluence drops sharply.

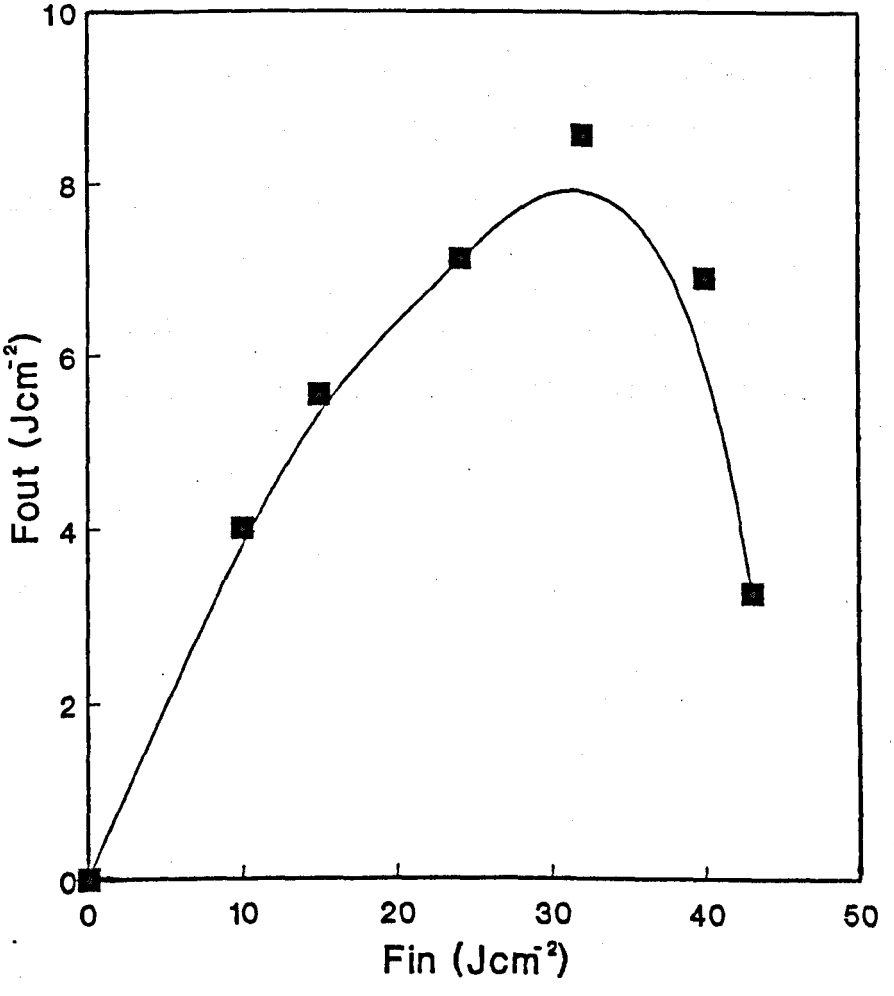

Fig. 6.10 - Plot of variation of output fluence with input fluence in a 15cm long fibre for multiline HF laser.

Tests of the fibre lifetime could only be carried out over a relatively small number of pulses because of the low pulse-rate of the laser. However, the limited results obtained indicated that for input fluences $\leq 15 Jcm^{-2}$ the fibre transmission remained constant for at least 700 pulses as shown in Fig. 6.11. At higher fluences not only was the initial transmission lower but this also continued to decrease with continued exposure as indicated, for example, by the results for a fluence of $24 Jcm^{-2}$ (Fig. 11). These results, together with those in Fig. 10, indicate that the present fluoride fibre would have practical utility for sub-microsecond HF laser pulse delivery provided the output fluence for a $\sim$1m long fibre was limited to $\leq 7 Jcm^{-2}$. For comparison it should be noted that long pulse ($\geq 70 \mu s$) solid-state lasers in this wavelength region can be transmitted through similar fibres at much higher fluence level ($\sim 240 Jcm^{-2}$) because of the lower irradiance involved (6).

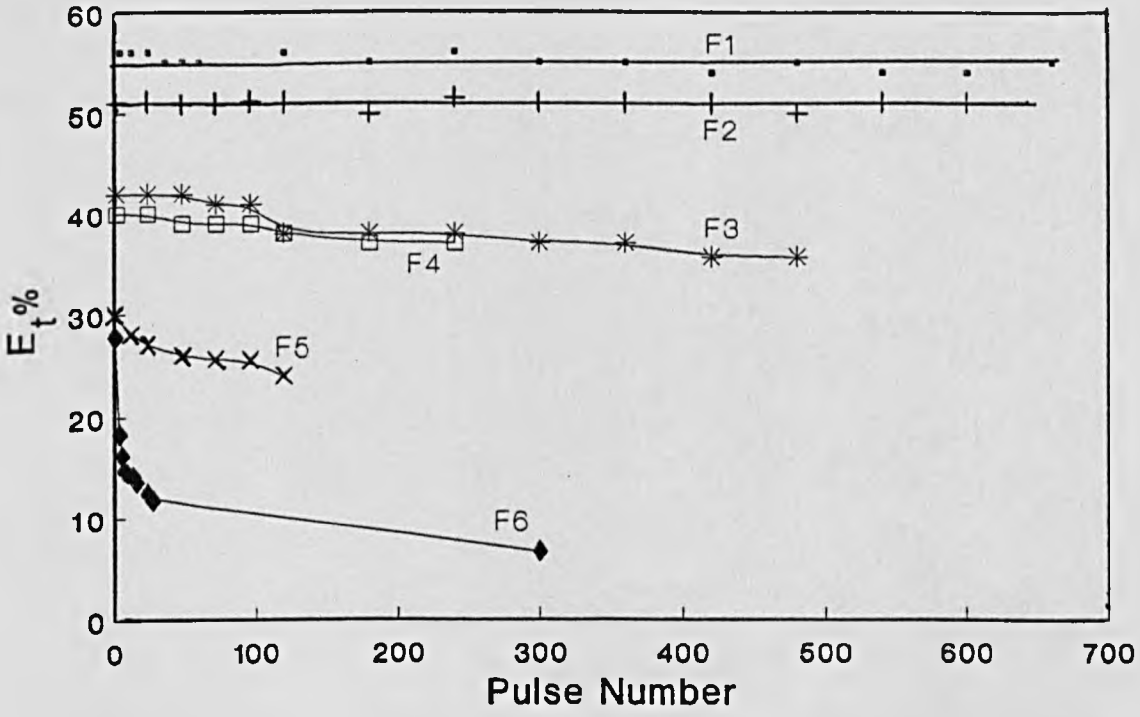

Fig. 6.11 - Fibre transmission as a function of number of laser pulses for various input fluences; F_1 = 10Jcm^{-2}, F_2 = 15Jcm^{-2}, F_3 = 24Jcm^{-2}. F_4 = 32Jcm^{-2}, F_5 = 40Jcm^{-2}, F_6 = 43Jcm^{-2}.

6.2.3 - Output beam divergence from fibre

In fibre based ablation it may often be necessary to have a spacing between the target tissue and fibre end rather than work in a direct contact mode. It is therefore important to determine the value of output beam divergence from the fibre in order to assess its effect on the laser-material interaction process. The HF laser beam was suitably imaged onto the entrance surface of a 15cm long sample of the 500μm core fluoride glass fibre using a NaCl lens of 50mm focal length operating at an aperture ratio of 7. This corresponds to an input full angle of about 8° (or ~140mr) which is within the maximum acceptance angle of the fibre given by $\sin^{-1} 0.22 \simeq 12^{\circ}$ (24° full-angle).

To determine the output divergence in air, an unexposed developed Polaroid film was ablated at different distances from the fibre tip. As seen from Fig. 6.12a it was observed that when the target was in contact or very close to the fibre end, the ablation was uniform and that the ablated area was comparable to the fibre core area. As the separation gradually increased so did the overall interaction zone (outer ring in Fig. 6.12a); however, the strong ablation zone (inner ring) became smaller and progressively weaker. This behaviour would be consistent with a transition from a uniform to non-uniform fluence peaking on axis such that the region of intense ablation decreases as the distance from the fibre tip increases. The output beam divergence was evaluated by plotting the measured values of outer ring radius against the corresponding distance and using the initial slope as shown in Fig. 6.12b. From these results the beam divergence

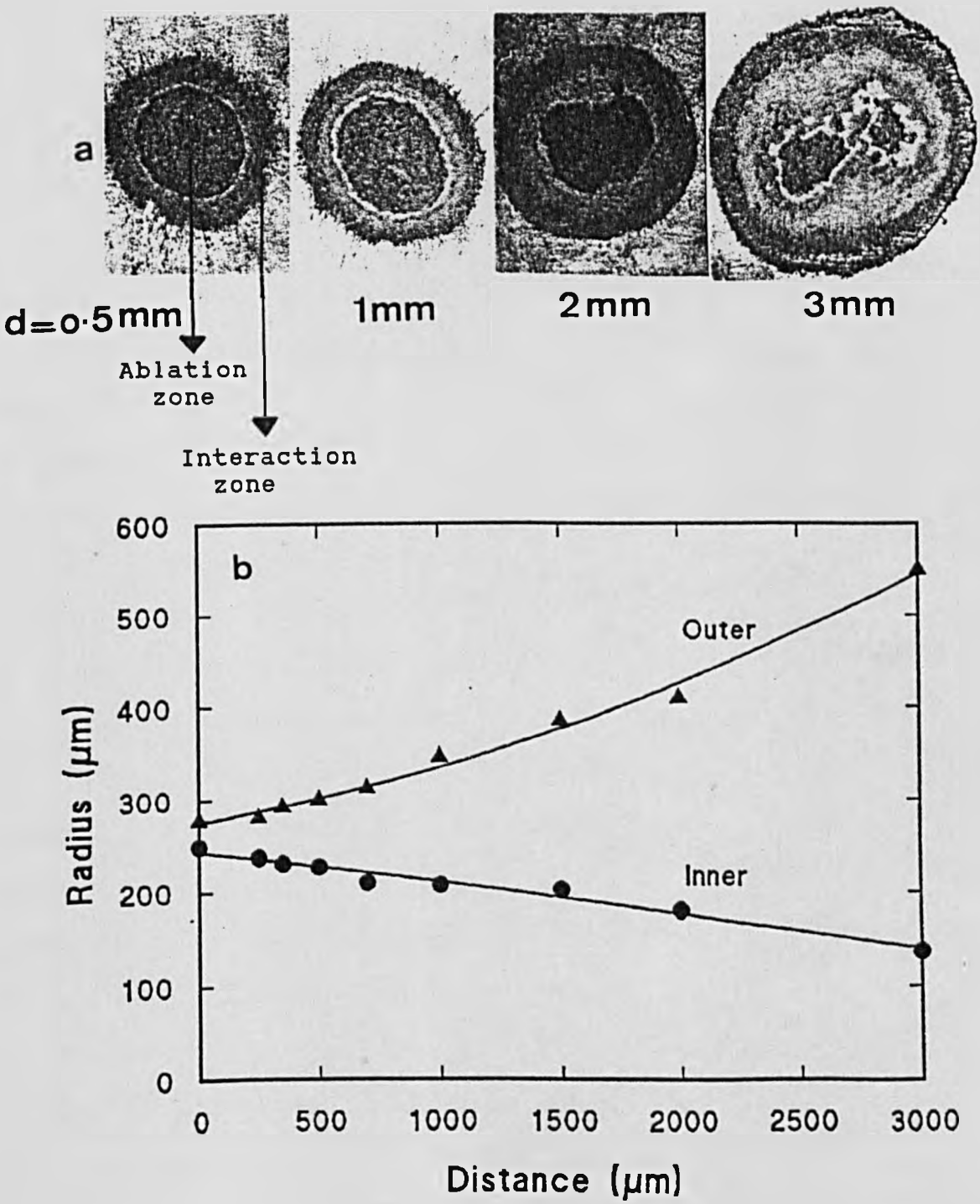

Fig. 6.12 - (a) Some examples of ablation of polaroid film at different distances from the fibre tip and (b) plot of outer and inner ring radii vs distance.

from the fibre was deduced to be about 140mrad (full angle) which is essentially identical to the range of input angles to the fibre for the optical arrangement used.

6.3 - Discussion

These experiments demonstrate that a relatively large diameter fluoride glass fibre ($\sim$500μm core) can be used to deliver the multiline HF laser at suitably high output fluences ($\leq$7Jcm^{-2}) for ablation studies. This size fibre was found, however, to be extremely brittle and great care was required when handling it; for many clinical applications it could, on this basis, be necessary to protect the fibre using a rigid guard limiting its usefulness in many procedures. However, for intraocular ablation work this is less of a problem, and indeed, a rigid delivery system may be advantageous in targetting sites for laser ablation.

The fluoride glass fibre distributed attenuation for the multiline HF laser (2.6-2.9) was measured to be 0.15 $\pm$ 0.03m^{-1} (0.65dBm^{-1}) which is considerably higher than specified by the manufacturer who claim values of $\sim$0.1dBm^{-1}. Details of their measurement technique were not available but are probably based on a low power IR radiation source. Here, with the pulsed HF laser, high irradiance levels are involved ($\geq$1MWcm^{-2}) which may enhance losses due to non-linear effects. Differences between the input coupling (ie numerical aperture of coupling lens) may also be contributory. In addition it was deduced from photoacoustic and transmission measurements that fibre end losses were fluence dependent again pointing to non-linear effects. To gain further insight into these bulk and surface loss mechanisms it would be of

interest to carry out studies on bulk samples of this fluoride glass at high irradiance levels in the 2-3μm spectral region.

1. Wolbarsht M.L.
Laser surgery: Co_2 or HF.
IEEE J.QE., 20:1427:1984.

2. Peyman G.A., Katoh N.
Effects of Er:YAG laser on occular structures.
Int. Ophthal., 10:245:1987.

3. Kopchock G.E., White R.A., et al.
Ho:YAG laser ablation of vascular tissue.
Laser Surg. Med., 10:4405:1990.

4. Seiler T., Marshal J., et al.
Potential of an infrared HF laser (3um) for corneal surgery.
Laser in Ophthal., 1:49:1986.

5. Leortscher H., Mandebaum S., et al.
Preliminary report on corneal incisions created by a HF laser.
Am. J. Ophthal., 102:217:1986.

6. Bonner R.F., Smith P.D., et al.
Quantification of tissue effects due to a pulsed Er:YAG laser at 2.9um with beam delivery in a wet field via zirconium fluoride fibres.
SPIE., 713:2:1986.

7. Whitehurst C., Dickinson M.R., et al.
Transmission of 2.94um laser radiation by zirconium fluoride optical fibres.
SPIE., 1048:141:1989.

8. Van Leeuween T.G., Maurits J., et al.
Noncontact tissue ablation Ho:YSGG laser pulses in blood.
Lasers in Surg. and Med., 11:26:1991.

9. Wüthrich S., Lüthy W., Heinz H.
Optical damage thresholds at 2.94μm in fluoride glass fibres.
Appl. Opt., 31:5833:1992.

10. Croitoru N., Gannot I.
Characterization of hollow fibres for the transmission of IR radiation.
Appl. Opt., 29:1805:1990.

11. Burt J.A., Ebeling K.J., et al.
Observation of the photoacoustic effect in an optical fibre.
Opti. Comm., 32:59:1980.

12. Taylor R.S., Leopold K.S., et al.
Dependence of the damage and transmission properties of fused silica fibres on the excimer laser wavelength.
Appl. Opt., 2:3124:1988.

Chapter 7

Interaction of Infrared laser with organic material

The purpose of this chapter is to study the potential of a fluoride glass fibre for delivering a multiline (2.6-3μm) HF laser with 400ns pulse width (FWHM) to ablate ophthalmic tissues in air and saline, and polymers in air.

7.1 - Ablation of biological tissues using fibre delivered HF laser

7.1.1 - Fibre - Cornea - Air

The experimental set up for ablation of bovine cornea and lens tissue in air was essentially similar to that in Fig. 6.3. The sample was mounted onto a purpose-built perspex holder fixed to an X-Y-Z translator allowing its accurate location with respect to the fibre tip. A stereo-optical microscope was used to allow in situ observation of the ablation site. The fibre face was positioned to be in intimate contact with the tissue surface prior to commencement of irradiation. Material removal measurements were made by exposing the samples to a predetermined number of laser pulses, n, and measuring the depth of material removed, Δ, using a high resolution optical microscope (Olympus BHM, $\pm$ 2μm depth resolution). The average etch rate (removed tissue depth per pulse) was then calculated from Δ/n. As no attempt was made to follow the retreating (ablated) surface into the tissue by repositioning the fibre, Δ was restricted to small values ($\leq$ 300μm) to avoid significant changes in the fluence due to beam divergence (Section 6.2.3, Chapter 6).

Initial experiments were carried out with tissues that had been fixed in glutaraldehyde formaldehyde solution prior to the experiment to prevent degradation. Although under these conditions results are not strictly appreciable to the clinical environment, SEM photographs are shown here for completeness and to allow a comparison with those obtained for fresh tissue. Fig. 7.1 shows the ablation site produced

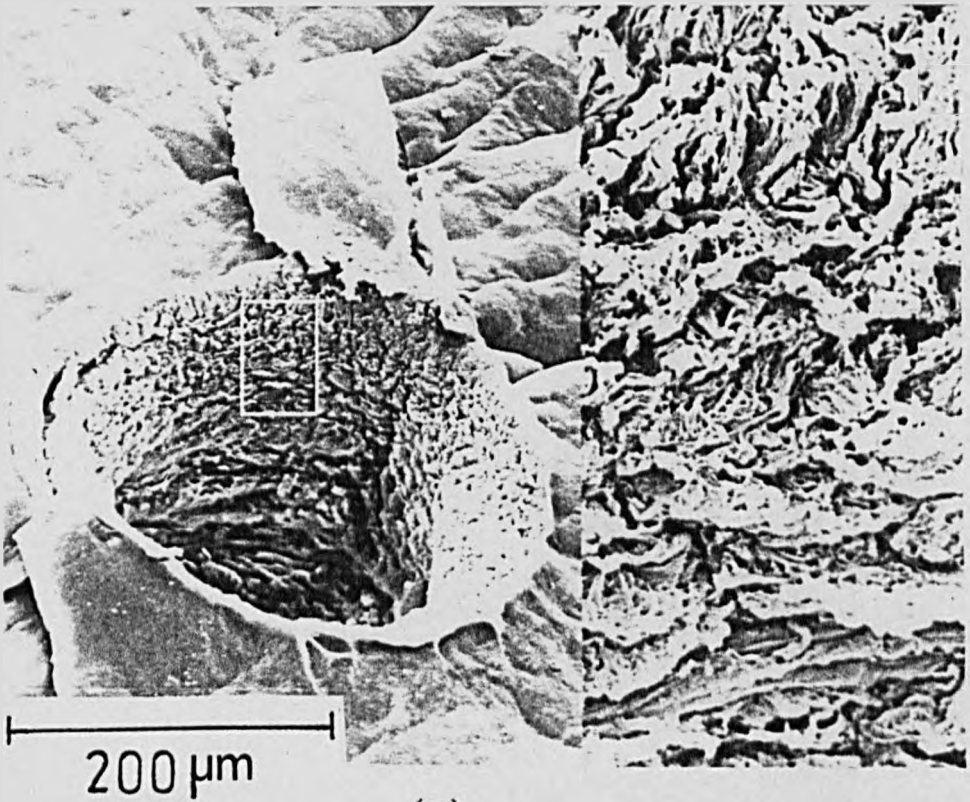

(a)

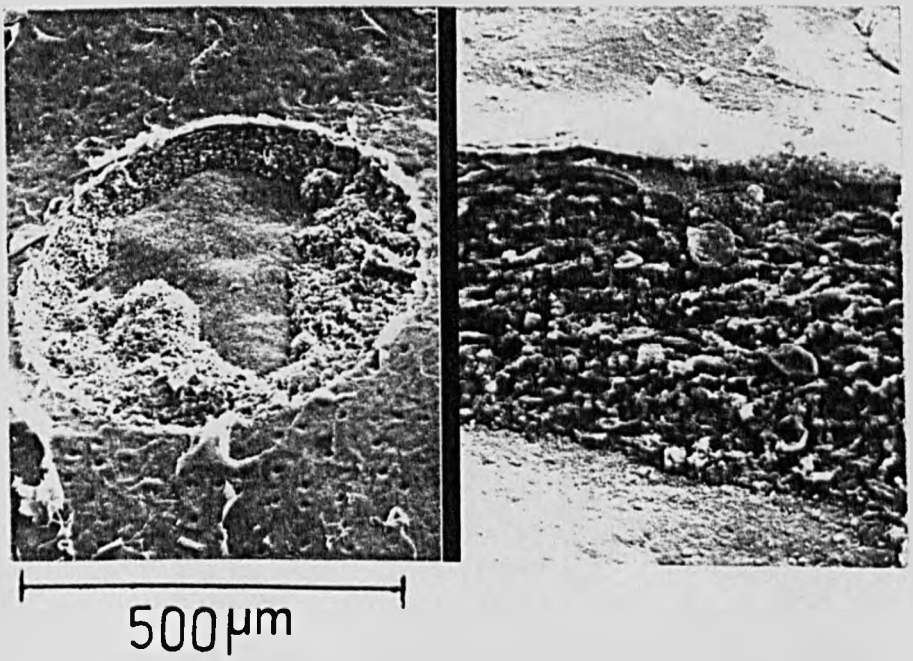

(b)

Fig. 7.1 - Ablation of fixed cornea with HF in air (a) without fibre at F~3Jcm^{-2}, 50 pulses and (b) with fibre at 1Jcm^{-2}, 120 pulses.

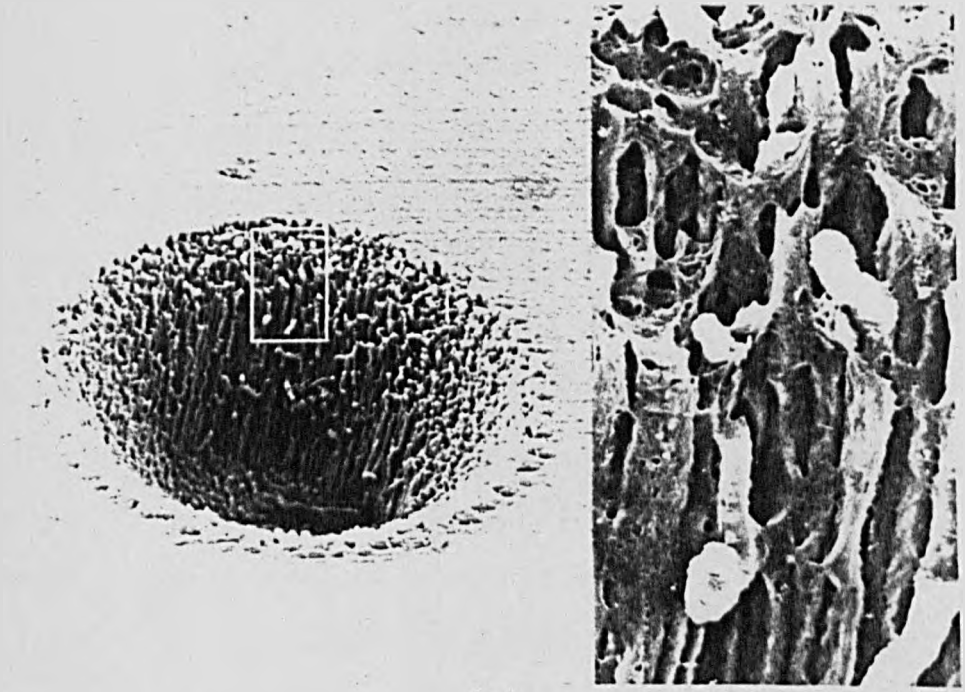

(a)

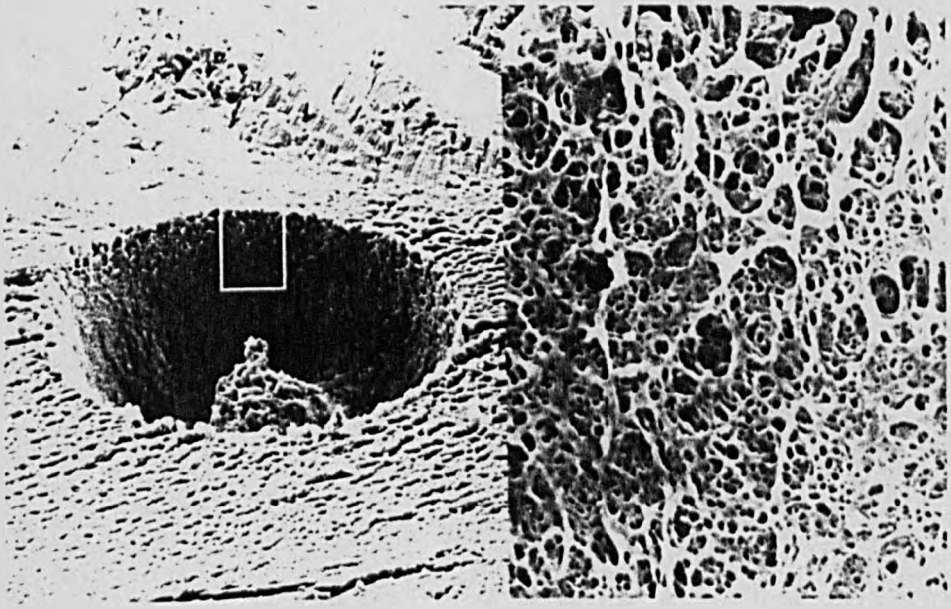

200 µm

(b)

Fig. 7.2 - Ablation of fixed lens with HF in air (a) without fibre (b) with fibre, (c) histological sample of lens cross-section, F~5Jcm^{-2}, 50 pulses.

by the HF laser of fixed bovine cornea in air with and without the fibre. In both cases a relatively smooth crater wall is produced similar to those obtained with the KrF laser (Fig. 4.11), and no apparent difference can be seen in cornea incision produced by with and without fibre. A similar incision quality was also obtained when bovine lens tissue was ablated (Fig. 7.2). The right hand side of each photo shows an enlarged version of the boxed region, from which it is evident that the lens fibres have been strongly affected by heating effects associated with HF laser interaction.

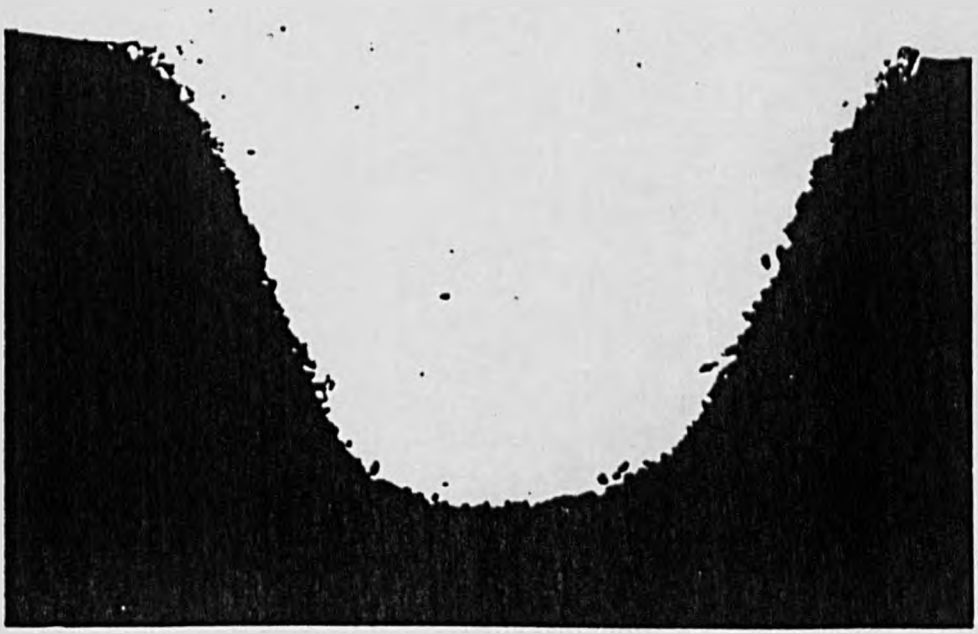

(Fig. 7.2C)

Subsequent experiments were performed with samples of cornea obtained from freshly enucleated bovine eyes which were isolated by a circumferential incision at the limbus. Tissue hydration was maintained prior to and between experiments by immersing the specimen in saline.

Following irradiation, tissues were then fixed in glutaraldehyde-formaldehyde (3ml glutaraldehyde (25%), 50ml formaldehyde (10%), 3g NaCl, 4.5g sucrose buffered with 0.1M phosphate to 100ml). For SEM evaluation of the ablation site the cornea samples were dried using a critical point drying apparatus so as to minimize structural deformation or collapse.

Fig. 7.3 shows the etch depth per pulse as a function of fluence for the fibre delivered HF laser ablation of cornea. Ablation is seen to commence at a threshold fluence of $\simeq$ 0.5 Jcm^{-2} which is similar to the value reported by Valderrama et al (1). Below 3 Jcm^{-2} the etch rate has an approximately linear dependence on the logarithm of fluence but above this it increases quite sharply such that at just below 8 Jcm^{-2} the etch rate reaches $\simeq$ 17μm per pulse. Similarly high values have been reported by Valderrama et al (1) using a single line (2.78 or 2.91μm) HF laser. Fig.7.4(a) and (b) show the ablated corneal surface using the fibre at output fluences of 3 and 4.5 Jcm^{-2}, respectively. In each case the exposure was for 60 pulses. In the lower fluence example (Fig.7.4a) the epithelium has been clearly penetrated and ablation of the superficial corneal stroma has occured.

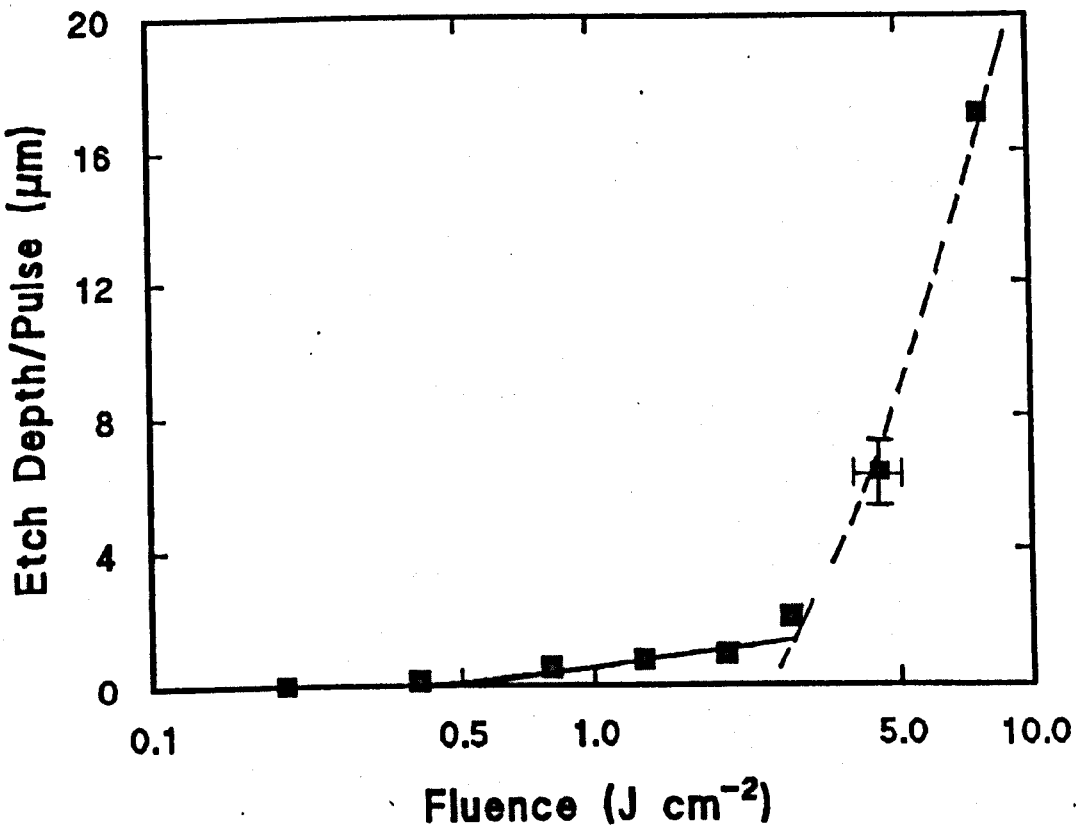

Fig. 7.3 - Etch depth per pulse for bovine cornea as a function of fluence for fibre delivered HF laser. The solid line is a least square fit to the data at low fluence assuming a logarithmic dependence is applicable. The dotted line assumes a linear dependence is applicable at higher fluence.

Material removal is restricted to a zone similar in size to the fibre core diameter although in the margin of the incision some distortion of the epithelium has taken place. This may be due to the ablation products being forced between the fibre face and tissue surface. This effect is also seen in the higher fluence example in Fig. 7.4(b). Here the ~380μm deep crater in the stromal cornea has sharply defined walls that are relatively smooth and free of fibrillar debris. The ablation crater is quantitively similar in appearance to that produced using the 248nm laser (2) and

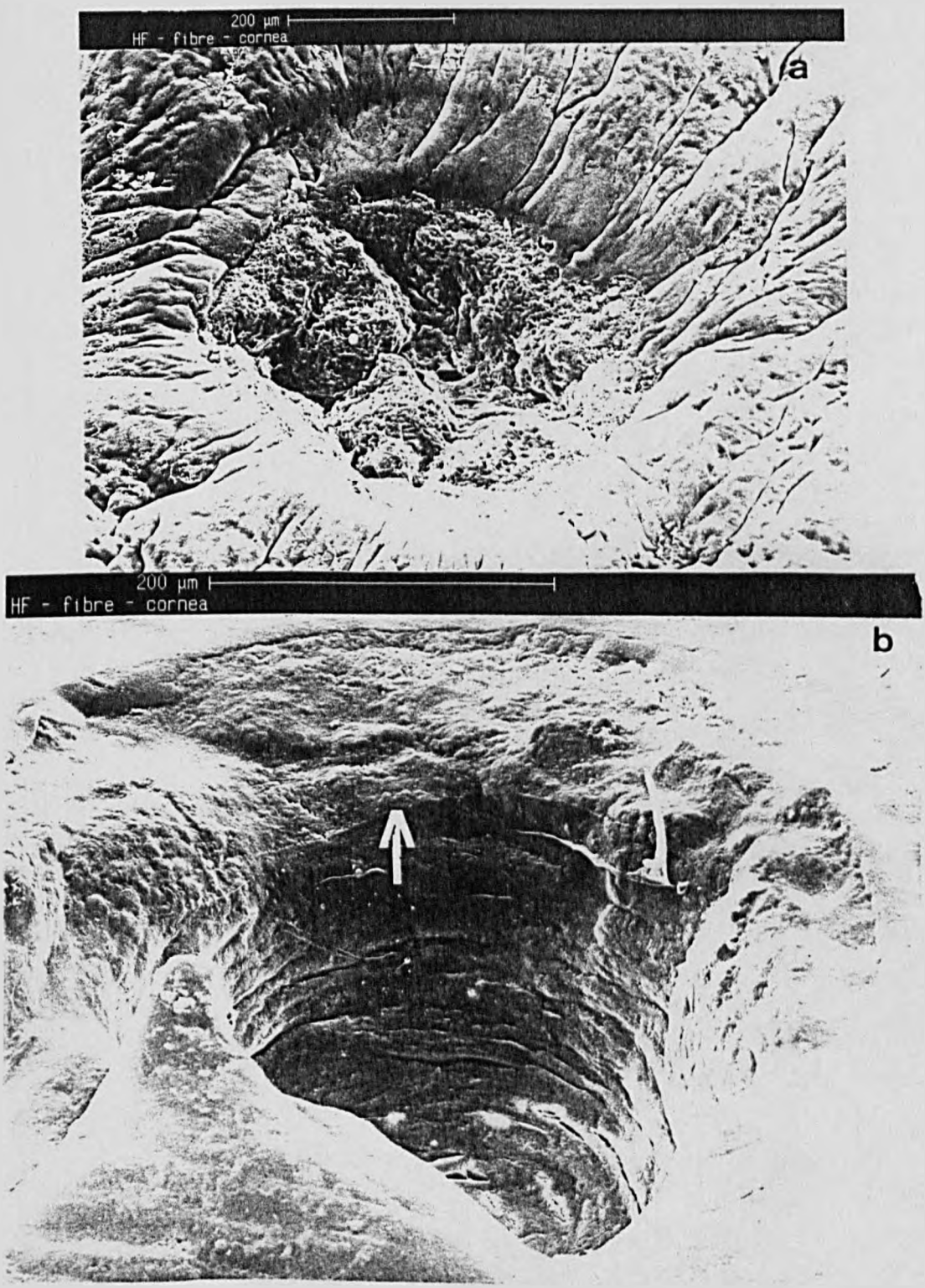

Fig. 7.4 - SEM of bovine cornea ablated in air using the fibre delivered HF laser (a) 60 pulses at 3Jcm^{-2} with contacted fibre, (b) 60 pulses at 4.5Jcm^{-2} with contacted fibre, the arrow marks the base of epithelium, (c) 50 pulses at 6.5Jcm^{-2} with fibre tip 1mm from the surface.

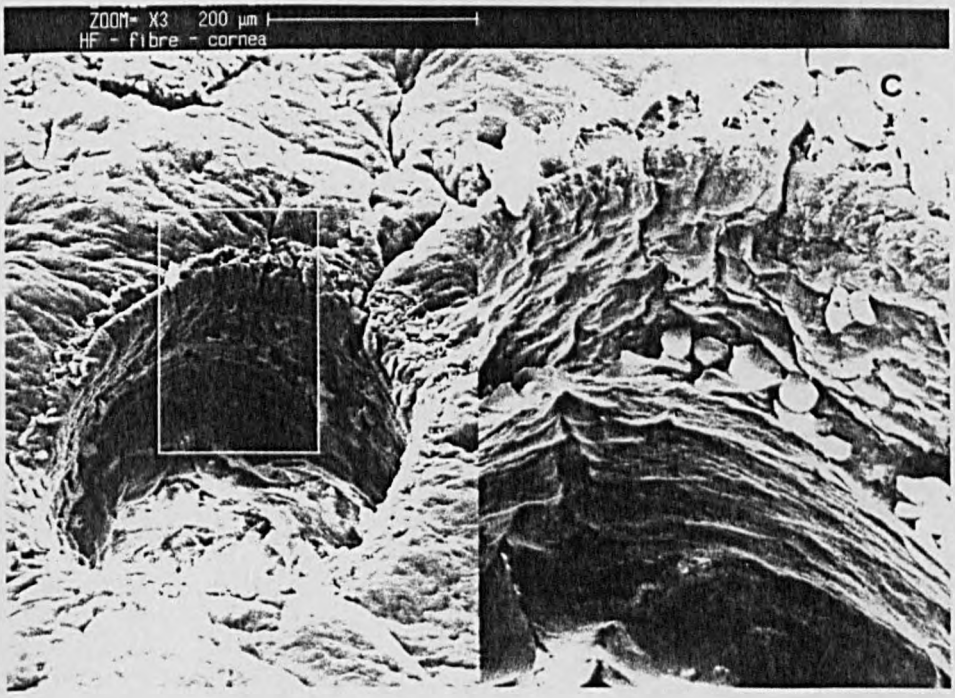
ZOOM= X3 200 µm
HF - fibre - cornea
C

is superior to results obtained using the 10.6μm TEA CO_2 which produces a cut with much more debris (3). Fig. 7.4(c) shows an SEM obtained for exposure to 50 pulses at 6.5 Jcm^{-2} with the fibre located 1mm from the corneal surface. Here there is no apparent damage or modification to the epithelium at the periphery of the ablation crater. This observation would appear to support the suggestion that confinement of the ablation products with the contacted fibre is responsible for the zone of distortion surrounding the incisions in Fig. 7.4(a) and (b). With the non-contacted fibre this effect is eliminated as the ablation products may readily escape from the crater. The diameter of the incision in Fig. 7.4(c) is about 350μm which is somewhat smaller than the core fibre. This is attributed to beam divergence which leads to the fluence distribution becoming non-uniform and broadened such that the tissue ablation threshold is only exceeded over a diameter that decreases with increasing distance from the fibre tip. This behaviour was confirmed by studies using other media (eg. unexposed, developed polaroid film) as discussed in Section 6.2.3, Chapter 6.

To interpret the variation of etch rate per pulse with the logarithm of the fluence for cornea shown in Fig. 7.3, a model (4,5) for polymer and tissue ablation issued in which absorption in both the sample and blow-off plume are taken into account. In the general case of a sample in which the laser is absorbed according to Beer's law with an absorption coefficient α in condensed phase, and in which ablation commences instantaneously once a threshold fluence F_{th} is exceeded, the etch rate per pulse is,

$$D_e = \frac{1}{\alpha_p} \ln\left[\alpha_p F/F_{th}\alpha - \alpha_p/\alpha + 1\right] \qquad 7.1$$

Here α_p is the absorption coefficient of the plume formed by the ablated material and F is the laser fluence. In deriving equation 7.1 it is assumed that thermal conduction loss is negligible during the ablation phase, which is valid provided the spot size and characteristic optical absorption depth large compared with the thermal diffusion depth, X_T, that applies during the laser pulse. This is given by,

$$X_T = (4k\tau)^{1/2} \qquad 7.2$$

where k, τ are the thermal diffusivity and pulse duration respectively. Taking $k = 1.3\times10^{-3}$ cm^2s^{-1} for cornea and τ = 400ns gives $X_T = 0.45\mu m$ which is smaller than but comparable to the smallest optical absorption depth (inverse of absorption coefficient ie, $1/1.2\times10^{4}$ cm^{-1}) of $\simeq$ 0.8μm for cornea at the 2.91μm HF laser transition (1). Thus, neglect of heat flow during the laser pulse is only marginally valid.

For the limiting case of a transparent plume ($\alpha_p \longrightarrow o$), equation (7.1) reduces to

$$D_e = \frac{(F-F_{th})}{F_{th}\alpha} \qquad 7.3$$

and the etch depth per pulse is linearly dependent on fluence. In contrast, if the plume retains the same absorption coefficient as the condensed phase so that $\alpha = \alpha_p$, equation (7.1) gives the well known Beer's law form (4)

$$D_e = \frac{1}{\alpha} \ln \frac{F}{F_{th}} \qquad 7.4$$

and the etch rate varies as the logarithm of fluence. It is

apparent that below $\simeq$ 3Jcm^{-2} the data in Fig. 7.3 agree quite well with equation (7.4), which predicts a linear dependence of the etch rate on the logarithm of fluence. A fit to the date for $F \leq 3Jcm^{-2}$ using equation (7.4) yields $F_{th} \simeq 0.42Jcm^{-2}$ and $\alpha = 1.2 \times 10^{4}$ cm^{-1} for the threshold and effective tissue absorption coefficient, respectively. In the higher fluence region ($\geq 3Jcm^{-2}$) the etch rate increases sharply and the data is better fit by a linear dependence on fluence which suggests a transition to a transparent plume (α_p=o) takes place. This is probably due to strong heating of the ablation products in the early stages of the laser pulses at high fluence and their degradation to low mass, relatively transparent, species.

If under these conditions, we assume α_p=o and use the equation (7.3) to fit the high fluence data, a value for $F_{th}\alpha$ of about 3.2×10^{3} Jcm^{-3} is obtained from the inverse slope of the line. Using $F_{th} \simeq 0.42Jcm^{-2}$ a value for α of 8×10^{3} cm^{-1} is then obtained which is consistent with the estimate made for the low fluence regime. These compare well with a value of $\alpha \simeq 9 \times 10^{3}$ cm^{-1} calculated from a weighted average for the spectral content of the multiline HF laser used in the experiments and the corneal absorption spectrum in the 2-3μm region (1). It is interesting to note that this interpretation of the HF laser does not necessitate postulating strong tissue bleaching (1) to explain why the etch depth greatly exceeds the characteristic optical penetration depth.

The sharply defined incisions produced in the cornea by the HF laser are consistent with the high effective absorption coefficient in this spectral region and the short laser

pulse duration which minimizes heat transfer to adjacent tissue (2). With the contacted fibre a peripheral zone of influence is evident in the SEM photographs (Fig. 7.4a) which is attributed to the containing effect the fibre has on the ablation products. This region extends over a width ($\sim$100μm) comparable to that of the fibre cladding and coating.

It is possible to estimate the temperature T_f of the front face of the tissue following the arrival of the laser pulse by neglecting heat flow from the irradiated volume and using:

$$T_f = \frac{(1-R)\ F\alpha}{\rho C} + T_i \qquad 7.5$$

Here T_i is the initial temperature, R is the surface reflectivity ρ and C are the density and heat capacity, respectively of the tissue. Assuming $\rho = 1 gcm^{-3}$ and $C=4.2 Jg^{-1}K^{-1}$ the final temperature at the surface of tissue at $0.1 Jcm^{-2}$ can be estimated to be about 570K which is very close to the tissue critical temperature.

7.1.2 - Fibre - cornea - saline

The reason for studying ablation of cornea in saline is not only due to fact that the cornea itself contains a considerable amount of saline, but also because 'in vivo' a relatively thick ($\sim$ 13μm) saline layer (tear film) covers the anterior surface of cornea. The tear is composed of three components: lipid layer (2-3μm), aqueous layer (6-10μm), and inner mucoid layer (0.02-0.05μm) which is in contact with the anterior corneal epithelium (6). Lacrimal glands provide the minute-to-minute supply of tears and their normal volume is

about 7-10ml. There is a continual secretion (nonreflex) rate of about 1ml/min (the range of flow rates being 0.5-2.2ml/min) from the accessory lacrimal glands (7,8).

The experimental arrangement for investigating the ablation of cornea with the fibre in saline is shown in Fig. 7.5. A 15cm long fluoride-glass fibre with $\simeq$ 500μm core diameter was cleaved and polished using aerosol cutting polish (RS 556-34), and then inspected using an optical microscope. It was then carefully placed inside the saline container (initially with no saline) and optimized as discussed previously. A region of uniform fluence from the laser output was selected using a circular aperture and imaged onto the fibre input face using an NaCl lens of 50mm focal length. An ir grade quartz beam splitter directed a small fraction of the output beam onto a joulemeter so that the relative laser output could be monitored on a shot-to-shot basis. The container was then filled with saline and the beam focusing was checked again, since the act of pouring saline could sometimes disturb the fibre position. The experiments were performed at a laser repetition rate of 0.2Hz.

Ablation rates for cornea with the contacted fibre in saline are shown in Fig. 7.6 as a function of fluence. An approximate threshold for ablation of about 0.4 Jcm^{-2} was obtained from the log-linear plot, which is similar to that measured for an air-based fibre. The removal rates are much lower, however, than in air particularly at high fluence and remain $\leq$ 1μm per pulse for fluences up to about 9 Jcm^{-2}. An effective attenuation coefficient of about $4x10^{4}$ cm^{-1} is derived from the slope of the etch rate-fluence plot in

Fig. 7.6 using the equation 7.4. This corresponds to an optical absorption depth of ~0.25μm which is smaller than the thermal diffusion depth (~0.45μm), thus heat flow outside the irradiated volume may not be neglected. Equation (7.5) can no longer be used but instead the heat diffusion model should be used to calculate the tissue temperature rise below the ablation threshold.

Measurements of the removal rate per pulse as a function of pulse number for several fluences showed that this varied relatively weakly beyond about 20 or so pulses. For example in Fig. 7.7a the etch depth per pulse at 2 Jcm^{-2} increased up to 20 pulses but beyond this tended to increase more slowly. Likewise at 5.5 Jcm^{-2} the etch depth per pulse remained almost constant after about 40 pulse (Fig. 7.7b). This is reflected in the plots of the total etch depth as a function of pulse number at these fluences which as shown in Fig. 7.8. are reasonably well approximated by straight lines passing through the origin.

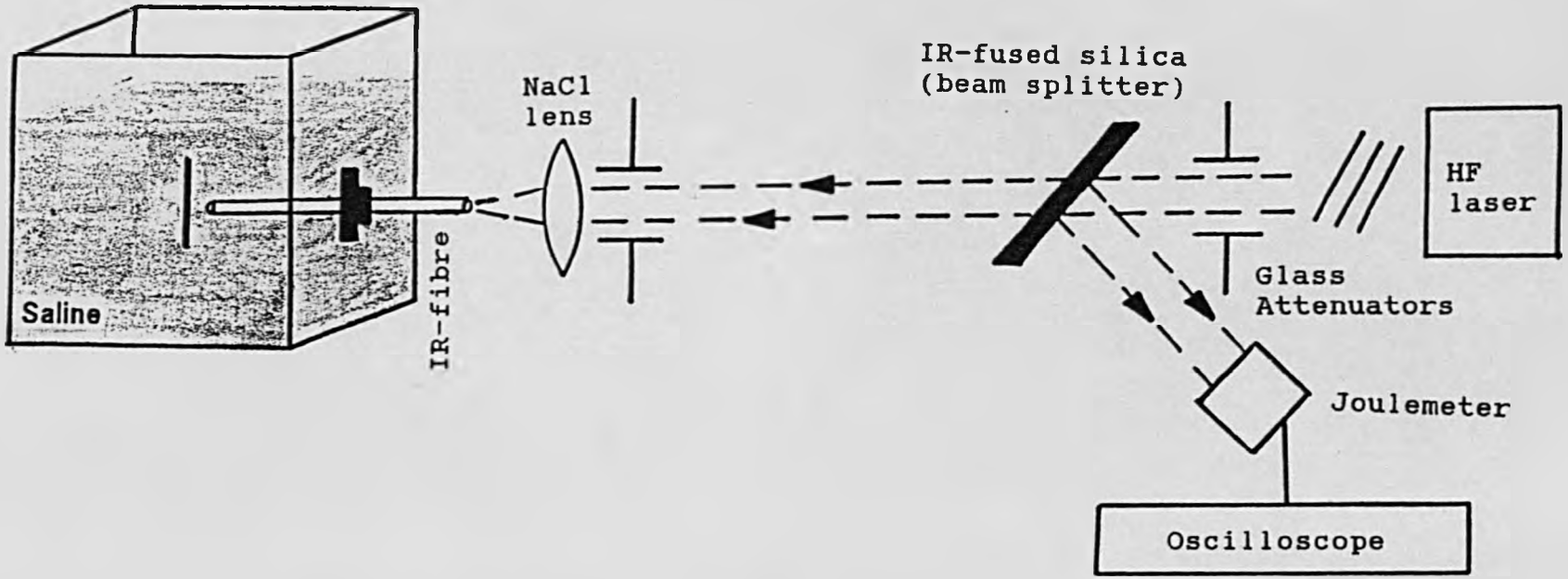

Fig. 7.5 - Experimental set up for fibre-delivered ablation of bovine cornea in saline with HF laser.

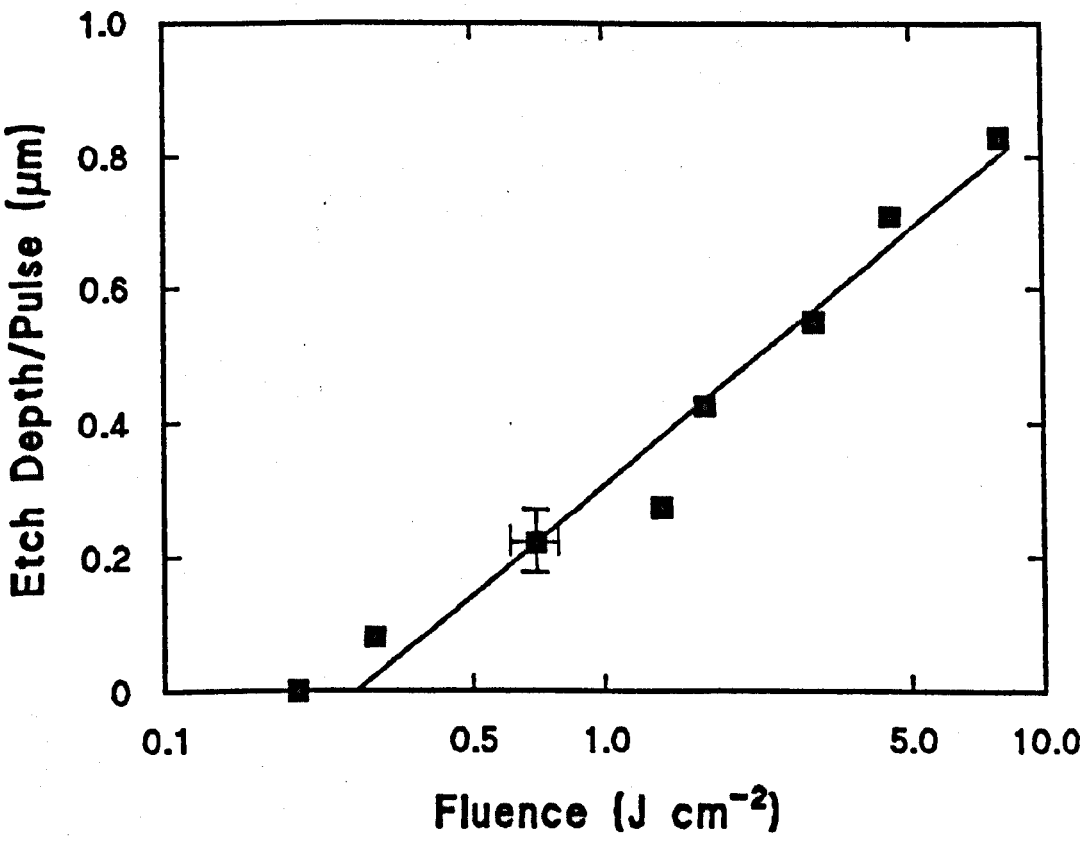

Fig. 7.6 - Average etch-depth per pulse for cornea with contacted fibre in saline as a function of HF laser fluence.

SEM photographs of the ablation site for the contacted fibre in saline are shown in Figs. 7.9a and b for exposures at 5Jcm^{-2} for 1 and 100 pulses. The interaction zone is significantly smaller in diameter than the fibre core, possibly because of some fluence non-uniformity at the fibre output surface. It is evident that the ablated surface is essentially free of fibrillar distortion or debris and that with 100 pulses a sharply defined incision is produced that clearly penetrates the epithelium and superficial stroma. This behaviour is closely similar to that for an air-based contacted fibre (Fig. 7.3).

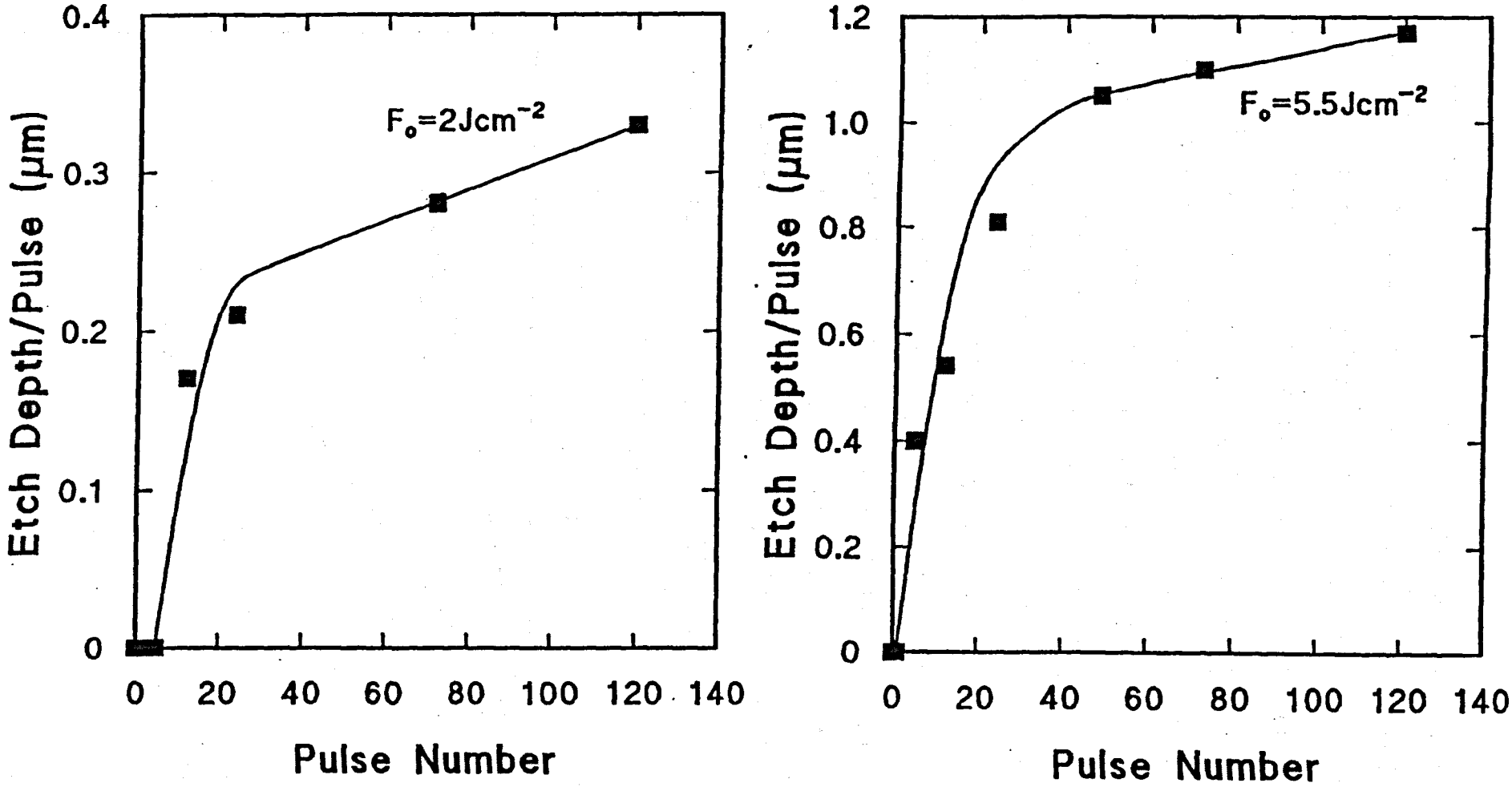

Fig. 7.7 - Average etch depth per pulse as a function of laser pulse number in saline at (a) 2Jcm^{-2} and (b) 5.5Jcm^{-2}.

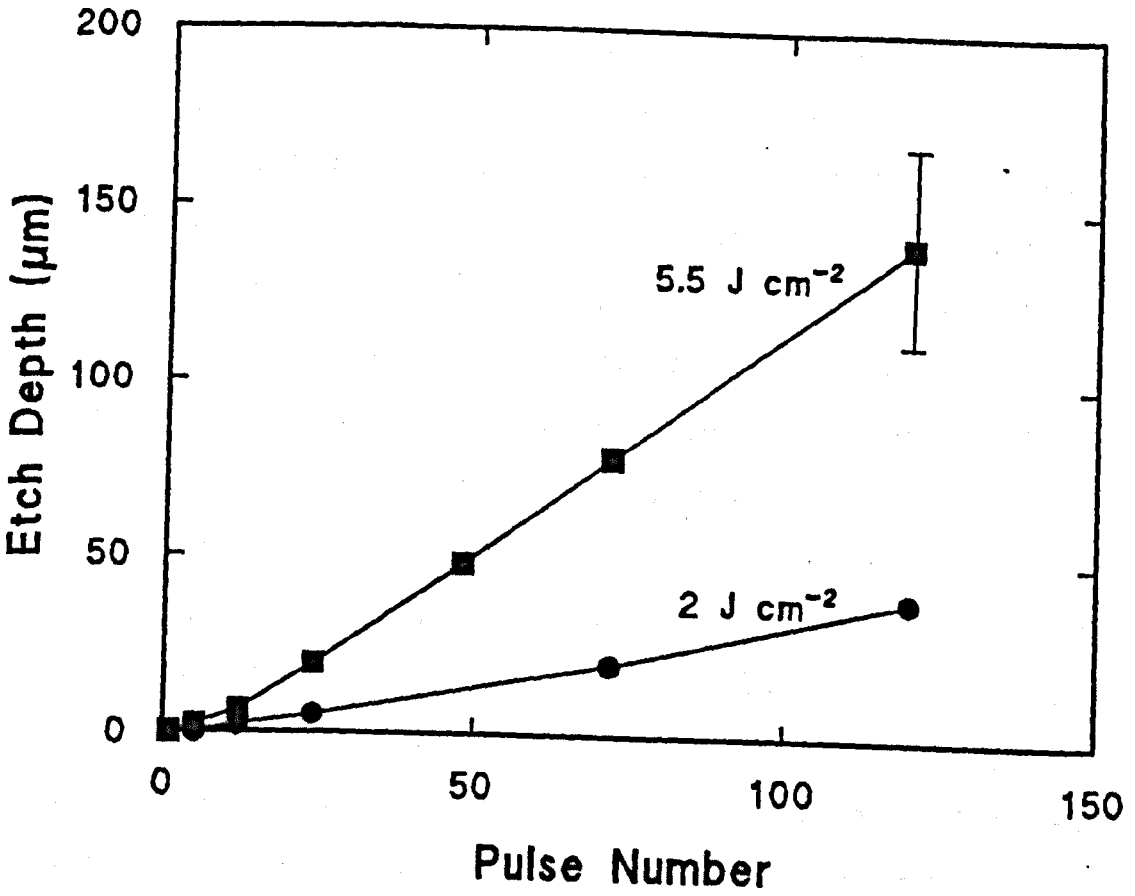

Fig. 7.8 - Etch depth as a function of ablating pulses at output fluences of 2 and 5.5 Jcm^{-2}.

SEM and optical microscope inspection was also carried out for corneal samples located at various distances, d, from the fibre tip in order to ascertain the damage range. In this way it was found, for example, that for multishot exposure at $5Jcm^{-2}$ observable damage of the sample only occured for $d \leq 250\mu m$. Fig. 7.10 shows an SEM of the corneal surface damage that resulted following 20 pulses at an output fluence of $5\ Jcm^{-2}$ with the fibre tip located about $200\mu m$ from the surface ie, close to the damage range limit under these conditions. There is extensive damage in the form of disruption and distortion of stromal collagen fibrils over a zone exceeding 1mm in diameter in sharp distinction to the results with the contacted fibre where the ablation crater is smooth and well defined (Fig. 7.9). Even at this small

separation the HF laser beam cannot penetrate saline so as to reach the sample surface so that it is necessary to conjecture that the damage is either produced by an expanding vapour bubble or is a result of mechanical disruption produced by an intense acoustic wave or possibly a combination of these effects. Similar measurements were also carried out for bovine retina samples. The retina samples were prepared by first extracting the content of the eyeball and then turning it inside out so that the retina which is attached to an underlying layer (choroid)faces outward. No attempt was made to detach the retina since it is very delicate tissue and technically difficult. Therefore the choroid layer was pinned down on the holder and used as a support plate. The differentiation between these two layers is relatively easy using an optical microscope due to transparency of retina in contrast to the light blue (outer surface) and dark velvet-type pigmented material (inner) of the choroid in the background. In this case it was found that local surface disruptions could be produced with the fibre tip at much larger distances from the sample; for example at 4.5Jcm^{-2} the damage limit range was d$\tilde{}$2mm. This is much larger than for cornea, a result that can be attributed to the greater sensitivity of this delicate tissue to damage.

In summary the ablation rate for cornea with the contacted fibre in saline falls well below that for air particularly at high fluence (eg. at 5Jcm^{-2}, this is about 0.8μm per pulse which is about ten times lower). Although at first sight this might be expected if an intervening water layer acts as to block the beam from the surface as etching

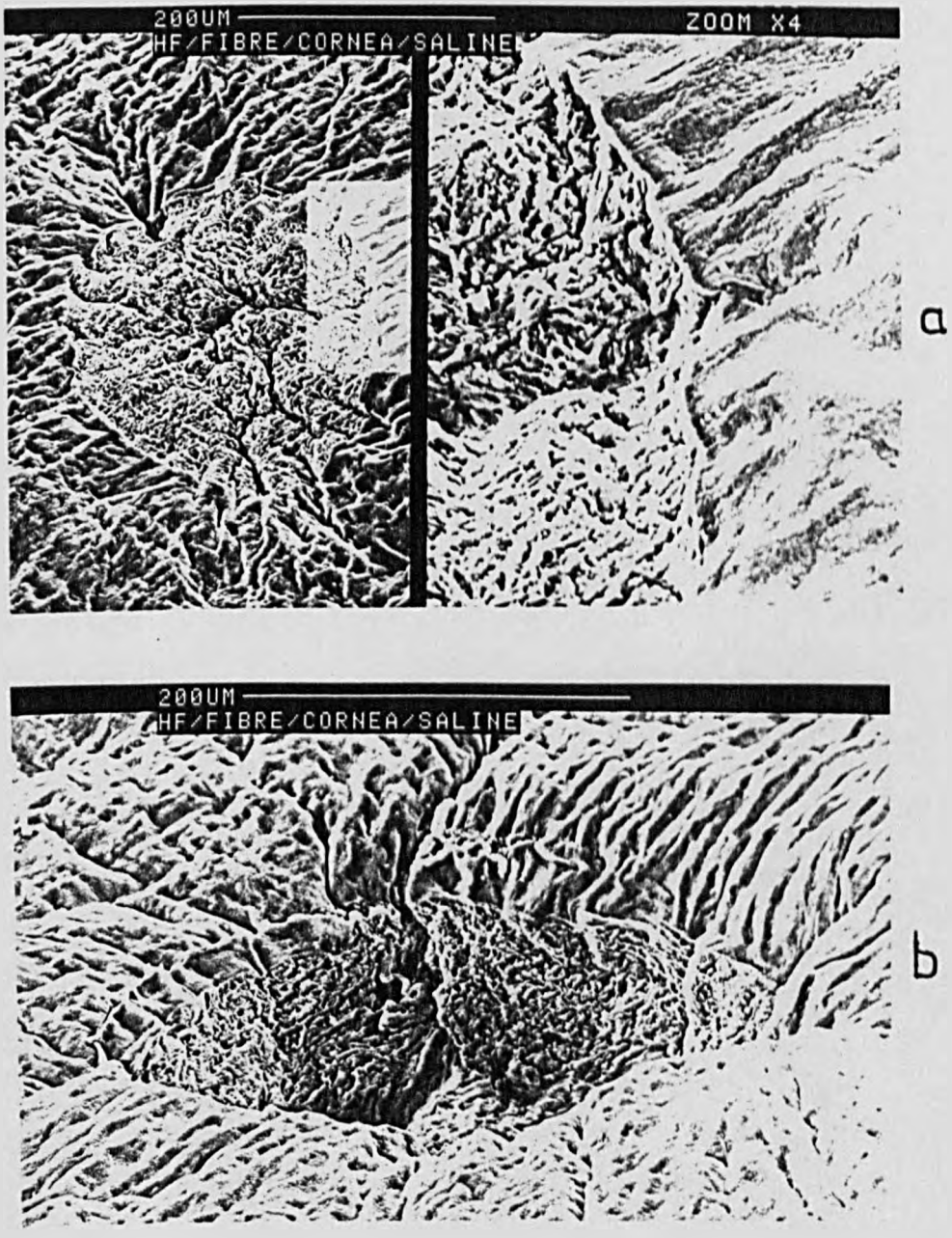

Fig. 7.9 - Scanning electron micrographs of cornea ablated in saline at 5Jcm^{-2} (a) contacted fibre, 1 pulse (b) contacted fibre, 100 pulses.

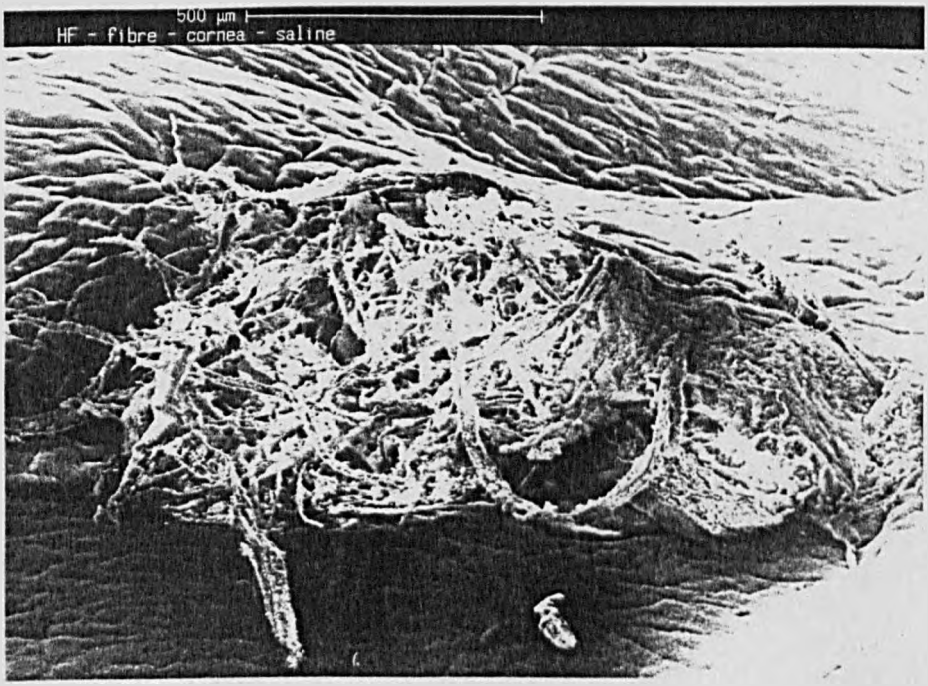

Fig. 7.10 - Surface of cornea following exposure to 20 pulses from HF laser with fibre tip located ~200µm from the sample in saline ($F \sim 5 Jcm^{-2}$).

proceeds to greater depths, the fact that the removal rate per pulse is approximately constant with pulse number (Figs. 7.7, 7.8) suggests this is not the case. A possible explanation for this behaviour is that gaseous ablation products remain trapped in the shallow ablation cavity and prevent water from filling this cavity. This would then allow the beam to reach the surface without significant attenuation. The difference in ablation rates for the contacted fibre in air and in saline would then be due to the saline preventing rapid expansion of the ablation products such that they were maintained at high density and continued to attenuate the beam during the laser pulse.

7.2 - Photoacoustic studies

7.2.1 - Cornea - Air

The experimental arrangement for ablation of fresh bovine cornea in air was similar to that shown in Fig. 4.15a where in this case the HF laser was focused to produce a spot size of about 500μm on a ~ 300μm thick tissue sample using an NaCl lens of 50mm focal length. The electrical out-put from the transducer was taken to a 1MΩ Tektronix plug-in amplifier providing a voltage response proportional to the normal force at the transducer (9).

At low fluence (~0.5Jcm^{-2}) the signal from the transducer was bipolar consisting of an initial compressive peak followed by a rarefaction component. This, as discussed in Chapter 4 (Section 4.3.2) is attributable to rapid heating and thermal expansion of the unconstrained surface of the sample ie, characteristic thermoelastic response. As the

fluence was raised the negative going (rarefaction) component became weaker, such that at between ~1.8-2Jcm^{-2} the signal became purely compressive. This behaviour is a result of the increasing compressive component generated by momentum transfer from the ablation products.

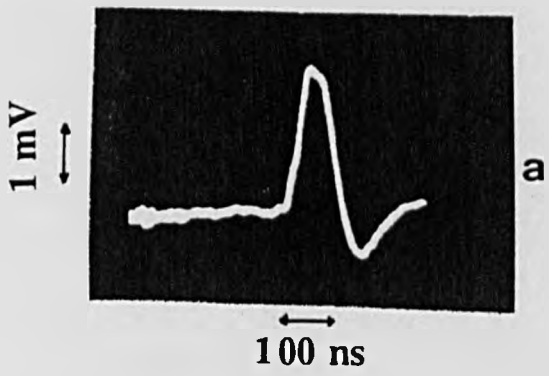

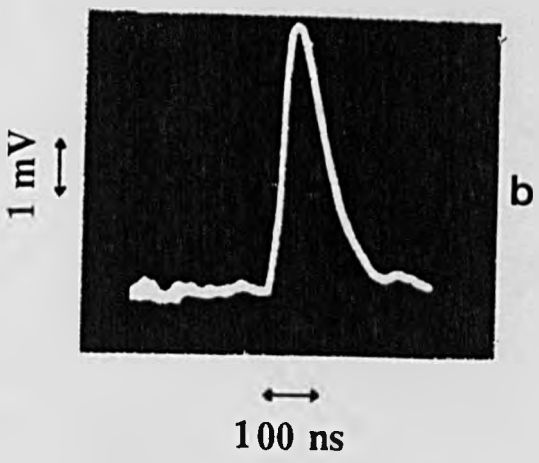

Fig. 7.11 - Acoustic transition detected for HF irradiated of bovine cornea in air (a) 1.8Jcm^{-2}, (b) 2Jcm^{-2}.

At high fluence (eg.2Jcm^{-2} Fig. 7.11b) the acoustic transient had a duration of about 100ns (FWHM) which is considerably shorter than the HF laser pulse (~400ns FWHM).

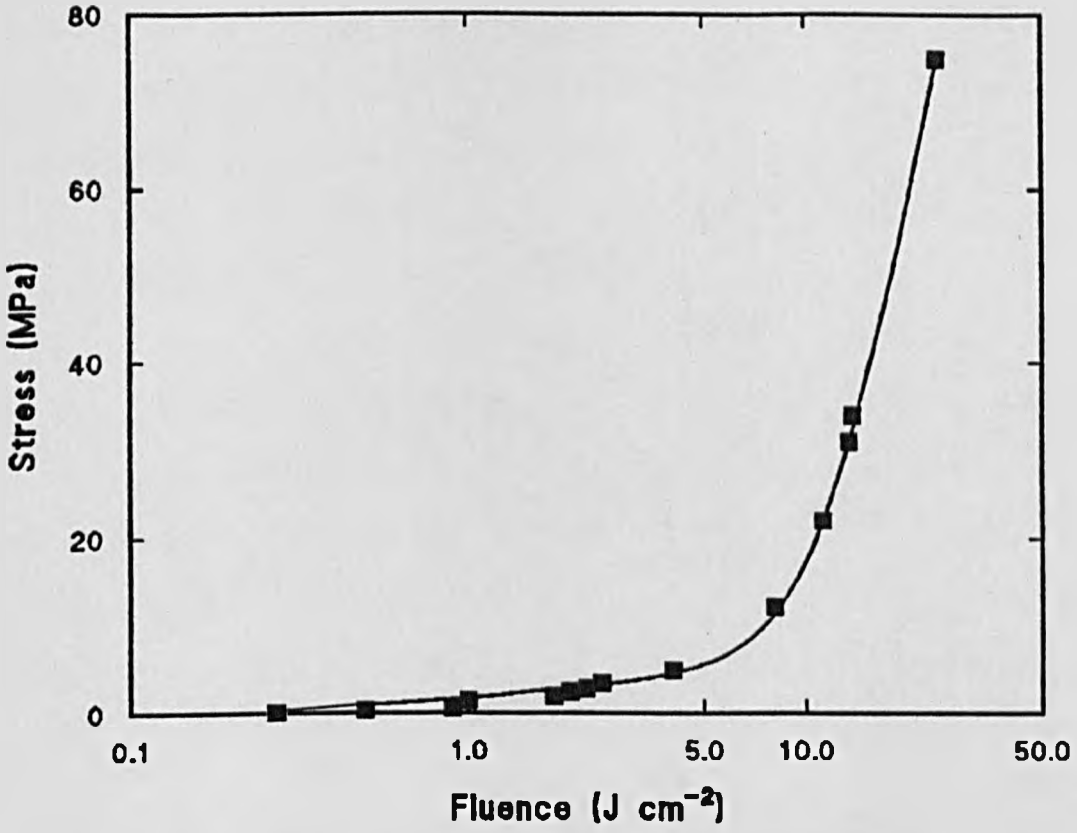

Fig. 7.12 - Peak stress deduced from the photo-acoustic transducer as a function of fluence for HF laser ablation of cornea in air.

The peak voltage from the transducer was used to determine the stress amplitude at the surface assuming plane wave propagation between the sample surface and transducer (Chapter 4). This as discussed in section 7.2.2 is only marginally valid for the spot size used in these experiments. The compressive stress amplitude as a function of fluence is shown in Fig. 7.12 where it can be seen that measurable stress signals begin in the range 0.5-1Jcm^{-2}. This coincides with the onset of ablation threshold of $\tilde{}$0.5Jcm^{-2} determined by removal rate measurements (Fig. 7.3). It is difficult to ascertain the ablation threshold from these measurements, however, because as noted above in the lower fluence range both thermoelastic and ablative components both contribute to the signal. It is apparent from Fig. 7.12 that the stress

increases quite slowly below 5Jcm^{-2} but beyond ~10Jcm^{-2} increases sharply reaching ~75MPa at 25Jcm^{-2}. This behaviour is consistent with results obtained with excimer and other lasers which have shown that ablation generates large transient pressures at the irradiated surface.

It must be noted that in these experiments the attenuation coefficient of tissue cannot be determined by plotting the logarithm of the amplitude versus time using the early stages of the compressive curve, since the laser pulse duration (400ns) is very much larger than that of the sound transit time in the absorption zone.

7.2.2 - Fibre - cornea - saline

The experimental arrangement shown in Fig. 7.13 is basically the same as that described in Chapter 4 (Section 4.3.2) for the excimer (KrF) laser except that in this case a 15cm long fluoride glass fibre was used to deliver the beam to target.

Measurements of the transient pressure pulse accompanying ablation for the contacted fibre (d=0) in saline were made for a ~ 300μm thick section of cornea mounted on the PVDF transducer. The transducer output signal shown in Fig. 7.14 for an output fluence of 2.5 Jcm^{-2} exhibited a fast rise time (~80ns), a duration of about 200ns (FWHM) and some ringing following the main pulse. The oscilloscope trace was triggered by the laser pulse using an IR photodiode and it was observed that the delay between pulses decreased as the fluence was raised. This delay has a fixed component set by the acoustic transit time in the sample (neglecting shock effects) and a component that depends on when ablation

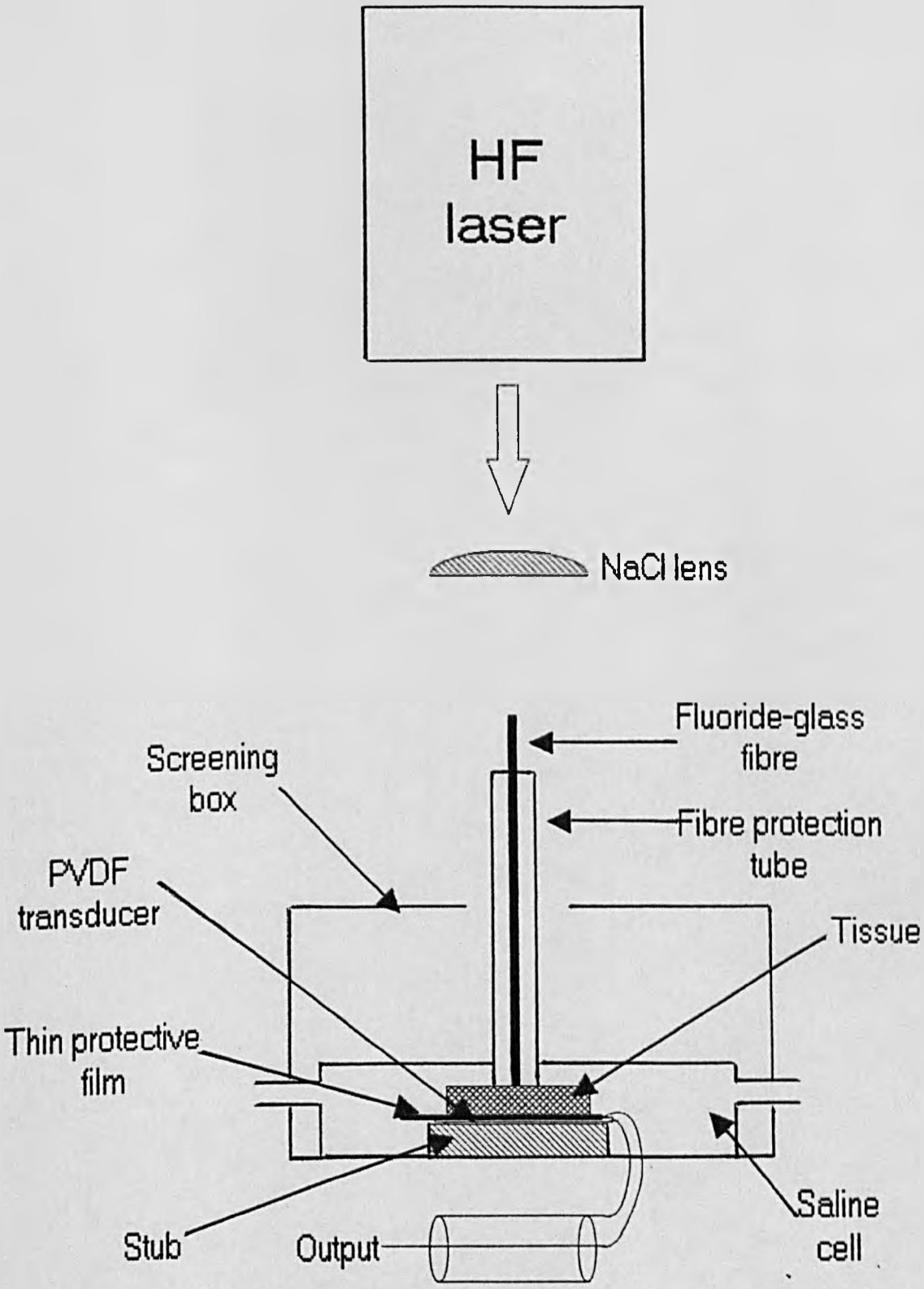

Fig. 7.13 - Experimental set up for photoacoustic studies of cornea in saline with fibre delivered HF laser.

commences during the laser pulse. It can thus be deduced that ablation occurs at earlier times as the fluence is increased.

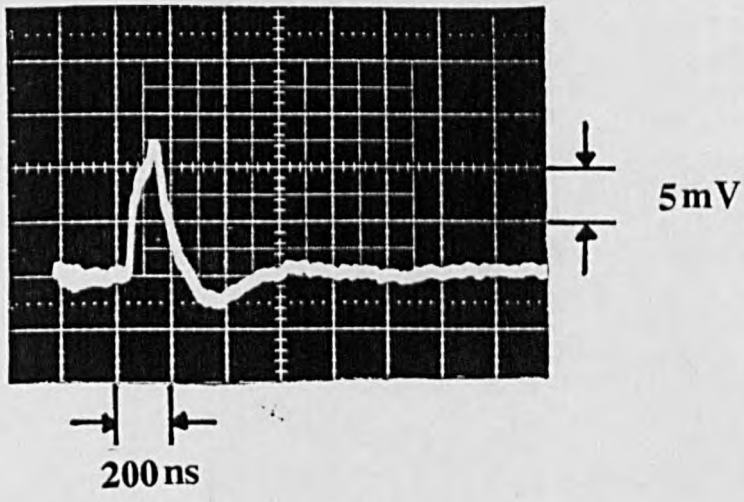

Fig. 7.14 - Transient pressure pulse produced by ablation of cornea with contacted fibre in saline ($\tilde{}$2.5cm^{-2}). The start of the trace is triggered by the HF laser pulse.

The peak output voltage from the PVDF transducer can be converted to a corresponding normal force (9) and hence to a pressure if the area of influence of the acoustic pulse can be defined. For this purpose it is assumed that a plane acoustic wave propagates between the tissue surface and transducer and the area is taken as that of the fibre area. It should be noted, however, that this is a relatively poor assumption in the present case because the transducer lies beyond the near field range, Z_R. This is given by (9)

$$Z_R = a^2/\lambda \qquad 7.6$$

where a is the fibre core radius and λ is the characteristic acoustic wavelength generated in the interaction. Taking a = 240μm, $\lambda \tilde{} 2c\Delta t$ where t is the width of the pressure pulse (Fig. 7.14) and c the sound speed for bulk longitudinal waves in the tissue (C$\tilde{}$ 1500ms-1), $Z_R \tilde{} 100\mu m$. This is considerably

smaller than the tissue sample thickness ($\simeq$300μm) so that significant 'edge' effect will occur ie, three dimentional expansion effects cannot strictly be neglected. This transition to nonplanar propagation may explain why a rarefaction component develops on the pressure pulse.

In spite of this limitation pressure amplitudes were calculated assuming plane wave propagation and the resulting pressure derived in this way is shown in Fig. 7.15 as a function of fluence. It is clear that large stresses are generated for the contacted fibre geometry, values exceeding 100MPa being recorded for output fluences above $\simeq$ 7 Jcm^{-2}. On longer timescales than shown in Fig. 7.14 the transducer output exhibited complex voltage oscillations, probably mainly arising from acoustic reflections at the many near-lying interfaces in the liquid cell. The photoacoustic measurements made for the fibre contacted (d=0) to the tissue surface show that detectable pressures occur for output fluences from the fibre exceeding about 0.9Jcm^{-2} and that the peak pressure increases steadily above this value (Fig. 7.15). This thereshold for detecting pressure pulses is higher than in air (Section 7.2.1) which is surprising given that saline would be expected to impede the expansion of ablation products and sustain pressures for longer durations. Differences in tissue state may explain this. For example in air dehydration of the surface region particularly when a large number of laser pulses is used could be influential. In saline, however, hydration would be maintained.

An estimate of the peak pressure generated under these conditions can be made as follows: it is assumed that

ablation commences at that time, t_a, during the pulse when the net fluence delivered to the surface reaches the threshold value and that the ablation products expand by compressing the tissue surface but not the fibre. If, as a result of ablation, a layer of material of thickness Δx is converted to an ideal gas, the pressure P is found using,

$$P = (\gamma - 1)\,\Delta F/\Delta x \qquad 7.7$$

where γ is the ratio of specific heats (4/3), and ΔF is the fluence delivered to the layer on the characteristic time-scale $\Delta\tau$, for pressure release to occur by expansion, $\Delta\tau$ is estimated as,

$$\Delta\tau = \Delta x/u = \Delta x\rho c/P \qquad 7.8$$

where u is the expansion rate of the gas cavity given by the local particle velocity produced in the confining tissue by the passage of a plane acoustic wave of pressure P, (shock effects are neglected and it is assumed that the fibre is incompressible). Then using $F = I(t_a)\Delta\tau$, where $I(t_a)$, is the laser irradiance at t_a, we obtain from equations (7.7) and (7.8):

$$P = [\rho c I(t_a)(\gamma - 1)]^{\frac{1}{2}} \qquad 7.9$$

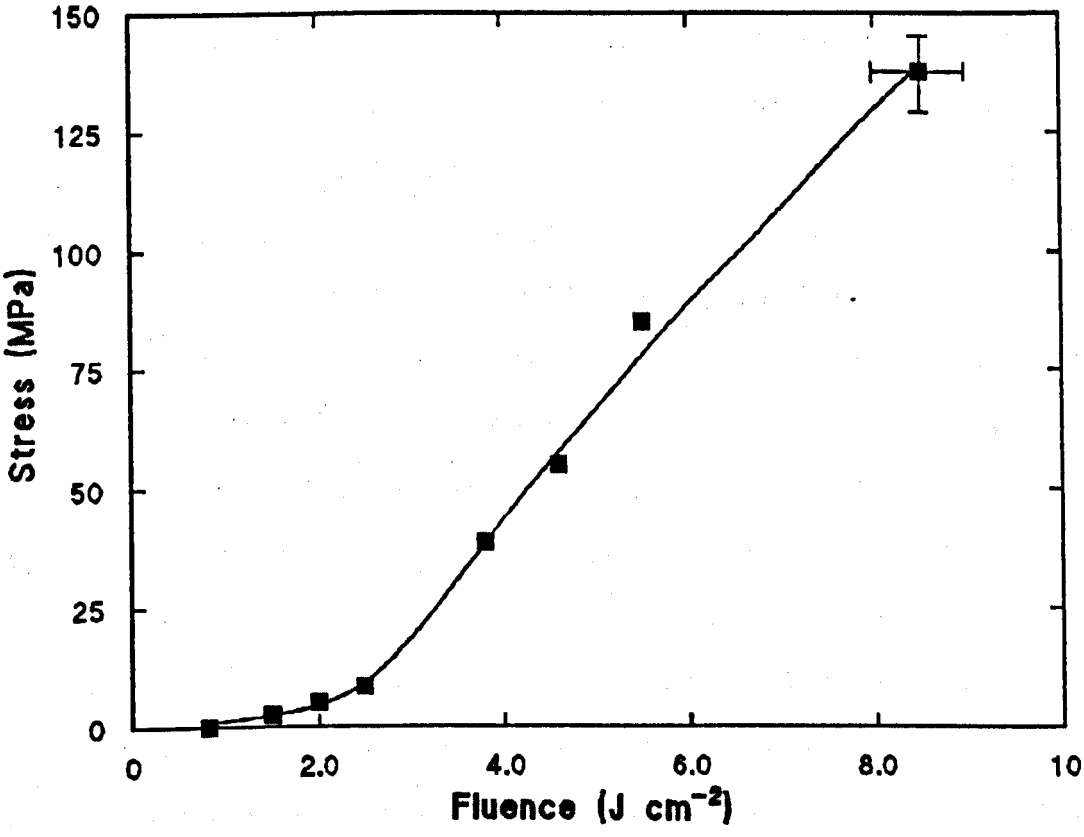

Fig. 7.15 - Peak stress deduced from the photo-acoustic transducer as a function of fluence for HF laser ablation of bovine cornea at d=0 in saline.

It is implicitly assumed in deriving equation (7.9) that the peak pressure occurs at the inception of ablation. This is reasonable if the laser irradiance satisfies $I<I(t_a)$ for $t>t_a$, making the expression applicable to fast rising but finite duration (and monotonically decreasing) laser pulses.

A similar expression has been used by Zweig and Deutsch (10) to describe pressures generated in the excimer laser ablation of polyimide in a liquid environment. In that case provided ablation commences at a fixed time near the peak of the laser pulse, the pressure scale as $(F/\tau)^{1/2}$ where F is the fluence and τ the pulse duration. In the present experiments using a fast rise-time but relatively long duration laser pulse ($\sim$900ns full duration) the pressure-fluence

dependence is anticipated to be more complicated than $F^{1/2}$. This is because for fluences near to but exceeding the threshold, ablation will commence near the end of the pulse producing low pressure because $I(t_a)$ is low. However, as the fluence is raised ablation will progressively occur at earlier times in the pulse leading to an increase in pressure that depends not only on fluence but the detailed shape of the laser pulse. Ultimately at high fluence ablation will occur at a fixed time near the peak of the laser pulse and the pressure will exhibit an $F^{1/2}$ dependence (10). This behaviour at least qualitatively can be used to explain the form of the variation observed in Fig. 7.15 where the pressure increases quite rapidly with fluence near threshold but starts to level out at high fluences. The fast rising form of the pressure transient (Fig. 7.14) and observation that the appearance of the pressure pulse moves to earlier times with increasing fluence also provides qualitative support for the model.

The peak pressures predicted using equation 7.3 are in broad agreement with the experimental findings; for example, at 5.5 Jcm^{-2}, assuming ablation occurs near the peak of the laser pulse, a calculated value of $P=1.8x10^{8}$ Pa, is obtained using $\gamma \simeq 1.16$ (10) compared with a measured value of $8.5x10^{7}$ Pa. Given that there is likely to be amplitude loss due to acoustic attenuation and beam expansion over the $\simeq$300μm tissue path between the tissue surface and transducer and that the model neglects fibre compression this agreement can be taken as satisfactory. The acoustic energy radiated into the tissue during the initial high pressure phase of the

cavity expansion can be estimated as,

$$\Delta E_A \simeq P^2 A \Delta t / \rho c \qquad 7.10$$

where A is the fibre core, Δt is the duration and P is the peak pressure respectively of the pressure pulse. At 5.5Jcm^{-2} where $P \sim 8.5 \times 10^7$ Pa and $\Delta t \sim 200$ns this corresponds to about 170μJ so that only a small fraction ($\sim$2%) of the input energy is converted to sound in the early phase of the expansion.

7.3 - Ablation of organic polymers using fibre delivered HF laser

Although there is considerable interest in infrared laser ablation of polymers no work using the pulsed HF laser appears to have been reported. Efforts have mainly concentrated on 9-10μm CO_2 devices which, under optimized conditions, can produce well defined etch crater but are not fibre deliverable. As many applications require small holes (order of few hundred microns) to be drilled in polymers the possibility of using the fibre delivered HF laser for this purpose was investigated.

Ablation experiments using the fibre delivered HF laser were carried out on two polymer systems - a polyimide (Upilex S and R type ICI Plc) and polyethylene terephthalate (PET). The experimental arrangement and procedure was as described for the ablation of cornea in air in section 7.1.1.

A feature of most polymers in the 2.6-3μm spectral region of the HF laser is relatively low absorption compared with either the mid to deep UV or long wavelength infrared (~10μm) regions. This is illustrated by the infrared transmission spectra for thin Upilex films recorded using a spectrophotometer shown in Fig. 7.16. For R and S type Upilex the largest absorption between 2.6-3μm occurs at 3470cm^{-1} (ie 2.88μm) where the absorption coefficients are α =160cm^{-1}, and 230cm^{-1} respectively.

As absorption varies significantly over the range of emission wavelengths of the HF laser (Fig. 7.16), transmission measurements were also carried out on thin films at low fluence using the laser to gain a suitably weighted value for

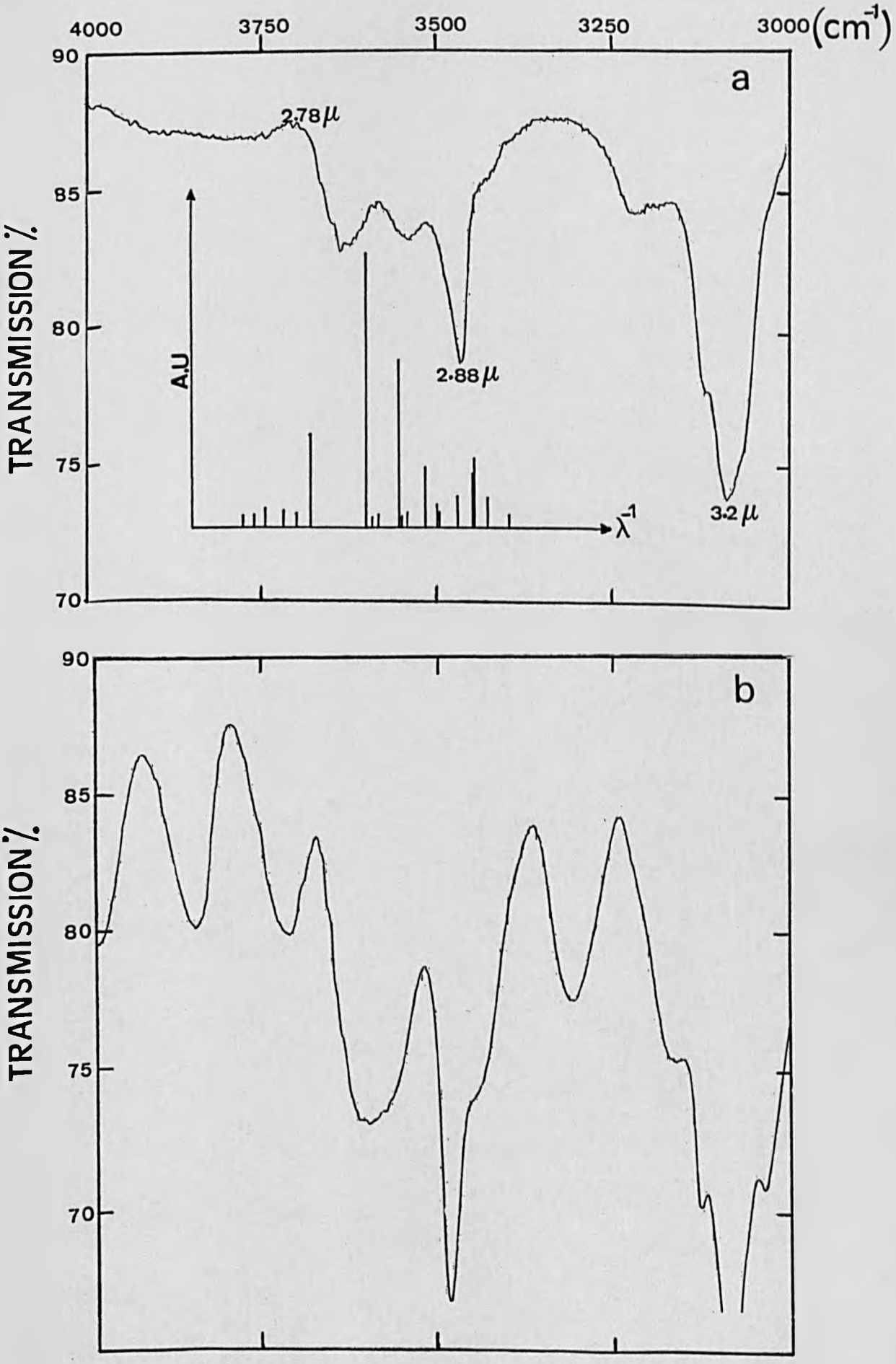

Fig. 7.16 - Small-signal IR absorption spectra of Upilex polyimide polymers (a) R-type (7.5μm) (b) S-type (20μm).

α. The energy transmission, E_T, was measured using a pyroelectric joulemeter and $\bar{\alpha}$ found using

$$E_T = (1-R)^2 \, e^{-\bar{\alpha} t} \qquad 7.11$$

where t is the film thickness and R$\tilde{-}$5% the film reflection loss. In this way $\bar{\alpha}$ was found to be $\tilde{-}$111cm^{-1} and 183cm^{-1} for R and S Upilex.

A noticable feature of etching these polymers with the HF laser was that a significant incubation delay occured before significant material removal was observed. This 'incubation' refers to the need to expose the surface to several pulses before ablation would commence. For example, for S-type Upilex 5 pulses were required at 5Jcm^{-2} before material removal was detected and for R-type this increased to about 12 pulses (Fig. 7.17a). Consequently a determination of the etch rate - fluence dependence could only meaningfully be made by averaging over a large number of pulses. In this way the data in Fig. 7.18 were obtained, yielding estimated threshold fluences of 1Jcm^{-2} for S-type and 2Jcm^{-2} for R-type Upilex films.

If the initial slope of the etch rate curves is used to derive an effective absorption coefficient α using equation 7.4 then the values are 2×10^4 cm^{-1} and 3.6×10^4 cm^{-1} for S and R type films respectively. In both cases this is much higher than the small-signal absorption coefficient and suggests that enhancement of the polymer absorption coefficent by repeated irradiation is responsible for the incubation effect (4,11).

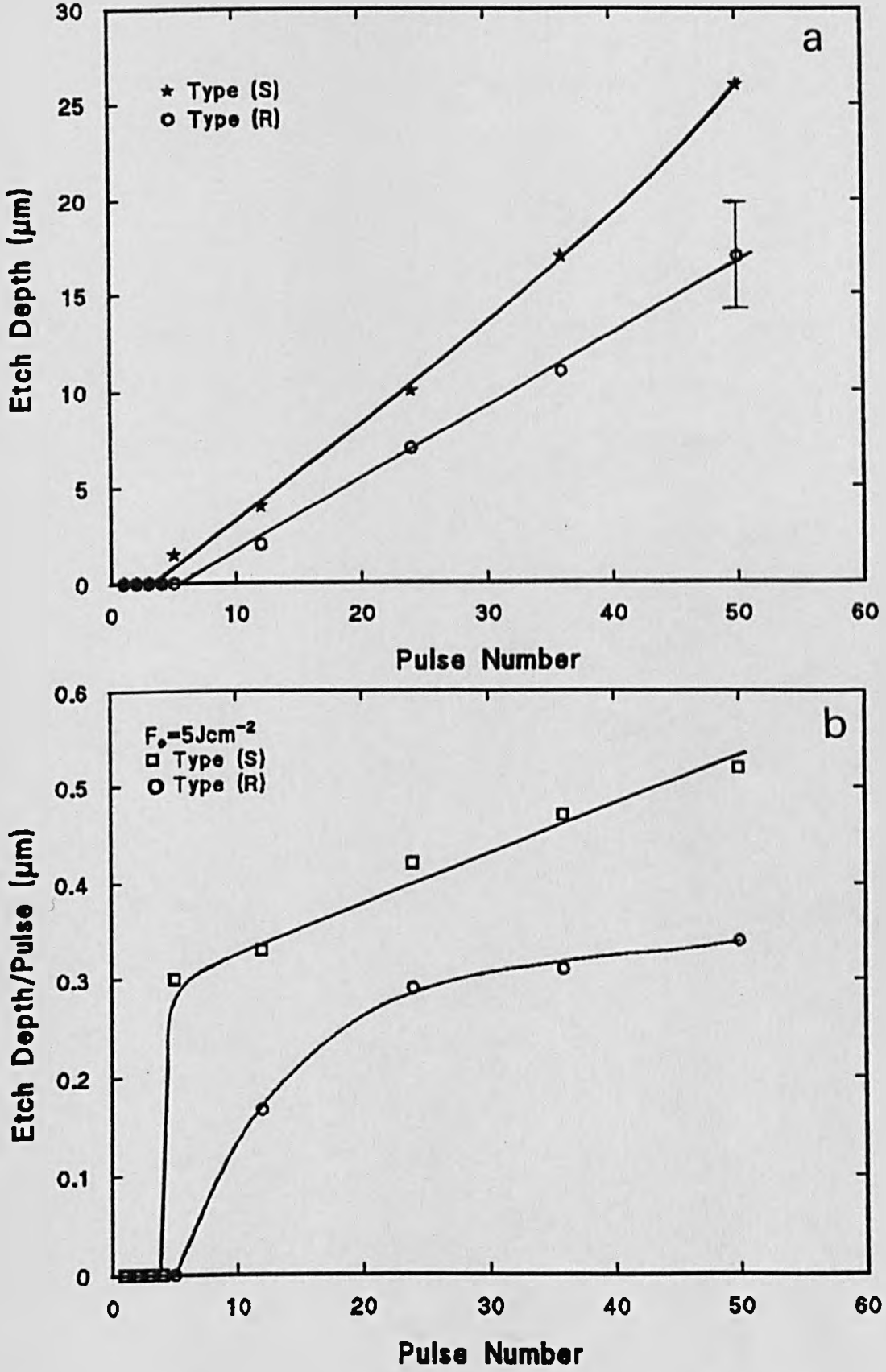

Fig. 7.17 - (a) Etch depth and (b) Average etch depth per pulse for Upilex films as a function of pulse number. Output fluence of 5Jcm^{-2} contacted fibre in air using HF laser.

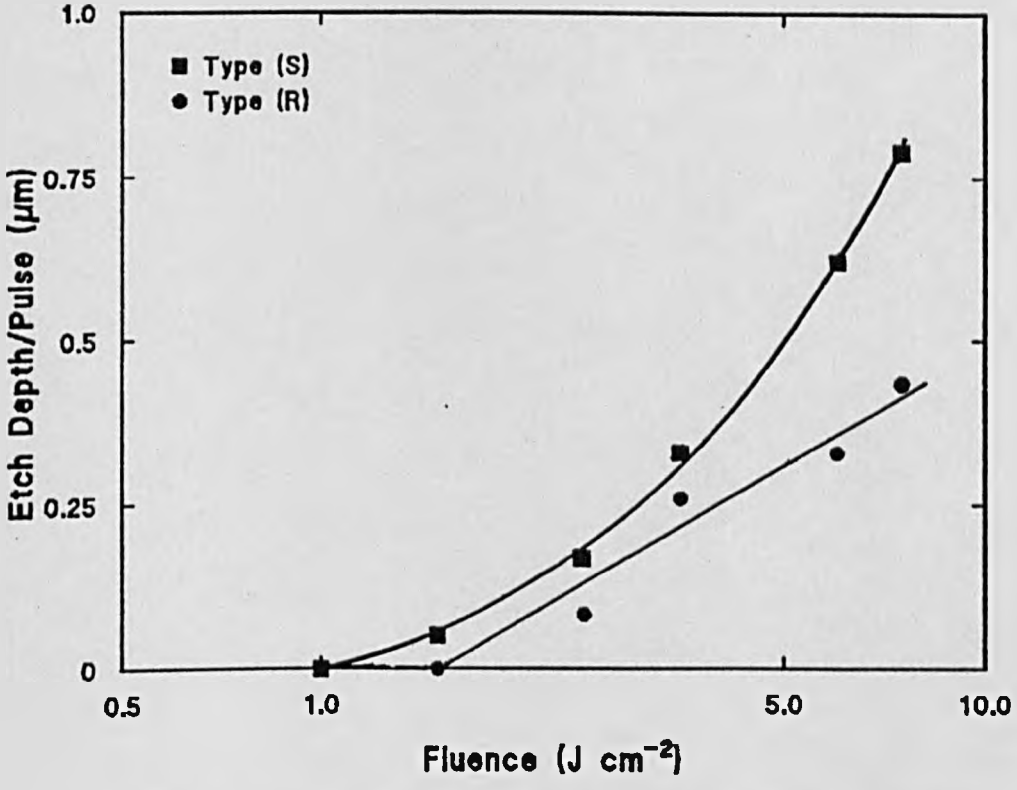

Fig. 7.18 - Ablation rate for polyimide films as a function of fluence for fibre delivered HF laser in air.

As photochemical processes are unlikely to be significant for the low photon energy HF laser (0.47-0.41eV in the range of 2.6-3μm) it is presumed that this modification is associated with repeated heating of the polymer in the initial exposures.

An estimate of the surface temperature of the films at the threshold fluence F_T can be found using equation 7.5 with $F = F_T$ and $\alpha = \bar{\alpha}$. For R - Upilex with R $\simeq$ 5%, C = 1.1Jg^{-1}C^{-1}, ρ = 1.39gcm^{-3}, α = 111cm^{-1} then $T_F \simeq$ 430K; likewise for S - Upilex with R $\simeq$ 5%, C = 1.13Jg^{-1} °C^{-1}, ρ = 1.47gcm^{-3}, α = 183 cm^{-1}, F_T = 1Jcm^{-2} then $T_F \simeq$ 398K. These temperatures are well below those at which significant thermal decomposition occurs ($\simeq$748K, ICI data sheet for Upilex) so that simple heating of the bulk polymer cannot explain the onset of damage and

material removal at these fluences. It should also be noted that accumulative heating was not important because of the low pulse repetition rate (0.2Hz) of the HF laser.

A plausible explanation for the 'incubation' effect and ultimate transition to a material removal regime can be found in terms of a model proposed by Butenin and Kogan (12, 13) to account for damage in transparent polymers. The mechanism of such damage is related to presence of opaque microinclusions (<< 1μm diameter) which are distributed throughout the material. When a laser pulse at relatively high irradiance interacts with such materials some of its energy is absorbed by these microinclusions which are heated to much greater temperatures than the bulk (essentially transparent) polymer. Associated temperature rise of the polymer adjacent to the embeded particle is sufficient to initiate local pyrolysis and degradation producing a carbonized layer (12, 13) which effectively increases the particle absorption cross-section. Repeated irradiation thus causes an increasing temperature rise, further enlarging the effective particle size and finally damage occurs under the influence of the pressure of the gaseous products of the pyrolysis of the polymer in the vicinity of the absorbing microparticles.

In steady state conditions the temperature rise T_s at the surface of an opaque, spherical microparticle of radius r, embeded in a material (polymer) of thermal conductivity K is (12):

$$T_s = \frac{\sigma I}{4\pi K r} \qquad 7.12$$

Here $\sigma = \pi r^2$ is the particle cross-section and I the laser

irradiance. The steady state is reached on timescales of $\tau \simeq r^2/k$ where k is the thermal diffusivity of the polymer. Even for the relatively short pulse duration of the HF laser near steady state conditions could prevail making equation 7.12 applicable to this case eg. for a 0.1μm particle, $\tau \simeq 60$ns compared with 400ns (FWHM) for the laser pulse. For submicron size particles and modest irradiance levels, T_s is large and sufficient to initiate local pyrolysis. For example for a 400ns HF laser pulse at 1Jcm^{-2}, I $\simeq$ 2.5x10^{6} Wcm^{-2} and for, r = 0.1μm, σ = 3.14x10^{-10} cm^2 and K = 1.6x10^{-3} cm^{2}s^{-1} (Upilex), T_s is found from equation 7.12 to be $\simeq$4200K. Even for particles as small as 0.01μm T_s is found to be 688K, which is probably high enough to initiate pyrolsis and associated carbonization. This process will be 'avalanche-like' as a result of the effective growth of σ ($\simeq r^2$) which increase T_s (equation 7.2), further increasing σ as a result of extended carbonization and so on. This mechanism would appear to produce a plausible explanation of polymer ablation with the HF laser, submicron carbon particles present in the polymer as impurities being the most likely origin of the initial absorbing centres.

SEM's of the irradiated surface are shown in Figs. 7.19 for R-type Upilex where it can be seen (Fig. 7.19a) that single pulse exposure at 5Jcm^{-2} leads to a smoothly raised topography with no apparent material removal having taken place. An example of similar but more extensive surface deformation is shown in Fig. 7.19b for exposure at lower fluence of 2.5Jcm^{-2} for 60 pulses. The material appears to have bubbled in small parts of the irradiated zone and in some cases 'blow-holes' in the raised region appear. This

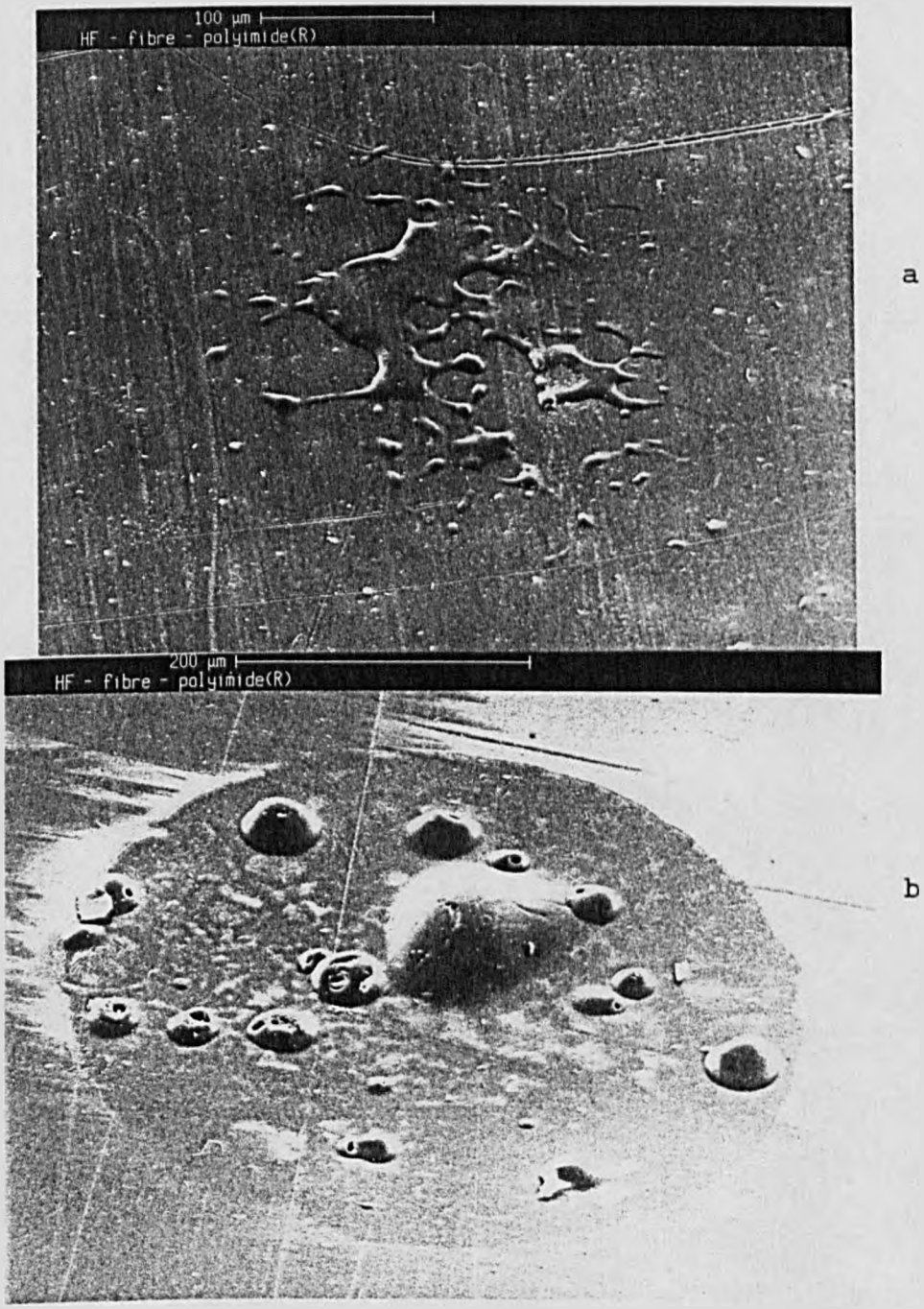

Fig. 7.19 - SEM of polyimide (R-Type) polymer irradiated in air with HF laser at (a) 5Jcm^{-2}, 1 pulse and (b) 2.5Jcm^{-2}, 60 pulses.

would be consistent with escape of volatile ablation products from the subsurface region of the film. There is very small depression of the entire irradiated surface as delineated by the circular zone in Fig. 7.19b.

Irradiating the S-type Upilex at 5Jcm^{-2} with 5 pulses produced no clearly defined etched zone (Fig. 7.20a) whereas after 24 pulses a distinct crater could be observed which was very shallow and exhibited similar bubbling to that in Fig. 7.19b for the R-type film. When the fluence was raised to 7.5Jcm^{-2} significant material removal in the form of a peeled-back layer of the surface (Fig. 7.20c,d) was apparent. The margins of the etched site were not cleanly defined, however, as the folded material remained attached to the boundary. For PET only SEM photographs were obtained; in this case both direct and fibre delivered irradiation with the HF laser led to the formation of holes in the film (Fig. 7.21 a and b) by a process that appeared to be mainly a result of local melting rather than substantial ablation (14). This is probably a result of raising the oriented semicrystalline polymer to above its melting temperature and subsequent movement of the melt region to the boundary due to both surface tension and intrisic stress in the oriented film (12-15).

The main differences between the interaction of the HF laser and the UV excimer or CO_2 laser with these polymer films can be attributed to the large differences in absorption coefficients involved. As noted above, the HF laser wavelengths are only weakly absorbed leading to a relatively small temperature rise throughout the bulk of the film. In

the case of Upelix the main removal mechanism appears to be due to the subsurface generation of degradation products presumably associated with particle mediated thermolysis of the polymers which ultimately generate sufficient pressure to cause delamination of relatively thick layer. This contrasts with results for the excimer laser or strongly absorbed CO_2 laser transitions where material is removed from the surface in the form of low mass species ranging from diatomic species to microparticles (16). For PET irradiated using the HF laser, only SEM evaluation was carried out and the extent of true material removal is difficult to gauge because of melting effects.

In both cases it is difficult to analyse the behaviour within the framework of previous ablation models for polymers because of the significantly different interaction mechanisms that are apparently involved with these weak absorbers. These preliminary experiments indicate that whilst the fibre delivered HF laser can produce holes in polyimide and PET polymers the quality is much poorer than with excimer or CO_2 laser (16,17). This is attributable to the weak absorption in the near IR (2.6-3μm) region.

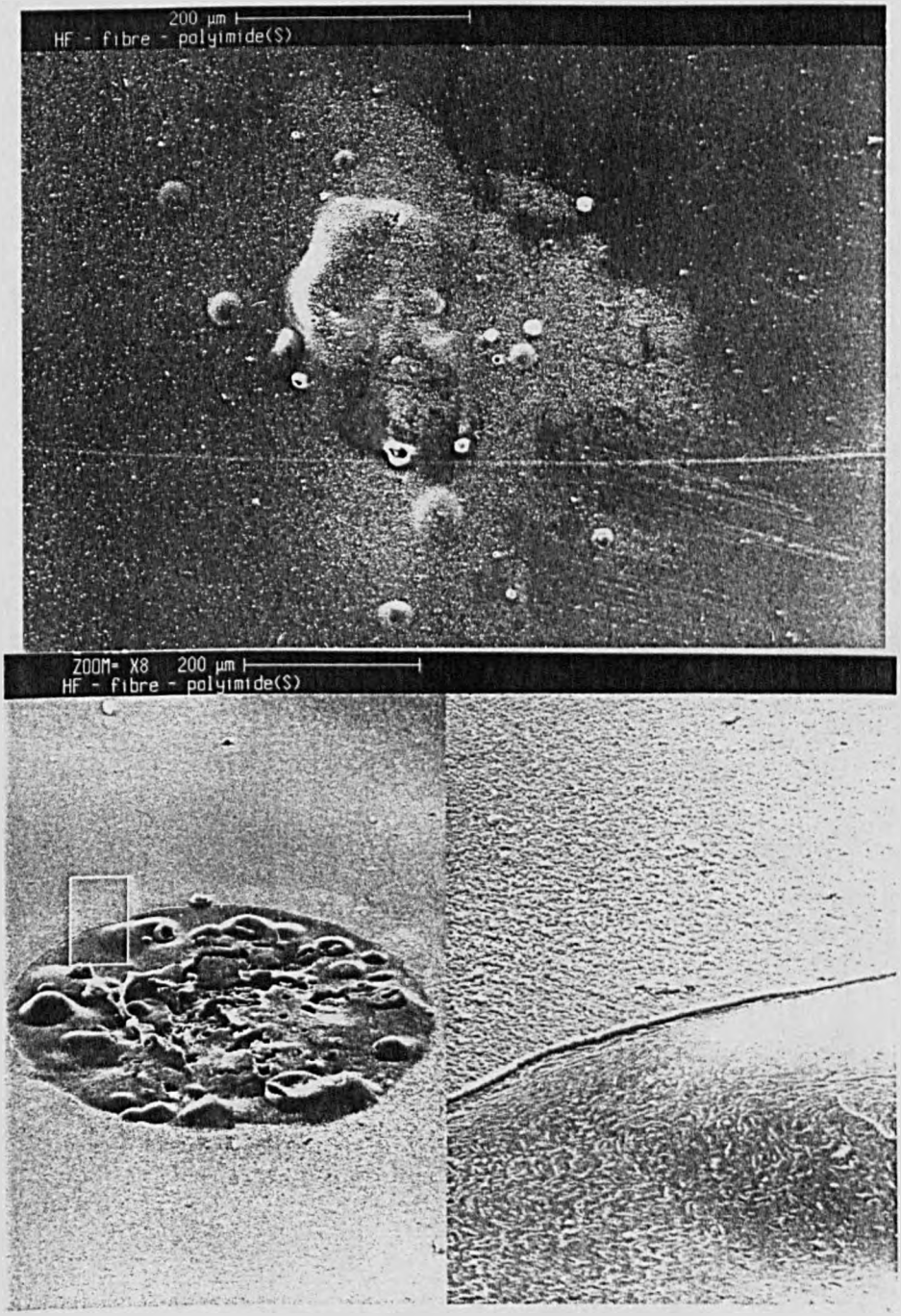

Fig. 7.20 - SEM of polyimide (S-Type) polymer irradiated in air with HF laser at (a) 5Jcm^{-2}, 5 pulse, (b) 5Jcm^{-2}, 50 pulses, (c,d) 7.5Jcm^{-2}, 24 pulses.

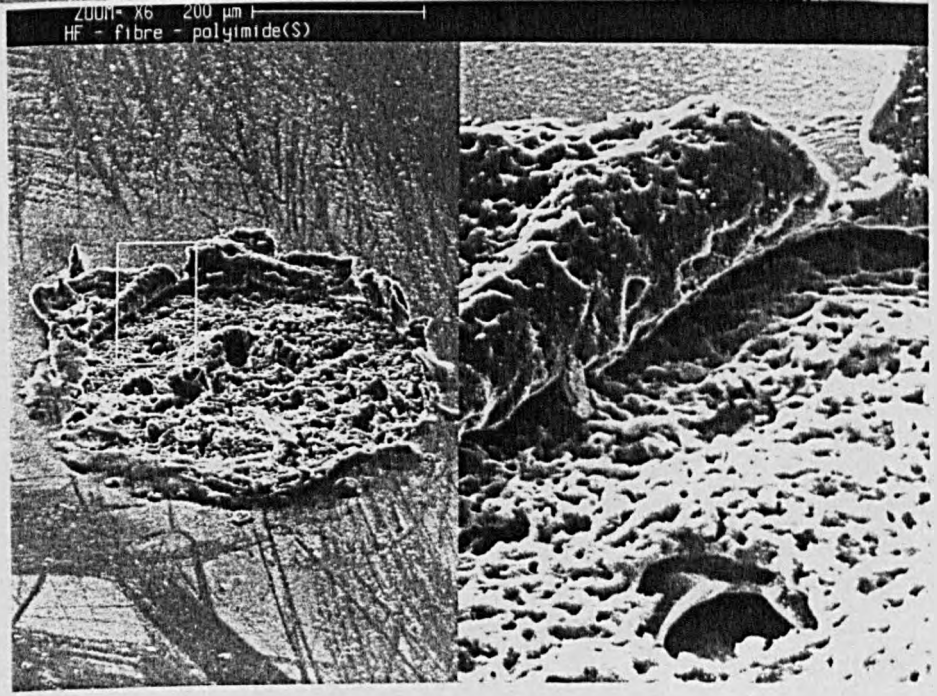

d

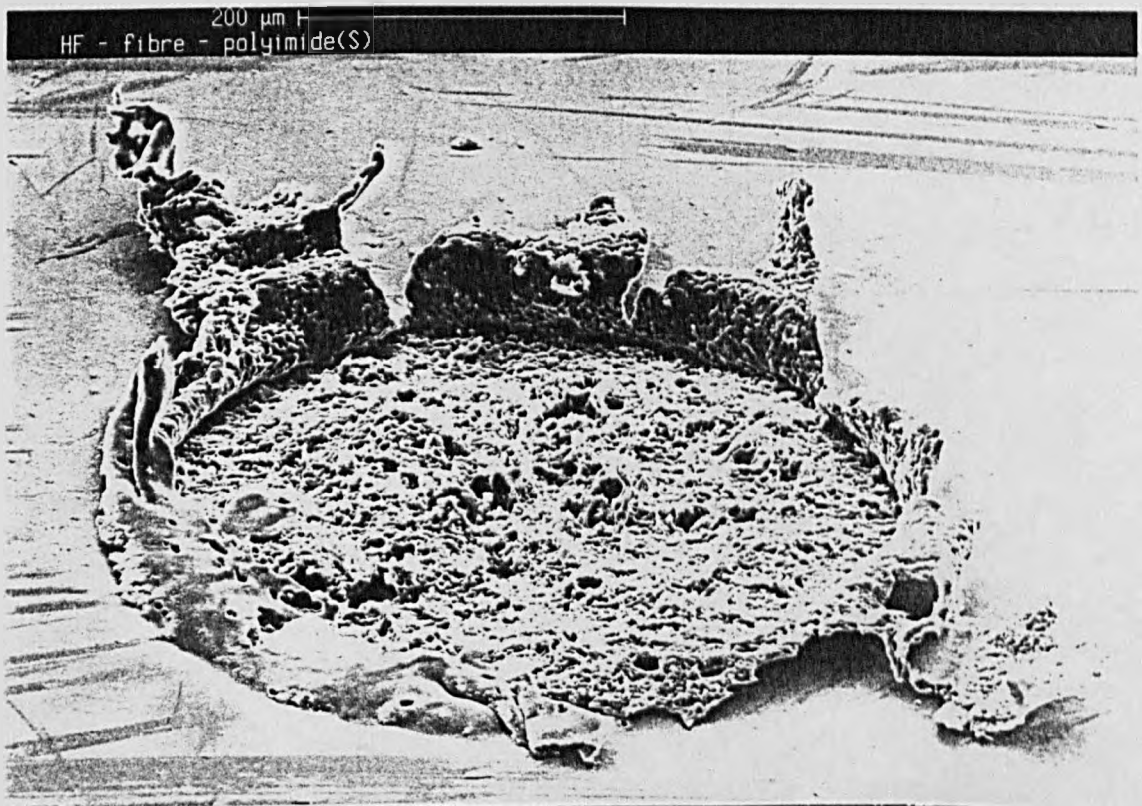

c

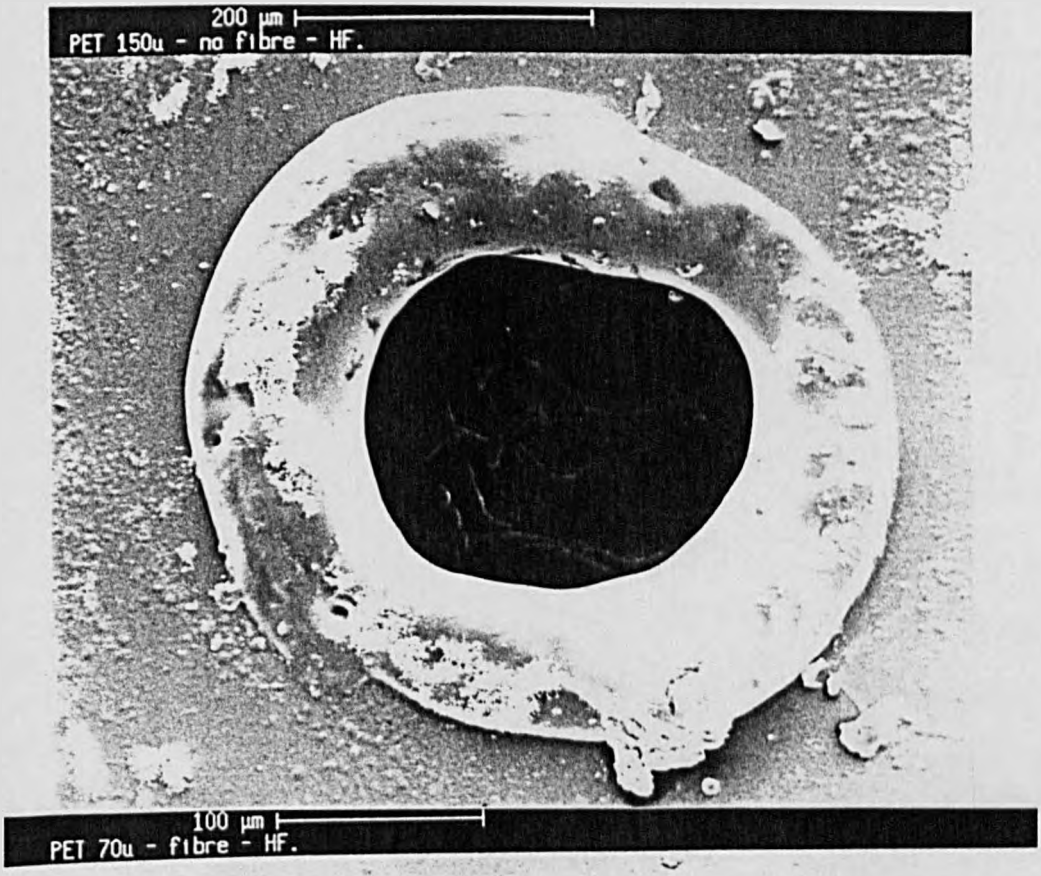

a

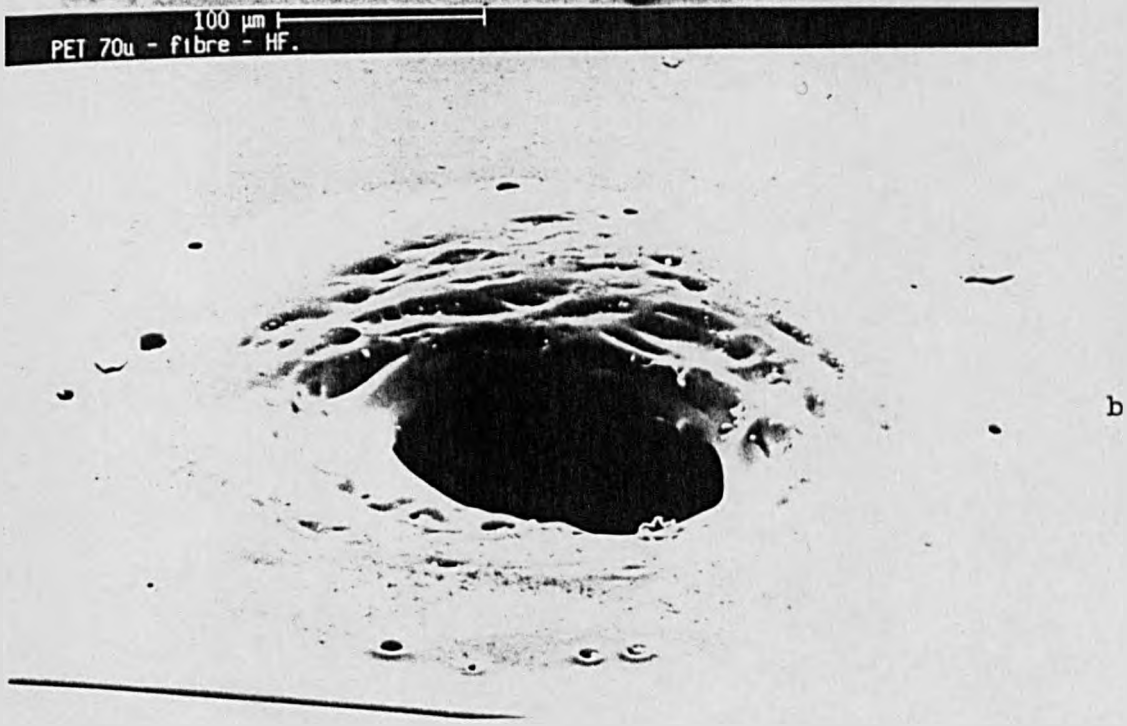

b

Fig. 7.21 – SEM of PET irradiated in air (a) without fibre at 73Jcm^{-2}, 1 pulse, (b) with fibre at 3.5Jcm^{-2}, 15 pulses.

7.4 - Discussion

In summary, the possibility of delivering submicrosecond HF laser pulses using a fluoride glass fibre at sufficiently high fluences to ablate soft tissue enhances the attractiveness of this laser for medical applications. High quality fibre delivered HF ablation of tissue in air and saline were obtained, and damage range found to be larger than e^{-1} depth in saline. Bubble formation and acoustic effects on tissue are discussed in detail in Chapter 8. Upilex polymers were ablated but with poorer quality than excimer and CO_2 lasers and significant etching only began at fluences close to upper limit of fibre output fluences. Removing the optical fibre can overcome some of the problems regarding the deposition of higher laser energy but the quality of ablation need further investigations.

1. Valderrama G.L., Menefee R.F., et al.
Chemical laser interaction with human corneal tissue.
SPIE., 1064:135:1989.

2. Leortscher H., Mandelbaum S., Parrish R.K., et al.
Preliminary report on corneal incisions created by a hydrogen fluoride laser.
Am. J. Ophthalmol., 102:27:1986.

3. Dyer P.E., Al-Dhahir R.K.
Transient photoacoustic studies of laser tissue ablation.
SPIE., 1202:46:1990.

4. Dyer P.E.
Laser ablation of polymers. In Jackman R., Boyd I. (eds) photochemical processing of electronic materials.
Academic press, 1992: Chap. 14.

5. Izatt J.A., Sankey N.D., Partoui F., et al.
Ablation of calcified biological tissue using pulse hydrogen fluoride laser radiation.
IEEE., J.QE., 26:2261:1990.

6. Holly F.J.
Am. J. Optom. Physiol. Opt., 58:324:1981.

7. Burstein N.L.
Trans Ophthalmol. Soc. UK., 104:402:1985.

8. Farris R.L.
Trans. Am. Ophthalmol. Soc., 83:501:1983.

9. Cross F.W., Al-Dhahir R., Dyer P.E.
Ablative and acoustic response of pulsed UV laser-irradiated vascular tissue in a liquid environment.
J. Appl. Phys., 64:2194:1988.

10. Zweig A.D., Deutsch T.F.
Shock waves generated by confined XeCl excimer laser ablation of polyimide.
Appl. Phys. B., 54:76:1992.

11. Srinivasan R., Braren B., Casey K.
Nature of 'incubation pulses' in the ultraviolet laser ablation of polymethyl methacrylate.
J. Appl. Phys., 68:1842:1990.

12. Butenin A.V., Kogan B.
Mechanism of damage of transparent polymer materials due to multiple exposure to laser radiation pulse.
Sov. J.QE., 6:611:1976.

13. Butenin A.V., Kogan B.
Mechanism of laser damage to polymer materials.
Sov. J.QE., 16:1422:1986.

14. Cozzens R.F., Fox R.
Infrared laser ablation of polymers.
Polymer Eng. Sci., 18:900:1978.

15. Manenkow A., Matyushin V.S., et al.
Nature of the cumulative effect in laser damage to optical materials.
Sov., J.QE., 13:1580:1983.

16. Dyer P.E., Oldershaw G., Sidhu J.
CO_2 laser ablative etching of Polyethylene Terephthalate.
Appl. Phys. B., 48:489:1989.

17. Braun R., Nowak R., Hess P.
Photoablation of polyimide with IR and UV laser ablation.
Appl. Surf. Sci., 43:352:1989.

18. Wallach-Kapon R., Saar A., et al.
Cutting of biological tissue underwater by CO_2 lasers:
using the 'cavitation effect'.
SPIE., Vol. 1202:317:1990.

Chapter 8

Shadowgraphic studies of HF laser-induced optical cavitation with fibres

8.1 - Introduction

Studies of pulsed multiline HF laser transmission in a fluoride glass fibre and ablation of cornea in air and saline were discussed in chapters 6 and 7. Lin et al (1) have recently shown that when ablation of tissue with 2.9μm Er:YAG laser is carried out in saline, bubble growth is initiated at the fibre tip because of the strong absorption in water which leads to the creation of a hot, high pressure vapour cavity. These 'optical cavitation' bubbles exhibit complex dynamics and can act as transmissive cavities that greatly extend the effective beam penetration range for relatively long pulse IR lasers (1-4) ie, comparable to the bubble growth time. Even in the absence of this effect, as the case with the short HF laser pulses used here, optical cavitation leads to energy being transported well beyond the laser beam penetration depth as a direct result of the bubble expansion following the pulse and large amplitude acoustic waves associated with bubble formation and decay. This may be advantageous in circumstances where it is desirable to achieve tissue modification or removal when a liquid layer intervenes and strongly attenuates the laser beam between the fibre tip and sample. However, such effects are undesirable under conditions where it is necessary to localize the interaction so as to minimize adjacent tissue damage (1) eg. in ophthalmic surgery when membranes are to be cut in the vicinity of the retina which is extremely sensitive to

damage.

In this chapter quantitative studies of the dynamics of bubbles produced by the HF laser at the tip of a fluoride glass fibre in saline are reported. Bubble growth and decay is observed using nanosecond dye laser shadowgraphy and the temporal evolution of bubbles compared with a theoretical model for spherical cavity growth in an incompressible liquid. The HF laser provides a well defined single pulse output of ~400ns, considerably shorter than these used in previous studies of this effect with fibre delivered IR laser (1).

8.2 - Experimental

The pulsed multiline (2.6-3μm) HF laser was coupled into a short length (150mm) of fluoride glass fibre (480μm core diameter). The fibre carried the ~400ns (FWHM) HF laser pulse into a small saline bath via a sealed bushing in the wall of the vessel (Fig. 8.1). Fast photograpic recording of bubbles produced in the vicinity of the fibre tip was implemented using the laser shadowgraph technique (4-6). This used the output from a fibre-delivered N_2-pumped dye laser suitably expanded to provide a 10mm diameter collimated beam traversing the liquid cell transverse to the fibre. The dye laser was pumped in a transverse focusing geometry and produced a few hundred microjoules of output for Rhodomine 6G with a grating tuned resonator. For these studies the wavelength was set to about 573nm, as measured using a Bentham Instruments monochromator. The emission pulse was recorded using a solid state photodiode, and as shown in Fig. 8.2, the pulse duration was ~4ns (FWHM). A polaroid camera was used to record the magnified (X 2.1) image of the laser illuminated fibre. An electronic pulse delay generator was used to trigger the HF laser and, after a variable time delay, the dye laser allowing a sequence of short time exposure pictures of the bubble to be built up. The time delay between the HF and dye laser pulses was measured for each exposure by recording their outputs using an InAs IR photodiode and silicon photodiode respectively and displaying these on a storage oscilloscope (Fig. 8.3).

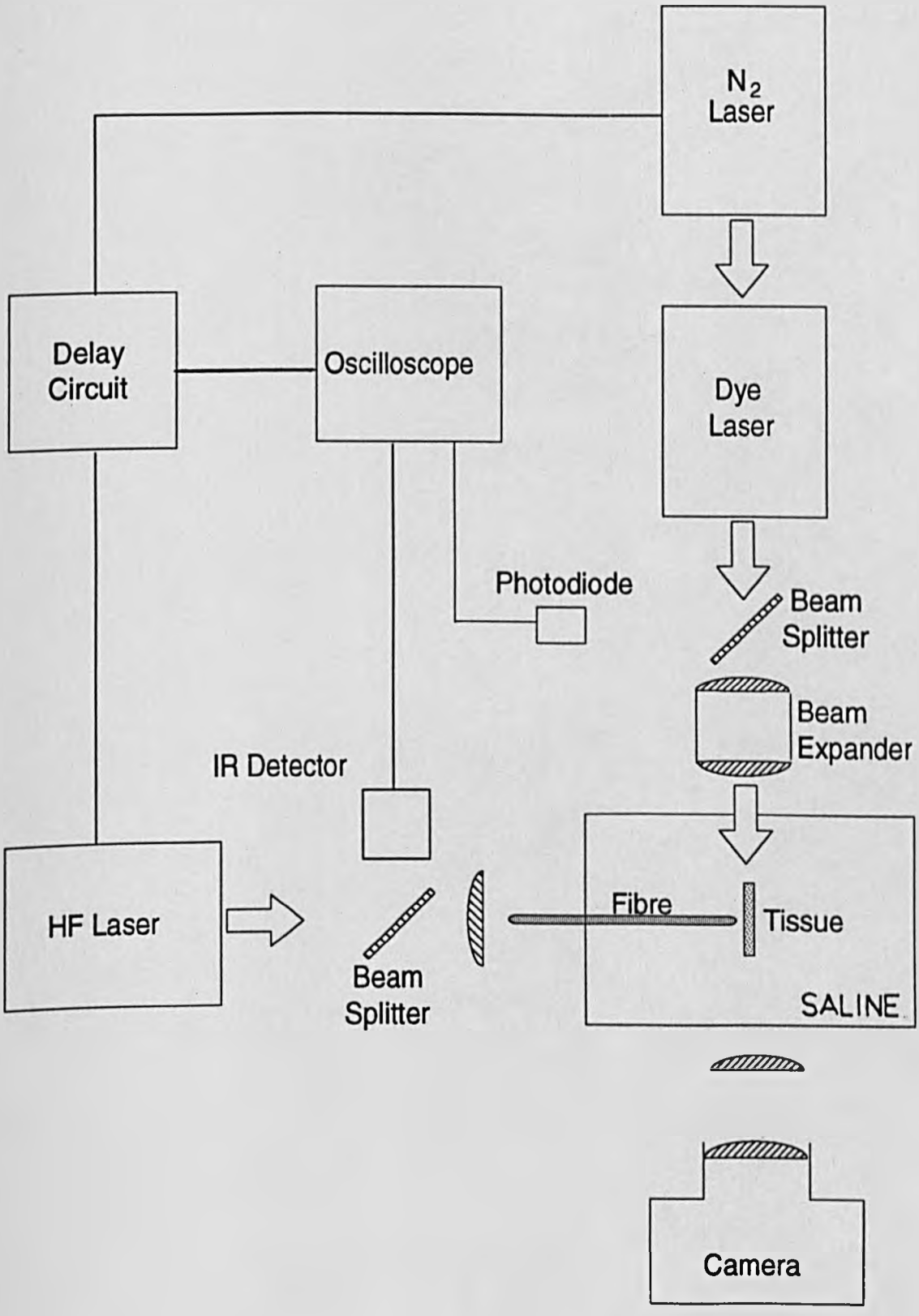

Fig. 8.1 - Experimental arrangement for shadowgraphy.

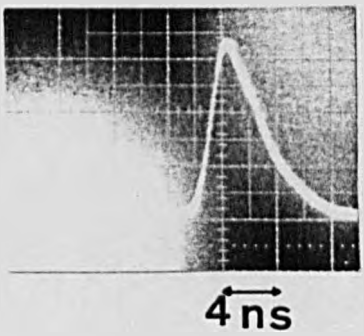

Fig. 8.2 - Emission pulse of N_2-pumped dye laser (573nm Rhodamine 6G).

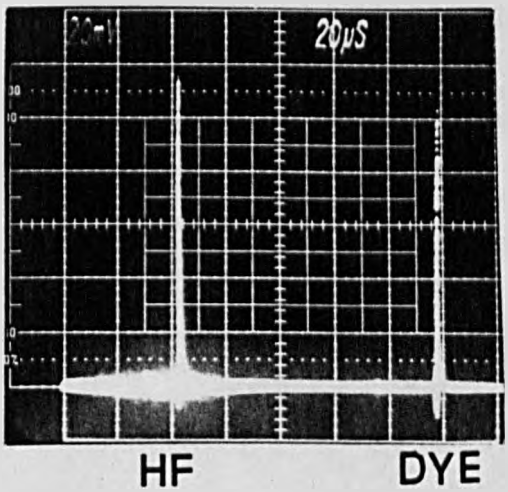

Fig. 8.3 - An example of time delay measurement, showing HF and dye laser pulses.

8.3 - Results and analysis

Shadowgraphs were recorded at various delay times with respect to HF laser pulse for several output fluences from the fibre and for various fibre-tissue sample geometries. Figs. 8.4 (a-c) show a sequence of photographs obtained at a fibre output fluences of 1, 2.5 and 5.5Jcm^{-2} respectively for the simplest configuration ie free saline and no tissue sample. Table 8.1 shows the maximum bubble diameter d_{max} transverse to the fibre axis and the distance x between the fibre tip and the front surface of the bubble for these fluences together with corresponding delay times d_t.

F_o (Jcm^{-2})	d_t (μs)	d_{max} (mm)	x (mm)
1	30	1.1	0.52
2.5	80	2.4	1.84
5.5	100	3.4	1.84

Table 8.1 - Values of maximum bubble diameter and propagated distance from the fibre tip at different fluences.

It is evident from these photographs that a vapour bubble expands from the fibre tip so as to form a cavity that is initially approximately spherical but somewhat flattened towards the fibre side. At a given fluence the bubble reaches a maximum diameter transverse to the fibre and then collapses producing a distinctly non-spherical cavity beyond $\simeq$ 40, 100 and 150μs at 1, 2.5 and 5.5Jcm^{-2} respectively. At 1Jcm^{-2} the bubble ultimately collapses at the fibre tip whereas at 2.5 and 5.5Jcm^{-2} the bubble moves away from the fibre tip at a velocity of $\simeq 10^5$ mms^{-1} for the front of the bubble. At a distance of about 3mm from the fibre tip close inspection of

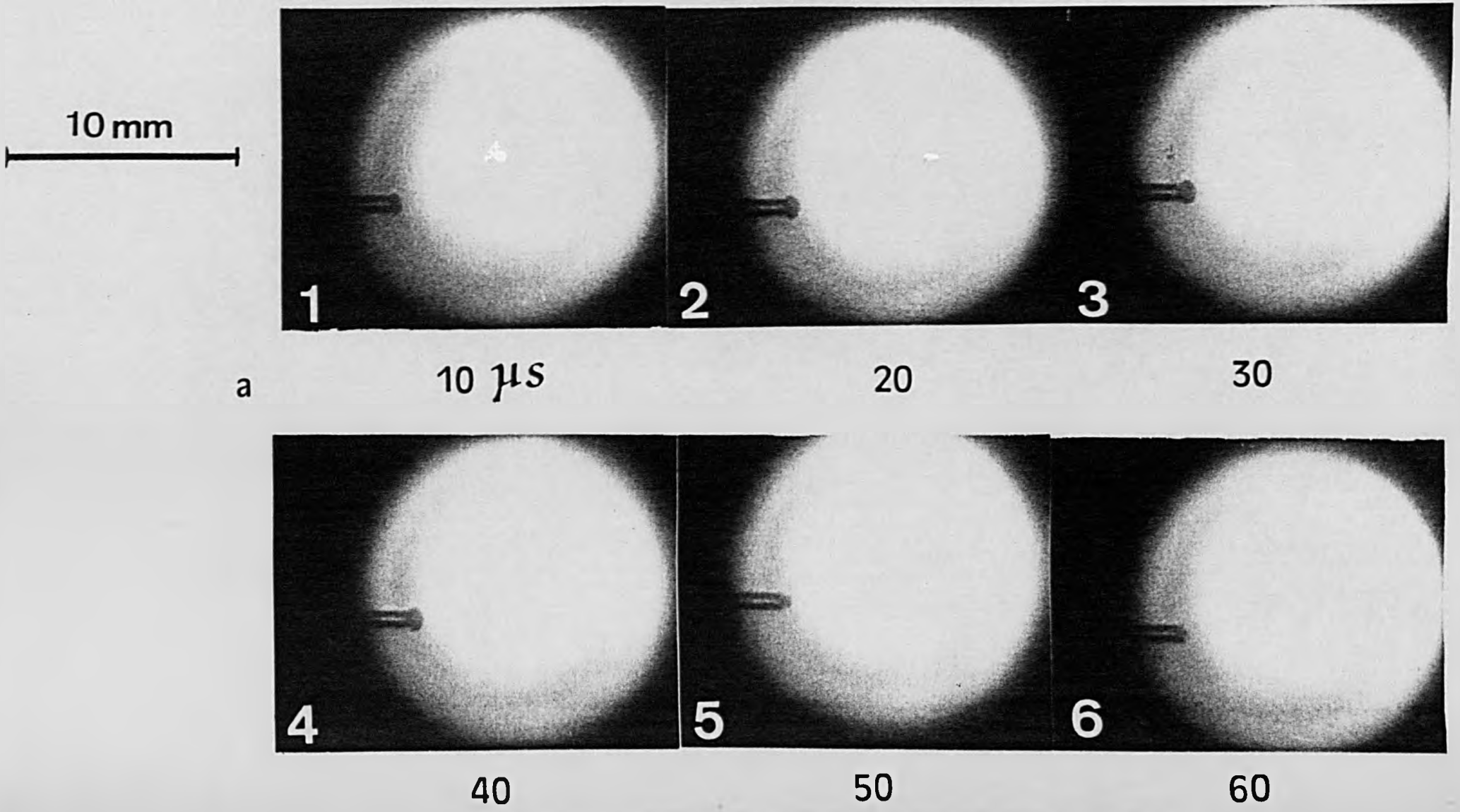

Fig. 8.4 - Sequence of bubble shadowgraphs obtained for fibre-delivered HF laser pulse at output fluences of (a) 1, (b) 2.5, (c) 5.5Jcm^{-2}.

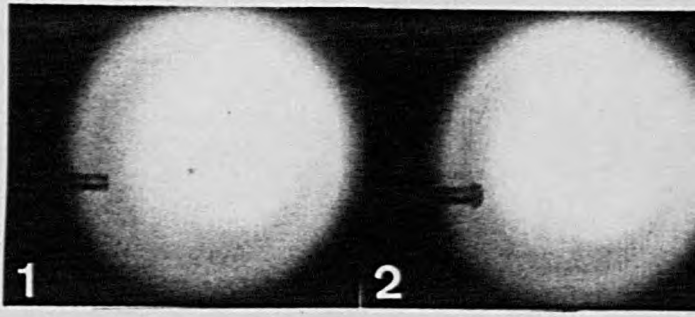

2 μs 4

b

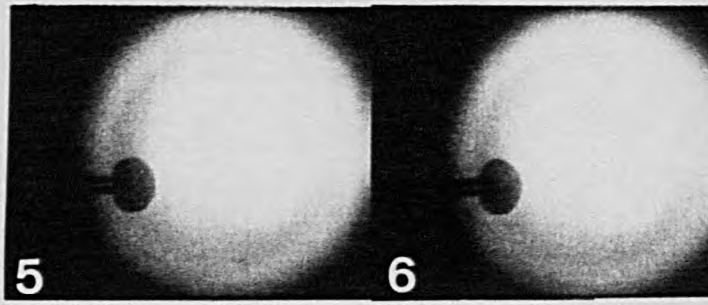

50 80

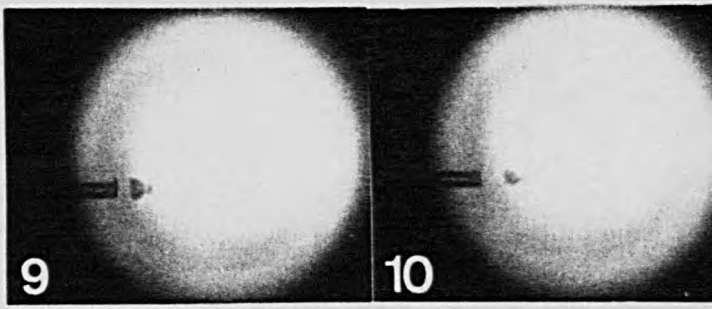

150 180

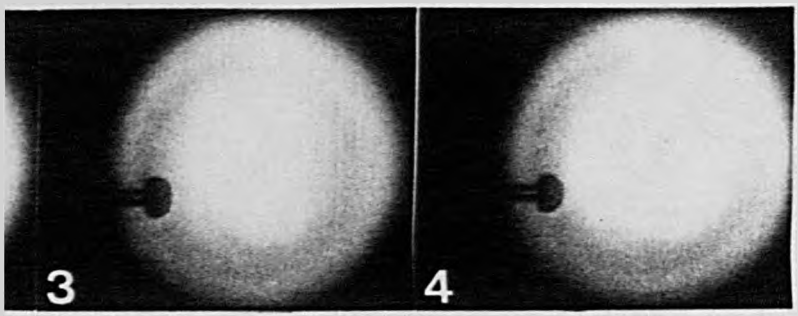

10 20

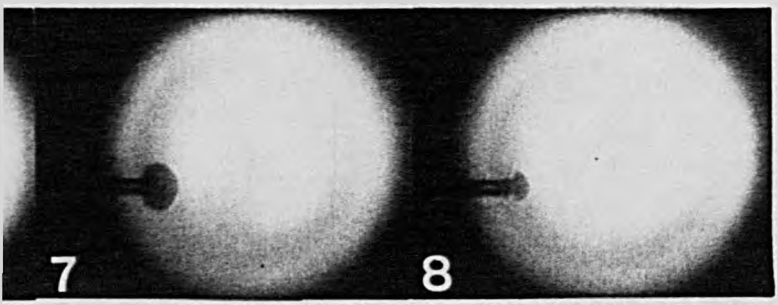

100 125

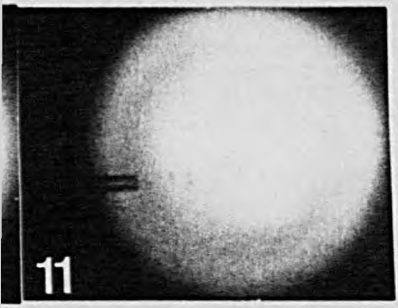

220

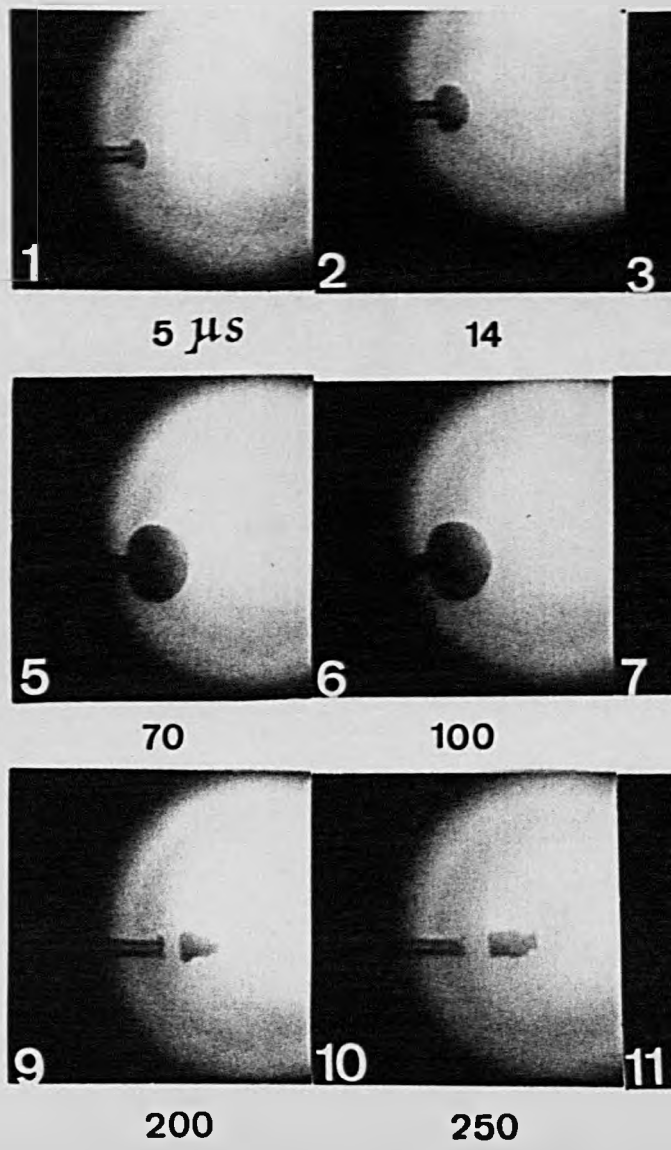
1
2
3
5 μs
14
C
5
6
7
70
100
9
10
11
200
250

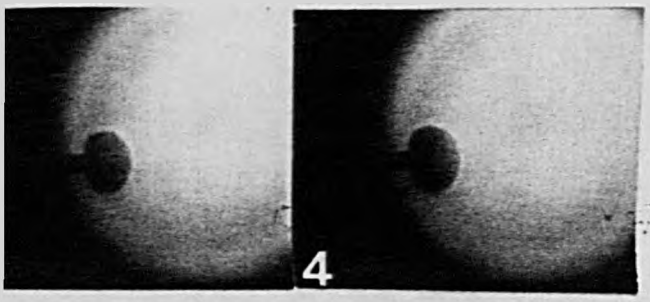

30 40

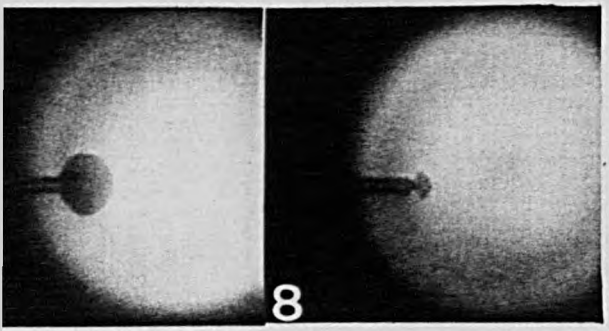

150 170

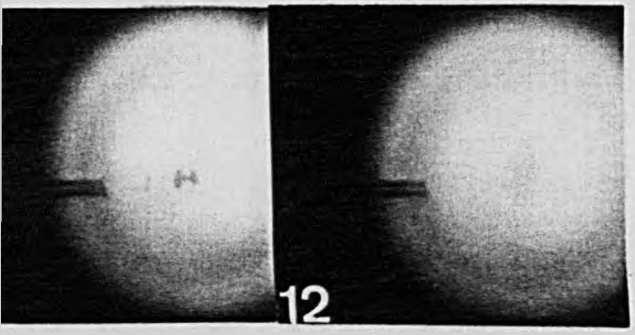

300 400

frames 11 and 12 in Fig. 8.4 (b,c) reveal that the bubble apparently breaks up, forming many smaller diameter bubbles. A similar behaviour has been reported by Lin et al (1) for a multiple pulse Er:YAG laser delivered using a fibre in saline.

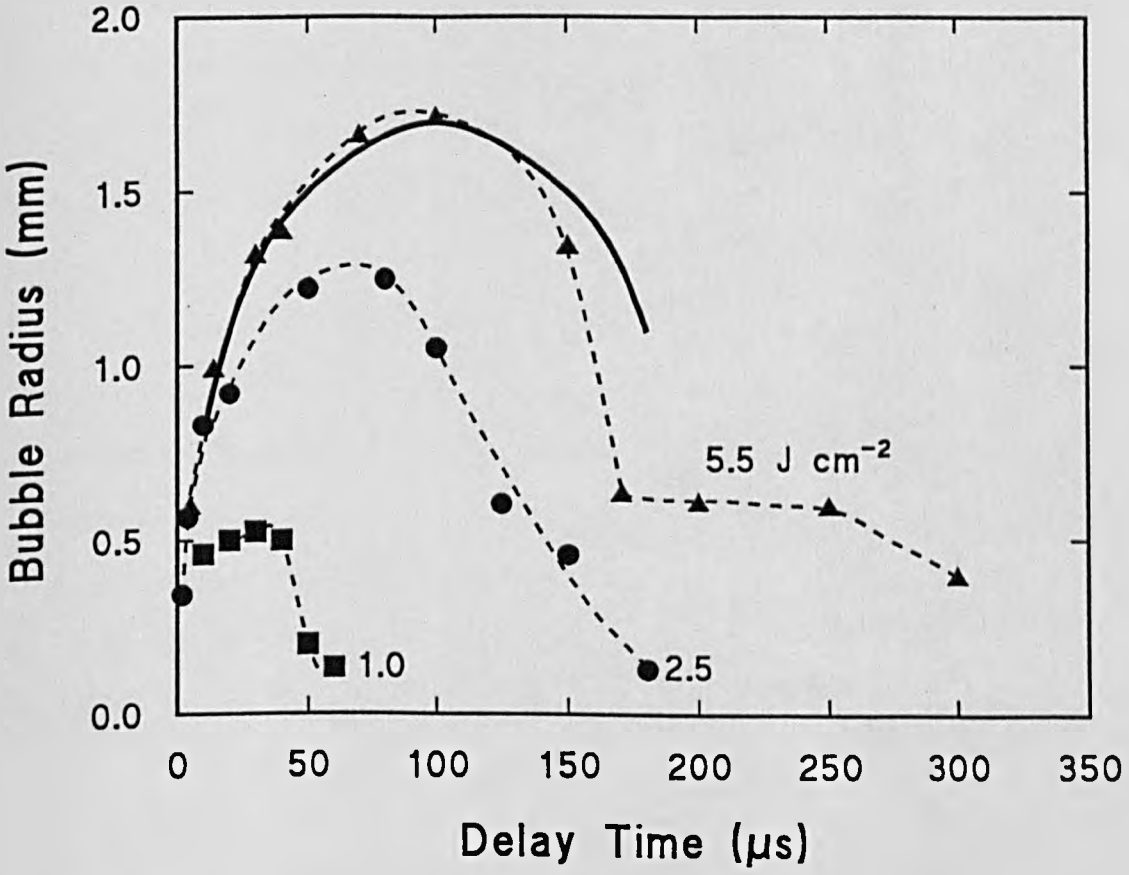

Fig. 8.5 - Bubble radius as a function of time for output fluences from the fibre of 1, 2.5, 5.5Jcm^{-2}. The broken lines are fits to the data to guide the eye. The solid line is the calculated bubble radius suitably scaled to have the same maximum radius as the experimental value at 5.5Jcm^{-2}.

Figure 8.5 plots the transverse radius of the bubble as a function of time for fibre output fluences of 1, 2.5 and 5.5Jcm^{-2}. In each case the bubble reaches a maximum size and then collapses; the maximum bubble size and the time scale for growth and collapse decrease as the fluence decreases. The bubbles in each example appeared to become unstable in

the final stage of collapse, dissipating through the generation of minute bubbles. The threshold output fluence for the onset of an observable vapour cavity using the shadowgraph technique was found to be about 0.6Jcm^{-2}; however, only for fluences exceeding about 2Jcm^{-2} did bubbles detach from the fibre tip and gain a significant forward velocity component as evident in Fig. 8.4 b and c.

Fig. 8.6 shows the plot of distance x between front surface of the bubble and the fibre tip for fluences of 1, 2.5 and 5.5Jcm^{-2}. The solid line shows where the bubble whether in expanding or collapsing phase is still attached to the fibre tip and the broken line where it detaches and moves in a forward direction. It was observed that at high fluences the interaction of the HF laser pulse with saline and the fibre tip caused many droplets scattered above the container which can distinctly be seen in Fig. 8.7. The fibre was positioned just below the surface of liquid and when the height of liquid above the fibre exceeded 1cm no such droplets were observed.

Shadowgraphs recorded for the fibre in intimate contact with cornea sample in saline are shown in Fig. 8.8. At a 4.5Jcm^{-2} after a 10μs delay small hemispherical cavity has already developed around the fibre tip as a result of the ablation products being forced between the core and jacket region of the fibre face into the surrounding liquid. This hemispherical expansion continues up to about 250μs and then collapse occurs, the bubble ultimately disappearing at ~400μs. For fluences exceeding ~5Jcm^{-2} with the contacted fibre, stress levels associated with cavitation were

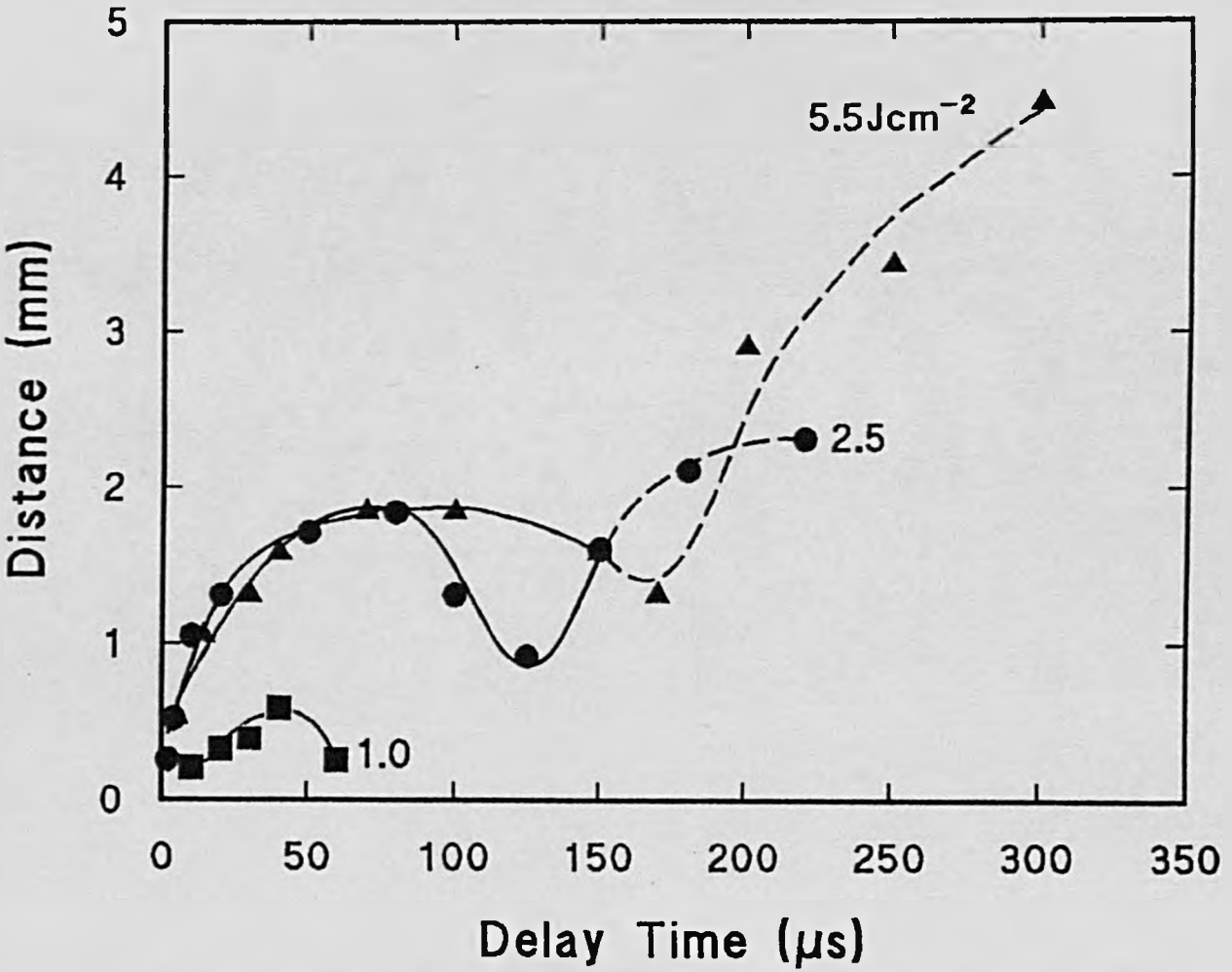

Fig. 8.6 - Distance x between front surface of the bubble and the fibre tip at various delay time and different output fluences.

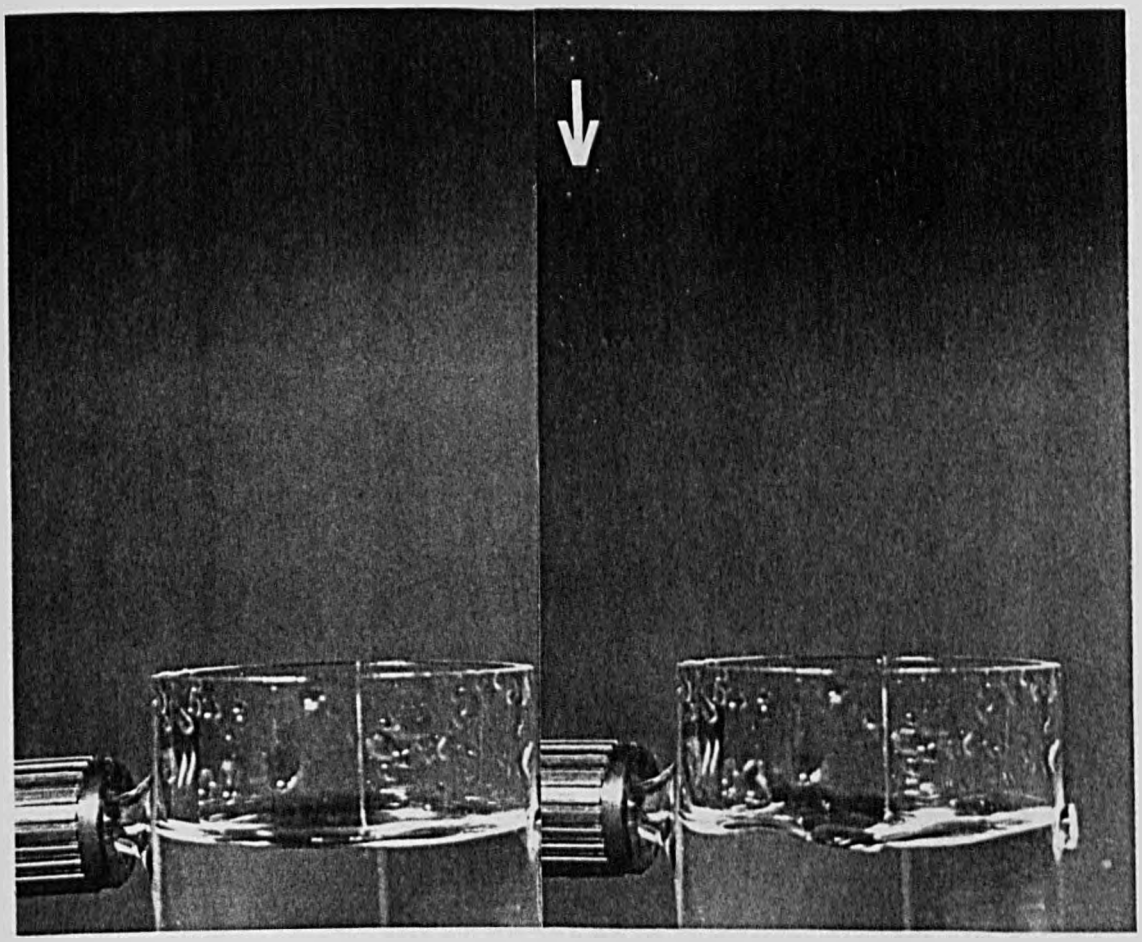

Fig. 8.7 - Demonstration of HF laser-induced droplets in saline which are scattered above the vessel. The fibre was positioned just below the surface of liquid.

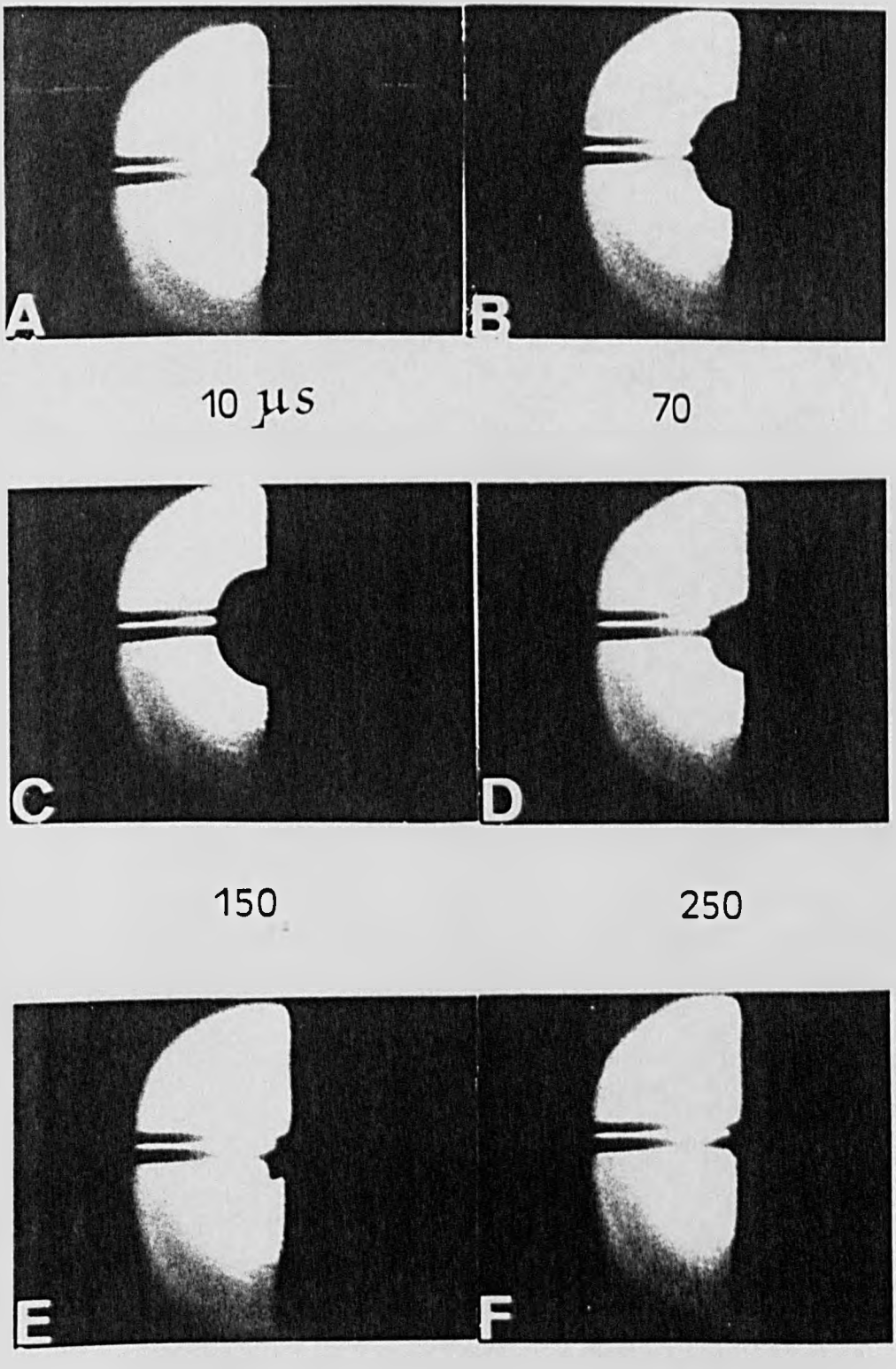

Fig. 8.8 - Shadowgraphs of fibre delivered HF laser in saline with fibre touching the cornea surface, $F_o \tilde{=} 4.5 Jcm^{-2}$.

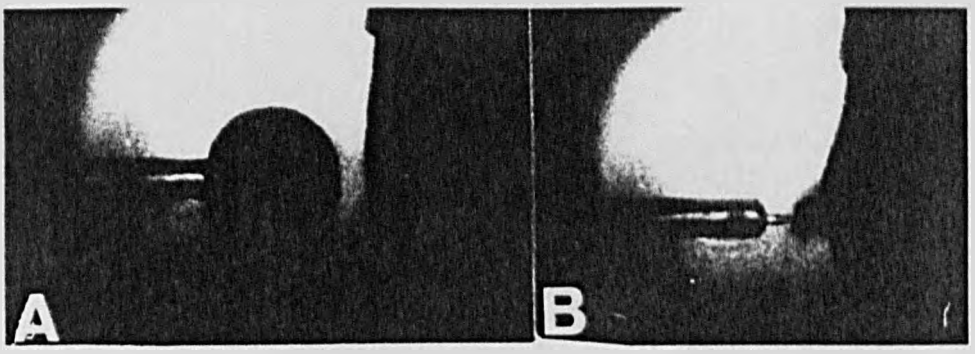

100 μs 300

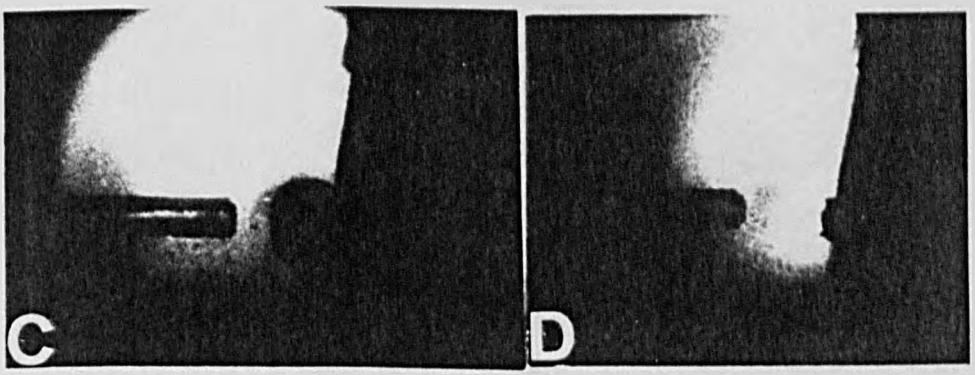

400 480

Fig. 8.9a – Bubble sequence for fibre in saline with tip positioned 2.5mm from a cornea sample, $F_o \sim 5 Jcm^{-2}$.

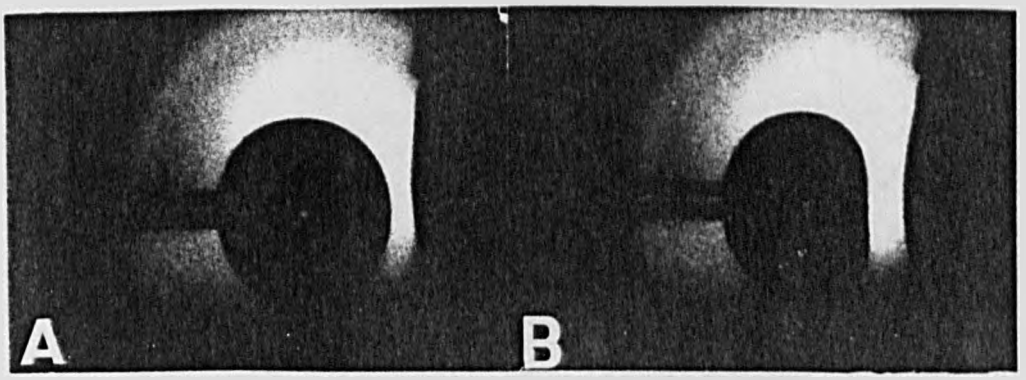

100 μs 200

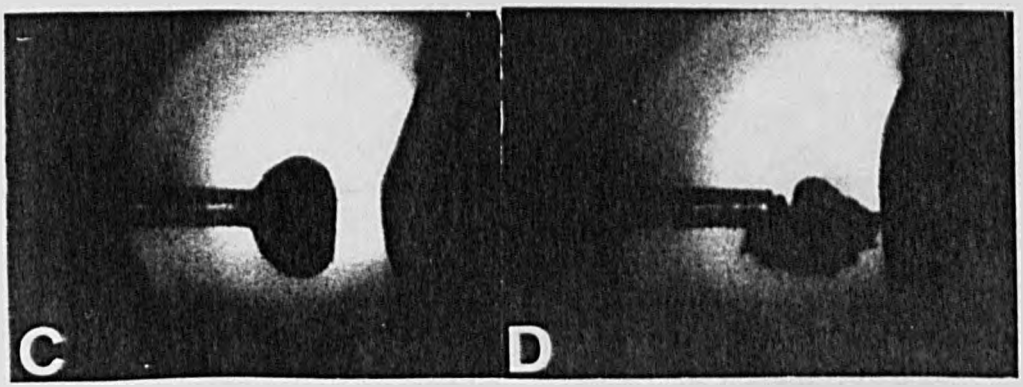

300 400

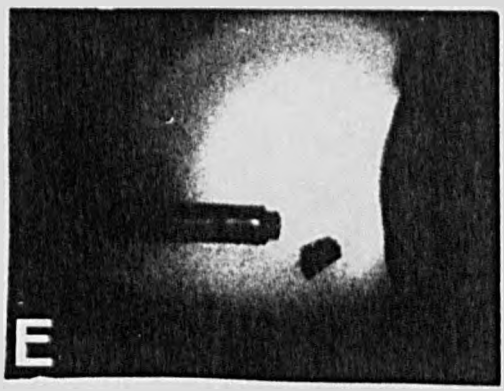

500

Fig. 8.9b - Bubble sequence for fibre in saline with tip positioned 2.5mm from a cornea sample, $F_o \tilde{-} 8 Jcm^{-2}$.

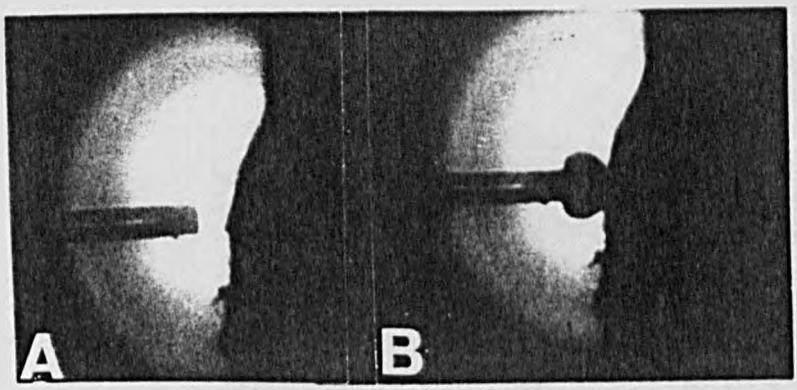

0 μs 6

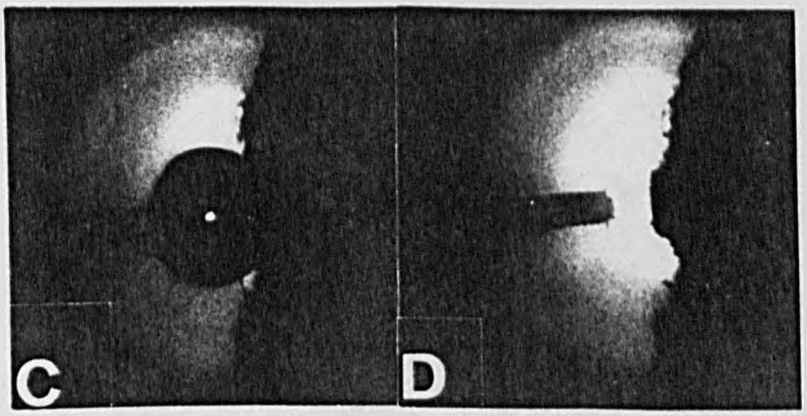

240 380

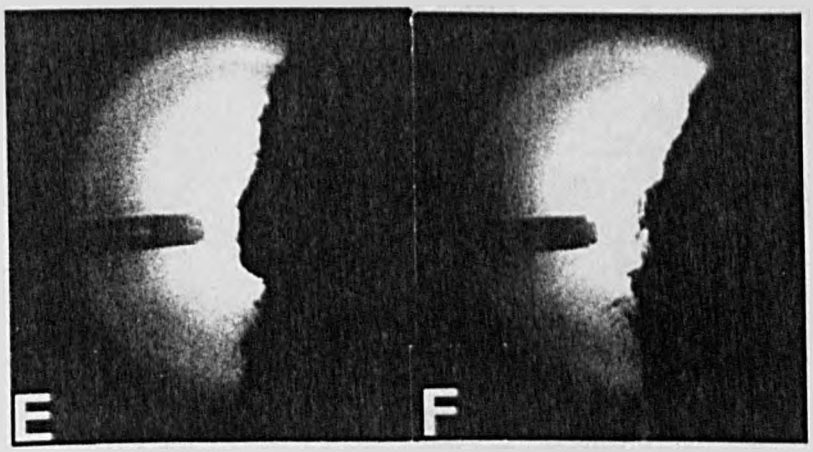

430 550

Fig. 8.10 - Bubble sequence for fibre in saline with tip positioned 2mm from a retina sample, $F_o \tilde{-} 4.5 Jcm^{-2}$.

sufficiently large to cause fracture and breakup of the acrylate jacket of the fibre in the vicinity of its tip. This effect was not observed for ablation in air (Section 7.2.1).

Figs. 8.9 (a,b) show the sequence of shadowgraphs for the fibre operating at output fluences of 5 and 8Jcm^{-2} with its tip located 2.5mm away from a cornea sample. Notable in these sequences are the (i) apparent 'jetting' behaviour of the cavity at ~300μs in frame B of Fig. 8.9a and its subsequent rexpansion and then collapse at times of 400μs and 480μs respectively, (ii) deformation of the cavity front surface beyond 100μs at high fluence as illustrated by frames B and C in Fig. 8.9b. The method of preparation and holding the retina sample during the experiment was discussed in Chapter 7. However, it must be mentioned that the retina was damaged much easier than cornea even at greater distances eg. 2mm from the fibre tip, Fig. 8.10.

The dynamics of laser-induced cavitation have been extensively studied and analysed for cases where a focused laser produces spherical bubbles either in free liquid or liquid in the vicinity of a plane solid or air boundary (7-12). For cavitation initiated by a fibre-delivered laser the situation is more complicated because ashperical growth is promoted by the planar geometry of the initial vapour cavity formed at the fibre tip and by the perturbing influence of the fibre during 'bubble' growth. This is evident from Fig. 8.4 where the vapour bubble is observed to be somewhat flattened in the direction parallel to the fibre axis. Given the lack of a readily applicable theory for aspherical growth an analysis based on a spherical cavity model is retained

here by assuming that is justifiable to define an equivalent spherical radius for the bubble. In Fig. 8.5 the bubble radius (transverse to the fibre axis) - time plot is seen to be approximately symmetrical and is similar to the behaviour observed for the growth and collapse of spherical bubble (11,13). The characteristic collapse (and growth) time for gas filled spherical bubble is given by (11).

$$\tau = 0.91\, R_m\, (\rho/P_0)^{\frac{1}{2}}\, [1 + P_f/P_0] \qquad 8.1$$

where R_m is the maximum bubble radius, ρ is the liquid density, P_0 is the liquid pressure (atmospheric pressure as hydrostatic contribution from the liquid is negligible) and P_f is the pressure in the fully expanded bubble. Estimates discussed below show $P_f/P_0 \leq 2.7\times10^{-2}$ so that τ is very close to that for collapse of an empty cavity ie. with $P_f=0$.

At an output fluence of 5.5Jcm^{-2} a value of τ = 100μs is obtained from Fig. 8.5 so that with $P_0 = 10^5$ Pa, R_m is calculated from equation 8.1 to be 1.1mm compared with $r_m \simeq$ 1.7mm for the measured maximum transverse radius of the bubble. On this basis the effective radius is substantially lower than r_m which is not unreasonable given that the bubble is a flattened sphere into which the fibre protrudes. In addition, volume may be lost due to liquid that penetrates into the axial regions of the bubble but is not detected in the shadowgraph which only delineates the cavity boundary.

The growth of a spherical vapour cavity can be described by the following equation which can be derived from energy considerations (14).

$$\rho\dot{R}^2 = \frac{2}{3}\frac{P_i}{(\gamma-1)}\left[\left(\frac{R_i}{R}\right)^3 - \left(\frac{R_i}{R}\right)^{3\gamma}\right] - \frac{2P_o}{3}\left[1 - \left(\frac{R_i}{R}\right)^3\right] \quad 8.2$$

Here R is the radius of the cavity, $\dot{R}$ the corresponding wall velocity. At t=0, the cavity velocity satisfies $\dot{R}$=0, R=R_i and the vapour pressure is P_i. It is assumed that in the subsequent expansion the vapour obeys an ideal adiabatic gas law of the form PV^{γ} = constant where $\gamma \simeq 4/3$ is the ratio of specific heats.

In deriving equation 8.2 it is assumed that surface tension and viscous effects are negligible and that the liquid is incompressible. The assumption of incompressibility leads to the cavity wall velocity being zero at t=0 and only increasing slowly with time at early stages of the expansion. This follows because the corresponding acoustic velocity in the liquid is infinite in this approximation and the gas cavity can not accelerate a finite mass of liquid instantaneously. Whilst this treatment is adequate for analysing the long-term expansion and contraction phase of bubbles it is necessary to take compressibility into account when estimating acoustic pressure levels produced in the initial stages of the laser interaction.

To evaluate equation 8.2 a value of $P_i = 8.5\times10^{7}$ Pa is used, based on the peak stress estimated from measurements using the photoacoustic transmission at 5.5Jcm^{-2} (Fig. 7.14 Chapter 7). The liquid pressure taken as $P_o = 10^{5}$ Pa. The resulting variation in velocity with radius is shown in Fig. 8.11, where $(3\rho/2P_o)^{1/2}\dot{R}$ is plotted as a function of R/R_i. In this case the maximum expansion ratio is R_m/R_i = 13.3 which with R_m = 1.1mm gives $R_i = 8.2\times10^{-2}$ mm for the

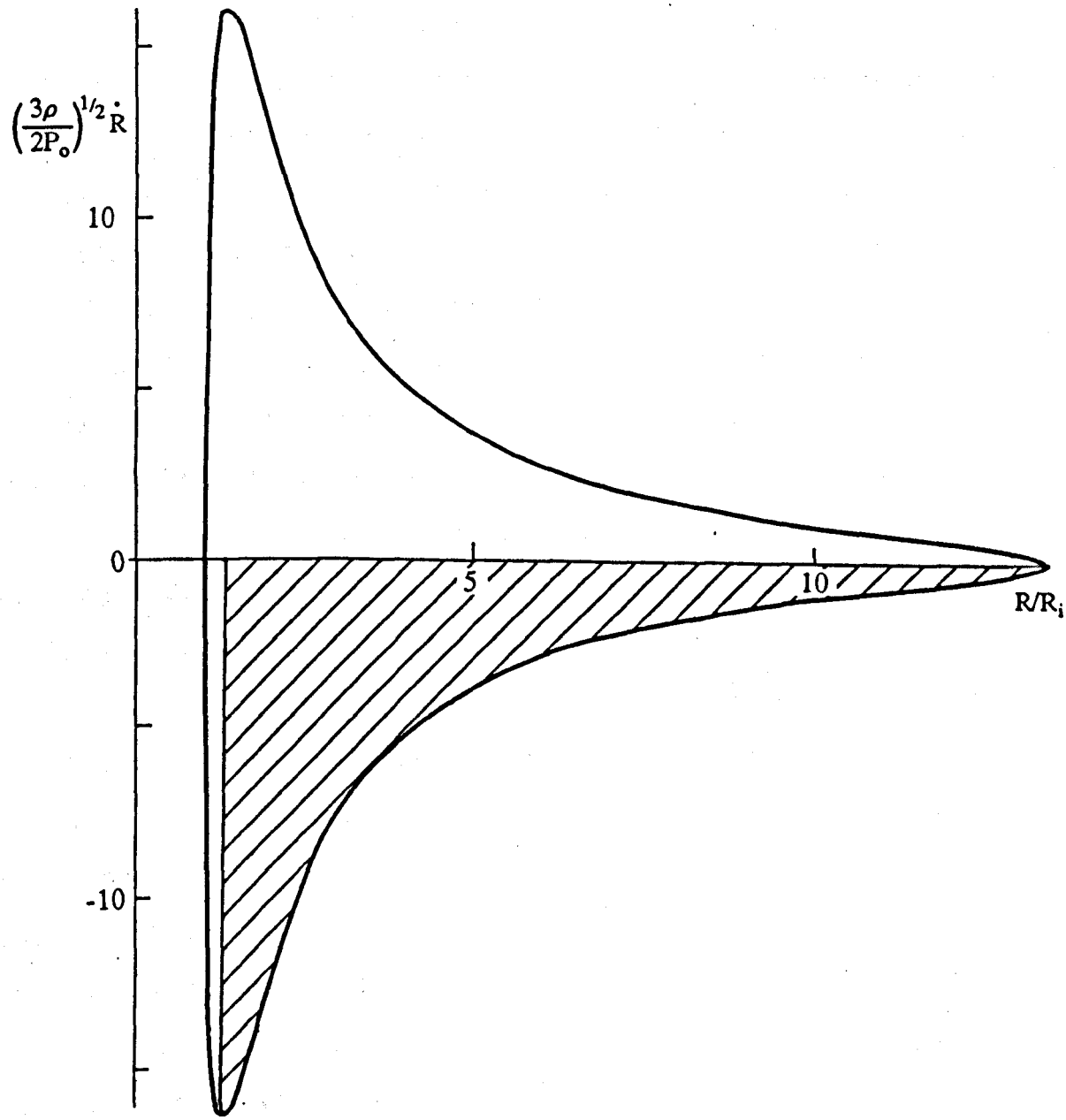

Fig. 8.11 - Normalized velocity of bubble; for initial radius R_i = 8.2x10^{-2} mm, the initial pressure P_i = 8.5x10^{7} Pa, γ = 1.33 and P_o= 10^{5} Pa. In the shaded region the liquid accelerates the wall of the vapour cavity.

radius of the initial (equivalent) spherical cavity. Assuming no dissolved air enters from the liquid, the pressure P_f, in the fully expanded cavity can be estimated using $P_f=P_i(R_i/R_m)^{3\gamma}$, to be $2.7\times10^{3}P_a$. This corresponds to $P_f/P_o=2.7\times10^{-2}$ indicating that the final pressure is substantially lower than the local hydrostatic pressure. A corresponding R-t plot derived by integrating equation 8.2 numerically is shown for comparison with the experimental data obtained at $5.5Jcm^{-2}$ in Fig. 8.5. The calculated value for R has been scaled by a factor of r_m/R_m to normalise the data at the maximum radius allowing direct comparison with the transverse radius obtained experimentally. It can be seen that this equivalent spherical model gives surprisingly good agreement with the experimental results in the expansion phase, especially given the considerable simplifications involved. For the collapse the agreement is less good particularly beyond $\sim$150μs, the time at which the bubble becomes aspherical and develops a significant forward velocity component (Fig. 8.4c). For $170 \leq t \leq 300\mu s$ it remains approximately constant in its transverse width and acquires a distinctly non-spherical shape, ultimately fragmenting at $t\sim300\mu s$ to produce many small bubbles.

The apparent instability of the cavity during the collapse phase is consistent with the onset of the Rayleigh-Taylor instability for a curved liquid-gas interface (13). Under these conditions boundary instability may occur when a dense fluid accelerates a less dense fluid (shaded region in Fig. 8.11) in contrast to a planar interface where the reverse applies. The bubble instability is presumably accentuated by the presence of the fibre and contrasts to laser

induced cavities produced in a free liquid which can remain stable and undergo multiple expansion and contraction phases (14). It is also of interest that above some critical fluence the bubble develops a significant forward velocity component during the collapse phase, a feature that appears to be peculiar to cavitation produced at a fibre tip (1). This differs from cavities produced near solid boundaries of large extent which are generally observed to be attracted towards the boundary (13). An understanding of this behaviour is lacking at present and requires further theoretical work.

At its maximum radius the velocity of the bubble wall and hence of the liquid falls to zero and from the work done on the liquid the potential energy E_o of the cavity is found to be:

$$E_o = 4\pi R_m^3 P_o/3 \qquad 8.3$$

Assuming that the R_m is given by the equivalent spherical radius this potential energy is calculated to be $E_o \simeq 0.55mJ$ at an output fluence of $5.5Jcm^{-2}$ when $R_m = 1.1mm$. This is much lower than the energy of 9.9mJ delivered to the liquid by the 480um core diameter fibre at this fluence. Similar findings have been reported by Teng et al (15) who attribute this to various losses in the expansion phase. The deficit, however, can largely be accounted for by the substantial difference in enthalpy for water ($\simeq 2500Jg^{-1}$) in the (expanded) vapour and the liquid phase, although there are small contributions due to heat conduction loss to the fibre tip and energy radiated as acoustic waves. The latter are evaluated in the following sections.

Laser-liquid interaction at fibre tip

Water exhibits strong absorption at the wavelengths emitted by the multiline HF laser and as a result energy is deposited in a very shallow region adjacent to the fibre tip (Chapter 7). For low fluences the heated depth, neglecting thermal conduction, is $\alpha^{-1} \simeq 1.6\mu m$ where α is the average absorption coefficient for the multiline HF laser ($\simeq 6 \times 10^{3} cm^{-1}$). Heating will lead to thermoelastic stress being generated due to the water expanding and if the fluence is high enough boiling can take place ie, if $T \geq 373K$ for $P_o \simeq 10^{5}$ Pa. Under conditions where the characteristic laser pulse duration, τ_L, is much longer than the timescale $(\alpha c)^{-1}$, for an acoustic zone, the peak thermoelastic stress can be shown to be

$$\sigma_T \simeq f \Gamma I_o / c \qquad 8.4$$

Here I_o is the peak laser irradiance, 'Γ' $\simeq$ 0.1 is the Grüneisen constant for water and $f \leq 0.5$ is a factor that depends on the precise laser pulse shape. For the present conditions estimates give f = 0.1 so that for $I_o \leq 10^{6} Wcm^{-2}$, $\sigma_t \leq 7 \times 10^{4}$ Pa, ie, the thermoelastic stress is relatively small. This is because stress relaxation by the propagation of an acoustic wave across the heated zone occurs on a timescale ($\simeq$0.6ns) that is much smaller than τ_L ($\simeq$400ns). In principle boiling of the heated water layer can take place once its temperature exceeds $\simeq$ 373K under conditions where the local pressure in the liquid is $\simeq 10^{5}$ Pa. However, because of the strongly nonequilibrium nature of the interaction we

postulate that substantial superheating occurs ie, the temperature exceeds $T(P_v)$=373K where $P_v \simeq 10^5$ Pa is the vapour pressure that exists under equilibrium conditions. This can be justified by noting that heat extraction by bubble growth from microscopic vapour pockets can only take place if the temperature and vapour pressure is sufficiently high to overcome surface tension effects (16). In addition, even if bubble growth is initiated, the large difference in volume between the liquid and vapour below the critical point together with the finite bubble growth velocity will limit the maximum rate at which energy can be transferred to the vapour. If this falls below the rate at which energy is input from the laser then the liquid temperature will continue to increase ie, superheating occurs.

On this basis it can be argued that the liquid is heated at approximately constant pressure ($\simeq 10^5$ Pa) to the critical temperature (T_c = 647K) at which point distinction between liquid and vapour is lost. The pressure then increases sharply and growth of a vapour cavity can take place. An estimate of the threshold fluence, F_T, for attaining the critical temperature can be obtained from:

$$F_T \alpha' = \Delta H_V \qquad 8.5$$

where α' is the mass absorption coefficient of water for the multiline HF laser and ΔH_v is the enthalpy difference between water at room temperature and the critical point ($\simeq 2000 Jg^{-1}$). If $\alpha' = \alpha/\rho$ is assumed to be constant with a value of approximately 6×10^3 $cm^2 g^{-1}$ derived from available room temperature data (17) suitably weighted for the laser

spectrum, then $F_T = 0.33 Jcm^{-2}$. A correction to account for heat loss by conduction to the fibre tip can be estimated from:

$$F_f = S(T_C - T_R)(4D\tau_L)^{\frac{1}{2}} \qquad 8.6$$

where $S \simeq 3.7 Jcm^{-3}K^{-1}$ is the mean volume heat capacity and $D \simeq 1.8 \times 10^{-3}$ cm^2s^{-1} is the mean thermal diffusivity of the flouride glass fibre (18). This gives $F_f \simeq 0.07 Jcm^{-2}$ and raises the threshold fluence to $\simeq 0.4 Jcm^{-2}$. This is considerably lower than the fluence at which a detectable cavity is revealed by the shadowgraph technique, ie, around $0.6 Jcm^{-2}$. It is noted, however, that this calculated 'threshold' corresponds to the attainment of the critical temperature at the water surface in contact with the fibre tip; substantially higher fluences are probably necessary to ablate a sufficiently large volume to produce bubble growth.

8.4 - Discussion

The study of the behaviour of cavitation bubbles close to rigid boundaries is of particular importance because of the associated phenomenon of cavitation erosion which arises from the resulting changes in pressure in the surrounding liquid. Cavitation is a group of phenomena which are associated with the occurrence of voids or cavities in liquids, especially their formation, motion, and the physical, chemical and biological effects thereby produced. A cavity in a liquid (cavitation bubble) is any bounded volume in space being empty or containing vapour or gas with a defined physical boundary. A cavitation can be produced by different methods like hydrolic, acoustic and optical which can either be transient or stable.

Transient cavitation is associated with the rapid growth and collapse of a cavitation bubble over a short period of time, the collapse being so violent that bubble itself is destroyed. Furthermore, due to the rapid increase in magnitude of the bubble radius within an acoustic cycle, the cavity contents at maximum radius are mainly water vapour molecules. Stable cavitation, on the other hand, refers to the oscillation of a gas bubble in an acoustic field for several acoustic cycle. The oscillation may or may not be vilent, but the bubble remains a separate and distinct entity (19).

The generation of sound by the absorption laser radiation in a liquid was first reported by Askaryan (20). The propagation of a high intensity of beam of light through a weak absorbing liquid exhibits dynamics such as dielectric

breakdown and optical cavitation as well as photochemical reactions (21). The dielectric breakdown and plasma formation will in turn initiate a violent localized interaction with the production of spherical acoustic transients. An optical cavitation is then induced due to rapid breakdown and heating of a small volume of liquid around the focus of converging lens. Early investigation of shock-wave pressure with shadowgraph and schlieren methods involved the use of ruby and Q-switched Nd:YAG lasers (22-26).

In the case of strongly absorbing liquids high energy deposition rates will lead to violent disruption of the liquid surface and the generation of shock waves in the gas above the surface and in the liquid. When the energy deposition is such that the temperature of the liquid does not reach the boiling point, the excitation of sound is due to the thermoelastic process which is associated with the thermal expansion of a rapidly heated volume of the medium. Efficient thermoelastic sound generation requires short laser pulses with duration in the nanoseconds. On the other hand, if the energy deposited in liquid is higher than vaporization threshold, escaping vapour gives rise to a reactive force in the liquid which usually exceeds the thermoelastic cavity and the formation of microbubbles. This has been shown by the interaction of a pulse from a TEA CO2 laser with the free liquid surface such as water (27-31).

The application of shockwave effects on biomaterial can both be unwanted as in ophthalmology and desirable for example in urology (32-35) provided its use is optimized. The process of fragmentation of biliary and urinary calculi

begins with the heating of the surface by absorbed laser light. Microscopic particles vaporized as blow-off material canal then form absorption sites in front of the stone and once a critical free-electron density is reached by laser-induced heating, either at the surface or at particles near the surface, a plasma forms. The plasma blocks further delivery of optical energy to the target by absorbing laser radiation through inverse bremsstrahlung. Finally, absorption of laser energy by the plasma results in rapid expansion and the generation of high pressure stress waves in the target and surrounding medium.

As is evident from Fig. 8.4 bubble growth is not fast enough to clear water between the fibre tip and sample at this range on the timescale of the laser pulse and the bubble cannot act as a transmissive cavity for the IR radiation (1,14). It can thus be deduced that this damage is not a direct result of laser photoablation. For the cornea the damage range is much smaller ($\sim$250μm, Chapter 7) and this matter could not be determined from the shadowgraphs because of the small spatial scale involved so it is necessary to estimate from theoretical considerations whether water clears the intervening space. This is difficult because of the geometry but if it is assumed that fluid compressibility defines the (initial) maximum flow velocity than in the plane wave approximation the clearance time is approximately a $\rho c/p$ where a is the fibre core radius. For $P \simeq 8.5 \times 10^7$ Pa corresponding to a fluence of 5.5Jcm^{-2} this gives 4μs which is significantly longer than the laser pulse. Thus, even for the small distances involved for cornea damage, water will likely

remain in the vicinity of the fibre tip on the time-scale of the laser pulse and hence attenuate the beam and prevent it reaching the tissue surface. This conclusion is qualitatively supported by the morphology of the damaged surface which differs significantly from that produced by direct HF laser photoablation (Section 7.2.1). The appearance of the SEM for the non-contacted fibre (Fig. 7.10) suggests that damage has produced a separation of collagen fibrils of the stroma of the cornea. This may be the result of pressure waves that have disrupted the normal light packing of the fibrils. The loose fibrils have then moved forward to be above the surface of the tissue (this may be an artifact associated with tissue swelling).

It is thus reasonable to deduce for both cornea and retina that either impingment of the hot vapour cavity and associated jetting effects (Fig. 8.9a) or large amplitude acoustic waves are responsible for the long range damage. Given the relatively low energy content of acoustic waves generated in the initial expansion phase of the cavity (Chapter 7) and the lack of any clear mechanistic origin for 'ablative' damage by such waves it is tentatively concluded that energy transferred to the surface by the cavitation bubble is the main source of this damage. It should be noted, however, that although acoustic waves may not be instrumental in removing significant levels of material from the surface they can be damaging to tissue cells over a relatively large range when ablation takes place in a confining liquid (36) as is the case here.

In terms of minimizing damage range associated with the

cavitation bubble and associated acoustic transients it would be of interest to use smaller diameter fibre cores as, for example, have been used for Ho:YAG surgery (37). The maximum bubble diameter can be estimated from equation 8.3 as:

$$R_m = (3\delta a^2 F/4P_o)^{1/3} \qquad 8.7$$

where F is the fluence at the fibre tip and the fraction of energy that is available to support bubble growth which is estimated to be $\simeq$ 5% in the present experiments. For a fixed fluence, R_m varies as $a^{2/3}$ so that the bubble range is reduced as the fibre core radius is decreased. In addition, the smaller effective acoustic source size would lead to a more rapid transition to three-dimensional acoustic wave expansion and hence sharper fall off in pressure with distance. Smaller fibres also have the advantage of improved flexibility and less suceptibility to breakage than the large diameters employed here. The penalty, however, would be lower tissue volume removal rates although this could, in principle, be offset by the use of a high repetition rate laser which could operate at low energies because of the reduced energy input needed for the fibre.

Finally in an 'invivo' operation such as vitreous surgery or diabetic retinopathy using the pulsed IR laser, great care must be taken to avoid thermal damage of surrounding tissue caused by possible reflected beam as well as heat diffusion. Application of Fresnel's equations demonstrate that significant laser reflection occurs at gas-fluid or fluid-gas interfaces, especially at high angles of incidence (Fig. 8.12). If photocoagulation must be performed

across an interface, the surgeon should minimize the angle of incidence of the treatment beam, use a divergent beam, and consider the location and intensity of the reflected beam (38). For the 2-3μm wavelength laser in a saline environment beam attenuatiion in the liquid would reduce the danger from this effect.

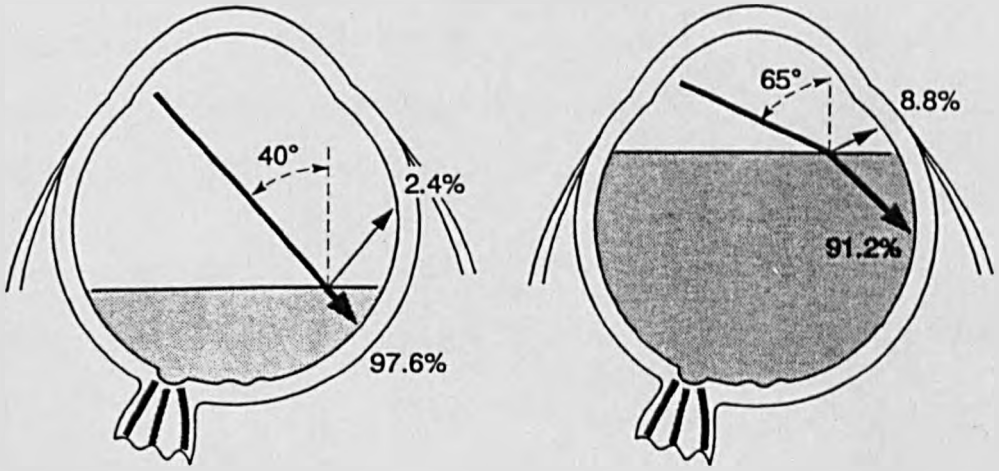

Fig 8.12 - Laser beam reflection off a gas-fluid meniscus in an eye of a supine patient(38).

1. Lin C.P., Stern D., Puliafito C.A.
High speed photography of Er:YAG laser ablation in liquid.
Invest. Ophthalmol. Vis. Sci., 31:2546:1990.

2. Isner J.M., De Jesus S.R., et al.
Mechanism of laser ablation in an absorbing fluid field.
Lasers in Surg. Med., 8:543:1988.

3. Wallach-Kapton R., Saar et al.
Cutting of biological tissue underwater by laser: Using the 'cavitation effect'.
SPIE., 1202:317:1990.

4. Van Leeuween T., Vander Veen M.J., et al.
Non contact tissue ablation by Ho:YSGG laser pulses in blood.
Lasers in Surg. Med., 11:26:1991.

5. Srinivasan R., Casey K.G., Haller J.D.
Subnanosecond probing of the ablation of soft plaque from arterial wall by 308nm laser pulses delivered through a fibre.
IEEE., J.QE., 26:2279:1991.

6. Yarborough J.M.
Taking confusion out of matching medical lasers to applications.
Photonics Spectra, p.88:Oct. 1992.

7. Lauterborn W., Bolle H.
Experimental investigations of cavitation-bubble collapse in the neighbourhood of a solid boundary.
J. Fluid Mech., 72:391:1975.

8. Stigeo F., Akamatsu T.
Effects of the non-equilibrium condensation of vapour on the pressure wave produced by the collapse of a bubble in a liquid.
J. Fluid Mech., 97:481:1980.

9. Tomita Y., Shima A.
Mechanisms of impulsive pressure generation and damage pit formation by bubble collapse.
J. Fluid Mech., 169:535:1986.

10. Blake J., Taib B., Doherty G.
Transient cavities near boundaries. Part I. Rigid boundary.
J. Fluid Mech., 170:479:1986.

11. Vogel A., Lauterborn W., Timm R.
Optical and acoustic investigations of the dynamics of laser-produced cavitation-bubbles near a solid boundary.
J. Fluid Mech., 206:299:1989.

12. Bourne N., Field J.
Shock-induced collapse of single cavities in liquids.
J. Fluid Mech., 244:225:1992.

13. Young F.R.
Cavitation.
McGrow Hill (Oxford) 1989.

14. Lauterborn W.
Finite amplitude wave effects in fluids.
Ed. Bjorno L., IPS Science and Tech. press, 1974.

15. Teng P., Nishioka S., et al.
Acoustic studies of the role of immersion in plasma-mediated laser ablation.
IEEE J.QE., 23:1845:1987.

16. Flowers B.H., Mendoza E.
Properties of matter.
Wiley (London), 1970.

17. Hale G.M., Querry M.R.
Optical constants of water in the 200nm to 200μm wave-length region.
Appl. Opt., 12:555:1973.

18. Parker J.M., France P.W.
Properties of fluoride glasses - Chapter 2 in Fluoride glass optical fibres.
Ed., P.W. France, Blackie (Glasgow), 1990.

19. Coleman A., Saunders J., et al.
Acoustic cavitation generated by a extracorporeal shockwave lithotripter.
Ultrasound in Med. and Biol., 13:69:1987.

20. Askaryan G.A., Prokhorov G.F., et al.
The effects of a laser beam in a liquid.
Sov. phys. JETP., 17:1463:1963.

21. Daree K.
Photochemical blooming of laser beams.
Opt. Comm., 4:238:1971.

22. Bell I.E., Landt J.A.
Laser-induced high pressure shockwaves in water.
Appl. Phys. Lett., 10:46:1967.

23. Barnes P., Rieckhoff K.
Laser-induced underwater sparks.
Appl. Phys. Lett., 13:282:1968.

24. Felix M.P., Ellis A.T.
Laser-induced liquid breakdown: a step-by-step account.
Appl. Phys. Lett., 19:484:1971.

25. Lauterborn W.
High-speed photography of laser-induced breakdown in liquids.
Appl. Phys. Lett., 21:27:1972.

26. Ward B., Emmony C.
Conservation of energy in the oscillations of laser-induced cavitation bubbles.
J. Acoust. Soc. Am., 88:434:1990.

27. Emmony D.C., Geerken B., Stranijer A.
The interaction of 10.6um laser radiation with liquid.
Infra. Phys., 16:87:1976.

28. Sigrist M.W., Kneubuhl F.K.
Generation of acoustic waves in liquids by pulsed lasers.
J. Acoust. Soc. Am., 64:1652:1978.

29. Emmony D.C., Geerken T., Klein-Battink.
Laser-generated high-frequency sound waves in water.
J. Acoust. Soc. Am., 73:220:1983.

30. Emmony D.C.
Interaction of IR laser radiation with liquids.
Infra. Phys., 25:133:1985.

31. Ward B., Emmony D.C.
Interferometric studies of the pressures developed in a liquid during infrared laser-induced cavitation-bubble oscillation.
Infra. Phys., 32:489:1991.

32. Ell C., Hochberger J., Miller D., et al.
Laser lithotripsy of gallstone by means of pulsed Nd:YAG laser-invitro and animal experiments.
Endosc., 18:92:1986.

33. Teng P., Nishioka S., et al.
Mechanisms of laser-induced stone ablation.
SPIE Proceedings, 72:161:1987.

34. Engolhardt R., Meyer W., Hering P.
Spectroscopy during laser-induced shockwave lithotripsy.
SPIE., 906:200:1988.

35. Steiger E.

A Q-switched Alexandrite laser for laser-induced shockwave lithotripsy (LISL).

Laser in Surg. Med., 2:43:1988

36. Yashima Y., Mcauliffe S., et al.

Lasers Surg. Med., 11:62:1991.

37. Borirakchanyavat S., Puliafito C.A., et al.

Holmium-YAG laser surgery on experimental vitreous membranes.

Arch. Ophthalmol., 109:1605:1991.

38. Whitacre M., Mainster M.

Hazards of laser beam reflections in eyes containing gas.

Am. J. Ophth., 110:33:1990.

Conclusions

In this thesis the possibility of optical fibre delivery of UV excimer and 2.3 - 3μm IR (HF) lasers under conditions suitable for the ablation of biological and organic materials was studied. Etch rate and photoacoustic measurements have been used to study the ablation process for both tissue and polymer samples. Wide bandwidth piezolectric transducers based on PVDF film enabled laser induced pressure transients to be investigated in tissue in both below and above threshold regimes. This method allows valuable information on the interaction to be obtained such as, for example, on the subthreshold laser attenuation coefficient in tissue (excimer lasers only) and the timescale and the magnitude of stress waves generated by the rapidly ablated material (excimer and HF lasers).

In Chapter 3 the experimental work was concerned with the coupling of UV radiation into different types of fused silica fibres and an investigation of their transmission properties for XeCl (308nm), KrF (248nm) and ArF (193nm) laser radiation. It was found as expected that the energy transmission decreased exponentially with increasing length of fibre. These losses are produced by absorption at impurities and defects and also by scattering. By far the best transmission was obtained for 308nm radiation using Superguide PCS rather than ordinary PCS fibre; this was shown by the smaller distributed loss co-efficient of 1.4×10^{-3} cm^{-1} for Superguide PCS compared with 2×10^{-3} cm^{-1} for ordinary PCS. This improvement is attributed to the purer core material of

the former fibre. Likewise the lower transmission of HCN fibre compared with PCS fibres is due to its higher level of core impurities.

The variation of the energy transmission with length for Superguide 'G' fibre was studied with the 248nm laser at various fluences. A transmission of more than 90% at 85mJcm^{-2} for a 15cm long fibre was achieved but as the fluence was increased to 460mJcm^{-2} and 2800mJcm^{-2} this decreased to just below 70% and 60%, respectively. This is mainly due to non-linear absorption at the front surface of the fibre which results in increased end losses associated with coupling energy into and out of the fibre. Results obtained with the ArF laser showed there was a severe limitation on transmission even at moderately low fluences. For example, the transmission of a 20cm Superguide PCS 600μm fibre was only about 50% at 60mJcm^{-2} and at 470mJcm^{-2} the transmission dropped to about 5%. As a result fibre-delivered ArF laser is restricted to use at low fluences which limits its useful ablation studies to materials that exhibits a low ablation threshold. This is unfortunate as the ArF laser produces exceptionally clean and well defined incisions in many tissues which makes it attractive for surgical applications.

In chapter 4 these fibres were utilized to study the ablation of organic polymers such as PET and Kapton, and biological lens tissue. The etch rate measurements and photoacoustic results were used to derive effective absorption coefficients and thresholds fluences for ablation with the fibre delivered excimer lasers (Tables 4.1 and 4.2). SEM photographs were also used to evaluate the ablation sites

produced with these lasers. It was found that highest etch rates were obtained using 308nm and the fibre tolerated much longer exposure compared with shorter wavelengths. The KrF (248nm) laser showed a relatively high transmission through Superguide 'G' fibre for ablation of tissue but was limited to low input fluences (eg. $\leq 2 Jcm^{-2}$). Very smooth incisions were obtained with the ArF laser but as noted above it was severely limited in terms of output fluence ($\leq 0.2 Jcm^{-2}$) and fibre lifetime hence restricting its practical uses.

Since the carcinogenic effects of UV excimer lasers are not completely resolved much attention has recently been given to development and application of pulsed mid-IR lasers as alternative sources for tissue ablation. Wavelength in the 2-3μm region where tissue, by virtue of its large water content, exhibits strong absorption are of particular interest. This is because the small absorption depth shown by analogy with the excimer lasers lead to very precise ablation. CO_2 lasers provide an alternative source but the delivery fibre limits their usefulness. Although lasers such as Er:YAG and Ho:YAG have already extensively been used for different clinical applications these studies have been restricted to long pulse durations (250μs) which leads to a relatively large thermal damage zone. To pursue this idea a short pulse (400ns), multiwavelength (2.6-2.9)μm HF laser was constructed (Chapter 5) to see if similar quality of incisions to those with the excimer lasers could be achieved.

In Chapter 6 studies of the delivery of pulsed HF laser radiation through a fluoride glass fibre ($\sim$500μm core) were reported. The experiments showed that this type of optical

fibre can be used to deliver the multiline HF laser at suitably high output fluences ($\leq$7Jcm^{-2}) for ablation of tissues. The distributed attenuation was measured to be 0.15 $\pm$ 0.03m^{-1} (0.65dBm^{-1}) which is close to but somewhat higher than specified by the manufacturer for this wavelength region (ie. $\sim$0.1dBm^{-1}, $\sim$2-3μm). This higher value for the pulsed laser is probably a result of the high irradiance levels involved $\geq$1MWcm^{-2} which enhance non-linear losses. The transmission measurements also revealed that the laser input and output coupling losses to the fibre were fluence dependent. This was confirmed by the photoacoustic measurements which showed fibre end losses were fluence dependent and set a maximum useful input fluence of $\sim$15Jcm^{-2}. Separate experiments showed that the full-angle for beam divergence from the fibre was $\sim$140mrad which is essentially identical to the range of input angles for the optical arrangement used (ie. $\sim$140mrad for an effective aperture ratio of 7).

It has been demonstrated in Chapter 7 that ophthalmic tissues (eg. bovine cornea, lens and retina) can be ablated in air and saline using the direct and fibre delivered HF laser. Etch rate measurements and photoacoustic studies were again used to provide information on the effective absorption coefficient and threshold fluences for these materials. SEM evaluation of the interaction zone was also carried out for specific tissue samples. For bovine cornea SEM evaluation of the irradiated site showed that the fibre-delivered HF laser produced sharply defined incisions. This is consistent with the high effective absorption coefficient in this spectral region (2-3μm) and the short laser pulse duration

which minimizes heat transfer to adjacent tissue. With the contacted fibre a peripheral zone of influence was evident in the SEM photographs which is attributed to the containing effect the fibre has on the ablation products. This region extends over a width ($\sim$100μm) comparable to that of the fibre cladding and coating. For multishot exposure at 5Jcm^{-2} observable damage of the cornea in saline only occured at distances $\leq$250μm.

Also it has been shown in chapter 7 that damage to retina can occur with 400ns HF laser pulses delivered by a fibre in saline with the fibre tip positioned beyond 2mm from this tissue. Bubble growth is not fast enough to clear water between the fibre tip and sample at this range on the timescale of the laser pulse and the bubble cannot act as a transmissive cavity for the IR radiation. The dynamics of cavitation 'bubbles' have been investigated using pulsed dye laser shadowgraphy for various fibre-tissue geometries and results in free liquid modelled using the Rayleigh-Plesset theory. Time resolved photoacoustic measurements have also been made and revealed that very large transient pressures are generated in tissue near the fibre tip when ablation occurs in liquid; for example, at 8Jcm^{-2}, peak pressures reached about 1.5×10^{8} Pa. When the fibre-to-tissue spacing was varied physical surface damage was evident out to distances of $\sim$250μm for cornea and 2mm for retina. As these are much greater than the characteristic beam absorption length in water ($\sim$1.6μm), the main damage mechanism is then not through photoablation but jetting or acoustic emission associated with optical cavitation.

For the cornea this matter could not be determined from the shadowgraphs because of the small spatial scale involved so it is necessary to estimate from theoretical considerations whether water clears the intervening space. Since the clearance time of saline from the fibre tip (4μs) is much longer than the laser pulse, therefore it is suggested that even for the small distances involved for the cornea water will remain in the vicinity of the fibre tip on the timescale of the laser pulse and attenuate the beam. This conclusion is qualitatively supported by the morphology of the damaged surface which differs significantly from that produced by direct HF laser photoablation.

It is reasonable to deduce from disruption of normal tight packing of the fibrils at a distance from the fibre tip for both cornea and retina that either impingment of the hot vapour cavity and associated jetting effects, large amplitude acoustic waves or possibly their combination is responsible for this. Given the relatively low energy content of acoustic waves generated in the initial expansion phase of the cavity and the lack of any clear mechanistic origin for 'ablative' damage by such waves it is tentatively concluded that energy transferred to the surface by the cavitation bubble is the main source of this damage. It should be noted, however, that acoustic waves can damage tissue cells over a large range despite their low energy for material removal when ablation takes place in a confined liquid as in this case. The ablation rate for cornea with the contacted fibre in saline falls well below that for air particularly at high fluence (eg. at $5Jcm^{-2}$ this is 0.8μm per pulse which is about ten

times lower). A possible explanation for this behaviour is that gaseous ablation products remain trapped in the shallow ablation cavity and prevent water from filling this cavity.

Some preliminary work has also carried out using the fibre delivered HF laser to ablate polyimide (R and S type Upilex). For this polymer ablation thresholds were relatively high (1-2Jcm^{-2}), and an incubation effect was observed. Material removal became significant only above 5Jcm^{-2} which is close to upper limit of the fibre capability and the quality of material removal was poor. Unlike for excimer and CO_2 lasers wavelengths, polyimide is relatively weakly absorbing at 2-3um and direct heating and degradation of the bulk polymer cannot explain ablation. A mechanism based on particle mediated absorption appears to provide the most likely explanation of the cummulative growth of absorption and ulitmate 'ablation' of this polymer.

Flouride fibres have been shown to be suitable for pulsed HF laser delivery, although at the large diameter used (500μm core) they proved to be very fragile and were easily destroyed by handling. As a future work it would be of interest to study the possibility of delivery submicro-second pulses through smaller core diameter fibres with better flexibility. These could also have the advantage of reducing the damage range associated with cavitation bubbles and acoustic transients generated at the fibre tip when working in a fluid. The smaller effective acoustic source size would lead to a more rapid transition to three-dimensional acoustic wave expansion and hence sharper fall off in pressure with distance. The disadvantage, however, would be lower tissue

volume removal rates although this could, in principle, be offset by the use of a high repetition rate laser which could operate at low energies because of the reduced energy input needed for the fibre. Whether or not this laser offers a viable alternative to solid-state devices such as Er:YAG for applications such as incising the intra-ocular scar tissue or membranes requires investigation.

Publications and Conferences:

Papers:

P.E. Dyer, M.E. Khosroshahi, S. Tuft
Optical fibre delivery and tissue ablation studies using a pulsed HF laser.
Lasers in Med. Sci., 3:331:1992.

P.E. Dyer, M.E. Khosroshahi, S. Tuft
Studies of Laser-induced cavitation and tissue ablation in saline using a fibre-delivered HF laser.
Appl. phys. B, 56:84:1993.

Conferences:

Ablation studies using photoacoustics
P.E. Dyer, R.K. Al-Dhahir, M.E. Khosroshahi
Gordon conference on photoacoustical and photothermal phenomena, June 1992 (USA).

Membrane ablation using a HF infrared laser: practical consideration.
S. Tuft, P.E. Dyer, M.E. Khosroshahi
Ablation congress of opthalmology,
Sept. 1992, Sydney (Australia).

Tissue ablation studies in air and saline using a fibre-delivered HF laser.
P.E. Dyer, M.E. Khosroshahi, S. Tuft
Cleo (SPIE), May 1993, Baltimore, Maryland (USA).